INVESTIGATION AND ANALYSIS OF FLOWS IN FLOTATION CELLS USING EXPERIMENTATION, COMPUTATIONAL FLUID DYNAMICS SIMULATIONS, AND MATHEMATICAL MODELS

by

Manjunath Basavarajappa

A dissertation submitted to the faculty of
The University of Utah
in partial fulfillment of the requirements for the degree of

Doctor of Philosophy

Department of Metallurgical Engineering
The University of Utah
May 2017

The University of Utah Graduate School

STATEMENT OF DISSERTATION APPROVAL

The dissertation of **Manjunath Basavarajappa**
has been approved by the following supervisory committee members:

Sanja Miskovic ,	Chair(s)	**05 May 2016** Date Approved
Jan D. Miller ,	Member	**05 May 2016** Date Approved
Michael Simpson ,	Member	**05 May 2016** Date Approved
Chen-Luh Lin ,	Member	**05 May 2016** Date Approved
Terry Arthur Ring ,	Member	**05 May 2016** Date Approved

by **Manoranjan Misra** , Chair/Dean of
the Department/College/School of **Metallurgical Engineering**
and by **David B. Kieda** , Dean of The Graduate School.

ABSTRACT

Froth flotation is a highly complex, multiphase, and multiscale process that is usually performed in large tanks called mechanical flotation cells. The aim of this research is to investigate the single and multiphase flow hydrodynamics in lab scale flotation cells by decoupling the hydrodynamics from physicochemical effects. Both experimental and numerical approaches are used to study the behavior of flows in lab and pilot scale flotation cells. Nonintrusive experimental techniques such as particle image velocity (PIV) and electrical resistance tomography (ERT) techniques are used to measure flow velocities, solids holdup, mixing efficiency, and to interpret flow pattern. Eulerian-Eulerian computational fluid dynamics (CFD) models are developed and tested for solid-liquid (slurry) and gas-liquid flows in stirred tanks and flotation cells.

Using single phase CFD simulations, the effect of flotation specific impeller blade shape and impeller size on mean flow and pumping behavior is tested in lab scale flotation cells for the first time. In the absence of a stator, the mean flow is found to transition from radial to axial type flow when the off-bottom clearance is below the critical value. This prediction is experimentally verified using time averaged PIV data. Based on the analysis of pumping and power number data, the rectangular shaped blade design is found to be the most efficient. The impeller blade shape is found to critically affect the flow in the vicinity of the impeller and a design with the largest surface area is needed to create an intense turbulence zone, needed for mixing and dispersion of incoming air. Eulerian-Eulerian CFD model is used to study the solid phase suspension and mixing characteristics for monosized silica particles. Experimental comparison with the results from the literature for stirred tanks and in-house ERT measurements suggest that the model performs reasonably well.

Population balance equation model (PBM) is coupled with CFD to study gas dispersion, mixing, and local bubble size distribution in the stirred tank and flotation cell

using quadrature method of moments (QMOM) approach in ANSYS Fluent solver. The default QMOM model in Fluent is found to be inaccurate due to independent solution of moment transport equations and therefore is supplied with a moment correction algorithm from the literature to successfully identify and correct the invalid moment sequence during the CFD simulation. The new model is found to be superior to the current models in its ability to satisfactorily predict the overall gas holdup and local bubble size distribution for stirred tanks under moderate aeration and agitation rates. This model is extended to study the development of flow regimes based on the gas dispersion pattern in a generic flotation cell. Though highly useful, the coupled CFD-PBM approach is computationally intensive and requires considerable effort to achieve an accurate solution. This motivated us to develop a PBM based on the high-order moment conserving method of classes (HMMC) approach for a pilot scale XCELL^{TM} flotation cell for frother concentration over critical coalescence concentration, thus, only considering breakage of bubbles. Nonlinear optimization solvers in Matlab are used to calculate the point estimates of adjustable parameters in breakage models. The 95% bootstrap calculated using empirical bootstrap indicates very high confidence in estimated parameters. The HMMC model provides an accurate description of steady state bubble size distribution and the mean number diameters only using overall gas holdup and specific energy as inputs.

To my parents.

CONTENTS

ABSTRACT iii

LIST OF TABLES x

ACKNOWLEDGEMENTS xii

CHAPTERS

1. INTRODUCTION AND OUTLINE **1**

1.1 Introduction 1
1.2 Thesis Outline 3

2. NUMERICAL AND EXPERIMENTAL INVESTIGATION OF SINGLE PHASE FLOWS IN STIRRED TANKS USING RUSHTON TURBINE AND FLOTATION IMPELLER **8**

2.1 Abstract 8
2.2 Introduction 9
2.3 Tank/Cell Configuration and Impeller Geometry 11
2.3.1 CFD Simulations 11
2.3.2 PIV Experiments 12
2.4 Computational Methodology 13
2.5 Governing Equations and Turbulence Models 13
2.5.1 Governing Equations 13
2.5.2 Turbulence Models 14
2.6 Results and Discussion 15
2.6.1 Rushton Turbine Flow Characteristics and Validation 15
2.6.2 Flotation Impeller: Validation 16
2.6.3 Flotation Impeller: General Flow Characteristics 17
2.6.3.1 Flotation Impeller: Effect of Turbulence Model 19
2.6.4 Flotation Impeller: Effect of Impeller Size 20
2.6.4.1 **FI-75** 20
2.6.4.2 **FI-100** 21
2.6.4.3 **FI-150** 22
2.6.5 Flotation Impeller: Effect of Off-Bottom Clearance 23
2.6.6 Power Number Calculation 25
2.7 Conclusions 26

3. NUMERICAL SIMULATION OF SINGLE PHASE FLOW IN FLOTATION CELLS - EFFECT OF IMPELLER OFF-BOTTOM CLEARANCE, BLADE SHAPE, AND REYNOLDS NUMBER **40**

3.1 Abstract . . . 40
3.2 Introduction . . . 41
3.3 Tank Configuration and Impeller Design . . . 43
3.4 Computational Methodology . . . 44
3.5 Governing Equations and Turbulence Modeling . . . 45
3.5.1 Governing Equations . . . 45
3.5.2 Turbulence Modeling . . . 46
3.6 Results and Discussion . . . 47
3.6.1 Validation of Numerical Approach . . . 47
3.6.2 General Flow Characteristics - $C = 50$ mm . . . 48
3.6.3 Effect of Impeller Design, $C = 50\ mm$ . . . 51
3.6.4 Effect of Impeller Design, $C = 25\ mm$ . . . 53
3.6.5 Mixing in Flotation Cells . . . 54
3.6.6 Performance of Flotation Impellers - Power and Flow Numbers . . . 55
3.6.6.1 Power Number Calculation . . . 56
3.6.6.2 Flow Number and Pumping Efficiency . . . 57
3.7 Conclusions . . . 58

4. NUMERICAL INVESTIGATION OF MODERATELY DENSE SLURRIES IN FLOTATION CELL USING EULERIAN-EULERIAN SIMULATIONS . . . 76

4.1 Abstract . . . 76
4.2 Introduction . . . 77
4.3 Systems Investigated . . . 81
4.4 Numerical Model . . . 82
4.4.1 Governing Equations . . . 83
4.4.2 Computational Domain . . . 85
4.4.3 Drag Correlations . . . 85
4.4.3.1 Fluid-Solid Exchange Coefficient . . . 85
4.4.3.2 Gidaspow Model . . . 86
4.4.3.3 Schiller-Naumann Model . . . 86
4.4.3.4 Brucato Correlation . . . 86
4.4.3.5 Modified Brucato Drag Correlation . . . 87
4.4.3.6 Pinelli Drag Correlation . . . 87
4.5 Results and Discussion . . . 87
4.5.1 Validation of Numerical Approach . . . 88
4.5.2 Qualitative Validation . . . 89
4.5.3 Mean Flow - Flotation Cells . . . 90
4.5.4 Effect of Particle Size and Agitation Rate . . . 92
4.5.4.1 160 Micron Particles . . . 92
4.5.4.2 520 Micron Particles . . . 94
4.6 Performance Analysis in Flotation Cells . . . 96
4.7 Conclusions . . . 98

5. USING ELECTRICAL RESISTANCE TOMOGRAPHY MEASUREMENTS AND CFD SIMULATIONS TO STUDY SOLID PHASE SUSPENSION AND MIXING 113

5.1 Abstract 113
5.2 Introduction 114
5.3 Experimental 116
5.3.1 Electrical Resistance Tomography 116
5.3.2 Experimental Details 117
5.4 Numerical Approach 119
5.5 Results and Discussion 120
5.5.1 Grid Independence Study 120
5.5.2 Eulerian-Eulerian CFD Predictions vs. ERT Measurements 121
5.5.3 Mixing Evaluation 123
5.5.4 CFD-DEM Predictions 124
5.6 Conclusions 125

6. INVESTIGATION OF THE GAS DISPERSION CHARACTERISTICS IN STIRRED TANK AND FLOTATION CELL USING A CORRECTED CFD-PBM QUADRATURE BASED MOMENT METHOD APPROACH 135

6.1 Abstract 135
6.2 Introduction 136
6.3 Numerical Model and Solution Strategy 140
6.4 Population Balance Equation 143
6.4.1 Bubble Breakage and Coalescence Kernels 145
6.4.2 Moment Sequence Corruption and Solution Procedure 146
6.4.3 Reconstruction Using Log-Normal Distribution 149
6.5 Tank/Cell Design and Operating Conditions 150
6.5.1 Stirred Tank Design 150
6.5.2 Flotation Cell Design 150
6.5.3 Flow Regimes - Flotation Cells 151
6.6 Results and Discussion 151
6.6.1 QMOM Correction 151
6.6.2 Grid Convergence Study - Stirred Tank 152
6.6.3 Predicted Bubble Sizes and Gas Holdup - Stirred Tank 154
6.6.4 Mean Flow and Gas Dispersion Behavior in Flotation Cells 157
6.6.5 Predicted Bubble Size Distribution - Flotation Cell 159
6.7 Conclusions 162

7. A HIGH-ORDER MOMENT-CONSERVING METHOD OF CLASSES (HMMC) BASED POPULATION BALANCE MODEL FOR MECHANICAL FLOTATION CELLS 176

7.1 Abstract 176
7.2 Introduction 177
7.3 Population Balance Model 181
7.3.1 High-order Moment Conserving Method of Classes 183
7.3.2 Breakage Modeling 185

7.4 Experimental Methods 188
7.5 Results and Discussion 190
7.5.1 HMMC Model Development 191
7.5.2 HMMC Model Extensibility 195
7.5.3 Breakage Model Comparison 196
7.5.4 Uncertainty in Predicted Parameters 197
7.5.5 Discussion and Future Work 199
7.6 Conclusions 200

8. SUMMARY AND RECOMMENDATIONS 217

8.1 Summary 217
8.1.1 Comments on Flotation Cell Design 219
8.2 Recommendations 220

9. WORKS CITED 223

LIST OF TABLES

2.1 Power number values calculated from torque τ ($N_{p\tau}$) and turbulence energy dissipation rate ϵ ($N_{p\epsilon}$) values obtained from CFD simulations. . 39

3.1 Power and flow numbers for different impeller designs 75

4.1 Variation coefficient σ_v, suspension quality χ, and power number $N_{p\tau}$ for flotation cell flows. 112

5.1 Details of the grid independence study used for Eulerian-Eulerian slurry flow simulations 134

6.1 Details of meshes used in grid convergence study and predicted holdup and diameters at impeller rotation speeds of 300 and 390 RPM and gassing rate of 0.7 vvm. 174

6.2 CFD predicted power number for different meshes along with power number predictions from correlations. The ratio of gassed to ungassed power consumption obtained from CFD predictions and correlations are also given. 174

6.3 Impeller agitation rate, superficial velocity, characteristic dimensionless numbers, overall gas holdup, and regime classification for different flow conditions considered in this work. The highlighted cases have been chosen for further analysis as shown in Figures 6.11 - 6.14. 175

7.1 HMMC model parameters used for optimization and model prediction. 212

7.2 PBM prediction versus experimental measurements of number mean and Sauter mean diameters using *Individual* optimization approach. All the parameters are estimated using *lsqnonlin* solver. The parameter values for two operating conditions at $V_{tip} = 6$ m/s are obtained by averaging optimized parameter values at V_{tip} values of 5 and 7 m/s. For Alopaeus model, k_3 is not fitted but fixed (*) based on recommendations from Laakkonen et al. [1]. 213

7.3 PBM prediction versus experimental measurements of number mean and Sauter mean diameters using *Common-Speed* optimization approach. All the parameters are estimated using $fmincon$ solver. The parameter values at $V_{tip} = 6$ m/s are obtained by averaging optimized parameter values obtained at V_{tip} values of 5 and 7 m/s. 214

7.4 PBM prediction versus experimental measurements of number mean and Sauter mean diameters using *Combined* optimization approach. All the parameters are estimated using $fmincon$ solver. The parameter values at $V_{tip} = 6$ m/s are obtained by averaging optimized parameter values obtained at V_{tip} values of 5 and 7 m/s. 215

7.5 95% CIs for breakage model parameters estimated using *Coupled–Speed* optimization approach and $fmincon$ solver. Bootstrap resampling technique with 500 repetitions is used to calculate the CIs. The original point parameter estimates are reported in Table 7.3. 216

ACKNOWLEDGEMENTS

I would like to thank my advisor Dr. Sanja Miskovic for taking me as a doctoral student and providing constant motivation and guidance over the last four years. I am also indebted to Dr. Terry Ring for his help with providing experimental setup for PIV experiments and answering my questions related to population balance models. I take this opportunity to thank Dr. Jan Miller to being a great teacher and mentor in our department. I would like to thank Dr. Misra for helping me out with funding issues during the last two years of my PhD and for giving me an opportunity to teach the Fluid Flow course.

I had a great group of friends in Salt Lake City and each one of them has directly or indirectly helped me during my time in SLC. I would like to especially thank Meenakshi for her help during many difficult times and for her support and friendship. I would also like to thank my close friends, Mani and Sriram, for their help over the years. I have been fortunate to make some good friends in our department and many have helped me at critical times. I would like to thank Haidong, Vu, Nakul, Kaustubh, and Veeren for their help.

I would like to thank Sarah, Kay, and Evelyn for doing their best in helping me with various administrative related issues over the years. I am also thankful to my committee members, Dr. Lin and Dr. Simpson, for agreeing to serve on my committee. I would also like to thank CHPC staff, especially David Heidorn for his help.

Finally, I am grateful to my parents and my brother, who have always encouraged and supported me.

CHAPTER 1

INTRODUCTION AND OUTLINE

1.1 Introduction

Froth flotation is a very widely utilized mineral extraction and separation process in which valuable minerals are separated from gangue or commercially worthless minerals in flotation cells. Mechanical flotation cells are a specialized class of equipment in which the froth flotation process is carried out by mixing ground ore particles in water and finely dispersed air bubbles. The valuable minerals are naturally hydrophobic or made hydrophobic by adding flotation reagents such as collectors, which helps in the formation of successful contact between valuable minerals and bubbles upon collision. The particle loaded air bubbles rise due to the action of buoyancy and facilitate the transport of valuable minerals from pulp to froth phase after which they are washed and sent for further processing.

The flow inside the mechanical flotation cell is multiphase (water + solid particles + air bubbles) and highly turbulent in nature [2–4]. Moreover, chemical reagents such as collectors, frothers, and conditioners among others affect the behavior of dispersed phases (solid particles and bubbles) considerably, making the system highly complex and introducing another level of complexity [2, 3, 5]. It is impossible to study the flotation process considering all its complexities and therefore one or more contributing factor needs to be studied separately to gain better understanding of this complex physico-chemical process.

In this work, recent developments made in both experimentation and numerical modeling areas are applied to single and multiphase (solid-liquid and gas-liquid) flows in lab scale flotation cells. Noninvasive and nonintrusive measurement techniques such as particle image velocimetry (PIV), electrical resistance tomography (ERT), and video analysis are used to make experimental measurements. The PIV technique is used to measure mean velocity components and flow patterns in stirred tanks

using flotation impeller and to study the effect of off-bottom clearance on mean flow behavior. The ERT technique is used to quantify the solid particle suspension and mixing behavior by measuring the solid phase concentrations at different axial positions in a lab scale flotation tank for slurry flows. Also, cloud height measurements are made by analyzing images taken from video recording of the transient behavior of particle cloud inside a Plexiglas flotation cell. The experimental measurements aided in the understanding of the complex flow hydrodynamics in lab scale flotation cells. More importantly, the data from the experimental measurements are used to validate the CFD and mathematical models developed and used in this work.

Over the past two decades, computational fluid dynamics (CFD) has evolved into a strong tool that is widely used to model and simulate complex flows in scenarios where making experimental measurements is often difficult [6]. However, the CFD models need to be thoroughly validated for specific geometry/design and flow type by carefully selecting submodels through experience and systematic testing, before they can be applied to generic cases such as flotation cell [6–8]. In this work, CFD methodologies are developed for single phase flows and the numerical methodology is validated by comparing the CFD predictions against PIV data. Power number and pumping number data along with passive scalar mixing simulations are used to compare the performance of impeller blade shapes. Significant mass fractions of solid particles are introduced in flotation cells. Understanding dispersed phase behavior at different operating conditions is essential for predicting the performance of flotation cells and guiding the development of novel designs. To this end, Eulerian-Eulerian and Eulerian-Lagrangian simulations of moderately dense and dilute slurry flows are performed in lab scale flotation cells. The numerical approach is validated by comparing predictions against experimental measurements made using ERT technique and cloud height measurements. Moreover, the numerical model used in our study is also validated for flows in stirred tanks. The validated CFD model is used to study homogenization behavior and identification of dead zones in flotation cell, which is not possible through traditional experimental approaches.

The gas-liquid flows in both lab and pilot scale flotation cells have been extensively studied experimentally by many groups [4, 5, 9, 10]. However, the development of

numerical models has been limited to the group led by Koh and co-workers, who have mainly performed experimental and numerical studies in proprietary flotation cell designs to develop their numerical models [3, 11, 12]. The application of CFD models to generic flotation cell design is seriously lacking in literature. In this work, population balance model (PBM), which is a mathematical framework for efficiently tracking the properties of a population of particles, is considered with CFD to study gas dispersion and mixing in flotation cells. Coupled CFD-PBM model using the quadrature method of moments (QMOM) approach is first validated for stirred tanks by comparing predicted air holdup and local bubble size distribution (BSD) against measurements reported by Laakkonen et al.[1]. Next, the model is used to study the effect of operating conditions such as aeration rate and impeller rotation speed on resulting flow regimes and bubble size distribution in a generic flotation cell design.

The CFD-PBM model, though very useful in providing detailed flow and mixing information in the flotation cell, still ends up being computationally expensive and requires specialized correction routines to make accurate predictions. Since the bulk frother concentration in flotation cells is near the critical coalescence concentration (CCC), it is reasonable to model the entire flotation cell as a homogeneous system. This assumption is frequently made when reporting bubble size distribution data for flotation cells [5, 9, 13, 14]. A high-order moment-conserving method of classes (HMMC) based PBM is developed by considering three breakage rate models from the literature. The experimental BSD measurements made in a pilot scale XCELL^{TM} (0.8 m^3) flotation cell are used to calculate adjustable parameter values found in the breakage rate equations utilizing optimization solvers in Matlab programming language. Different optimization approaches are explored and the developed model is found to satisfactorily predict overall BSD and number mean diameters (D_{10}). However, the Sauter mean diameters (D_{32}) are under-predicted because the HMMC predicted number frequencies are under-predicted at larger bubble classes.

1.2 Thesis Outline

The chapters of this thesis are written as papers with the intention of submitting them to peer-reviewed journals. Different chapters included in this thesis are in

different stages of journal publication. Since each of the chapters is written as a paper, every chapter contains an extensive literature review and background material on the topic of interest along with pertinent conclusions. Therefore, in the interest of avoiding redundant text, a standalone literature review chapter is not included in this thesis. However, a final chapter summarizing the major findings of this work and recommendations for future work are given. The outline of the rest of the thesis is as follows:

- **Chapter 2:** In this study, CFD simulations are performed to study single phase turbulent flow generated by flotation impeller in stirred tank considering different geometric variations. Reynolds number (Re) of the flow based on impeller diameter is varied between 29,000 – 120,000, which falls under the turbulent regime. Two–dimensional Particle image velocity measurements are made on an axial plane near the impeller to validate the CFD approach. The normalized velocities are found to be invariant with flow Re both through simulations and experiments. On the changing the impeller off-bottom clearance from 100 to 60 mm, the mean flow transitioned from radial to axial-type flow, a behavior previously reported for Rushton turbine impeller. This mean flow transition is correctly predicted by the CFD model and verified through local velocity measurements and velocity vectors. Using CFD data, power numbers for flotation impellers are predicted and the drop in power number on flow transition is also captured.

- **Chapter 3:** The impeller blade shapes play a key role in determining the local flow behavior and turbulence level close to the impeller. Using the numerical model established in the previous chapter, a series of CFD simulations are performed to understand the flow and mixing characteristics in a lab scale flotation cell. Four impeller blade shapes of varying surface area and lip lengths, reflecting the general shapes used in the industrial designs, are considered. The blade with shortest lip length resulted in comparatively higher axial velocity component close to impeller. Both radial and tangential velocities are found to be high close to impeller with tangential velocities dropping significantly on

encountering the stator blades for all designs. Existence of asymmetric trailing vortex is confirmed through visualization of vorticity and swirling strength contours. The largest values of turbulence kinetic energy and its dissipation rate are found close to impeller blades and on the stator walls, where the radial jet interacts with stator. The change in off-bottom clearance from 50 to 25 mm showed no noticeable change in mean flow behavior. Based on the comparison of power number and pumping number data, the rectangular blade shape is found to be most efficient.

- **Chapter 4:** CFD simulations and ERT measurements are made to investigate the mixing and suspension characteristics of moderately dense slurry flows in lab-scale flotation cells. The Eulerian-Eulerian two fluid model (TFM) is validated both for stirred tank and flotation cell flows. For stirred tank, the CFD approach is validated by comparing the mean solids concentration from the measurements of Micheletti et al. [15] against CFD predictions for monosized particles of 600 microns. For flotation cell, by comparing the CFD predicted solids concentration and in-house ERT measurements along with comparison of cloud heights, the CFD model is further validated. The effect of drag model on CFD prediction is analyzed and based on the comparison for stirred tank geometry, the models proposed by Gidaspow and Brucato are found to perform better than other models. Using the developed CFD model, the behavior of the dispersed phase is studied at different operating and geometric conditions. The slip velocities are found to be significant only in the close vicinity of the impeller. Also, large gradients in solids concentration are observed close to impeller where the particles have a tendency to segregate into bands. Moreover, both CFD predictions and ERT measurements are used to study mixing behavior at different operating conditions by calculating global homogeneity values and mixing indices.

- **Chapter 5:** A coupled CFD-PBM approach is proposed that is capable of accurately predicting gas holdup and local bubble size distribution. The QMOM approach is used to solve the moment transformed population balance equations

coupled with a correction algorithm to identify and correct corrupt or invalid moment sequences in ANSYS Fluent solver. The choice of drag model is found to critically affect the accuracy of the numerical solution. Based on preliminary investigations in stirred tank, the drag model proposed by Lane et al. [16] is found to perform satisfactorily over other models. The model is first validated by comparing the predictions against measurements of Laakkonen et al. [1] made in stirred tanks. Next, the numerical approach is used to characterize development of different flow regimes at different operating conditions. Using the moments obtained from the QMOM solution, number and Sauter mean diameters (SMD) are calculated. Also, two reconstruction techniques are used to reconstruct the full BSD from moments at four discrete locations in the flotation cell. Small bubbles are observed to form close to the impeller in the highly turbulent region. These bubbles recirculate in the lower part of the cell before finally rising along the wall. Larger bubble sizes are observed in the upper part of the cell where low turbulence levels facilitate bubble coalescence.

- **Chapter 6:** A high-order moment-conserving method of classes (HMMC) based population balance model is developed for pilot scale flotation cell that is capable of accurately predicting full bubble size distribution and mean diameters from moments of the predicted distribution. Experimental measurements of bubble size distributions made in the past by Miskovic [4] are used to calculate the adjustable parameters in the PBM. All the experimental measurements are made for gas-liquid flows using methyl isobutyl carbinol (MIBC) frother at bulk concentration of 20 parts per million (PPM), which is over critical coalescence concentration [9, 17, 18]. Therefore, only breakage terms are retained in the resulting population balance equation. Three breakage rate models proposed in the literature for gas-liquid flows that have adjustable parameters, which can be adapted for flows in flotation cells are considered. Nonlinear optimization solvers in Matlab namely, $fmincon$ and $lsqnonlin$ are used to minimize the objective function and calculate the point estimates of the adjustable parameters using three optimization strategies. The developed model is found to provide

accurate description of bubble size distribution with satisfactory prediction of bubble diameter corresponding to peak number frequency value, across all the optimization procedures. Moreover, the 95% confidence intervals are calculated for point estimates using empirical bootstrap technique and the resulting confidence intervals are found to lie within 1.5% of point estimate values, suggesting very high confidence in calculated parameters.

- **Chapter 7:** An overall summary of the work is presented along with the recommendations for future work, both based on further development of models presented in this work and a pathway for doing fundamental experimental measurements and simulations to develop better understanding of breakage and coalescence processes specific to flotation process.

CHAPTER 2

NUMERICAL AND EXPERIMENTAL INVESTIGATION OF SINGLE PHASE FLOWS IN STIRRED TANKS USING RUSHTON TURBINE AND FLOTATION IMPELLER

2.1 Abstract

In this study, computational fluid dynamics (CFD) simulations are used to investigate turbulent single phase flow characteristics in lab-scale stirred tanks with different geometric variations. Water at standard conditions is used as operating fluid. Rushton turbine (RT) and flotation impeller (FI) are used to agitate the fluid leading to turbulent flows in the tank. For FI, impeller diameter, d, is varied and three sizes corresponding to d values of 75, 100, and 150 mm are considered. Additionally, for 75 and 100 mm FI, off-bottom clearance, C, is varied from 100 ($D/3$) to 60 mm ($D/5$). The impeller based Reynolds number, Re, ranged from 29,000 to 120,000. CFD results are compared with LDA data from the literature for RT and in-house PIV data for FI. CFD predictions for FI are found to match experimental measurements satisfactorily with accurate prediction of flow transition at lower C. The normalized flow properties are observed to be invariant with Re for both impellers in fully turbulent regime. Mean flow characteristics for FI suggests that the flow is characterized by strong radial and tangential velocities close to impeller with peak values along disc level. Turbulence kinetic energy profiles close to impeller are characterized by two peaks suggesting development of trailing vortex which is further verified using swirling strength visualization. For FI with diameter equal to 100 mm, flow transition in which mean flow changes from radial flow (double loop) to axial-type (single loop) flow is observed when C is reduced. Both PIV measurements and CFD simulation are able to predict this transition accurately. Using both torque on rotating parts

and volume averaged dissipation rate of turbulence kinetic energy, power numbers are calculated for both impellers. The axial-type flow at smaller clearance is marked by significant drop in power number value.

2.2 Introduction

Stirred tanks are extensively used in chemical, pharmaceutical, oil and gas, and minerals and metallurgical industries or blending, suspending, contacting, and dispersing applications. The flows generated in the stirred tanks are predominantly turbulent due to high impeller rotation speeds used to achieve necessary process conditions. Radial impellers are mainly used for dispersion and mixing applications and for processes that require high values of turbulence kinetic energy (k) and turbulence energy dissipation rate(ϵ) [19]. Various factors like tank size, impeller shape, impeller size, number of impeller blades, number of blades, and off-bottom clearance affect the flow in stirred tanks. Recently, Joshi et al. [19, 20] reviewed CFD results reported in the literature for single and multiphase flows in stirred tanks using radial and axial impellers, respectively. Furthermore, Joshi et al. [19] compared results predicted by different turbulence models with experimental laser Doppler anemometry (LDA) measurements. Joshi et al. [20] have reviewed all the widely used modeling approaches in the literature and summarized the shortcomings associated with each of them. Based on their comparison of CFD predictions and experimental measurements, they recommend using large eddy simulation (LES) to obtain accurate predictions of turbulent quantities in the impeller region. However, LES is still very expensive for industrial size tanks at high Reynolds numbers and requires modeling of filtered scales that are not completely resolved.

For the radial impellers, the off-bottom clearance plays an important role in determining the type of flow pattern that is developed. Montante et al. [21, 22] have investigated the effect of changing clearance for Rushton turbine and noticed the mean flow to transition from double-loop to single-loop type as the clearance is suitably reduced. Li et al. [23] have conducted particle image velocimetry (PIV) measurements and LES of stirred tank flows by varying impeller sizes, Re, and clearance. Consistent with the observations of Montante et al.[22], transition of flow

from double to single-loop type at low clearance is also reported by [22, 23]. Li et al. [23] varied the impeller diameter from one-third to one-half of tank diameter, D, at constant clearance of 0.15 times tank height, H, and Re equal to 64,000. Li et al. [23] reported the critical clearance at which flow transitions to strongly depend on impeller diameter. Furthermore, Li et al.[23] recommended using a smaller sized impeller for single-loop flow. Galletti et al. [24] have made experimental measurements of Reynolds stresses in the impeller region using 3-D LDA. They found the highest levels of turbulence anisotropy not only close to impeller but also close to vessel bottom and near the centers of the flow recirculation loops.

Recently, Murthy et al. [25] have performed numerical simulations to assess different turbulence models in stirred tanks agitated by both axial and radial impellers. They found LES to predict the flow most accurately and Reynolds stress model (RSM) to perform well in the recirculation region but under-predict k in the impeller region. More recently, Singh et al. [26] performed CFD simulation of Rushton turbine driven stirred tank at Re equal to 28,830. Singh et al. [26] reported that the two equation turbulence models do not predict the secondary vortex motions based on swirling strength isosurfaces visualization. Furthermore, they reported the two equation models to incorrectly predict the location of peak values for both k and ϵ. Of all the turbulence models considered, Singh et al. [26] recommend using shear stress transport (SST) model with curvature correction, which is a combination of $k-\epsilon$ and $k-\omega$ models. Gimbun et al. [27] argue that $k-\epsilon$ model is able to predict both radial and tangential velocities well except in the close vicinity of trailing vortices where the flow is extremely anisotropic. However, authors observed that $k-\epsilon$ under-predicted k close to impeller while detached eddy simulation (DES) provided a better prediction on a sufficiently fine grid. Recently, Basavarajappa and Miskovic [28] numerically investigated turbulent single phase flow developed by flotation specific impeller but provided no direct validation of their approach.

In the current work, steady state CFD simulations of turbulent single phase flows are carried out in lab-scale stirred tanks. The objective of this work is to use the CFD model to analyze flow generated by a generic flotation type impeller and validate the model against experimental measurements. Rushton turbine and flotation impeller

are used to agitate the fluid, and the impeller rotation is modeled using multiple reference frames (MRF) approach. Validation of numerical results is achieved by comparing CFD results with experimental measurements from the literature for RT. In-house 2D PIV experiments are performed for flotation impeller and mean x and y velocity components are compared with CFD results. The geometry of the FI used in CFD simulations and experiments matched to ensure comparison of identical systems.

The design of flotation impeller is entirely conceived by authors based on literature review, process characteristics, and experience, and the design is representative of flotation impellers employed in commercial flotation machines. Reynolds number in the range of 29,000 - 120,000 in the fully turbulent flow regime is used. Furthermore, for the flotation impeller study, impeller size, and clearance are varied to study their effect on averaged flow pattern. Turbulence in the flow is modeled using realizable $k-\epsilon$ model, which is better suited for rotating flows [29]. In addition to geometrical variations, an RSM turbulence model is used to study the effect of turbulence model on predictions. Based on the analysis of velocity and turbulence characteristics, average flow features produced by flotation impeller are summarized.

2.3 Tank/Cell Configuration and Impeller Geometry

2.3.1 CFD Simulations

A cylindrical tank of diameter, T, and tank height, H, both equal to 300 mm is used. The tank is closed at the top to avoid interaction with air which is a common practice employed for single phase simulations [30]. Four equally spaced baffles of width, $W = T/10$, are used to contain fluid rigid-body rotation and improve mixing efficiency. A six blade Rushton turbine (RT) of diameter, d, equal to 100 mm is used. A circular shaft of diameter equal to 20 mm ($D/15$) supports the RT. The clearance, C, defined as the distance from the tank floor to RT disc is kept constant at 100 mm ($D/3$). To avoid using full names of impellers tested, a concise notation with impeller name followed by its diameter is used in rest of the paper. Detailed schematic of $RT-100$ is shown in Figure 2.1(a).

For the flotation impeller (FI), the same tank, shaft, and baffle dimensions are used. FI has six blades supported from the disc. For FI with d equal to 100 mm,

blades are parallel to tank wall for 25 mm ($a = d/4$ for other sizes) and taper inwards towards shaft at an angle of 45^o. The vertical length of inclined part h is equal to 20 mm ($d/5$ for other sizes). A schematic of FI is shown in Figure 2.1(b) with design parameters a and h. To study the effect of blade size, three blade sizes with disc to tank diameter ratios, namely $d/D = 1/4$, $1/3$, and $1/2$ corresponding to d values of 75, 100, and 150 mm, respectively, are used. The other geometrical dimensions are proportionally varied for different sized impellers. The impellers are concisely named $FI-75$, $FI-100$, and $FI-150$. In addition to impeller size, off-bottom clearance for $FI-75$ and $FI-100$ is also varied by decreasing it from $D/3$ to $D/5$. A schematic of the stirred tank fitted with a FI is shown in Figure 2.2.

All the simulations presented in this work are for single phase flow and the working fluid used is water at 20^o ($293\ K$) and fluid is initially at atmospheric pressure. The Re of the flow is obtained using the impeller diameter as characteristic length scale, $Re = \mathrm{N}\rho d^2/\mu$, where, N is impeller speed in revolutions per second, ρ is fluid density in kg/m^3, d is impeller diameter in m, and μ is dynamic viscosity of fluid in kg/(s.m). All the flows considered have Re equal to 29,000 and over. Therefore, the flows fall under fully turbulent regime. Even though the flows are transient, the most important (mean) characteristics for turbulent flows can be studied by assuming steady state conditions.

2.3.2 PIV Experiments

PIV experiments are conducted in a clear plexiglass tank of diameter equal to 300 mm. The PIV system used in this work is manufactured by LaVision. The measurements are made on surface of approximately $116\ mm \times 116\ mm$. More than 700 image pairs are processed to obtain mean velocity and turbulent data. $FI-100$ impeller is used in the experiments at two C values of 100 and 60 mm. The shaft and the impeller mounting mechanism used in the experiments is different from the numerical geometry described earlier. The thickness of the impeller disc used in experiments is 13 mm and different attachment mechanism is used to secure the impeller to the shaft. The Re based on the impeller rotation speed is calculated to be 40,375.

2.4 Computational Methodology

The single phase flows are solved numerically using finite volume approach in ANSYS Fluent 14.5 commercial solver [29]. The computational mesh is created using mesh generation software ANSYS ICEMCFD 14.5. Mesh is made finer in the impeller swept region where the velocity gradients are expected to be high. Also, the mesh is made considerably finer around baffles to capture recirculation regions near them. For all the cases considered here, the total number of cells approximately varied between 500 k - 600 k. Based on the review of the literature [19] and grid sensitivity analysis, the mesh used in this work is expected to give accurate predictions of mean flow characteristics.

Second order discretization scheme is used for momentum and turbulent quantities. For pressure, PRESTO scheme is used, which is reported to provide better predictions for flows with strong swirl [29]. The velocity and pressure coupling is achieved using semi implicit method for pressure linked equations (SIMPLE) scheme. The under-relaxation factors are lowered at the beginning of the simulation to maintain stability and achieve solution convergence. The flow is assumed to be converged when the residuals of continuity dropped under 10^{-4} and 10^{-5} for velocity and turbulence quantities respectively. The impeller rotation is modeled using steady state MRF technique, which required splitting computational domain into two zones namely inner and outer zone or domain. The inner zone encloses the rotating impeller and its size is large enough to capture the rotational flow features close to impeller. The outer zone contains the stationary parts of the of the tank, like baffles, and models the effect of stationary parts where the effect of impeller can be ignored. The two zones exchange information through a mesh-interface created along the outer and inner boundaries of inner and outer zones, respectively.

2.5 Governing Equations and Turbulence Models

2.5.1 Governing Equations

To solve the flow inside stirred tanks, a discretized form of governing equations is solved. Solving mass and momentum conservation (Navier-Stokes, NS) equations provides the solution of primitive flow variables, namely the velocities and pressure. The velocity and pressure solutions are linked through the SIMPLE algorithm. Continuity

or mass conservation equation in cartesian co-ordinates (x,y,z) for incompressible flow is given by

$$\frac{\partial u}{\partial x} + \frac{\partial v}{\partial y} + \frac{\partial w}{\partial z} = 0 \tag{2.1}$$

The momentum conservation or NS equations for incompressible flow in cartesian co-ordinates (x,y,z) are given by:

$$\rho\frac{Du}{Dt} = \rho g_x - \frac{\partial p}{\partial x} + \mu\left(\frac{\partial^2 u}{\partial x^2} + \frac{\partial^2 u}{\partial y^2} + \frac{\partial^2 u}{\partial z^2}\right) \tag{2.2}$$

$$\rho\frac{Dv}{Dt} = \rho g_y - \frac{\partial p}{\partial y} + \mu\left(\frac{\partial^2 v}{\partial x^2} + \frac{\partial^2 v}{\partial y^2} + \frac{\partial^2 v}{\partial z^2}\right) \tag{2.3}$$

$$\rho\frac{Dw}{Dt} = \rho g_z - \frac{\partial p}{\partial z} + \mu\left(\frac{\partial^2 w}{\partial x^2} + \frac{\partial^2 w}{\partial y^2} + \frac{\partial^2 w}{\partial z^2}\right) \tag{2.4}$$

where, u, v, w are the fluid velocities in the x, y, and z directions and p is the local pressure. The details of SIMPLE algorithm and other numerical details are not provided here for brevity and can be found in [29].

2.5.2 Turbulence Models

The Reynolds averaged Navier-Stokes (RANS) equation is derived by splitting the instantaneous velocity and pressure components into average and random components and substituting them in the NS equations. The standard $k-\epsilon$ turbulence model involves solving transport equations for k and ϵ with relevant models for closing unknown terms. In the present work, realizable $k-\epsilon$, model which involves alternative formulation for turbulent viscosity and a modified transport equation for ϵ based on the transport equation of mean-squared vorticity fluctuation [29] is used. Realizable $k-\epsilon$ model is reported to perform better than standard $k-\epsilon$ model for flows with streamline curvature, vortices, and rotation, all of which are native to stirred tank flows. Therefore, realizable $k-\epsilon$ model is used for all the cases and the transport equations for k and ϵ are given by:

$$\frac{\partial}{\partial t}(\rho k) + \frac{\partial}{\partial x_j}(\rho k u_j) = \frac{\partial}{\partial x_j}\left[\left(\mu + \frac{\mu_t}{\sigma_k}\right)\frac{\partial k}{\partial x_j}\right] + G_k - \rho\epsilon \tag{2.5}$$

$$\begin{aligned}\frac{\partial}{\partial t}(\rho\epsilon) + \frac{\partial}{\partial x_j}(\rho\epsilon x_j) = \frac{\partial}{\partial x_j}\Bigg[\left(\mu + \frac{\mu_t}{\sigma_\epsilon}\right)\frac{\partial \epsilon}{\partial x_j} + \rho C_1 S\epsilon \\ -\rho C_2\frac{\epsilon^2}{k+\sqrt{\nu\epsilon}}\end{aligned} \tag{2.6}$$

where,

$$C_1 = \max\left[0.43, \frac{\eta}{\eta+5}\right], \eta = S\frac{k}{\epsilon}, S = \sqrt{2S_{ij}S_{ij}} \tag{2.7}$$

In Eqn. 2.6, G_k represents the generation of k due to mean velocity gradients. μ_t is turbulent viscosity. The model constant values are unchanged and their values are $C_{1\epsilon} = 1.44$, $C_2 = 1.9$, $\sigma_k = 1.0$, and $\sigma_\epsilon = 1.2$. LRR (Launder-Reece-Rodi) variant of Reynolds stress turbulence model (RSM) [29] is also considered for comparison with realizable $k-\epsilon$ model but the transport equations for RSM are not presented for RSM for brevity. For more information on the transport equations of turbulence models and associated constants, the reader is referred to the [29] and [31].

2.6 Results and Discussion

2.6.1 Rushton Turbine Flow Characteristics and Validation

The Rushton turbine, RT, or disk impeller is one of the mostly widely studied and used radial impellers. In this work, RT impeller simulations are carried out to validate the numerical methodology adopted. Figs. 2.3(a) and 2.3(b) show the experimental and CFD radial and tangential velocities normalized by tip speed at a radial distance of $1.064r$ ($r = d/2$) from the shaft axis. The experimental velocity measurements are from Wu and Patterson [32], which has been extensively used to validate CFD results in the literature. The normalized radial velocities are slightly under-predicted by CFD, but the profiles match qualitatively. Normalized tangential velocity is predicted more satisfactorily by CFD, though the axial location of peak is shifted below the disc level by a small amount. The reasons for under-prediction of velocities by CFD are mainly due to the difference in the impeller geometry (blade and disc thickness) and inability of $k-\epsilon$ model to accurately predict flow in the impeller region. In the current work, blade thickness t_b equal to 5 mm is used. However, this information is not provided by Wu and Patterson [32]; thicker blades are known to produce lower peak velocities and power numbers as reported by Rutherford et al. by [33]. Furthermore, the predictions of wider velocity profiles by CFD in comparison to experimental data can be attributed to differences in impeller and disc designs in present study and experiments of Wu and Patterson [32].

The k profiles normalized by the tip speed at different Re close to the impeller are shown in Figs 2.3(c) and 2.3(d). The normalized profiles are identical for all Re investigated (29,000 - 80,000). The two peaks predicted by CFD correspond to trailing vortex pair formed due to the impeller motion. The velocity and k profiles match other CFD results in the literature [22, 23, 25], and therefore the CFD model is established to provide satisfactory predictions for other radial impellers.

2.6.2 Flotation Impeller: Validation

PIV measurements are performed only for $FI - 100$ impeller and the results are compared against CFD predictions in Fig 2.4. It must be noted here that the design of the impeller used in PIV experiments differed from the design described previously for CFD simulations. For the impeller used in PIV experiments, the disc thickness is increased from 5 mm to 13 mm to secure the impeller to shaft and an attachment mechanism is used which resulted in a different shaft diameter close to impeller. These design modifications are included in the CFD model to ensure a close match between the geometries. These modifications in CFD model are only made for a particular case comparing CFD and PIV results, and a disc with 5 mm thickness and regular shaft is used for other CFD results. Using the PIV data, it is possible to estimate the temporal variance of velocity components by calculating standard deviation about the mean value. The shaded region in Fig 2.4 represents one standard deviation of velocity component on either side of the mean value. It is clear from the plots in Figure 2.4 that the highest temporal variation in velocity components is observed about peak value and the CFD predicted values are well within the range of values measured experimentally.

CFD predicted trends are identical to PIV measurements for x and y velocity components at both radial distances (5 and 15 mm from the blade tip) as shown in Figure 2.4 at both C values. In general, CFD predictions are in line with trends measured experimentally and fall within the range of values measured. For C value of $D/3$, the PIV measurements and CFD data agree well. However, PIV measured peak x velocity component (U_x) is lower compared with CFD predicted velocity at 15 mm at the disc level ($z = 0.1$ m). The y velocity components (U_y) at C equal to

$D/3$ are shown in Figs 2.4(c) and 2.4(d) and the agreement is only qualitative. The trends are correctly predicted at 5 mm, but the peak value is over-predicted below disc level. At 15 mm, the measured and predicted U_y do not match, especially around the disc region and only qualitative agreement is observed with lower velocities predicted by CFD in general. The differences observed U_y is attributed to inability of $k-\epsilon$ turbulence model to accurately predict mean velocity components especially close to impeller as previously reported by Singh et al.[26]. At lower C value of $D/5$, the peak velocity magnitudes are much lower compared with higher C due to transition of flow from radial to axial-type flow. The x velocity components predicted by CFD match the PIV measurements well along the disc region, though differences are obvious close to the tank floor. It is expected that the level of turbulence close to tank floor would be high as a result of interaction of jet with bottom wall. The differences in CFD predictions and PIV measurements near the bottom can again be attributed to inability of $k-\epsilon$ turbulence model to correctly predict mean flow in highly turbulent regions. Furthermore, U_y values predicted by CFD match the measurements at 15 mm but are over-predicted at 5 mm. Overall, the match between the CFD predictions and PIV measurements are found to be satisfactory and trends are correctly predicted by CFD, though close match is not observed in high turbulence region.

2.6.3 Flotation Impeller: General Flow Characteristics

The CFD predicted normalized axial, radial, and tangential velocities in axial direction at different radial distances from shaft axis for $FI-100$ and $C = D/3$ (100 mm) are shown in Figs. 2.5(a), 2.5(b), and 2.5(d). The normalized components in the axial direction are taken at radial distances of 5, 15, 30, and 50 mm from the blade tip corresponding to r = 55, 70, 80, and 100 mm from the shaft axis. All the CFD results discussed from here on are for impeller with disc thickness of 5 mm and regular shaft of 20 mm diameter. Normalized velocities are found to be invariant with impeller speed as demonstrated by radial velocity profiles in Figure 2.5(a). For clarity, only velocities at Re = 40,000 are presented for other components. The axial velocity shows interesting behavior close to the impeller. At r = 55 mm, the axial velocity is negative above the disc and positive below the disc. However, at r =

65 mm, the axial velocity is positive at disc level and its peak value is significantly higher compared to peak value at $r = 55$ mm. Very close to the impeller the upper and lower recirculation regions interact, and at the disc level upper recirculation pushes and forces the lower recirculation downward imparting negative axial velocity component. However, moving away from the impeller blade at $r = 65$ mm, the radial jet from the impeller is significantly stronger and therefore imparts a positive axial velocity due to pumping action of the larger disc. Moving further away from the blade tip, the axial component does not show much variation and shows almost no change with axial distance at $r = 100$ mm.

The normalized radial velocities in the axial direction are presented in Figure 2.5(a). The radial velocity component is highest close to the impeller at $r = 55$ mm as the momentum is effectively transferred from impeller blade to surrounding fluid but drops considerably at $r = 65$ mm. The radial component decreases further when moving away from the impeller blade at radial locations of 80 and 100 mm. As previously seen in the case of k profiles, the peak shifts in the axial direction implying the presence of some axial velocity component to the radial jet.

Normalized tangential velocity components are presented in Figure 2.5(d). Tangential velocity component is imparted to fluid due to the rotation of impeller blades. As expected, the peak tangential velocity is observed close to the impeller and the magnitude becomes considerably smaller away from the impeller. At $r = 100$ mm, the tangential component is very low and has a magnitude of less than 20% of tip speed. The tangential component causes shearing of flow close to impeller and results in the formation of trailing vortices. Also, away from the impeller, the radial component still retains significant magnitude compared with tangential component suggesting the jet initially has both radial and tangential behavior but becomes more radial in nature for $r \geq 80$ mm. The velocity vector plots shown later also highlight the behavior of flow close to the impeller. The strong axial component close to the impeller due to curving of the flow below the disc is clearly observed.

Fig 2.5(d) shows the k profiles in the axial direction normalized by the square of tip velocities for different Re for $FI - 100$ and $C = 100$ mm. As previously observed for the case of RT by Li et al. [23, 34], the normalized k profiles remain unchanged

after flow becomes fully turbulent for $FI - 100$. Based on the shape of the k profile at $r = 55$ and 65 mm, the presence of two trailing vortices can be verified by the peaks along the disc level $z = 100$ mm. Going from r value of 55 to 65 mm the value of k increases and the peaks are shifted in the axial direction and the strength of the lower vortex is fairly higher than the upper peak as evidenced by its longer peak. Moving further away from the blade tip at $r = 80$ mm, the peaks disappear leading to a single sharp peak above the disc level. At $r = 100$ mm, a parabolic profile with peak higher than the peak at $r = 80$ mm is observed. Based on the k profiles, it can be concluded that peak values of k are generated at a distance of about 15 mm from the blade tip, and the spatial location of peak values conforms with the position of trailing vortex pair in the flow.

2.6.3.1 Flotation Impeller: Effect of Turbulence Model

To study the effect of turbulence model on the velocity and turbulence component predictions, RSM is used for $FI - 100$ at $Re = 40{,}000$. RSM does not make the isotropic assumption of turbulence and is therefore expected to produce more accurate predictions compared with two equation derived turbulence models, like standard and realizable $k - \epsilon$ models. It should be noted that the same grids were employed for both turbulence models and no model parameters are varied.

By comparing the normalized k profiles (not included here) in axial direction at different radial locations, it is found that RSM model severely under-predicts k values almost by a factor of four between the axial distances of approximately 80-110 mm. The $k-\epsilon$ model is previously reported to dampen turbulence and under-predict turbulence levels close to the impeller region [20, 35]. Inability of RSM to give better predictions of k could be due to insufficient grid resolution close to the impeller which has been reported by earlier CFD studies of stirred tanks employing RT [35]. Normalized radial velocity profiles predicted by both turbulence models are shown in Figure 2.6. It can be clearly seen that both models perform equally well and predict identical values in most of the regions. However, some differences can be observed at $r = 100$ mm, with RSM predicting a slightly higher peak value which is shifted down slightly. Furthermore, the profile at r equal to 100 mm is much sharper as predicted by

RSM. Similar observations are made for normalized tangential velocities, with RSM predicting sharper profile away from the impeller. The normalized axial velocities are also identical close to the impeller but are slightly different at r equal to 85 and 100 mm.

2.6.4 Flotation Impeller: Effect of Impeller Size

Process and mixing requirements sometimes demand the use of different sized impellers. In the current work, the size of FI is varied to study the flow characteristics at equivalent Re. Three impeller diameters, d, equal to 75, 100, and 150 mm corresponding to d/D ratio of 1/4, 1/3, and 1/2 are used and named $FI-75$, $FI-100$, and $FI-150$, respectively. For $FI-75$ and $FI-100$ the off-bottom clearance is also varied - the variation in flow results as a result of clearance change is discussed in the following section. To keep the Re of the flow constant, the impeller rotation speed is suitably varied and flows correspond to Re of 40,000, 80,000, and 120,000 are investigated. It should be noted that for $FI-75$ the simulations did not converge for the highest Re of 120,000 since the tip speeds used are significantly higher. Therefore, results only for Re of 40,000 and 80,000 are presented here. The results presented in this section are only for clearance $C = 100$ mm.

2.6.4.1 FI-75

The smallest impeller size considered corresponds to one-fourth of tank diameter, D. To achieve the same Re across all the impeller sizes, $FI-75$ is rotated at considerably higher speeds. The higher speeds result in extreme shearing of flow close to the impeller and produce high levels of turbulence in the impeller discharge zone. As previously ascertained for $FI-100$, the normalized flow characteristics for $FI-75$ too remain invariant for fully turbulent flow. The velocities and k data in the axial direction are extracted at distance of 5, 15, 30, and 50 mm from the impeller tip, which corresponds to r equal to 42.5, 52.5, 67.5, and 87.5 mm from the shaft axis. Figure 2.7(d) shows the normalized k profiles. At $r = 42.5$ mm, two peaks are observed indicating the presence of a vortex pair. However, at $r = 52.5$ mm only single peak of higher magnitude is seen. The k magnitudes decrease further away from the blade. The normalized k values for $FI-75$ and $FI-100$ are comparable in

magnitudes, but the k peak location in axial direction does not vary appreciably for $FI-75$ in comparison with $FI-100$. This observation implies that the jet produced by $FI-75$ is more horizontal compared with $FI-100$. This is further established by comparatively lower normalized axial velocities for $FI-75$.

The normalized radial velocities are presented in Figure 2.7(a). The radial component is highest at $r = 42.5$ mm as evidenced by a sharp peak at the disc level. Moving away from the blade at $r = 52.5$ mm, the peak radial velocity falls by 33%. The radial velocities below the disc are negative due to the interaction of trailing vortex pair with radial jet. The radial velocity component decreases moving further away from blade tip and the profile becomes wider as seen at $r = 67.5$ and 87.5 mm. The peak values of radial velocities at all r locations nearly fall along the same axial position. Normalized axial velocities follow the expected trend with negative velocities above disc level close to impeller, and positive velocities for radial locations away from the impeller below disc level as shown in Figure 2.7(b). Normalized tangential velocities are presented in Figure 2.7(c) and follow typical trends previously observed for $FI-100$. Maximum tangential velocities are observed close to impeller and decrease rapidly moving away from it, which is previously observed for in the case of $FI-100$ as well. Radial velocities clearly dominate the flow away from impeller before the flow encounters the baffles.

2.6.4.2 FI-100

The general flow features produced by $FI-100$ are already discussed in the preceding section (Section 2.6.2). The impeller rotation results in the formation of a trailing vortex pair. Figure 2.9 shows the trailing vortices for a constant swirling strength of 0.2 and the isosurface is colored by k magnitude for all the impellers. It is clear from the isosurface plot that the lower vortex is slightly larger in size and originates from the angled edge of the impeller blade. Comparing the normalized velocities of $FI-75$ and $FI-100$, the peak normalized tangential velocities generated by $FI-100$ are higher compared with $FI-75$ at similar distances away from the blade tip. The peak normalized radial velocities are almost identical for $FI-100$ and $FI-75$ at a distance of 5 mm from the blade tip. However, the peak normalized radial

velocities at subsequent locations are smaller for $FI-75$, and the peaks for all the radial positions fall roughly along the same axial distance (z) for $FI-75$. For $FI-100$, the axial location of peak values of normalized radial and tangential velocities do not fall along the approximately similar z location, which can be attributed to development of considerable axial velocity in the jet.

2.6.4.3 FI-150

The normalized velocity component and k plots for $FI-150$ impeller at clearance $C = 100$ mm are presented in Figure 2.8. The normalized radial velocity component is very close to tip speed velocity V_{tip} at $r = 80$ mm. Unlike the two smaller impellers, the normalized radial velocity remains high for $r = 90$ and 100 mm. The strong radial velocity component for $FI-150$ can be attributed to the large surface area of the impeller blades and comparatively lower rotation speed of the impeller, which results in high radial velocity compared to tangential velocity. The behavior of normalized tangential velocities partially follows the trends observed for smaller impellers. The normalized tangential velocity is high at $r = 80$ and 90 mm and drops significantly for $r = 100$ mm. The peak normalized radial and tangential velocity values of $FI-150$ are significantly higher compared to peak values at similar radial locations for $FI-75$ and $FI-100$. The peak (positive) of normalized axial velocity for $FI-150$ at $r = 80$ mm is about 35 mm below disc level and is positive for the most part below disc level, suggesting the presence of upward flow stream close to the impeller blade. The axial velocity at $r = 90$ mm has both negative and positive peaks - the negative peak corresponds to the flow originating from the upper recirculation region and is located above the disc level. The positive peak due to the lower recirculation region is located slightly lower than the peak at $r = 80$ mm. The positive peak at $r = 100$ mm is shifted in the axial direction to disc level.

The normalized flow velocities and k are extracted along axial direction at radial distances of $r = 80$, 90, and 100 mm from the shaft axis, which corresponds to r value of 5, 15, and 25 mm from the blade tip. Consistent with flows observed for $FI-75$ and $FI-100$, the normalized flow components are identical across the investigated Re range for $FI-150$ (therefore, not included here). The normalized k profiles are

shown in Figure 2.8(d) and the two peaks observed for $FI-75$ and $FI-100$ close to blade tip are not as pronounced for $FI-150$, which is also evident from isosurface contours of swirling strength shown in Figure 2.9(c). The k magnitude of the lower peak value is only about 30% of the upper peak. However, at $r = 100$ mm, the k profile still has two peaks and the lower peak has higher value compared to the upper peak. Clearly, the distribution of k is dependent on the impeller size and shows remarkably different behavior for different impeller sizes.

Figure 2.9 shows the trailing vortices for $FI-75$ and $FI-100$ impellers for a constant swirling strength value of 0.2. Swirling strength provides information about the local rate of rotation of the flow and large values suggest region of high shear and vorticity. It should be noted that the $k-\epsilon$ turbulence model has a tendency to dampen large scale turbulent structures in the flow. Since all length scales are modeled, secondary vortex motions away from the impeller are not predicted for the chosen swirling strength as previously reported by Singh et al. [26]. In Figure 2.9, impeller blades and disc have been made semitransparent to allow visualization of isosurfaces colored by velocity magnitude. $FI-75$ and $FI-100$ have almost identical trailing vortex pairs shown by the isosurface of swirling strength value of 0.2. The lower vortex is visibly bigger than the upper vortex and can be seen to originate from the angled edge of the impeller blade.

2.6.5 Flotation Impeller: Effect of Off-Bottom Clearance

Off-bottom clearance, C, is also varied for $FI-75$ and $FI-100$ from C value of 100 to 60 mm. For $FI-100$, flows at Re equal to 40,000, 80,000, and 120,000, and for $FI-75$ flows at Re of 40,000 and 80,000, are investigated at both clearances in the CFD simulations. For $FI-75$, the flow behavior did not change with decrease in C from 100 ($D/3$) to 60 ($D/5$) mm and the radial flow is observed at both C. Both CFD predictions and PIV measurements showed this behavior for $FI-75$ impeller (not shown here). However, for $FI-100$, the flow transitioned from double to single loop flow with reduction of C. Similar observations have been made for RT of comparable size by many authors [23, 36].

The CFD predicted normalized velocities and k plots for $FI-100$ and $C = 60$ mm are presented in Figure 2.10. The CFD velocity vector plots for $FI-100$ at both C

values and Re of 40,000 are shown in Figure 2.11. Fig 2.12 shows the velocity vectors obtained using 2D PIV at both C values. It must be noted that the disc thickness in velocity vector plots for both CFD and PIV is 13 mm. The mean velocity contour plot with respective colobar and scale is also offered in this figure. It should be noted that the mean velocity is comprised of only two velocity components since the PIV measurements are performed only in 2D, which explains some differences observed, especially at C equal to $D/5$. Both PIV and CFD are able to predict the transition of flow correctly and it further demonstrates that MRF approach performs satisfactorily for flotation impellers.

The behavior of the jet can be better understood by observing the velocity vector plots in Figs. 2.11 and 2.12. The jet travels towards the tank floor and splits into two streams separated by a stagnation or elliptic point for both clearances; local high pressure regions are developed at stagnation points. For low C, lower recirculation loop is restricted to a region close to the impeller and can be characterized by an elliptical shape. The upper recirculation region extends all the way to the tank floor, with the center of the loop located below disc level. This type of flow transition for radial impellers was first observed, both experimentally and numerically, for Rushton impellers by Montante et al. [21, 36]. The transition of flow for FI shows that the transition is independent of the radial impeller design in general but depends largely on the impeller size and clearance values relative to the tank size. The transition of flow from double to single loop configuration leads to possibility of using lower clearances for two phase solid-liquid flows where off-bottom suspension of solid particles is critical to achieve high process efficiency. With maximum energy of the jet going to the tank floor, effective momentum exchange is possible between the fluid and dispersed phase, thus, optimally utilizing both mean and turbulent energy in the flow to suspend particles.

The effect of C can be evaluated by comparing the normalized flow variables and velocity vector plots in Figs. 2.10 and 2.11. At low C, normalized axial velocity profile at $r = 55$ mm transitions from negative to positive at approximate z value of 0.04 m. Peak value of axial velocity occurs around $r = 65$ mm and decreases for locations further away from the impeller blade. The axial position of the peak

axial velocity decreases along r suggesting that the jet is not parallel to the floor, but instead travels towards it. Normalized tangential velocities are high at $r = 55$ mm but drop significantly moving away from the impeller blade. At $r = 100$ mm, the tangential velocity is almost negligible at the disc level but increases slightly close to the tank floor. The normalized radial velocities are smaller in comparison to tangential velocities and their peak values can be seen shifting towards the tank floor at increasing r values. The flow transition results in lower radial and tangential velocities at lower C, value since the jet strikes the tank floor at an angle. Also, the velocity gradients are sharper close to the tank floor for $C = 60$ mm compared with $C = 100$ mm. The effect of decreasing C causes significant drop in power consumption as demonstrated by power number values for the two C in Table 2.1. More detailed numerical simulations are required to accurately predict the exact clearance at which the flow transition occurs from double to single loop configuration.

2.6.6 Power Number Calculation

Using CFD data, power numbers, N_p, are calculated for both RT and FI using two methods. In the first method, torque generated on rotating parts, namely, impeller blade, disc and shaft, is used to calculate power number $N_{p\tau}$ using Eqn. 3.10. In the second method, the turbulence energy dissipation rate (ϵ) is integrated over the entire flow domain to obtain $N_{p\epsilon}$ using Eqn. 2.9. The power number formulas are given by:

$$N_{p\tau} = \frac{2\pi N\tau}{\rho N^3 d^5} \tag{2.8}$$

$$N_{p\epsilon} = \int \frac{\rho\epsilon dV}{\rho N^3 d^5} \tag{2.9}$$

where, N is impeller rotational speed in rps, τ is the torque on impeller blades, ρ is the fluid density, d is the impeller diameter, V is the flow domain or tank volume. No experimental torque measurements are made. Therefore all the data presented here are from CFD predictions.

Table 2.1 shows the values of power numbers calculated using the two methods for all the cases considered in this work. Note that the impeller disc thickness is 5 mm for the power number data. The highest values of N_p are observed for the largest impeller $FI - 150$, which is $N_{p\tau} = 8.065$. All the calculated power number values

fall in the range expected for radial flow impellers as reported in [19] and references therein. For $FI-100$, the flow transitions from radial to axial-type flow causing $N_{p\tau}$ to drop by approximately 70%. The $N_{p\tau}$ values at $C = 60$ are representative of power numbers usually observed for axial flow impellers [20].

Figure 2.13 shows variation of $N_{p\tau}$ with Re for a few selected cases. Again, $N_{p\tau}$ values remain mostly constant over the Re range used in this study. Consistent with the observations of Singh et al. [26], the $N_{p\tau}$ are slightly larger than $N_{p\epsilon}$. Singh et al.[26] found ϵ values to be under-predicted by all the turbulence models considered in their work including the $k-\epsilon$ model. Therefore it is evident that $N_{p\epsilon}$ values are also under-predicted. Furthermore, $N_{p\tau}$ can be safely assumed to be more representative of true power numbers. Power number is known to decrease with increasing impeller blade thickness [33, 37]. The low values of N_p for RT are because of relatively thick blades (5 mm) used in this study. The N_p for $FI-100$ at 100 mm clearance is about 70% higher than N_p for RT across the Re range investigated in this work which quantifies the effect larger impeller surface and disc on power number magnitude.

2.7 Conclusions

Steady state CFD simulation results are presented for Rushton and flotation impellers (FI) in stirred tanks operated at different Re. Numerical model is tested by comparing CFD results with experimental measurements for Rushton turbine and flotation impellers respectively. Consistent with the findings for the Rushton turbine in the literature, normalized flow characteristics are found to be invariant with Re. Presence of trailing vortex pair behind the impeller blade is observed, but secondary vortex motions are not observed due to the inability of $k-\epsilon$ to correctly model small scale turbulent structures. For FI, impeller size, d, and off-bottom clearance, C, are varied. With the decrease in C for $FI-100$ impeller, flow transition from double (radial) to single-loop (axial) configuration is observed. The transition is not observed for smaller impeller $FI-75$, which suggests that impeller size and distance from the tank floor to the impeller base, c, may also affect the critical transition clearance. For $FI-150$, significant ϵ values are observed on the surfaces of the tank wall and baffles, implying that such large impeller sizes are unsuitable for lab-scale tanks especially

when operated at high speeds.

Reynolds stress model (RSM) is used for $FI-100$ at Re = 40,000 and its predictions are compared against the predictions of $k-\epsilon$ model. The normalized peak values of k predicted by RSM are found to be four times smaller than $k-\epsilon$ model at radial locations of $r = 55$ and 65 mm. The velocity components predicted by both the turbulence models are mostly identical for radial locations close to impeller but some deviations are observed for $r = 100$ mm. The use of a more complex, Reynolds stress turbulence model does not show any improvement in predictions at current mesh refinement level. Power numbers, N_p, are calculated using the CFD generated torque values, τ, on rotating parts (blade, disc, and shaft) and total ϵ value integrated over the tank volume. Large deviation is observed for $N_{p\epsilon}$ values calculated using RSM indicating severe underestimation of ϵ by RSM. Highest N_p values are observed for the largest impeller size and the magnitudes did not change appreciably with Re. For $FI-100$, the N_p decrease by almost 70% with the decrease in C from 100 to 60 mm as the flow transition from double to single loop configuration.

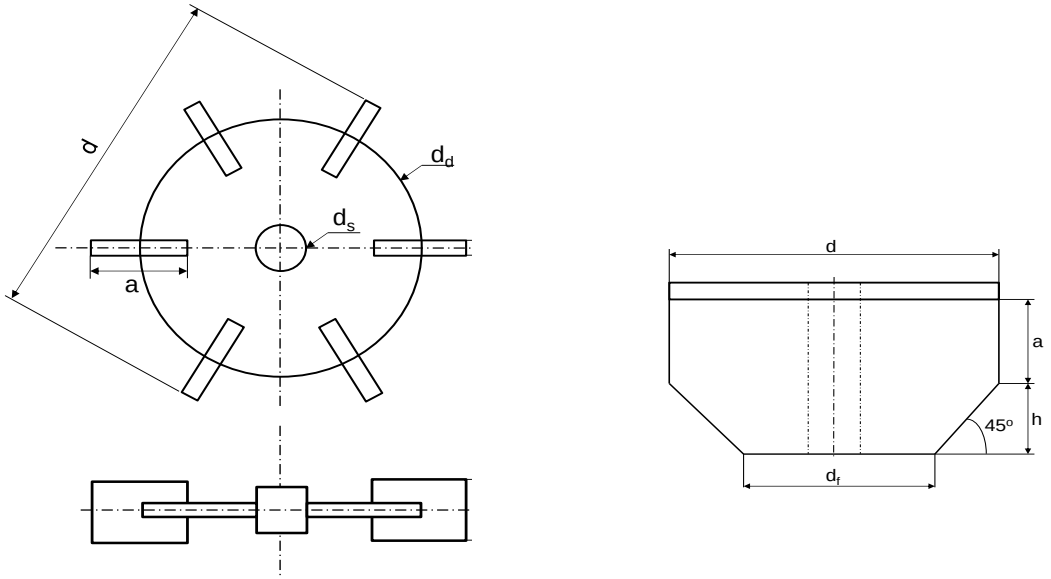

(a) Rushton turbine RT (b) Flotation impeller FI

Figure 2.1. Schematics of Rushton turbine RT and flotation impeller FI with relevant dimensional details.

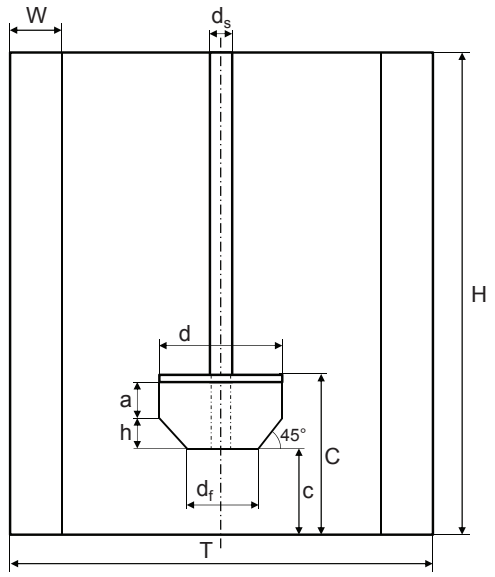

Figure 2.2. Schematic showing tank fitted with flotation impeller FI.

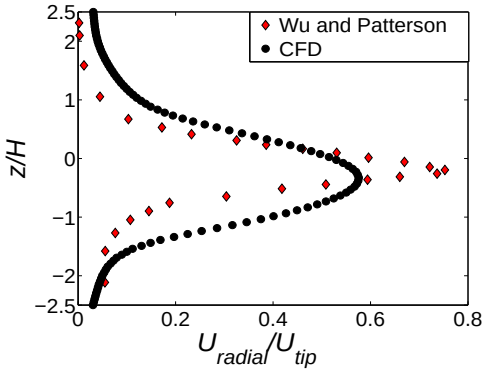

(a) Normalized radial velocity

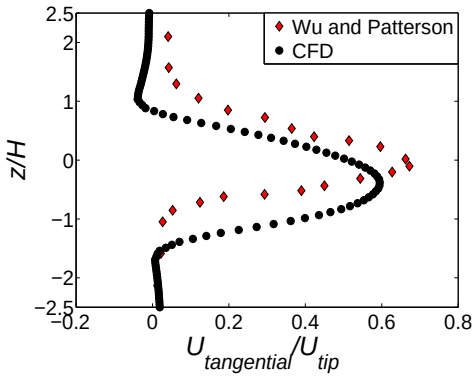

(b) Normalized tangential velocity

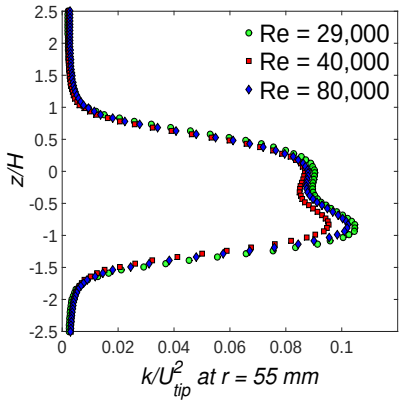

(c) Normalized k at $r = 55$ mm

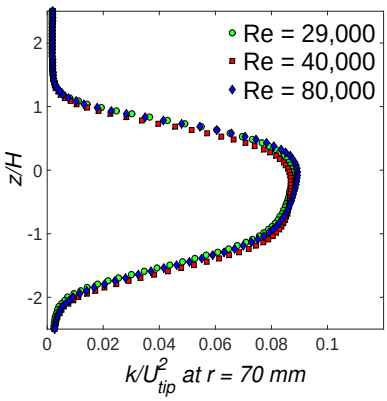

(d) Normalized k at $r = 70$ mm

Figure 2.3. Normalized axial profiles of velocity components and turbulence kinetic energy (k) for Rushton turbine impeller. Figs. 2.3(a) and 2.3(b) show the comparison of LDA and CFD results.

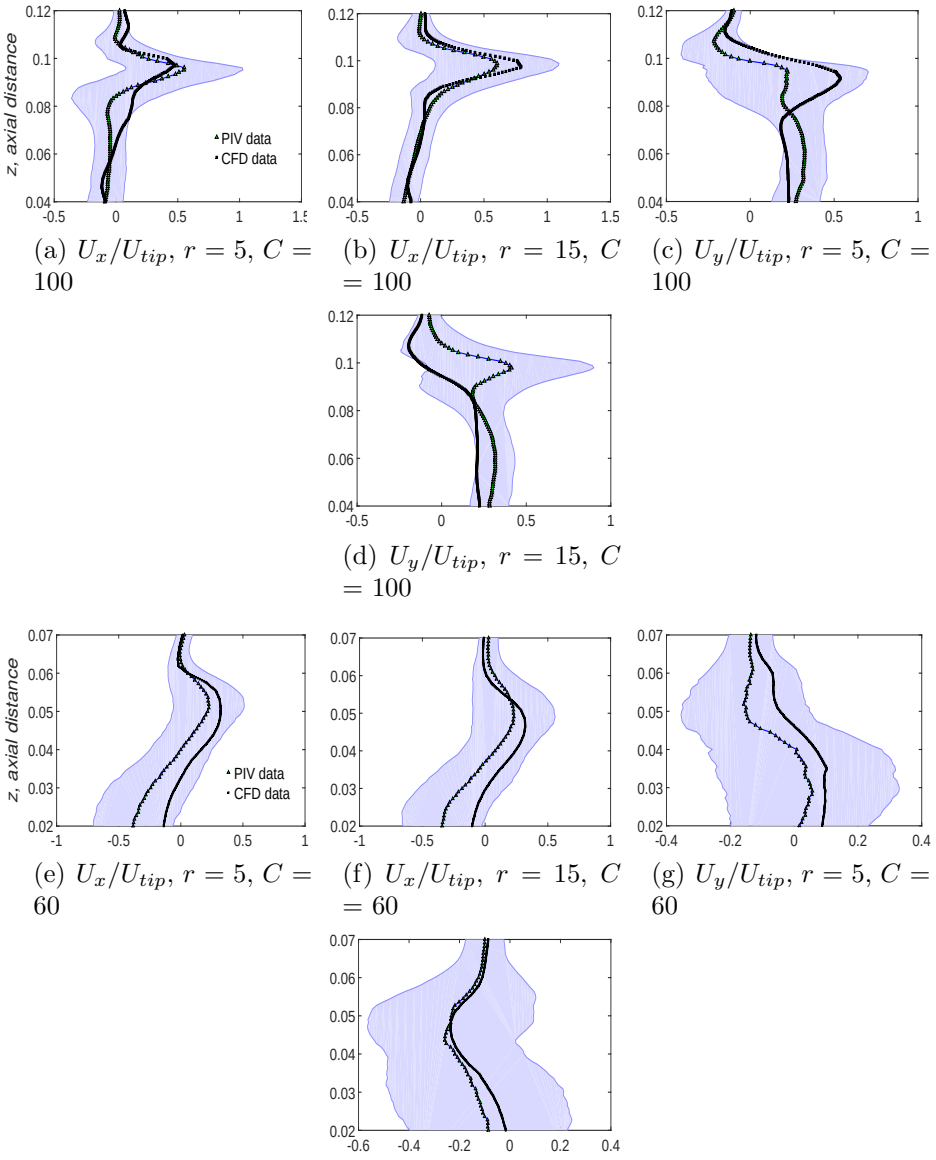

(a) U_x/U_{tip}, $r = 5$, $C = 100$

(b) U_x/U_{tip}, $r = 15$, $C = 100$

(c) U_y/U_{tip}, $r = 5$, $C = 100$

(d) U_y/U_{tip}, $r = 15$, $C = 100$

(e) U_x/U_{tip}, $r = 5$, $C = 60$

(f) U_x/U_{tip}, $r = 15$, $C = 60$

(g) U_y/U_{tip}, $r = 5$, $C = 60$

(h) U_y/U_{tip}, $r = 15$, $C = 60$

Figure 2.4. Normalized CFD and PIV velocity components for $FI-100$ at $C = 100$ mm and 60 mm and $Re = 40{,}000$ along with temporal variance of velocity components from PIV (shaded region around mean). Both r and C are in mm.

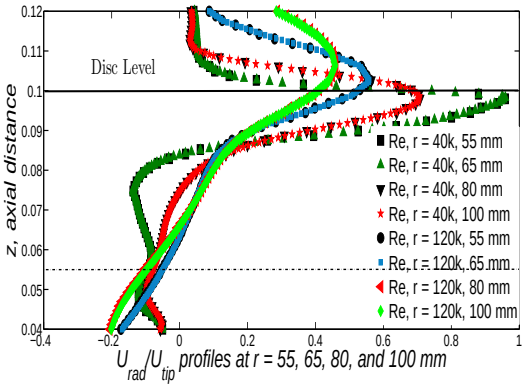

(a) Normalized radial velocity (U_{rad}) for $Re =$ 40 and 120k

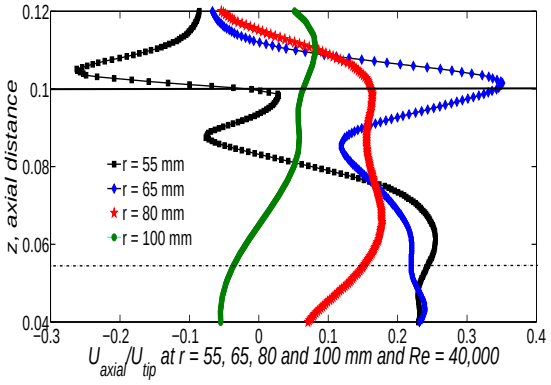

(b) Normalized axial velocity (U_{axial})

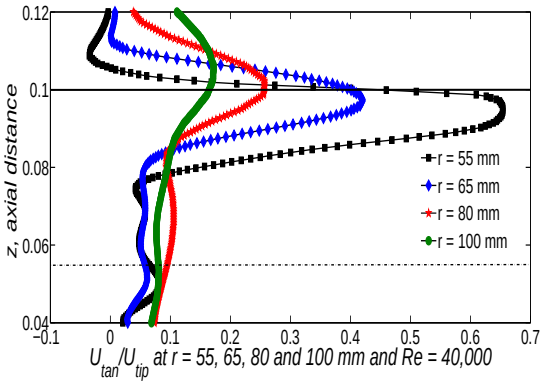

(c) Normalized tangential velocity (U_{tan})

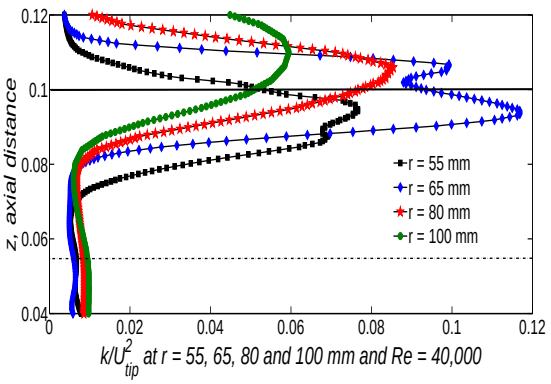

(d) Normalized k profiles

Figure 2.5. CFD predicted normalized flow characteristics for $FI - 100$ in the axial direction at different radial distances.

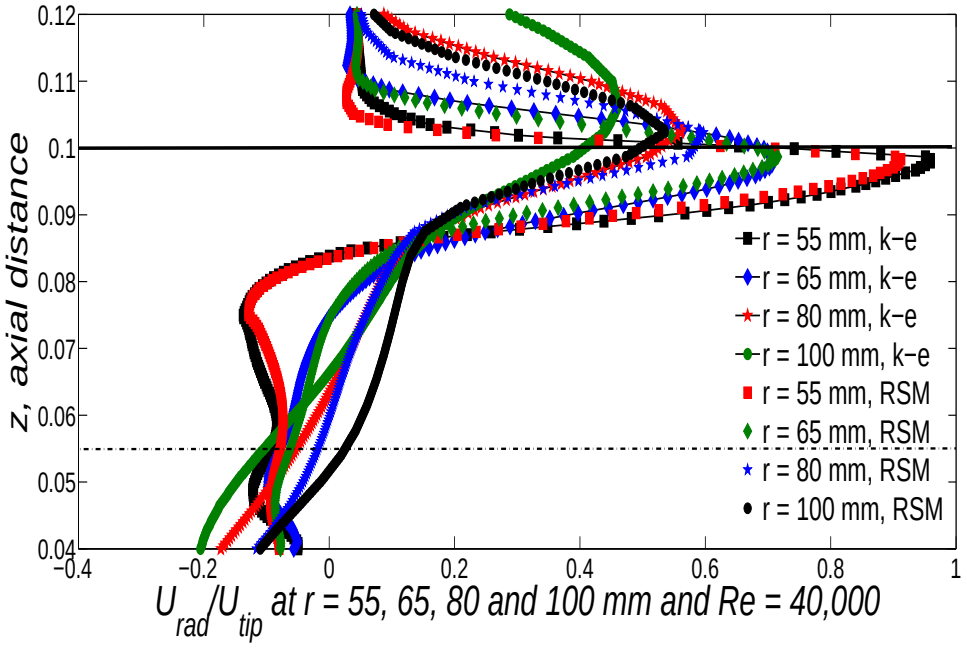

Figure 2.6. Comparison of CFD predicted normalized radial velocities from $k-\epsilon$ model and Reynolds Stress Model (RSM) for $FI-100$ at $Re = 40{,}000$.

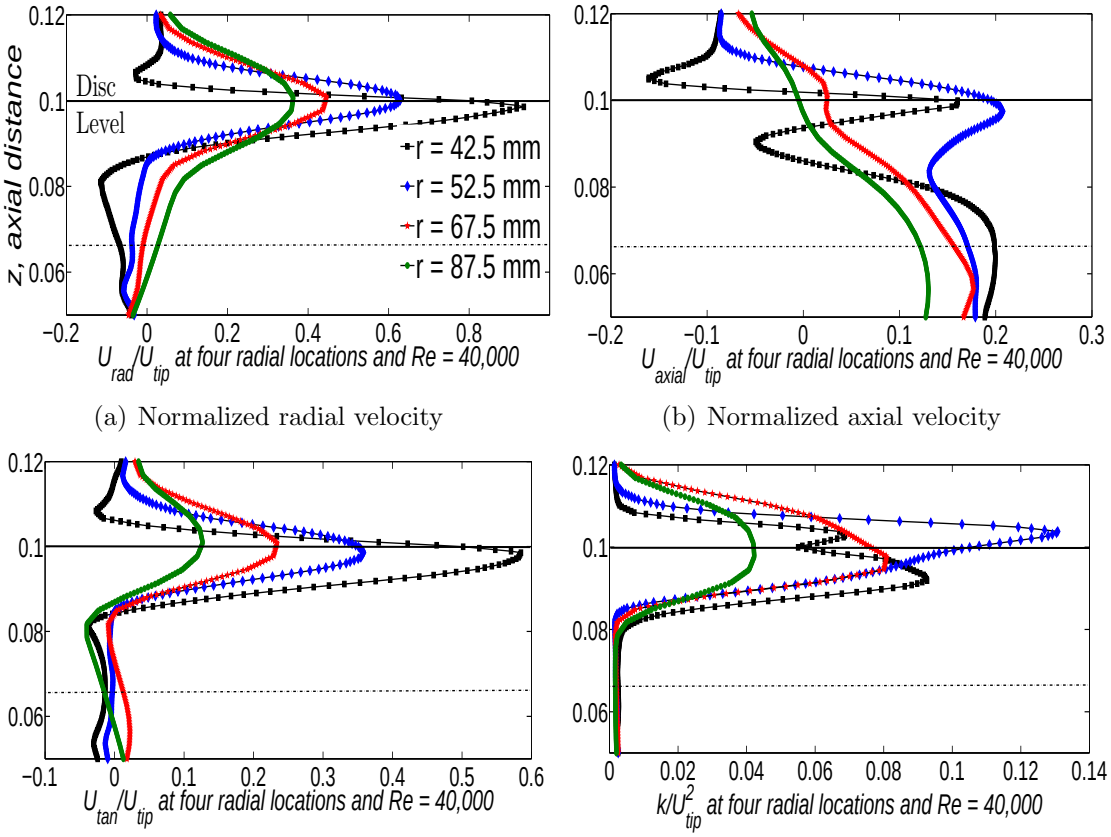

(a) Normalized radial velocity

(b) Normalized axial velocity

(c) Normalized tangential velocity

(d) Normalized k profiles

Figure 2.7. CFD predicted normalized flow characteristics for $FI - 75$ in the axial direction at different radial distances.

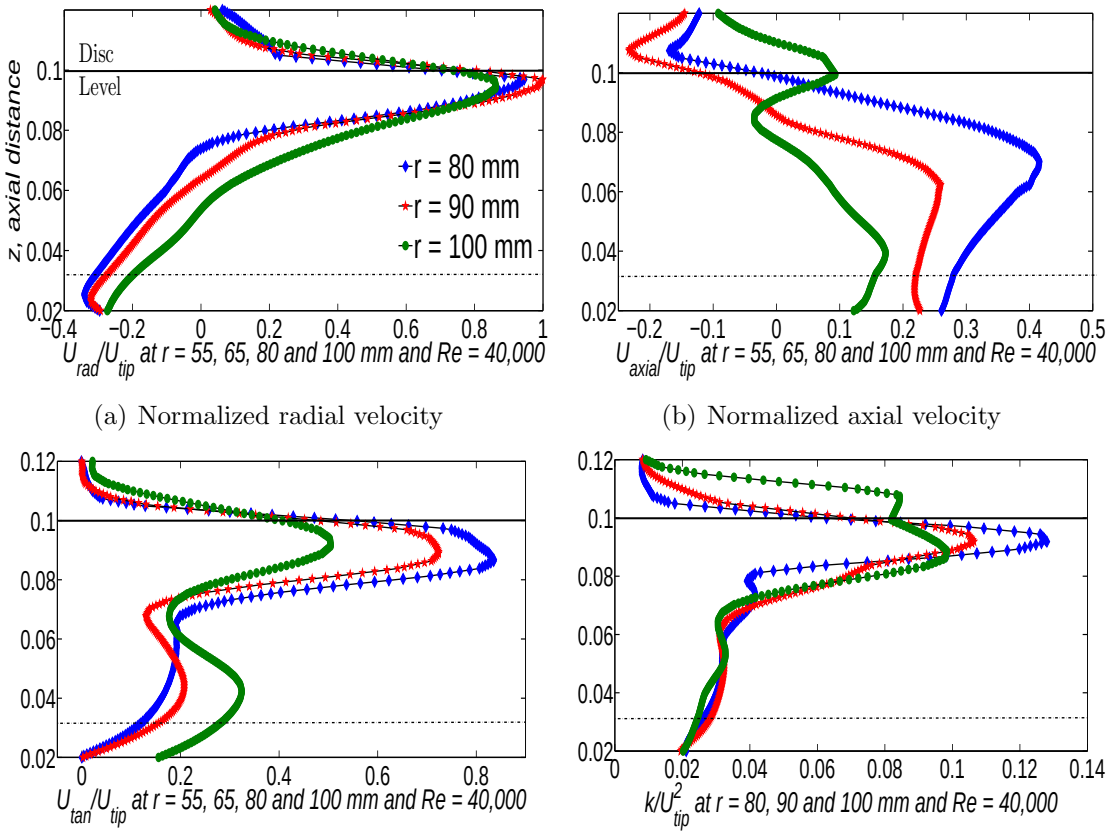

(a) Normalized radial velocity

(b) Normalized axial velocity

(c) Normalized tangential velocity

(d) Normalized k profiles

Figure 2.8. CFD predicted normalized flow characteristics for $FI - 150$ in the axial direction at different radial distances.

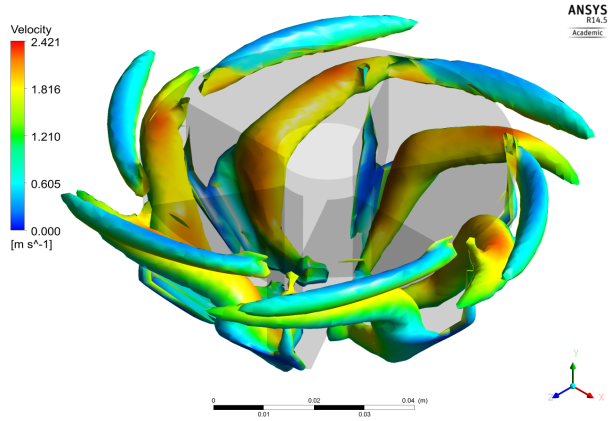

(a) $FI - 75$

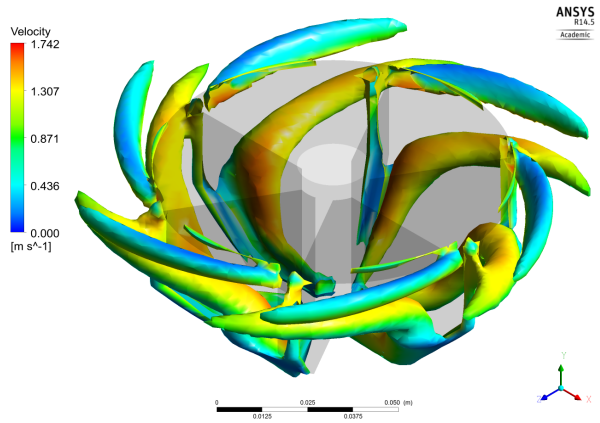

(b) $FI - 100$

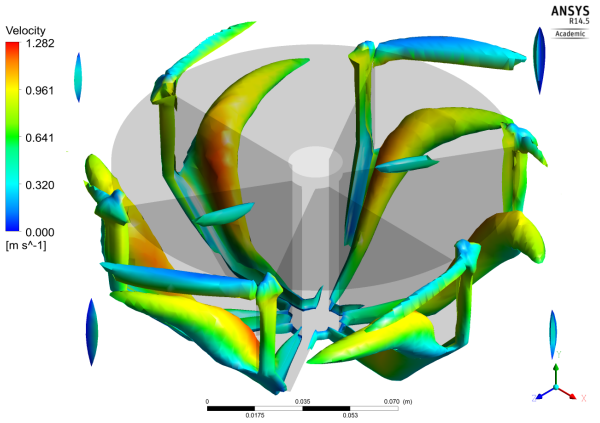

(c) $FI - 150$

Figure 2.9. Isosurface of trailing vortices visualized for a constant swirling strength of 0.2 for constant clearance of $C = 100$ mm at $Re = 40,000$.

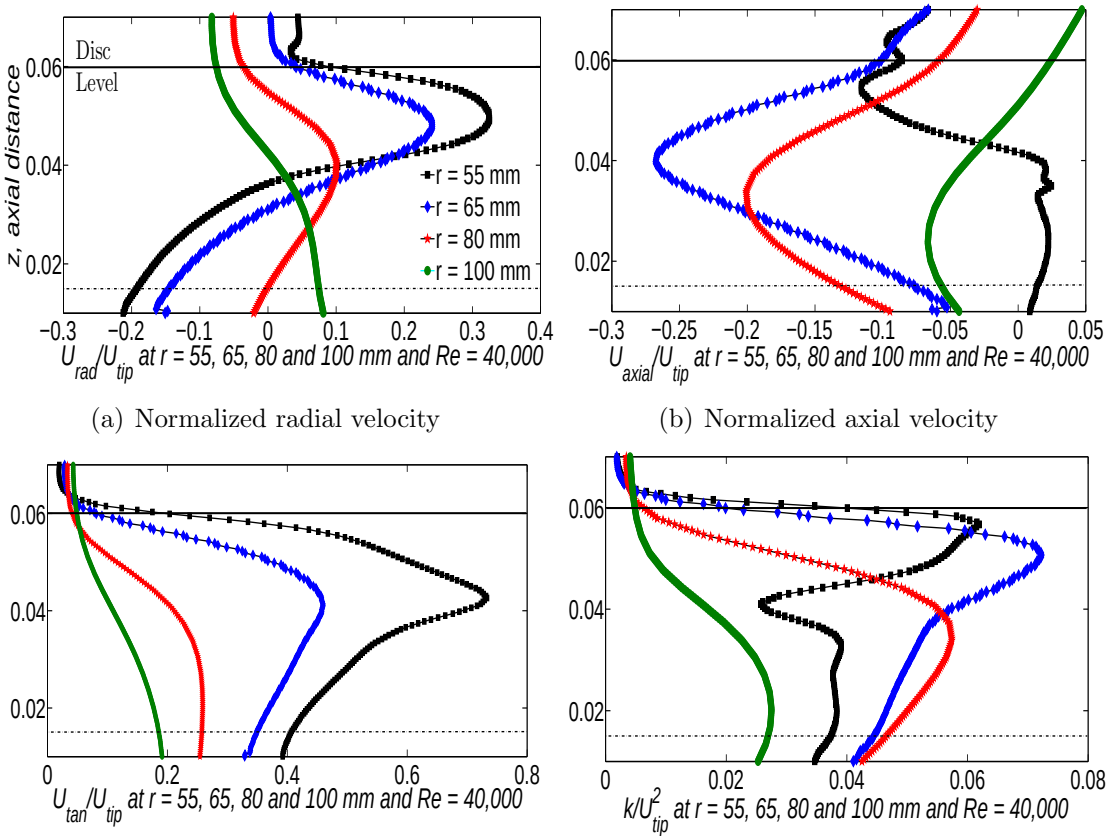

(a) Normalized radial velocity

(b) Normalized axial velocity

(c) Normalized tangential velocity

(d) Normalized k profiles

Figure 2.10. CFD predicted normalized flow characteristics for $FI - 100$ at off-bottom clearance $C = 60$ mm.

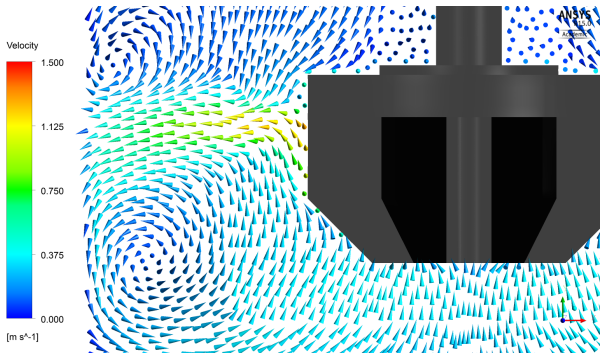

(a) Clearance, $C = 100$ mm

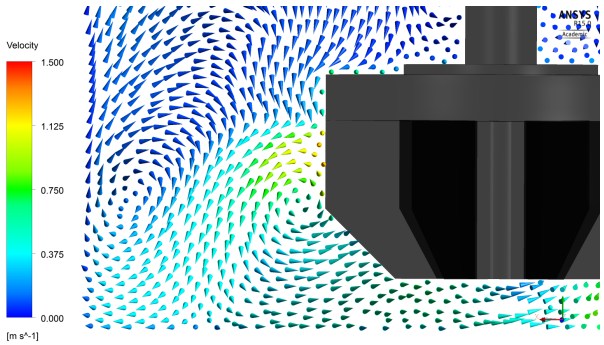

(b) Clearance, $C = 60$ mm

Figure 2.11. CFD predicted velocity vectors for $FI - 100$ at C equal 100 mm (a) and 60 mm (b) showing the transition of flow from radial to axial type.

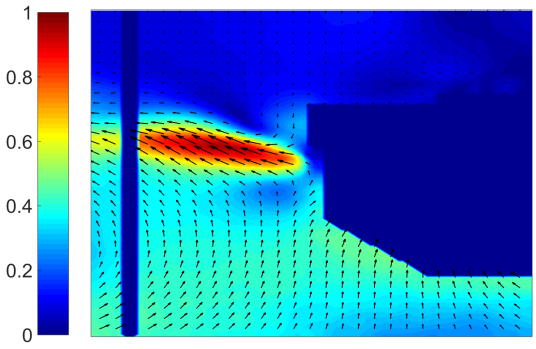

(a) Clearance, $C = 100$ mm

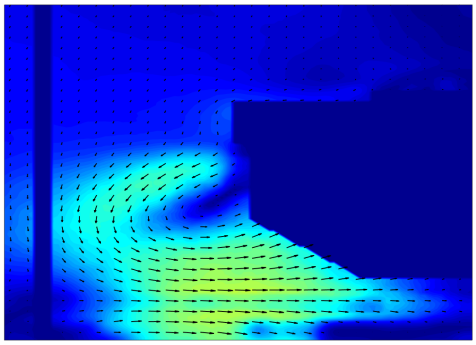

(b) Clearance, $C = 60$ mm

Figure 2.12. Velocity vectors for $FI-100$ at C equal 100 and 60 mm obtained from PIV measurements overlaid on mean velocity contours, units are in (m/s).

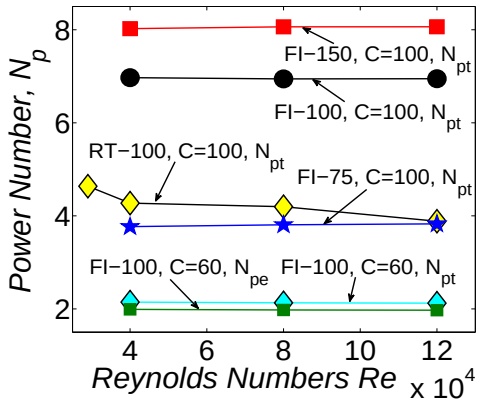

Figure 2.13. Power number N_p versus Re for different impellers at different C values.

Table 2.1. Power number values calculated from torque τ ($N_{p\tau}$) and turbulence energy dissipation rate ϵ ($N_{p\epsilon}$) values obtained from CFD simulations.

Impeller Size	C mm	Re	$N_{p\tau}$	$N_{p\epsilon}$
$FI-75$	60	40,000	4.31	3.77
$FI-75$	60	80,000	4.35	3.81
$FI-75$	60	120,000	4.36	3.83
$FI-75$	100	40,000	6.86	5.91
$FI-75$	100	80,000	6.77	5.77
$FI-75$	100	120,000	7.41	6.35
$FI-100$	60	40,000	2.15	1.99
$FI-100$	60	80,000	2.13	1.98
$FI-100$	60	120,000	2.12	1.97
$FI-100$	100	40,000	6.97	6.03
$FI-100$(RSM)	100	40,000	6.53	2.36
$FI-100$	100	80,000	6.94	6.00
$FI-100$	100	120,000	6.95	6.01
$FI-150$	100	40,000	8.02	6.61
$FI-150$	100	80,000	8.06	6.66
$FI-150$	100	120,000	8.06	6.66
RT	100	29,000	4.64	3.39
RT	100	40,000	4.27	3.41
RT	100	80,000	4.20	3.44
RT	100	120,000	3.89	1.80

CHAPTER 3

NUMERICAL SIMULATION OF SINGLE PHASE FLOW IN FLOTATION CELLS - EFFECT OF IMPELLER OFF-BOTTOM CLEARANCE BLADE SHAPE, AND REYNOLDS NUMBER

3.1 Abstract

A series of numerical simulations of turbulent single phase flows is performed to understand the flow and mixing characteristics in lab scale flotation tanks. Four impeller blade shapes, covering a wide range of surface areas and lip lengths, are considered to highlight and contrast the flow behavior in the impeller stream. The mean flow close to the impeller is fully characterized by considering velocity components in axial direction at different radial locations. Consistent with earlier observations, the normalized velocity and turbulence quantities are found to be invariant in fully turbulent regime. Normalized results suggest development of a comparatively stronger axial velocity component for a blade design with the smallest lip length, called big-tip impeller here. Both normalized radial and tangential velocities are found to be high close to the impeller. Tangential velocities decrease once the mean flow interacts with the stator, which directs the mean flow in radial direction and results in enhanced mixing and recirculation. Normalized turbulent kinetic energy profiles close to the impeller reveal the existence of asymmetric trailing vortex pair. The highest turbulence kinetic energy dissipation rates are observed close to the impeller blades and stator walls - where the radial jet strikes the stator walls periodically. Changing off-bottom clearance has no significant effect on the mean flow profile, though peak values of velocities are noted to differ slightly. In addition, liquid phase mixing in the flotation cell is studied using transient scalar tracing simulations. Average mixing times and dead regions are identified in the tank using evolving scalar concentration in the bulk

and selected discrete locations. Finally, pumping capacity and efficiency of different impeller designs are calculated and the impeller blade design with rectangular blade design is found to perform most efficiently.

3.2 Introduction

Mechanical flotation cells are commonly used in the mineral processing industry to concentrate valuable minerals from the accompanying gangue material. The flow inside the flotation cell is typically very turbulent in nature due to high agitation rates [38, 39]. Moreover, presence of dispersed phases makes the flow highly non-uniform and complex [40, 41]. The length and time scales of processes occurring inside flotation cells span many orders of magnitude [38, 41]. In the remainder of this section, past studies using computational fluid dynamics (CFD) for flotation research with a focus on hydrodynamics are briefly reviewed and the motivation for the current work is highlighted.

The earliest application of CFD to understand flotation microprocesses is performed by Koh et al. [42], who studied bubble-particle collisions in mineral flotation cells. Closely following their pioneering work, Koh and co-workers published a number of papers in which they developed flotation kinetic rate model for lab scale flotation cells [12, 38, 40, 43]. Evans et al. [12] studied mixing and gas dispersion in lab scale flotation cells using Eulerian multiphase CFD simulations. Liu and Schwarz [44] used numerical simulations to study isolated bubble-particle collisions in the presence of turbulent flow. Recently, Karimi et al. [41] developed and implemented CFD model for prediction of flotation rate constant and compared their predictions against experimental measurements of Newell [45]. However, both experimental measurements of Newell [45] and CFD simulations of Karimi et al. [41] are performed in a stirred tank using Rushton turbine.

Local flow measurements in flotation cells, especially in the impeller region are not reported in the literature. However, few numerical studies have been performed using commercial CFD tools. Recently Xia et al. [46] performed numerical simulations of single phase flow in Outotec tankcell. They compared three turbulence models, namely, standard $k-\epsilon$, realizable $k-\epsilon$ and Reynolds stress model (RSM), and

reported observing two recirculation zones typical of radial impellers at intermediate clearance. Trailing vortices characterized by high velocity close to the impeller are also observed, and the stator is found to weaken the tangential component of the flow to very low levels in the bulk of the tank. More recently, Basavarajappa et al. [47] performed particle image velocimetry (PIV) and CFD simulation of flows developed by a flotation impeller in a cylindrical mixing tank. They reported important differences in mean local flow behavior created by different impeller blade designs and suggested a similar exercise for flotation cells. Shi et al. [48] used PIV measurements and CFD simulations to study the effect of the impeller blade angle on mean flow characteristics in a KYF flotation cell. Based on their analysis of power draw behavior, Shi et al. [48] recommend backward impeller design for efficient operation.

The impeller blade shape is known to critically affect dispersion, mixing and turbulence level in mixing vessels [49]. In multiphase flows, especially gas-liquid flows, breakage of gas bubbles occurs in the regions of high dissipation rate [39, 50, 51], usually in the impeller stream. Also, particles have been shown to preferentially concentrate in regions of high or low vorticity based on their size [52].

Even though some attempts have been made to characterize flows inside flotation cells [11, 48], systematic evaluation of different design features on mean flow characteristics are not reported in the open literature on flotation cell hydrodynamics. Recent studies have shown that CFD simulations can be successfully used to study effect of flotation component design to understand local and overall hydrodynamics in flotation cells [28, 48].

Stirred tank reactors share many design similarities with flotation cells and the advances made in modeling and simulating flows in a stirred tank can be directly applied to flotation cells. A significant number of experimental and numerical studies have been reported in the literature for chemical stirred tank flows using a Rushton turbine and axial flow impeller, which are recently reviewed by Joshi et al. [20] and references therein. A number of studies have shown the nature of turbulence to be anisotrpic in the impeller stream, especially when using a radial flow impeller [35, 53–55]. CFD simulations of stirred tanks using a Rushton turbine have been able

to satisfactorily predict mean flow behavior in the impeller stream [56]. Kumaresan and Joshi [49] demonstrated that CFD can be successfully applied to study average flow characteristics in stirred tanks and correctly predict average mixing times using scalar mixing studies.

Turbulent flow close to the impeller region for Rushton turbine has been extensively investigated in the literature [30, 37, 53, 54, 57]. Ng and Yianneskis [30] reported that 31% of the total energy is dissipated in the impeller stream from their CFD predictions. In addition, Huchet et al. [57] have performed high resolution PIV measurements in the impeller flow stream and found that dissipation rate can be calculated from measurements along a single plane. They further reported that the instantaneous dissipation rate shows periodicity, with trailing vortices contributing significantly to overall dissipation rate.

Following a brief review of literature presented thus far, it is clear that a systematic investigation on the effects of flotation cell internals (i.e., impeller and stator design) on mean flow behavior, is not reported as yet for flotation cells. In this study, we systematically study the effect of the impeller blade shape, off-bottom clearance, and the impeller rotation speed on mean flow and mixing characteristics in a generic lab-scale flotation cell using CFD simulations. In order to study the effect of the impeller blade shape, four distinct impeller blade profiles are considered. Furthermore, using the steady state CFD predictions, pumping number and pumping efficiency of different impeller blade profiles are reported, which makes the comparison of the impeller blade designs practical and of interest to industrial flotation cell manufacturers. Transient scalar mixing simulations are additionally performed on relatively coarser grids to understand the mixing process and calculate average mixing time in flotation cells.

3.3 Tank Configuration and Impeller Design

A lab-scale cylindrical tank of diameter (D) and height (H) equal to 300 mm is considered. Cylindrical shaft of diameter (d_s) equal to 20 mm ($D/15$) supports the impeller. A schematic of flotation cell used in CFD simulations with all relevant design parameters is shown in Figure 3.1. Four flotation impeller blade designs are used in this study, namely, standard blade (SB), rectangular blade (RB), big-tip

(BT), and small-tip (ST). All the impellers have six blades and their diameter d is equal to 60 mm, which is one-fifth (20%) of tank diameter. A schematic of all the impeller designs used in this study is shown in Figure 3.2(a). Two off-bottom clearance (C) values of 25 and 50 mm are used to study the effect on mean flow and pumping behavior. The impellers are concisely named depending on the impeller design and clearance. For instance, $SB-25$, represents standard blade impeller at $C = 25$ mm. The stator used here has 12 blades held between two circular rings as shown in Figure 3.2(b). Four short legs support the stator which are fixed to the bottom of the tank. Dimensions of various stator design parameters used in this work are: $W_s = 20.5$ mm, $h_{IS} = 12$ mm ($d/5$), $h_r = 5$ mm, h_s= 47 mm, and $h_b = 15$ mm.

For the purpose of validation, Rushton and flotation impellers without stator in lab-scale stirred tank are considered. More details about the setup used in the validation cases can be found in [28, 47]. In both cases, an impeller of diameter equal to 100 mm is used. The Rushton turbine considered here is identical to design used by Wu and Patterson [32] and Deglon and Meyer [56]. The fluid used is water and all the single phase simulations are conducted at room temperature and pressure. Reynolds number (Re), defined as the ratio of inertial to viscous forces in the flow, takes the form $Re = \mathrm{N}\rho d^2/\mu$ for mixing vessels, where, N is impeller speed in revolutions per second, ρ is fluid density, d is impeller diameter, and μ is dynamic viscosity of fluid. The Re considered in this work falls in the turbulent regime.

3.4 Computational Methodology

In this work, unstructured mesh exclusively made up of hexahedral cells is created using ANSYS ICEMCFD 14.5 software. The total number of cells used in steady state MRF simulations is approximately 1.5 million, which is found to be adequate based on grid convergence study considering local velocity and power draw variation. For unsteady MRF simulations of scalar mixing, a relatively coarser mesh with approximately 450,000 cells is used. This simplification is necessary to ensure practically relevant compute times. However, this simplification is bound to result in under-prediction of turbulent quantities close to the impeller, but mean velocities will be accurately predicted even at this refinement level [19, 56].

The numerical solution is obtained by solving the discretized form of governing equations using ANSYS Fluent 14.5 solver. Spatial derivatives are discretized using second order upwind schemes. Pressure is discretized using PRESTO scheme, which is suited for rotating flows [29]. Semi-implicit method for pressure linked equations (SIMPLE) scheme is used to achieve velocity and pressure coupling. The under-relaxation factors are reduced at the beginning of the simulation to maintain stability and avoid divergence of the solution. The solution is considered to be fully converged when the scaled residuals for continuity dropped below 10^{-4}, and for velocity and turbulence quantities dropped below 10^{-5}. The impeller motion is modeled using MRF technique and realizable $k-\epsilon$ model is used to model the turbulence in the flow. For tracer mixing studies, additional transport equation for a user defined scalar (UDS) is solved. The tracer is injected directly below the impeller in a cylinder of height and radius equal to 10 mm (12,400 cells) in a fully developed flow field. The transport of scalar is monitored continuously at four discrete locations in the tank and the data are used to calculate the average mixing time.

3.5 Governing Equations and Turbulence Modeling

3.5.1 Governing Equations

The conservation of mass and momentum equations are solved to obtain solution for flow variables, namely, velocity components and pressure. Continuity or mass conservation equation in cylindrical co-ordinates (r,θ,z) for incompressible flow takes the form:

$$\frac{1}{r}\frac{\partial}{\partial r}(r u_r) + \frac{1}{r}\frac{\partial}{\partial \theta}(u_\theta) + \frac{\partial u_z}{\partial z} = 0 \tag{3.1}$$

The momentum conservation equations for incompressible flow takes the form of Navier-Stokes equations, which in cylindrical co-ordinates (r,θ,z) are given by:

$$\rho\left[\frac{D u_r}{Dt} - \frac{u_\theta^2}{r}\right] = -\frac{\partial p}{\partial r} + f_r + \mu\left[\nabla^2 u_r - \frac{u_r}{r^2} - \frac{2}{r^2}\frac{\partial u_\theta}{\partial \theta}\right] \tag{3.2}$$

$$\rho\left[\frac{D u_\theta}{Dt} + \frac{u_\theta u_r}{r}\right] = -\frac{1}{r}\frac{\partial p}{\partial \theta} + f_\theta + \mu\left[\nabla^2 u_\theta - \frac{u_\theta}{r^2} + \frac{2}{r^2}\frac{\partial u_r}{\partial \theta}\right] \tag{3.3}$$

$$\rho\frac{D u_z}{Dt} = -\frac{\partial p}{\partial z} + f_z + \mu\nabla^2 u_z \tag{3.4}$$

where, u_r, u_θ, u_z are the radial, tangential, and axial fluid velocity components, p is the local pressure, f_r, f_θ, f_z are the body force components in the radial, tangential, and axial directions.

The scalar transport equation is given by:

$$\frac{\partial \rho\phi}{\partial t} + \frac{\partial}{\partial x_i}\left(\rho u_i \phi - D_{eff}\frac{\partial \phi}{\partial x_i}\right) = S_\phi \tag{3.5}$$

where, ϕ represent the scalar, D_{eff} represents effective turbulent diffusion coefficient of scalar which is implemented as a user defined function, and S_ϕ represents the source term. Effective turbulent diffusion coefficient is calculated as:

$$D_{eff} = D + \frac{\nu_t}{Sc} \tag{3.6}$$

where, D is molecular diffusivity, ν_t is turbulence viscosity, and Sc is Schmidt number which is assumed to be 0.7.

3.5.2 Turbulence Modeling

Instantaneous velocity and pressure can be split into average and random components, and substituting them in the NS equations results in RANS equation. Turbulence modeling involves solving transport equations for turbulence kinetic energy (k) and its dissipation rate (ϵ) with relevant models for closing unknown terms. Realizable $k-\epsilon$ model involves alternative formulation for turbulent viscosity μ_{turb}, and a modified transport equation for ϵ based on the transport equation of mean-squared vorticity fluctuation is used [29]. The transport equations for Realizable $k-\epsilon$ model are given as:

$$\frac{\partial}{\partial t}(\rho k) + \frac{\partial}{\partial x_j}(\rho k u_j) = \frac{\partial}{\partial x_j}\left[\left(\mu + \frac{\mu_t}{\sigma_k}\right)\frac{\partial k}{\partial x_j}\right] + G_k + G_b - \rho\epsilon - Y_M \tag{3.7}$$

$$\frac{\partial}{\partial t}(\rho \epsilon) + \frac{\partial}{\partial x_j}(\rho \epsilon x_j) = \frac{\partial}{\partial x_j}\left[\left(\mu + \frac{\mu_t}{\sigma_\epsilon}\right)\frac{\partial \epsilon}{\partial x_j} + \rho C_1 S\epsilon - \rho C_2 \frac{\epsilon^2}{k + \sqrt{\nu\epsilon}} + C_{1\epsilon}\frac{\epsilon}{k}C_{3\epsilon}G_b\right] \tag{3.8}$$

where,

$$C_1 = max\left[0.43, \frac{\eta}{\eta+5}\right], \eta = S\frac{k}{\epsilon}, S = \sqrt{2S_{ij}S_{ij}} \tag{3.9}$$

In Eqn. 3.8, G_k and G_b represent the generation of k due to mean velocity gradients and buoyancy, respectively. Y_M in this case will be negligible as the flow is

incompressible. μ_t is the eddy or turbulent viscosity. Default model constant values are used, and the default constants are $C_{1\epsilon} = 1.44$, $C_2 = 1.9$, $\sigma_k = 1.0$, and $\sigma_\epsilon = 1.2$. For more information on the transport equations of turbulence models and associated constants, the reader is referred to the [29] and [31].

3.6 Results and Discussion

3.6.1 Validation of Numerical Approach

The numerical model used in this work is validated by comparing CFD predictions against experimental velocity component measurements reported by Wu and Patterson [32] for *RT*. Figure 3.3(a) shows the comparison of normalized radial velocities from CFD predictions and LDA measurements of Wu and Patterson [32] in the axial direction, at a radial distance (r) equal to 5 mm from the impeller tip. Impeller tip in this context refers to the outermost edge of the impeller. General trend and the location of peak radial velocity is correctly captured by CFD. The difference in the magnitude of the peak values between CFD and measurements can be attributed to using somewhat thicker impeller blades (5 mm) in CFD simulations, since these values are not reported by Wu and Patterson [32]. Here it is assumed that the thickness of impellers in experiments of Wu and Patterson[32] is less than 5 mm, which is generally true [33]. Moreover, two equation based turbulence models are well known to under-predict peak values very close to the impeller [19].

In addition to *RT*, validation of numerical model is also carried out for flotation impeller in stirred tank as shown in Figure 3.3(b), which shows normalized radial velocity comparison of CFD and PIV data at a distance of 15 mm from the impeller. The readers are referred to recent paper by Basavarajappa et al.[47] for detailed information on the numerical and experimental setup used. Due to the presence of stator, it is difficult to make PIV measurements in laboratory flotation cells, especially in the impeller stream. Therefore, no direct validation is performed for flotation cells using rotor-stator configuration. Moreover, the objective of this work is to characterize the flows using different impeller blade designs. To this end the validation efforts for Rushton turbine and flotation impeller are considered acceptable, considering the lack of reasonable local measurements in flotation cells.

3.6.2 General Flow Characteristics - $C = 50$ mm

To illustrate the nature of mean flow inside the flotation cell, mean flow velocity components and turbulence kinetic energy profiles are considered in the impeller stream for standard impeller (SB) design at $C = 50\ mm$. The axial profiles of velocity components (u_a, u_r, and u_t) and turbulence kinetic energy (k) normalized by the impeller tip speed ($u_{tip} = 4.21\ m/s$) at Re equal to 80,000 are shown in Figure 3.4. The axial profiles shown are taken at a distance of 3, 8, 15 and 30 mm from the impeller tip, which corresponds to distance of 33, 38, 45, and 60 mm from the tank center axis. The normalized velocities for all the impeller designs are found to be invariant with Re, which has been previously verified for stirred tanks using flotation impeller [47] and Rushton turbine impeller [23]. To avoid redundancy, the results for Re equal to 40,000 are not presented here. The normalized u components and k for SB are assumed to fully characterize the mean flow behavior. Also, velocity vectors on the vertical plane colored by their magnitude are shown in Figure 3.5(a).

All three velocity components are observed to be high close to the impeller blade tip at r equal to 33 mm. Peak velocities are predicted approximately along the impeller disc level (represented by solid horizontal line at $z = 0.077\ m$ in all figures). The axial velocity component (u_a) drops significantly moving away from the impeller and it further drops to low values at r equal to 45 and 60 mm. The strong axial velocity component close to the impeller is a result of high axial momentum contained in the flow rising up from below the impeller, produced due to pumping mechanism of impeller motion. The impeller rotation results in creation of strong radial and tangential momentum close to the impeller and it is clearly seen through their axial profiles at r equal to 33 mm in Figure 3.4(b) and 3.4(b), respectively.

In general, all the profiles are broader at $r = 33\ mm$ and become narrower moving away from the impeller. This behavior results from momentum transfer from confined radial jet to bulk flow as the jet travels from the impeller towards tank wall. The profiles at r equal to 45 and 60 mm pass along the stator ring; therefore, all the velocities go to zero on the surface and discontinuity exists near top and bottom for these profiles. The gradient in the u_r in the vicinity of disc is high with sharper increase to peak u_r value approximately occurring at disc level. Negative u_r values

can be seen after some distance below the impeller, which is due to recirculating flow in the lower region. The radial velocities remain significant in the impeller region even at r equal to 60 mm as observed by peak u_r value of approximately 0.4 times the tip velocity (u_{tip}). The tangential velocities are high near the disc, close to the impeller and remain high up to r equal to 45 mm. However, u_t value drops considerably at r equal to 60 mm as the flow encounters stator ring, which suppresses u_t by providing physical barrier to the flow. Low negative u_t values at r equal to 45 and 60 mm are due to small recirculating flow loops between the stator blades. The average flow is characterized by two recirculation loops and the velocity vector plot shown in Figure 3.5(a) shows the lower recirculation loop on a vertical plane. High fluid velocity can be observed in the region between the impeller blades as the fluid rushes in to low pressure region and gains additional momentum due to the impeller action. Away from the impeller, velocities are generally low. The impeller blade passage creates low pressure wake causing the flow below the impeller to accelerate.

Normalized turbulent kinetic energy (k) profiles for SB at Re equal to 80,000 are shown in Figure 3.4(d). Close to the impeller, k profiles are characterized by two peaks indicating the presence of a trailing vortex pair close to the impeller. Radial flow impellers have been previously reported to generate trailing vortex pairs equaling the number of blades [23, 47, 55, 58]. The k value remains high at r equal to 45 mm, where the trailing vortices and radial jet interact, thus creating a region of high turbulence along the inner region of stator. However, the profile has a single peak indicating the absence of trailing vortex at r equal to 45 mm. Figure 3.5(b) shows the contour plot of k on the vertical plane taken between two impeller blades. Regions of high k values are found between the impeller-stator gap in the impeller stream. Looking from the top on horizontal plane, located at 75 mm from tank floor in Figure 3.5(c), high values of k can be seen occurring as a result of radial jet interacting with stator blades. The velocity vectors shown in Figure 3.5(c) suggest that the flow splits into two streams upon encountering the stator blade. Furthermore, a small recirculation region develops next to high velocity stream as a result of this splitting action.

Contour plots of dissipation rate of turbulence kinetic energy (ϵ) are presented in Figure 3.6 (note: scale and colorbar are common for both the plots). The regions of

high ϵ are found near the surface of the impeller blade and upper part of the stator blade, where the radial jet strikes the stator as shown in Figure 3.6(a). Also, a small region of high ϵ can be seen close to the impeller just below the disc level. By carefully observing the horizontal contour plot shown in Figure 3.6(b), better understanding of the ϵ around the stator can be obtained. The horizontal plane used in Figure 3.6(b) is 75 mm from tank floor, which is 2 mm below the disc. The region between the impeller and stator is also characterized by high values of ϵ. Generally, most of the ϵ is contained in a volume close to the impeller with peak ϵ predicted on the surface of the impeller and stator blades.

Vorticity contour plot on a vertical plane passing through the impeller blades along with isosurface of constant swirling strength (λ) is shown in Figure 3.7(a). Vorticity represents the amount of local rotation present in the flow and calculated mathematically as curl of local velocity field. From Figure 3.7(a) it can be observed that the regions of high vorticity occurs along the length of the impeller blade as a result of impeller motion, which imparts high shear rates to nearby fluid, thereby resulting in high ω values. The regions of high vorticity are aligned with the position of trailing vortices, visualized here by isosurface of λ. High ω values are also present at a short distance away from the impeller, concentrated in two regions, which accompanies the cores of trailing vortex pair. The isosurface of constant swirling strength in Figure 3.7(a) has a value of 0.165, which represents a region of high rotation in the flow. Swirling strength is commonly used to visualize vortices in turbulent flow fields [59]. Substantial ω values are also seen below the impeller, where pressure field causes intense rotation of fluid. Vorticity in the lower part of the flotation cell aids in the suspension and mixing of the solid phase. Furthermore, preferential concentration of different sized solid particles can be estimated from the vorticity magnitude [52]. Generally, larger particles have a tendency to concentrate on the periphery of a vortex and smaller particles concentrate in the vortex core [52].

Magnitude of turbulent length scales in the flow directly affects a number of secondary processes like mixing and dispersed phase interaction in multiphase flow etc. Size of turbulent eddies, which directly control these turbulent length scales, are useful in modeling of gas-liquid flows, since many bubble breakage models hypothesize

a successful breakage event as a consequence of interaction of turbulent eddy and isolated bubble [50]. Local turbulent length scales directly control the local bubble size distribution (BSD); only eddies smaller than bubbles are capable of causing breakage when they have sufficient inertial energy. The larger eddies merely transport the bubbles without causing breakage [39, 50, 51].

Contour plot of turbulent length scale on a horizontal plane 62.5 mm from tank floor is shown in Figure 3.7(b). The length scale (l) is calculated using the relation $l = C_{\mu}3/4k3/2/\epsilon$, where, C_{μ} is taken to be 0.09 [26]. In the impeller stream, l values are low especially behind the blades in the swept region. Also, low l values are observed around stator blades where both k and ϵ values are found to be higher. Higher values of l are found close to the wall where the effect of turbulence is diminished due to the interaction of turbulent fluctuations with mean flow in the bulk. Singh et al. [26] noticed that $k - \epsilon$ model tended to over-predict l in comparison to other improved models tested in their work, possibly due to under-prediction of both k and ϵ.

3.6.3 Effect of Impeller Design, $C = 50$ mm

The normalized axial velocities u_a for four different designs, namely, SB, $SB-NR$, RB, and BT at three radial locations of r equal to 33, 38, and 45 mm are shown in Figure 3.8. $SB - NR$ represents SB impeller-stator configuration without the stator top ring. ST impeller is not considered in this comparison because its mean flow behavior is found to be generally identical to RB impeller. At r equal to 33 mm, CFD predicts peak u_a for SB impeller exactly at the disc level. $SB - NR$ and BT impeller also predict fairly high u_a at disc level, but the u_a profile for BT with high values is spread over shorter axial distance possibly due to its smaller vertical blade length creating a weaker jet. RB impeller predicts peak u_a value slightly below disc level at r equal to 33 mm as shown in Figure 3.8. At r equal to 38 mm, peak u_a values for all the impeller designs decrease considerably. Surprisingly, BT impeller predicts maximum peak u_a value at r equal to 38 mm. This behavior can be explained considering the effect of vertical portion of blade on mean flow. The vertical portion of blade imparts tangential momentum to flow coming towards the impeller from lower recirculation loop. In case of BT, the vertical portion of the blade is shorter

compared to other designs. This results in flow retaining more axial momentum and having lower tangential momentum compared to other designs. This behavior is exemplified by considering axial and tangential velocity profiles at r equal to 38 mm in Figure 3.8(b) and Figure 3.10(b), respectively.

For $SB-NR$ impeller, it is anticipated that the absence of top ring might lead to higher u_a close to the impeller. The u_a generated by $SB-NR$ are appreciably lower in comparison to SB for a short distance below the disc. However, the flow above disc has some negative u_a values for $SB-NR$ since there is no physical barrier to direct the flow coming from upper recirculation region in the radial direction. Moving further away from the impeller at r equal to 45 mm, u_a for all the designs are within 12% of u_{tip}. The discontinuity in the u_a profiles are due to the presence of stator ring for all the cases except $SB-NR$. The profiles for SB, $SB-NR$, and BT are identical below disc level at r equal to 45 mm.

Normalized radial velocities are shown in Figure 3.9. In general, high u_r values are expected close to the blade for all impellers. At r equal to 33 mm, all the designs follow the general trend with low u_r above and below disc and peak u_r values occurring at disc level. At r equal to 38 mm, peak u_r value predicted by RB is considerably larger than other designs. At r equal to 45 mm, profiles start to converge suggesting that velocities in the bulk are invariant to small changes in blade shape. Generally, RB impeller predicts highest peak values of u_r close to the impeller. Figure 3.10 shows the axial profiles of normalized tangential velocities. High u_t are generated when the vertical part of the impeller blade imparts tangential momentum to nearby fluid. At r equal to 33 mm, SB and RB predict largest peak u_t values and BT predicts the smallest peak u_t at the disc level. At r equal to 38 mm, RB predicts a slightly higher peak u_t than at $r = 33$ mm, though, the position of the peak is shifted in axial direction. The drop in peak u_t for BT is more pronounced than for SB and the position of peak does not shift at 38 mm for BT. Clearly, the blade design with largest vertical lip length (RB) produces highest peak tangential velocities close to the impeller.

Figure 3.11 shows the comparison of normalized k profiles. At r equal to 33 mm, all the k profiles are characterized by two peaks, one above the disk and one below

the disk level which is larger in magnitude than the upper peak. The two peaks correspond to the presence of a trailing vortex pair. Both SB and BT predict almost identical peak k values, though the spread of k profile for BT is narrower compared to all the other cases as expected. RB impeller predicts lower k values compared to other impellers. At r equal to 38 mm, the upper peak becomes more dominant and peak k value increases in comparison to r at 33 mm. The k profiles at 45 mm are characterized by single peaks for all the designs with $SB - NR$ predicting the largest peak value. One possible reason for lower variation in the k profiles for different designs could be due to the use of relatively thick blades in numerical simulations (h = 5 mm). Previous studies have shown that thin blades create higher velocities and turbulence in comparison to thicker blades [19, 33].

The absence of a top ring resulted in slightly higher levels of turbulence as demonstrated by higher k for $SB - NR$ at r equal to 33 and 38 mm. In general, RB impeller creates low u_a values compared to other impellers, since the availability of larger vertical face of the blade is utilized to pump the fluid resulting in higher u_t and u_r values. BT impeller creates high values of all three u components close to the impeller (r = 33 mm). However, considerable drop in peak u_r and u_t is observed moving away at r equal to 38 mm for BT. Low u_a are observed at r = 45 mm for all the impellers with lowest values predicted by RB. The absence of stator top ring only altered the mean flow behavior above the disc level, for most parts, $SB - NR$ predicted values are identical to predictions by SB.

3.6.4 Effect of Impeller Design, C = 25 mm

In order to study the effect of C on mean flow behavior, C is reduced from 50 ($D/6$) mm to 25 mm ($D/12$). Basic flow pattern and behavior did not change significantly on reduction of C. Since many similarities exist between the flows at both clearances, only differences observed are discussed in this section. Predictions for different impeller blade designs at r equal to 38 mm are shown in Figure 3.12.

In general the averaged flow at low C behaves identically to flow described earlier for high C (50 mm). The normalized u_a profiles follow similar trends with SB and BT impellers predicting high peak $u_a$value compared to RB impeller. However, peak u_a values are marginally smaller at low C for SB and BT impeller at all three radial

locations. For RB impeller, no noticeable changes are obvious. The normalized u_r profiles also follow very identical trends at both clearances. Peak u_r values at all three r locations closely match at both clearances. The normalized u_r away from disc level and close to tank floor are different from each other at low C, which is not the case at high C where the profiles converge closer to floor. This behavior suggests that impeller blade shape controls the local flow behavior close to tank floor at low C, but the effect of blade shape is not as pronounced when the impeller is used at relatively high C values. The normalized u_t and k profiles are also very identical at both clearances with similar profile shapes and peak values at all r locations. The contour plots of k and ϵ are also found to be very similar for both clearances, which suggests that changing C from 50 to 25 mm has very little effect on the mean flow close to the impeller.

3.6.5 Mixing in Flotation Cells

In order to study the mixing behavior in flotation cells, a set amount of scalar is injected below the impeller inside fully developed single phase flow. The total mixing time is defined as the average time taken by scalar to reach steady state condition at four discrete locations in the flotation tank. The position of the four monitor points where the concentration is monitored is shown in Figure 3.13(a). The monitor points are located on X-Y plane (X - horizontal) and their positions are: point-1 (0.145, 0.005), point-2 (0.145, 0.295), point-3 (0.015, 0.295), and point-4 (0.075, 0.15). The points are chosen such that both bulk and dead mixing regions are accounted for and the average mixing time is calculated based on the time taken by scalar to reach a steady value at these representative locations.

Scalar mixing simulation is performed for SB, RB, and BT impeller designs for C equal to 25 mm and Re equal to 80,000 (1,340 RPM). The scalar injection volume is kept constant for all the cases and the scalar is injected in a cylindrical volume consisting of 12,383 cells. To understand the scalar mixing in the bulk, contour plots of scalar concentration along an axial plane for SI are shown in Figure 3.13 at different times. Figure 3.14 shows the normalized scalar concentration values at four locations for RB and BT impellers. By combining the information from point and

planar concentration data, detailed temporal and spatial scalar transport behavior are obtained.

Average mixing times are presented for two impeller designs, namely, RB and BT impellers, which represents contrasting designs (in terms of surface area) of impeller blade shape considered in this work. Average mixing time (t_{mix}) is defined as the arithmetic mean of the time taken for the scalar concentration (C_t) at each monitor point to reach within 5% of final concentration value at that point, which is the scalar concentration value at steady state (C_{steady}). For RB and BT impellers, t_{mix} is found to be 4.87 and 4.64 s, respectively. From Fig 3.13 7(a) it can be seen that point-4 for RB takes considerably longer than other points to reach C_{steady}, thereby causing t_{mix} to increase. Even in the case of BT, Point-4 takes longest time to reach C_{steady} value, but it is smaller in comparison to RB.

Figure 3.13(a) shows the distribution of scalar just 0.05 s after scalar is injected. The scalar is initially mixed in the radial direction as evidenced by distribution of scalar shown in Figure 3.13(a)-(c). After 5 s the scalar is uniformly mixed in the bulk of the tank except around the shaft and the area of release. This indicates that the upper recirculation loop generated by the impeller motion is unable to transport the scalar effectively around the shaft, and a dead mixing zone can be seen near the top in Figure 3.13(e), even after 9 s. Point-4 considered for the calculation of t_{mix} falls in the dead zone, and therefore takes considerably longer compared to other points to reach C_{steady} as mixing is dominated by diffusion in dead zones.

3.6.6 Performance of Flotation Impellers - Power and Flow Numbers

Using the bulk flow data from CFD, dimensionless numbers are calculated for direct comparison of different impeller designs used in this work. Power numbers and flow numbers in particular are useful in direct comparison of power consumption characteristics and pumping capacity of the impellers [49, 60, 61]. Using the ratio of pumping number to power number, pumping efficiency for each design is also calculated.

3.6.6.1 Power Number Calculation

Using CFD data, power number(N_p) based on torque (τ) ($N_{p\tau}$), and ϵ ($N_{p\epsilon}$) are calculated. Torque (τ) values generated on rotating parts of the tank and the total ϵ in the tank are used for power number calculations. $N_{p\tau}$ is calculated as [26] (Note: $N_{p\tau}$ based on torque generated on stationary parts, stator and walls, also resulted in similar values):

$$N_{p\tau} = \frac{2\pi N\tau}{\rho N^3 d^5} \tag{3.10}$$

By integrating the total ϵ in the tank, $N_{p\epsilon}$ (volume averaged) is calculated using the relation:

$$N_{p\epsilon} = \int \frac{\rho\epsilon dV}{\rho N^3 d^5} \tag{3.11}$$

Previous studies by Singh et al. [26] and Murthy et al. [35] have established the higher accuracy of $N_{p\tau}$ over $N_{p\epsilon}$. N_p based on ϵ is consistently under-predicted by 20–25% by CFD when using two equation turbulence models [26]. One reason for severe under-prediction using ϵ can be attributed to inability of $k-\epsilon$ models to predict ϵ correctly, especially close to the impeller where rate of dissipation is highest. Since experimental N_p are not available for the impellers tested, discussion will be centered on highlighting the similarities and differences in the performance of different designs based on CFD predicted values. The N_p values obtained from both the methods are tabulated in Table 3.1.

With exception of RB at C equal to 50 mm ($D/6$) and BT at both C's ($D/6$) all the predicted $N_{p\tau}$ are over 5, which is the most commonly observed value for radial flow impellers [19]. The highest $N_{p\tau}$ value at C equal to 50 mm is predicted for $SB-NR$ impeller and at C equal to 25 mm for ST impeller. As expected and previously observed by [58], BT impeller predicts the lowest $N_{p\tau}$ of all the designs. Due to the design of the impeller blades and lower blade surface area, both form drag and skin friction drag for BT will be considerably lower compared to the other impellers. Also, $N_{p\tau}$ is shown to be invariant for radial impellers operating in turbulent regime in the previous works [19, 58] and it can be verified in this work by comparing the $N_{p\tau}$ for SB at Re equal to 40,000 and 80,000. In line with the previous studies, $N_{p\epsilon}$ are approximately 23–33% smaller than predicted $N_{p\tau}$.

3.6.6.2 Flow Number and Pumping Efficiency

Flow numbers are calculated by calculating volumetric flow rate through a minimal cylindrical surface enclosing the impeller [61]. The cylindrical surface considered has radius, R_b, of 30.5 mm (0.5 mm from impeller surface) and extends along the height of the impeller. The radial discharge of the flow is calculated by integrating u_r on the cylindrical surface using the equation give by:

$$w_d = \int_{A_r} \rho V dA_r = \int_{z_b}^{z_t} 2\pi_b u_r dz \tag{3.12}$$

where, A_r is the surface area around the impeller, z_b and z_t are the distances from bottom of the tank to the impeller bottom and top, respectively. The value of z_b is equal to clearance and z_t is clearance plus 32 mm for all the cases. The impeller flow number (N_d) can be calculated using the following equation as:

$$N_d = \frac{w_d}{\rho N d^3} \tag{3.13}$$

where, N is impeller speed in revolutions per second (rps). Using the power and pumping numbers obtained from CFD data, pumping efficiency (η_{pump}), expressed as pumping capacity per unit power consumed is calculated as:

$$\eta_{pump} = \frac{N_d}{N_{p\tau}} \tag{3.14}$$

Both N_d and η_{pump} are tabulated in Table. 3.1. Figure 3.15 shows N_d and η_{pump} versus surface area of single impeller blade. Highest surface area corresponds to RB and lowest area correponds to BT impeller, respectively. It is clear from the plots that both N_d and η_{pump} are higher at higher C values across all the designs. The relationship between N_d and impeller surface area can be approximated by a straight line for the designs tested.

The impeller design with the highest surface area has maximum N_d value indicating higher surface area of radial impeller is used to pump fluid more effectively. Also, the gap in the predicted N_d values at two clearance values are close to each other as the impeller surface area is increased. This can be easily verified by comparing the N_d values of BT and RB. Furthermore, the increase in N_d at C equal to 25 mm with increase in surface area is higher compared to C equal to 50 mm. The N_d values

are invariant with Re for fully turbulent flows which can be verified by comparing N_d values for SB impeller at Re equal to 80,000 and 40,000. Absence of a stator top ring decreases the pumping capacity of the impeller, since the flow agitated by the impeller has a greater chance of gaining axial momentum, which would not be possible in the presence of a stator ring. Though the drop in N_d in the absence of a stator top ring is small in this case, for larger impeller diameters the drop could be significant.

Useful information can be obtained by comparing η_{pump} for both different impeller designs and clearances. Since the predicted N_d are smaller at C equal to 25 mm than at 50 mm, η_{pump} are also smaller at $C = 25$ mm. At $C = 50$ mm, BT impeller has higher value than SB due to high $N_{p\tau}$ value predicted for SB. For ST and RB impellers, η_{pump} are higher compared to both BT and SB. At $C = 50$ mm, η_{pump} increases with increase in surface area, though the relationship is not linear. The difference in η_{pump} values at two clearances is higher for BT, but decreases for SB and ST impellers before increasing again for RB. Based on the above discussion, it is clear that RB impeller performs better than other impellers because (a) it pumps a considerably higher volume of fluid compared to impellers as quantified by high N_d value and (b) has highest pumping efficiency (pumping capacity per unit of power consumed) among all the designs tested.

3.7 Conclusions

Detailed CFD simulations of single phase turbulent flows in flotation cells are performed using realizable $k - \epsilon$ turbulence model. The numerical approach used is validated by comparing our CFD predictions against data from literature for Rushton turbine and in-house PIV measurements. Normalized flow quantities are invariant with Re for the turbulent flow regime tested in this work. Turbulent flow is fully characterized by comparing normalized velocity components at different radial locations and discussing the behavior of mean flow. Mean flow is found to have considerable axial velocity close to the impeller. However, the axial component quickly diminishes considerably after a short distance from the blade. BT impeller predicted highest peak values of axial velocity. On the other hand, RB impeller

predicted highest values of radial velocities. A trailing vortex pair develops close to the impeller due to development of pressure gradient and local shearing and rotation of fluid caused by the impeller motion. Changing the off-bottom clearance from 50 to 25 mm does not effect the mean flow behavior close to the impeller based on normalized velocity and turbulence predictions. An estimation of local turbulence length scale using CFD could be used to better design the flotation cell internals such as impeller blade shape, number of blades, stator design, etc. such that turbulence generated is sufficient to produce required BSD and distributed over a large volume close to the impeller such that large number of bubbles are subjected to eddy-bubble interactions.

Mixing inside flotation cell is studied both qualitatively and quantitatively by tracking the distribution of scalar with time in transient simulations. The average mixing time for three impeller designs tested is between 4.5 – 5 seconds. Likewise, dead mixing zones are identified which could be potentially used to improve flotation cell design in the future. Using the torque on rotating parts and overall dissipation rate in the tank, power numbers are calculated. In general, the power number decreased when clearance is reduced except for rectangular blade impeller. Furthermore, the power number is found to be invariant with Re as expected in the turbulent regime. Pumping or flow numbers are calculated by calculating the radial discharge across a coaxial cylinder surface around the impeller. Rectangular blade impeller is found to have the highest and big-tip impeller is found to have the lowest pumping capacity, which indicates that the impeller with larger surface has higher pumping capacity in general. Also, pumping numbers at larger clearance are found to be higher than at lower clearance. By comparing the pumping efficiency it is found that rectangular blade impeller has highest pumping capacity per unit power consumed. Again, the pumping efficiency at larger clearance is higher except for standard blade impeller.

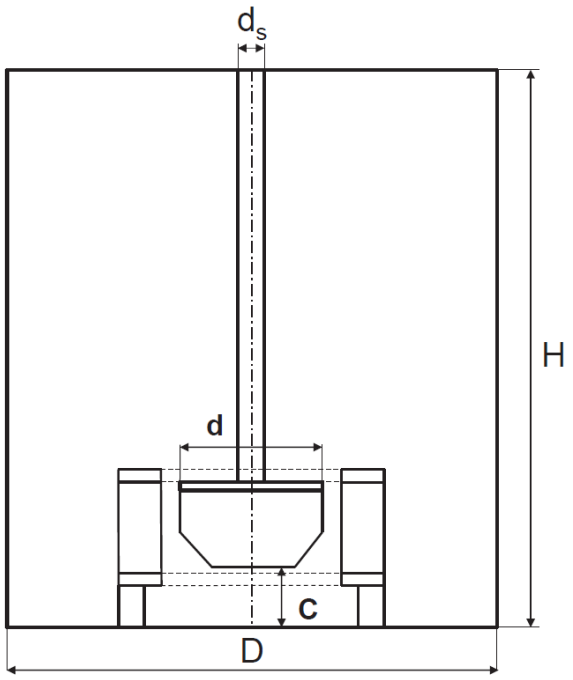

Figure 3.1. Schematic of flotation cell design used in this study.

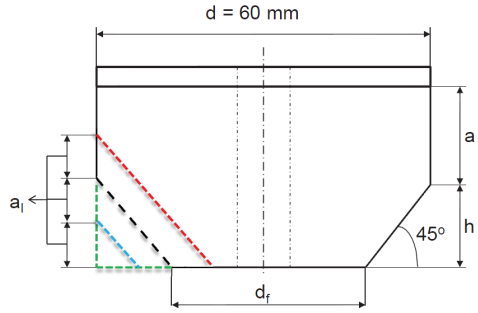

(a) Schematic of the impeller blade profiles

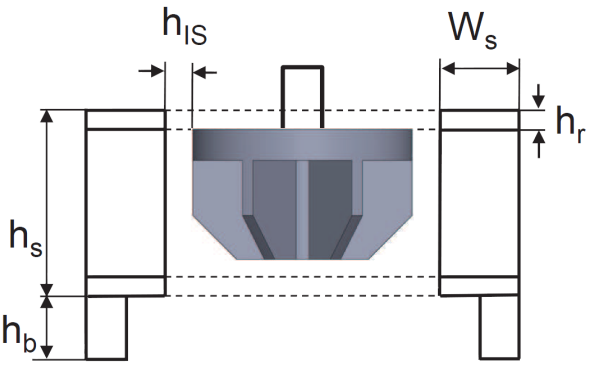

(b) Schematic of the impeller-stator design

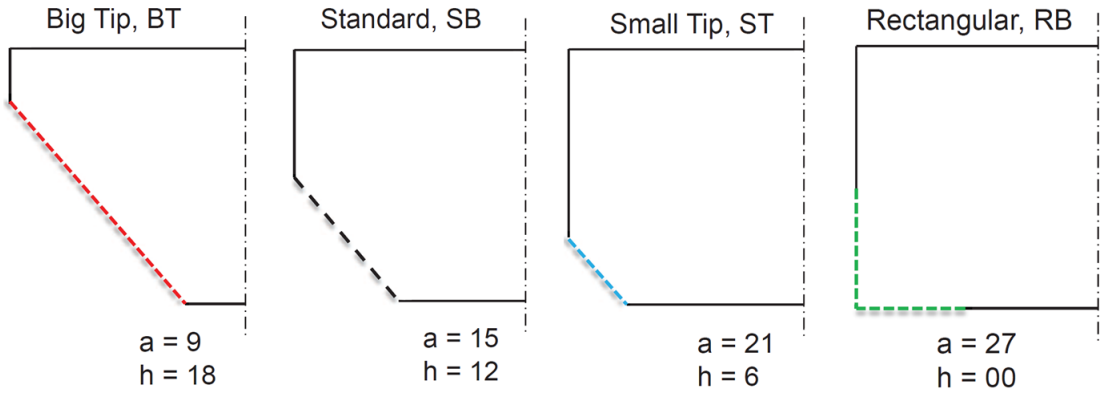

(c) Differences in vertical blade lip length

Figure 3.2. Schematics of the impeller profiles and impeller-stator configuration used in this work.

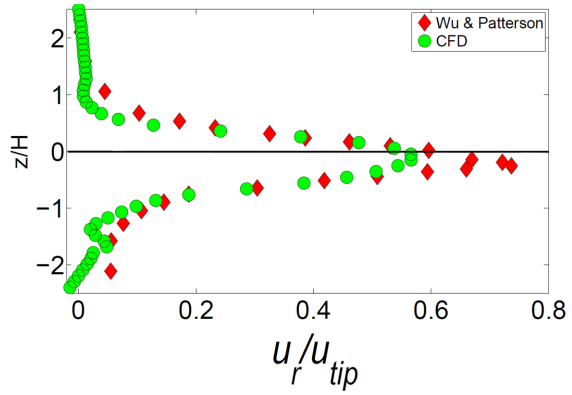

(a) Normalized radial velocity versus axial height at $r = XX$ mm

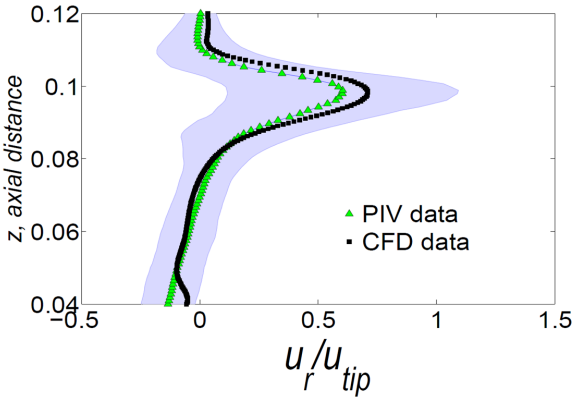

(b) Normalized radial velocity versus axial height at $r = XX$ mm

Figure 3.3. CFD model is validated by comparing the predictions against experimental measurements performed in stirred tank using (a) Rushton turbine (b) Flotation impeller.

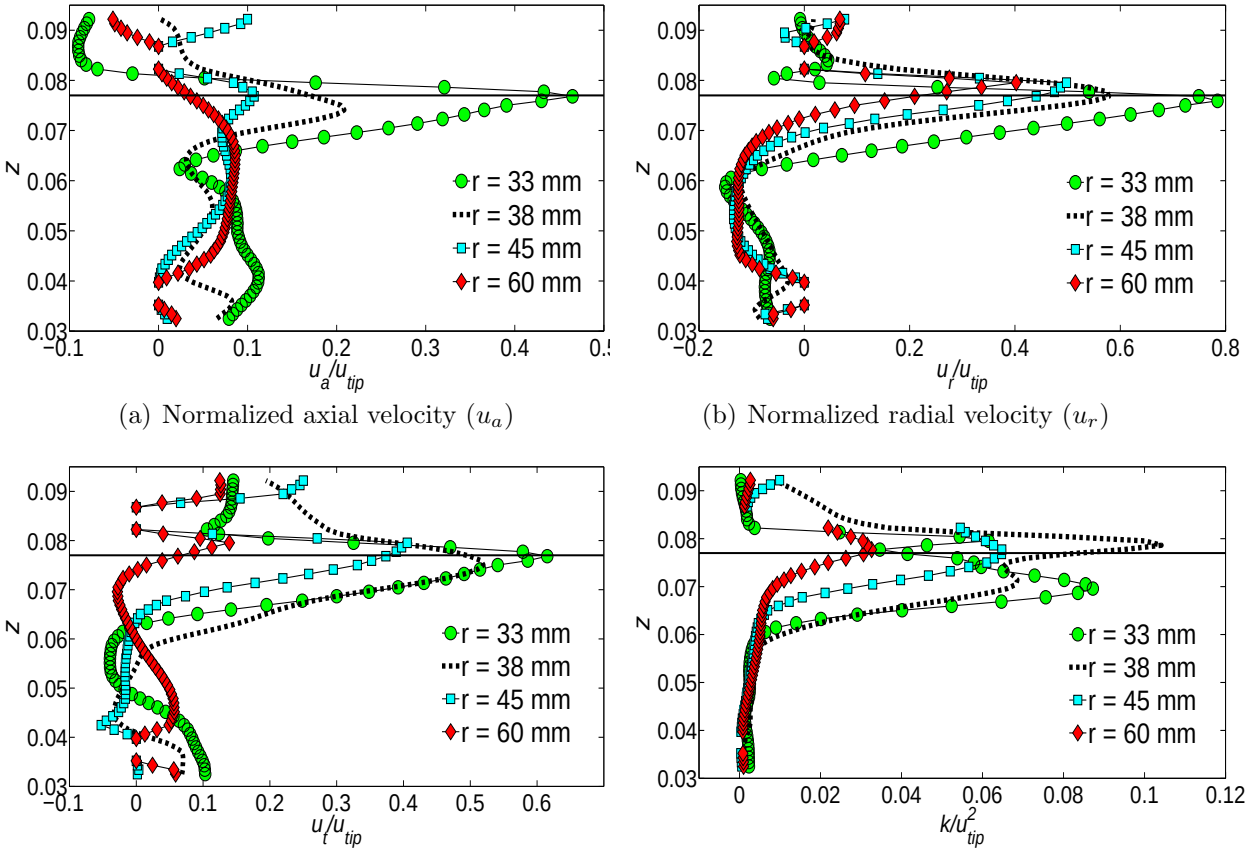

(a) Normalized axial velocity (u_a)

(b) Normalized radial velocity (u_r)

(c) Normalized tangential velocity (u_t)

(d) Normalized turbulence kinetic energy (k)

Figure 3.4. Normalized axial profiles of velocity components and turbulence kinetic energy for SB impeller at Re equal to 80,000 and $C = 50\ mm$ at radial distances equal to 33, 38, 45 and 60 mm from shaft axis.

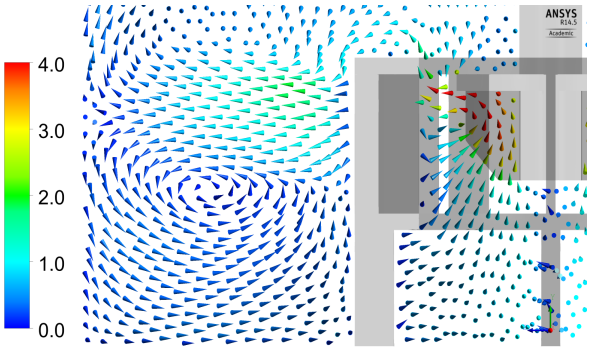

(a) Velocity vectors for SB at C = 50 mm

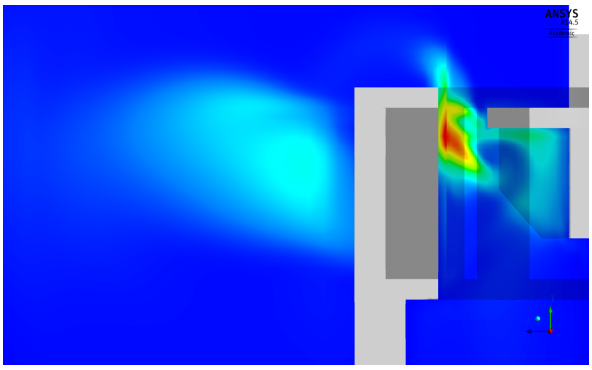

(b) k contour plot - vertical plane, scale shown below

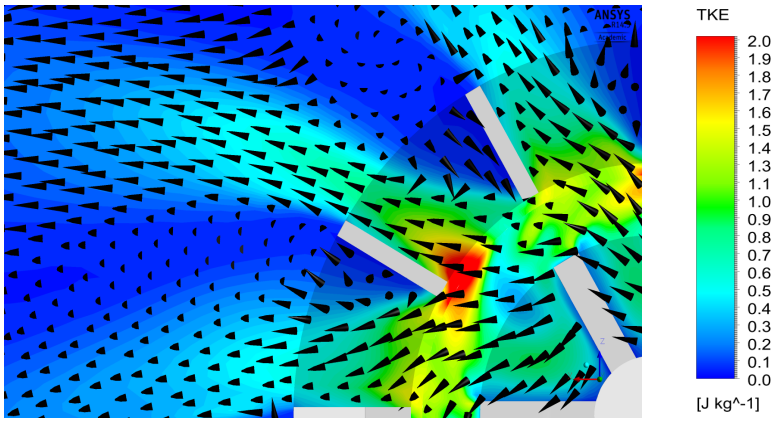

(c) k contour plot - horizontal plane, k colorbar and scale on right

Figure 3.5. Mean flow and turbulence characteristics: (a) Velocity vector plot on a vertical plane midway between two impeller blades, (b) k contour plot on a vertical plane, and (c) k contour plot on horizontal plane that is 75 mm from tank floor for SB impeller at Re equal to 80,000 and $C = 50$ mm.

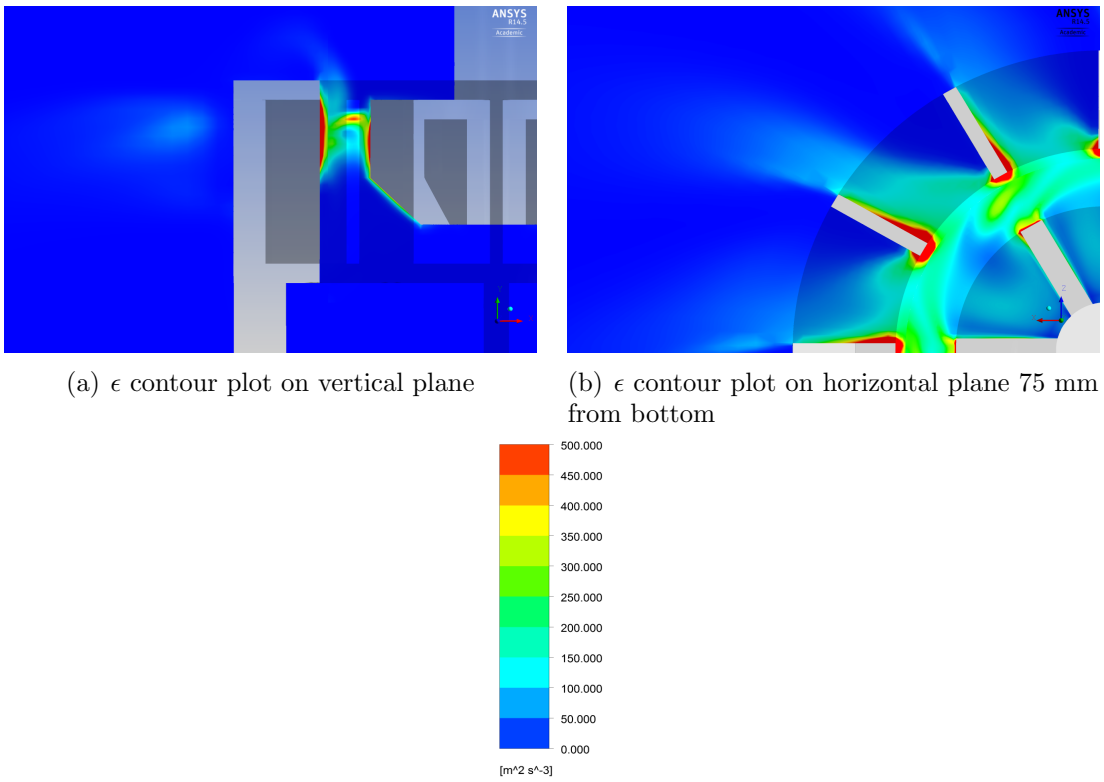

(a) ϵ contour plot on vertical plane

(b) ϵ contour plot on horizontal plane 75 mm from bottom

Figure 3.6. Contour plots of ϵ for SB impeller at Re equal to 80,000 (scale on right is common to both).

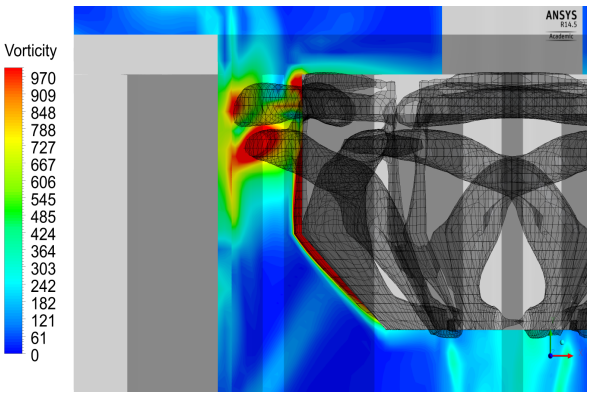

(a) Trailing vortex visualized by swirling strength on vorticity contour

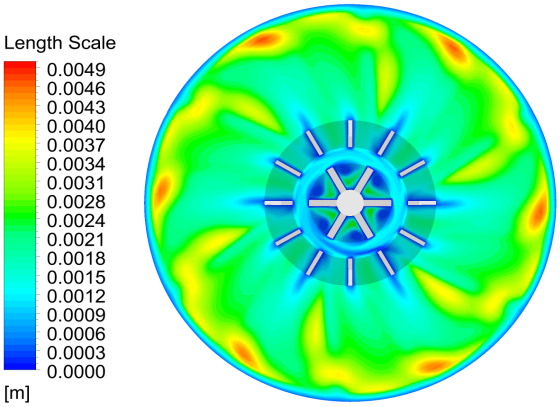

(b) Turbulence length scale contour plot

Figure 3.7. Trailing vortices visualized by isosurface of constant swirling strength value of 0.165 on vorticity contour plot (left) and contour plot of turbulence length scale (right) on horizontal plane 62.5 mm from tank floor.

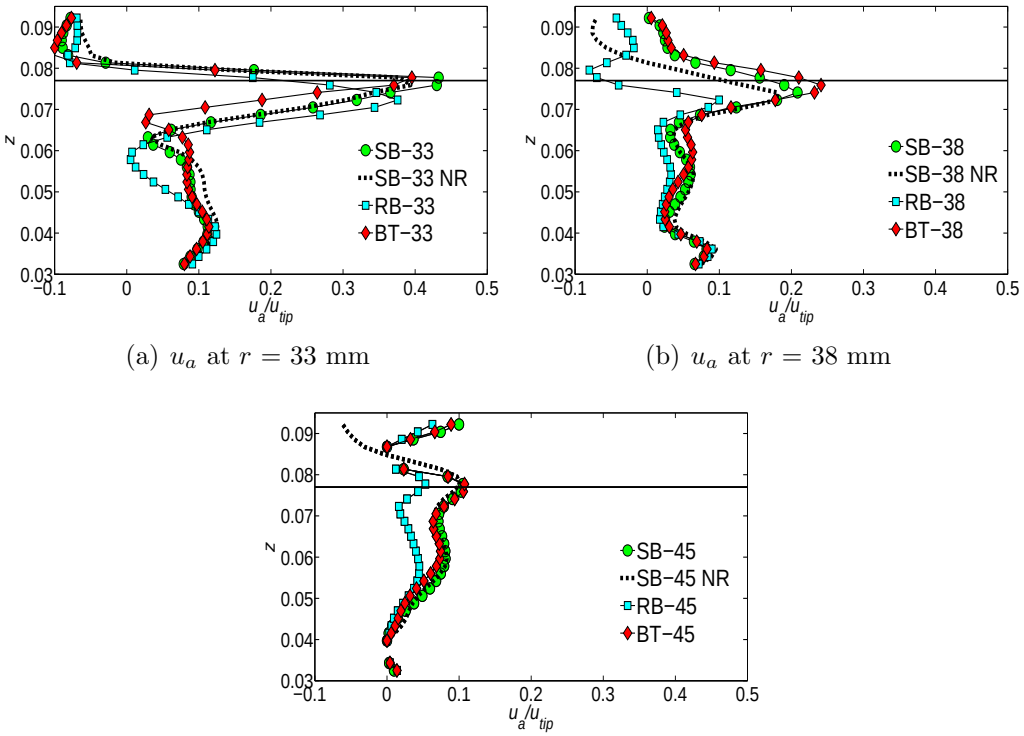

(a) u_a at $r = 33$ mm

(b) u_a at $r = 38$ mm

(c) u_a at $r = 45$ mm

Figure 3.8. Comparison of normalized axial u_a velocities profiles for four cases at three radial distances of 33, 38, and 45 mm. Legends: green circles are for SB, dotted line for $SB - NR$, cyan squares for RB, and red diamonds for BT.

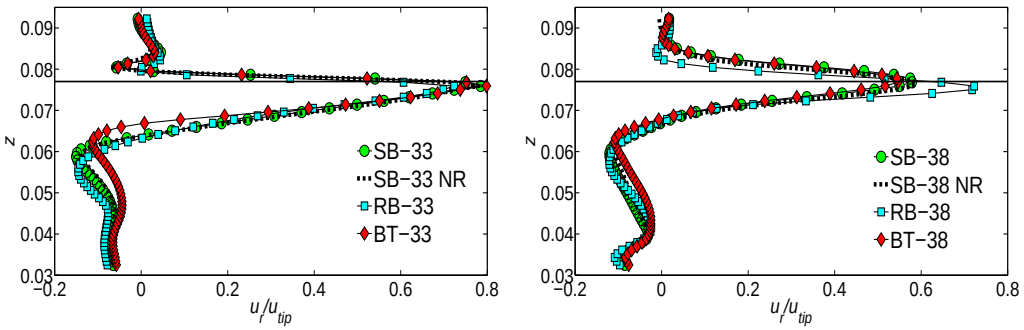

(a) u_r at $r = 33$ mm

(b) u_r at $r = 38$ mm

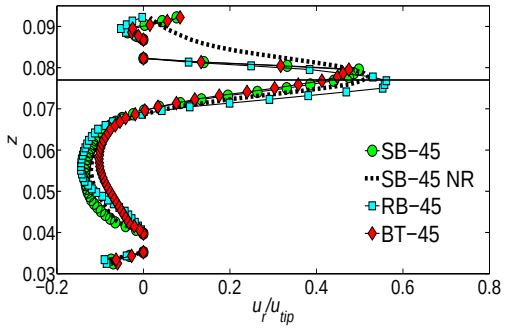

(c) u_r at $r = 45$ mm

Figure 3.9. Comparison of normalized radial velocities u_r profiles for four cases at three radial distances of 33, 38, and 45 mm.

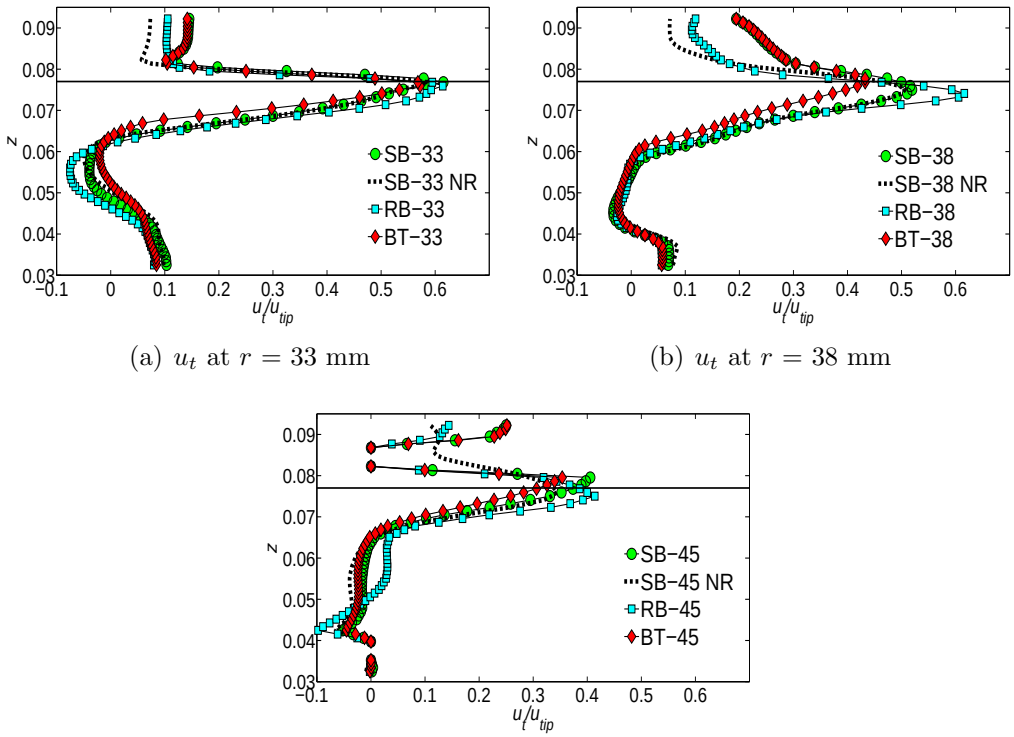

(a) u_t at $r = 33$ mm

(b) u_t at $r = 38$ mm

(c) u_t at $r = 45$ mm

Figure 3.10. Comparison of normalized tangential velocities u_t profiles for four cases at three radial distances of 33, 38, and 45 mm.

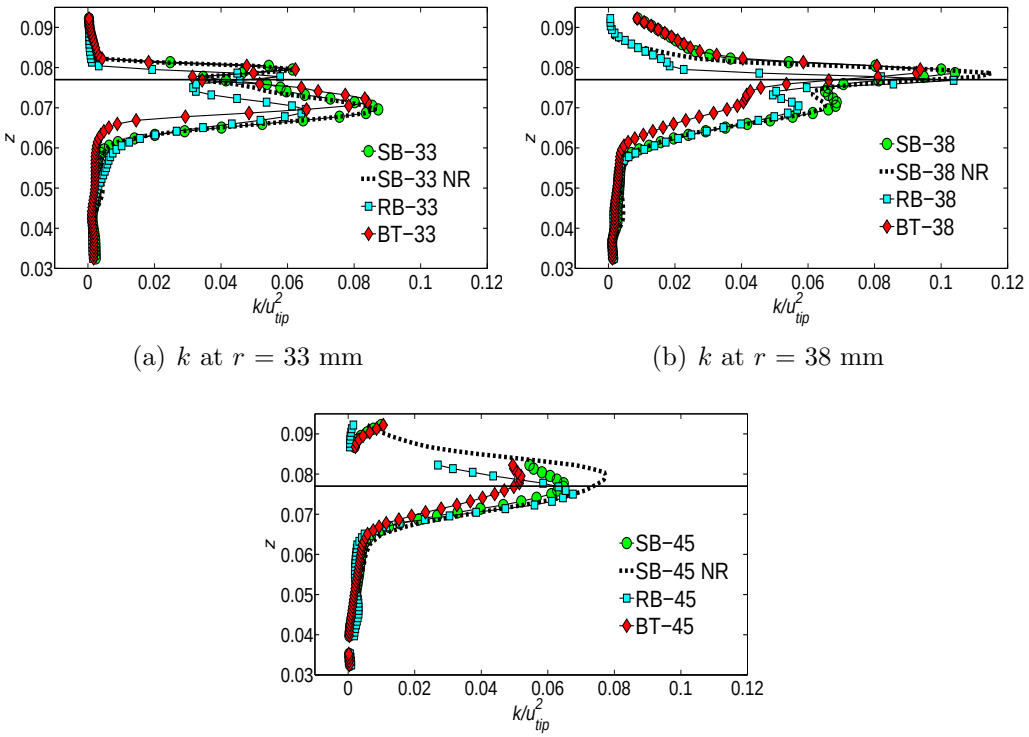

(a) k at $r = 33$ mm

(b) k at $r = 38$ mm

(c) k at $r = 45$ mm

Figure 3.11. Comparison of normalized turbulent kinetic energy k profiles for four cases at three radial distances of 33, 38, and 45 mm.

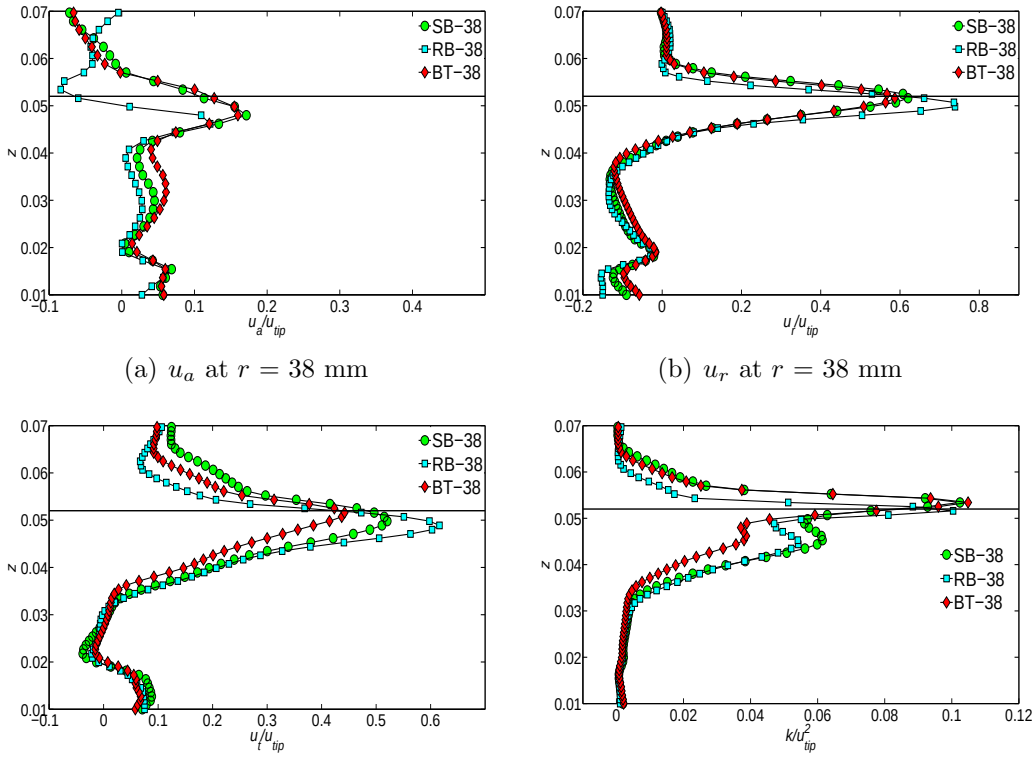

(a) u_a at $r = 38$ mm

(b) u_r at $r = 38$ mm

(c) u_t at $r = 38$ mm

(d) k at $r = 38$ mm

Figure 3.12. Comparison of normalized axial u_a velocities profiles for four cases at three radial distances of 33, 38, and 45 mm for $C = 25$ mm. Legends: green circles are for SB, dotted line for $SB - NR$, cyan squares for RB, and red diamonds for BT.

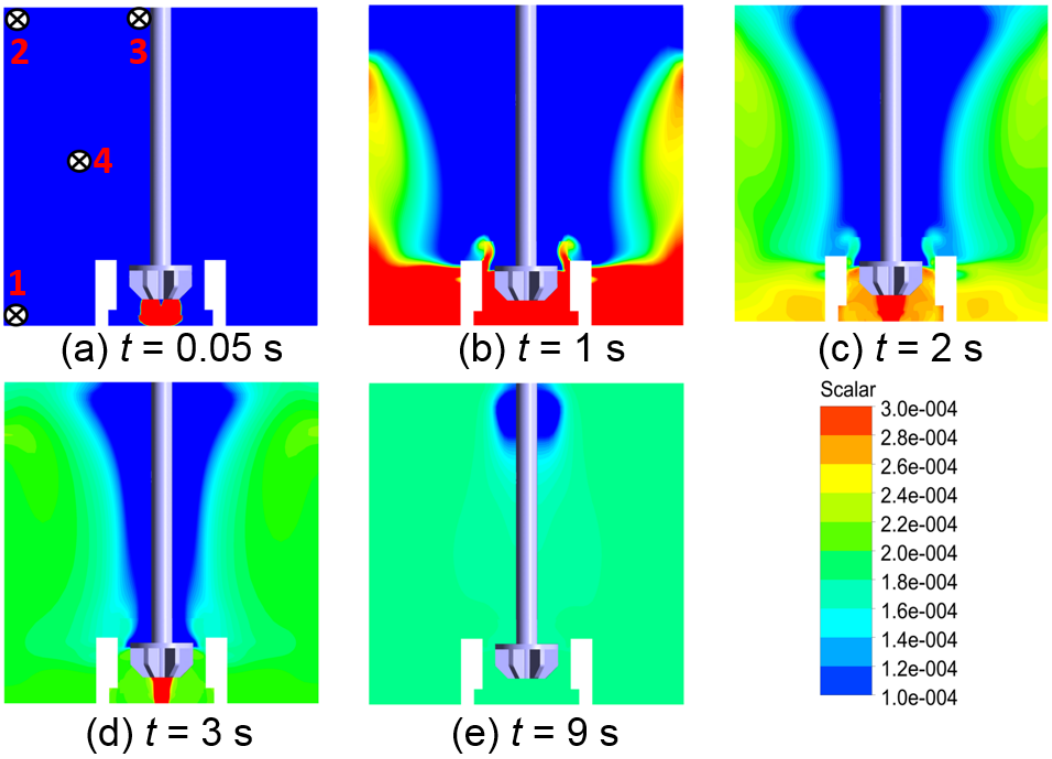

Figure 3.13. Contours of scalar evolving with time for SB.

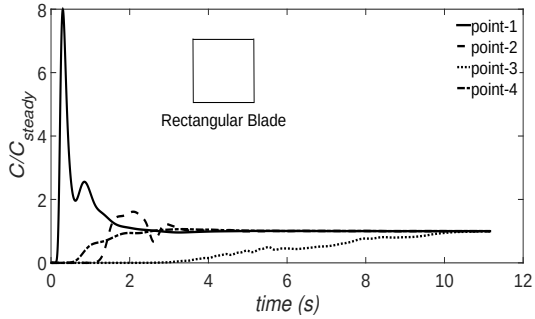

(a) Normalized scalar concentration vs. time for RB

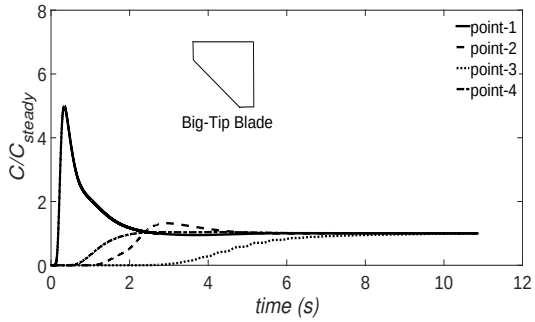

(b) Normalized scalar concentration vs. time for BT

Figure 3.14. Normalized scalar concentration versus time (s) at four discrete locations for RB and BT impellers.

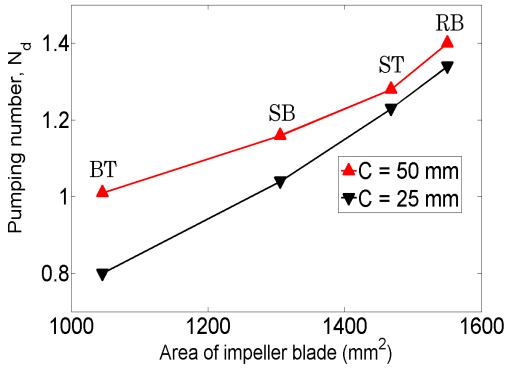

(a) Plot of pumping number (N_d) versus impeller blade surface area

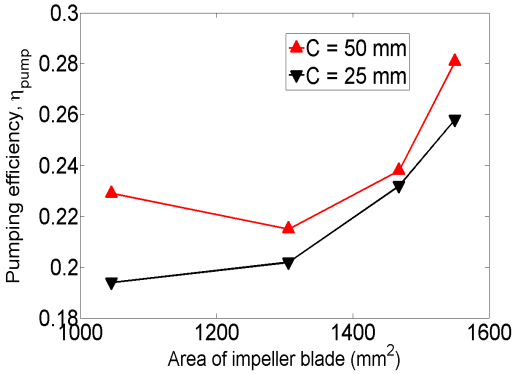

(b) Plot of pumping efficiency (η_{pump}) versus impeller blade surface area

Figure 3.15. Plots showing behavior of pumping or flow number and pumping efficiency versus impeller blade surface area of a single blade.

Table 3.1. Power and flow numbers for different impeller designs

Impeller Type	C (mm)	Re	$N_{p\tau}$	$N_{p\epsilon}$	N_d	η_{pump}
RB	50	80,000	4.99	3.60	1.40	0.281
ST	50	80,000	5.38	3.97	1.28	0.238
SB	50	80,000	5.39	3.97	1.16	0.215
$SB - NR$	50	80,000	5.44	4.16	1.13	0.208
BT	50	80,000	4.42	3.14	1.01	0.229
RB	25	80,000	5.19	3.48	1.34	0.258
ST	25	80,000	5.31	3.77	1.23	0.232
SB	25	80,000	5.15	3.74	1.04	0.202
BT	25	80,000	4.13	2.90	0.80	0.194
SB	50	40,000	5.38	3.93	1.17	0.217

CHAPTER 4

NUMERICAL INVESTIGATION OF MODERATELY DENSE SLURRIES IN FLOTATION CELL USING EULERIAN-EULERIAN SIMULATIONS

4.1 Abstract

In this work, mixing and suspension characteristics of moderately dense solid-liquid flows or slurries are studied using computational fluid dynamics (CFD) simulations in lab scale flotation cells. Eulerian-Eulerian multifluid model (MFM) is used to model the transport of continuous and disperse phases and standard $k-\epsilon$ mixture turbulence model is used to model turbulence in the two-phase flow. The multiphase CFD model is validated by comparing our predictions against experimental measurements of local solid phase volume fractions in stirred tanks from literature Micheletti et al.[15]. The CFD model is found to make good predictions with close match found in the high turbulence zone near the impeller. Furthermore, qualitative comparison of cloud height measurements and predictions are also performed and satisfactory agreement is found. Different drag models are considered for flotation cells and their predictions are compared for two particle sizes at similar mass loading and impeller rotation speed. Gidaspow and Brucato drag models are found to perform better than other models tested and therefore are adopted for further analysis. Using results from steady state simulations, important flow features and suspension characteristics are described for flotation cell. Slip velocities are found to be significant only in the impeller swept region. Steady state dispersed phase velocities in the axial direction at different radial locations reveal presence of large velocity gradients at the impeller level, which are limited to a small region in the impeller stream. Particle size is found to affect the suspension condition significantly with heavier, 520 micron particles not

suspending completely even at the highest speeds tested (2000 RPM). Based on the CFD results, suspension quality and mixture homogeneity are reported at different speeds and predictions are compared for different drag models.

4.2 Introduction

Two phase solid-liquid flows are commonly encountered in various process applications such as crystallization, catalytic reaction, leaching, fluidization, pharmaceutical, mineral processing, coal preparation among many others. Suspension and mixing of solid phase directly controls the efficiency of such processes, and therefore, is related to quality of the product. For chemical slurry reactors, complete off-bottom suspension condition is loosely defined as the suspension in which a majority of the particles in the system (approximately 99%) spend less than 1-2 seconds on the tank floor [8, 62]. The speed at which complete suspension occurs is commonly known as just suspension speed (N_{js}), which was first proposed by Zwietering [62], hence is also known as Zwietering speed.

A number of experimental and numerical studies reported in the past have consistently found Zwietering just suspension speed to grossly over-predict complete suspension condition in stirred tanks [63–66]. Some of the limitations of Zwietering's correlation are discussed in detail by [65–67].

In most cases, the extra energy utilized to suspend statistically insignificant number of particles cannot be not justified by a proportional small increase in process efficiency or performance [63]. This is especially true for froth flotation in mechanical flotation cells, where only suspension of majority of particles is required while complete homogeneity is not. In froth flotation, the objective is to introduce the maximum number of particles in the turbulent zone around the impeller and in that way increase the probability of collision between the solid particles and air bubbles.

Recently, Tamburini et al. [8] compared just suspension speeds using different experimental, theoretical, and numerical techniques reported in the literature along with their own experimental and numerical findings. Their findings showed a large variation in the predicted N_{js} between different techniques, with Zwietering's correlation consistently over-predicting just suspension condition compared to more recent

experimental and numerical techniques [8]. Tamburini et al.[8] also suggested using a more conservative speed called sufficient suspension speed (N_{ss}), first proposed by Micale et al. [68], which is lower than N_{js}. Tamburini et al. [8, 63] proposed a two-phase numerical model based on a multifluid model (MFM) for slurry flows and reported good agreement with experimental results for axial solids concentration. More recently, Shah et al. [69] reviewed solid phase suspension and methods to characterize suspension quality in stirred tanks using CFD approach.

Experimental solids suspension studies have been conducted in pilot scale flotation cells for gassed and ungassed conditions by Van der Westhuizen and Deglon [70, 71]. They reported complete off-bottom suspension for 100% N_{js} with significant sedimentation for speeds under 60% N_{js}. Moreover, Van der Westhuizen and Deglon [71] proposed a Zwietering type correlation for flotation cells under gassed conditions. The authors found that the critical impeller speed strongly depends on particle size, solids density, and air flow rate, with solids loading having less of an influence.

Recently, Van der Westhuizen and Deglon [72] applied just suspension correlation similar to Zwietering expression for bench-scale Denver and WEMCO flotation cells. However, information on mixing level and flow behavior are not reported in their work. Bakker et al. [73] studied formation of cavern, which is defined as the region of non-Newtonian yield stress fluid around the stator that moves in the tangential direction around the impeller. They considered pilot scale flotation cells and modeled the non-Newtonian slurry (fibrous nickel ore slurry) as Bingham plastic. The authors reported close agreement between prediction and measurement for cavern boundaries. Furthermore, Bakker et al. [74] extended their work by proposing a semiempirical model to predict cavern height but noted that constants used in the model must be obtained for different cell geometries either through experiments or computational prediction.

More recently, Shabalala et al. [75] experimentally studied the effect of slurry rheology on gas dispersion behavior in pilot scale Batequip flotation cell and reported decrease in bubble size and gas hold up at high solids loading. The authors attributed this behavior to formation of slurry cavern around the impeller, which results in lower gas hold up at high speeds. The formation of cavern in flotation cells is possibly due

to preferential concentration of particles in turbulent flows [52]. The review of open literature on froth flotation reveals that a systematic study of two-phase slurry flows using Eulerian-Eulerian CFD model has not been performed and reported as of yet.

The CFD has been extensively used to study dilute, moderately dense, and dense solid-liquid flows in stirred tanks [8, 63, 76–78]. For dense solid-liquid flows, Eulerian two fluid model (TFM) is used to describe the transport of continuous and dispersed phases. The interaction between continuous and dispersed phases is modeled using the interphase exchange term, which consists of formulations for all the interphase forces. Many CFD studies in the past have shown that drag [39, 76] and turbulent dispersion [63, 76] are the dominant forces, while other forces, namely, lift, Basset, Saffman forces can be safely ignored without significantly affecting the accuracy of the simulated results [63, 76, 78–80]. The drag force is modeled using a drag function that includes drag coefficient C_D, which depends on relative Reynolds number. For moderate and dense suspensions, selecting the correct drag function has significant effect on the accuracy of results as shown by [63, 76, 81, 82] for slurry reactors. Brucato and Brucato [83] proposed a corrected drag correlation taking free stream turbulence into effect for low and moderately dense slurries. Pinelli et al. [84] also proposed an empirical drag correlation for stirred tank reactor applications based on their experimental measurements.

The corrected drag functions proposed by Brucato and Pinelli have recently been compared by [8, 63], who reported the Brucato drag correction function, which is based on the local turbulence correction factor, to predict the solid concentration better than other models. Ochieng and Onyango [80] also found Brucato drag correlation to perform better than other drag correlations considered in their study, especially for high solids loading in the impeller region. Recently, Wadnerkar et al. [82] also compared different drag laws and concluded that Brucato and modified Brucato drag model predict the dynamics accurately compared to Gidaspow and Wen and Yu drag model. A brief review of literature presented here shows that the majority of the studies found the Brucato drag model to perform better than other models for stirred tank applications. However, some studies reported encouraging predictions using Gidaspow [80], Modified-Brucato [76, 78], and Pinelli [84] models.

The scientific literature in the case of mechanical flotation cells is even more scarce, with very little attention paid to the development of advanced CFD models for slurry flows. Recently, Su et al. [85] performed numerical investigation of gas-solid-liquid flows and reported velocities for gas and solid phase but provided no validation of their numerical approach. Most other studies have concentrated on visual measurements to determine N_{js} in flotation cells [70, 71]. An attempt to understand the mean behavior of solid phase inside lab-scale cells using CFD has not been reported in the literature yet.

With falling ore grades around the world, large quantities of milled particles are concentrated using froth flotation process, which represents about 15% of the total plant power consumption [4]. This has also led to an increase in the sizes of froth flotation machines with the largest commercial cells reaching capacities of over 600 m^3 [4]. Inefficient operation of froth flotation cells could lead to low recovery of valuable minerals and increased specific power consumption. Therefore, it is of practical importance to study the suspension characteristics of solid particles in generic flotation cells to gain a better understanding of complex slurry flows in these systems.

In the current study, the knowledge and recent developments made for slurry reactors are extended for froth flotation cells through the use of improved drag correlations for moderately dense slurry suspensions. The CFD model adopted in this work is validated against published axial solids concentration profiles in stirred tank employing Rushton turbine impeller by Micheletti et al. [15]. Qualitative comparison of particle cloud heights obtained experimentally using image analysis of transient cloud height behavior and numerically using CFD is also performed. This work represents the first attempt to investigate the effect of drag correlations on solids suspension characteristics for mechanical flotation cells. It is expected that the results of this study can be used to facilitate development of new or improved froth flotation machine designs.

4.3 Systems Investigated

In this work, solid-liquid CFD simulations of two systems, namely stirred tank reactor and flotation cell are performed. The design used for stirred tank is identical to the experimental setup described by Micheletti et al. [15] and Tamburini et al. [63]. A schematic of the stirred tank fitted with four baffles and six-blade Rushton turbine is shown in Figure 4.1(a). The stirred tank is fitted with baffles of width (W) equal to 10% of tank diameter (D) ($W = D/10$, $D = 300\ mm$). The height of the tank (H) is equal to the tank diameter, $H = 300\ mm$. The Rushton impeller diameter (d) and off-bottom clearance (C) are equal to one-third of tank diameter ($d = C = D/3 = 100\ mm$). Rushton impeller design parameters a and h are equal to $d/4$ and $d/5$, respectively. The shaft diameter (d_s) is equal to 20 mm.

A schematic of the flotation cell with relevant components is shown in Figure 4.1(b). The impeller design selected for this study resembles the general design used in many industrial flotation cells. Detailed schematic of impeller-stator assembly with relevant design parameters is presented in Figure 4.2(a). The diameter and height of flotation cell is identical to stirred tank described earlier. The flotation impeller diameter (d_f) is 60 mm, which is equal to 20% of the tank diameter. The off-bottom clearance (C_f) in case of flotation cells is defined as the distance between the impeller base to the tank floor, and is equal to 25 mm. Detailed flotation impeller design is shown in Figure 4.2(b) with dimensions given in mm. The stator used here has 12 blades equally spaced between two circular rings. The lower ring is supported by four legs which are fixed to the tank floor. The width of stator blades (W_s) is 20.5 mm. The gap between impeller and stator (h_{IS}) is 12 mm ($d/5$). Both top and bottom rings are 5 mm thick. The total height of stator ring h_s, which includes ring and stator blades is 47 mm. The legs (h_b) supporting the stator ring are 15 mm tall. The flotation impeller diameter (d_f) and off-bottom clearance critically affect the suspension characteristics and they are kept constant in all the simulations.

In all simulations, spherical silica particles are used as dispersed phase. The density of the solid particles is assumed to be 2470 kg/m^3 [8]. The continuous phase is water at 20^oC with dynamic viscosity equal to 0.001 $Pa\text{-}s$. Three particle sizes of average particle diameter corresponding to, 160, 520, and 655 μm (microns) are

considered in this work. For the stirred tank simulations, 655 micron particles are used and the impeller rotation speed is fixed at 700 RPM. For flotation cell simulations, 160 and 520 micron particles are considered. The impeller speeds for both particles are varied between 1000-2000 RPM to test the effect of impeller speed on suspension characteristics. In all the simulations, the mass fraction of solid/dispersed phase is fixed at 20%, which corresponds to 9.2% volume fraction (20% (w/w)).

4.4 Numerical Model

When the concentration of dispersed phase is considerable, usually over 5-10% (v/v) depending on the application, it has to be modeled explicitly [8, 69, 76]. In the present work, Eulerian-Eulerian (E-E) approach, which models both continuous and dispersed phases as interpenetrating continua, is used. The interaction between the phases is modeled by considering interphase exchange forces, namely, drag, lift, Basset, and virtual mass. Though lift and virtual mass forces can be significant in some cases, for stirred tank application they have been shown to be negligible [79]. Basset force, an unsteady force due to lagging boundary layer development on the particle, is also shown to be negligible [79] for stirred tank applications. Good predictions have been reported by considering only drag force by many authors [8, 63, 64, 76]. However, recently, Gohel et al. [86] showed that inclusion of turbulence dispersion force results in accurate prediction of cloud height. Therefore, turbulence dispersion force is considered along with the drag force in all the simulations performed in this work.

The discretized flow equations are solved in ANSYS Fluent 14.5 commercial solver. To model the impeller rotation, steady state multiple reference frames (MRF) technique is used. The averaged flow quantities, which are of particular interest, are predicted satisfactorily by MRF approach [8, 76, 80]. Pressure-velocity coupling is achieved using phase coupled SIMPLE approach. High accuracy of the solution is ensured by using second order schemes for flow variables. To ensure numerical stability, the simulations are initiated with low relaxation factors which are increased to higher values as the flow develops.

4.4.1 Governing Equations

In the E-E approach, conservation of mass and momentum equations are solved for both phases. The dispersed phase is treated as granular phase based on the kinetic theory of granular flows (KTGF) proposed by Lun et al. [87]. The mass conservation equation for phase q is given by [76]:

$$\nabla.(\alpha_q \rho_q \vec{v_q}) = 0 \tag{4.1}$$

The momentum conservation equation for phase q is given by [76]:

$$\nabla.(\alpha_q \rho_q \vec{v_q} \vec{v_q}) = -\alpha_q \nabla p - \nabla p_q + \nabla.\overline{\tau}_q + \alpha_q \rho_q \tilde{g} + \sum_{q=1}^{n} \tilde{R}_{pq} + \tilde{F}_{td,q} \tag{4.2}$$

also, the following equation must be satisfied:

$$\sum_{q=1}^{n} \alpha_q = 1 \tag{4.3}$$

where, α_q represents the volume fraction of phase q, ρ_q is the density of phase q, and $\vec{v_q}$ is the velocity of phase q. Pressure (p) field is shared by both phases. The stress tensor $\overline{\tau}_q$ and solids pressure term ∇p_q are obtained by KTGF as outlined by Lun et al. [87]. In the Euler-Granular approach, an additional equation for granular temperature encompassing the kinetic energy associated with particle velocity fluctuations is also solved. The term, ∇p_q, is zero for liquid phase as the pressure field is shared by both phases. The interaction term for phases p and q, R_{pq}, is a product of interphase momentum exchange coefficient (K_{pq}) and relative velocity, i.e., the difference between the phase velocities, $(\vec{v_p} - \vec{v_q})$. Therefore, the interaction term is defined as:

$$\sum_{q=1}^{n} \vec{R}_{pq} = \sum_{q=1}^{n} K_{pq}(\tilde{v_p} - \tilde{v_q}) \tag{4.4}$$

The turbulent dispersion force arises as a consequence of averaging interphase drag term and causes diffusion of dispersed phase. In the present work, turbulent dispersion model proposed by Simonin [29] is used, which is given as:

$$\vec{F}_{td,q} = -\vec{F}_{td,p} = -K_{pq} \vec{v}_{dr} \tag{4.5}$$

where, $\vec{v}_{dr}$ is the drift velocity of the dispersed phase due to turbulent fluid transport. The drift velocity using Simonin model [29] is given by:

$$\vec{v}_{dr} = \frac{D_{t,pq}}{\sigma_{pq}} \left(\frac{\nabla \alpha_p}{\alpha_p} - \frac{\nabla \alpha_q}{\alpha_q} \right) \tag{4.6}$$

where, $D_{t,pq}$ is equal to the mixture turbulent kinematic viscosity in this case. Dispersion Prandtl number (σ_{pq}) is unchanged from a default value of 0.75.

The lift force ($\vec{F}_{lift,q}$) and virtual mass force ($\vec{F}_{vm,q}$) are ignored in equation 4.2 as they are reported to be negligible in previous studies [76]. The force due to gravity is represented by the term $\alpha_q \rho_q \vec{g}$ in equation 4.2. The interphase exchange coefficient (K_{pq}) is specified in terms of drag function and represents the drag force experienced by solid phase. The KTGF involves a number of parameters which are unchanged and default values in Fluent solver are retained.

The flows investigated in this study are turbulent in nature owing to high RPM used to achieve suspension and mixing of solid phase. To close the additional terms arising as a result of Reynolds averaging, it is necessary to solve for turbulence quantities in the flow. Mixture $k-\epsilon$ turbulence model has been found to perform satisfactorily for the volume fraction range considered in this study [8, 63, 64, 76, 80]. The governing equation for turbulence kinetic energy (k) is given by:

$$\nabla.(\rho_m \vec{v}_m k) = \nabla.\left(\frac{\mu_{t,m}}{\sigma_k}\nabla k\right) + G_{k,m} - \rho_m \epsilon + \Pi_{k_m} \tag{4.7}$$

and, turbulence dissipation rate (ϵ) is given by:

$$\begin{aligned} \nabla.(\rho_m \vec{v}_m \epsilon) = \nabla.\left(\frac{\mu_{t,m}}{\sigma_\epsilon}\nabla \epsilon\right) + \\ \frac{\epsilon}{k}\left(C_{1\epsilon} G_{k,m} - C_{2\epsilon}\rho_m \epsilon\right) + \Pi_{\epsilon_m} \end{aligned} \tag{4.8}$$

where the mixture properties, namely the mixture density (ρ_m) and mixture velocity ($\vec{v}_m$), are calculated as:

$$\rho_m = \sum_{i=1}^{N} \alpha_i \rho_i \tag{4.9}$$

and

$$\vec{v}_m = \sum_{i=1}^{N} \alpha_i \rho_i \vec{v}_i / \sum_{i=1}^{N} \alpha_i \rho_i \tag{4.10}$$

Mixture turbulent viscosity ($\mu_{t,m}$) is computed from:

$$\mu_{t,m} = \rho_m C_\mu \frac{k^2}{\epsilon} \tag{4.11}$$

The kinetic energy production term ($G_{k,m}$) is computed as:

$$G_{k,m} = \mu_{t,m}\left(\nabla \vec{v}_m + (\nabla \vec{v}_m)^T\right) : \nabla \vec{v}_m \tag{4.12}$$

Π_{k_m} and Π_{ϵ_m} are the source terms which model the turbulent interaction between continuous and dispersed phase. The model constants in the governing equations for k and ϵ are $C_{1\epsilon} = 1.44$, $C_{2\epsilon} = 1.92$, $C_\mu = 0.09$, $\sigma_k = 1.0$, and $\sigma_\epsilon = 1.3$. The reader is referred to [29] and references therein for further information on the turbulence model.

4.4.2 Computational Domain

The computational mesh is generated using meshing tool ANSYS Icemcfd 14.5. The mesh is unstructured and consists only of hexahedral cells. The total number of cells for both stirred tank and flotation cell is approximately 550,000. Through grid convergence studies, comparing overall power draw and local velocity variation, the grid with 550,000 cells is chosen and found to provide good compromise between accuracy and speed. The mesh close to impeller is made finer to capture strong gradients developed due to impeller rotation. To improve the accuracy of the results, the mesh in the region between impeller and stator in flotation cell is made sufficiently fine.

4.4.3 Drag Correlations

In this work, five drag models are tested for stirred tank reactor, namely (a) Gidaspow, (b) Schiller-Naumann, (c) Brucato, (d) modified Brucato, and (e) Pinelli correlations, are compared.

4.4.3.1 Fluid-Solid Exchange Coefficient

The fluid-solid interaction term in Eq. 4.2 consists of exchange coefficient term (K_{pq}) which for two phase solid-liquid flow is represented by K_{sl} hereon. The general form of K_{sl} is given by:

$$K_{sl} = \frac{\alpha_s \rho_s f}{\tau_s} \tag{4.13}$$

where, f is drag factor and τ_s is the particle relaxation time. The coefficient of drag (C_D) is included in the definition of f and K_{sl} formulations for different models as shown in the following sections.

4.4.3.2 Gidaspow Model

The Gidaspow model has been extensively applied for fluidized bed and stirred tank applications [80, 82] and shown to provide consistently good predictions for both dilute and dense flows. If the liquid volume fraction $\alpha_l \geq 0.8$, then K_{sl} according to the Gidaspow model [88] is given by:

$$K_{sl} = \frac{3}{4} C_D \frac{\alpha_s \alpha_l \rho_l |\vec{v}_s - \vec{v}_l|}{d_s} \alpha_l^{-2.65} \tag{4.14}$$

where,

$$C_D = \frac{24}{\alpha_l Re_s} \left[1 + 0.15(\alpha_l Re_s)^{0.687}\right] \tag{4.15}$$

where, Re_s is the relative Reynolds numbers based on the relative velocity between phases.

4.4.3.3 Schiller-Naumann Model

The drag function for the Schiller and Naumann Model is based on Stoke's law of free settling. Since Stoke's law is applicable in the limit of very low Re, Schiller-Naumann proposed an empirical equation applicable for a broader range of Re_s, which is given by:

$$f = \frac{C_D Re}{24} \tag{4.16}$$

The C_D for Schiller-Naumann model is given by:

$$C_D = \begin{cases} \frac{24}{Re_s}(1 + 0.15 Re_s^{0.687}) & if \quad Re_s \leq 1000 \\ 0.44 & if \quad Re_s > 1000 \end{cases} \tag{4.17}$$

The K_{sl} equation for Schiller and Naumann model is identical to one shown in Eq. 4.13.

4.4.3.4 Brucato Correlation

Brucato and Brucato [83] proposed an equation that includes the effect of free stream turbulence in the drag factor equation, which is prescribed through an empirical modification based on their experimental measurements. The equation is give by:

$$C_{D,Brucato} = C_D \left[1 + 8.76 \times 10^{-04} \left(\frac{d_p}{\lambda}\right)^3\right] \tag{4.18}$$

where, $C_{D,Brucato}$ is Brucato drag correlation. Here, C_D is obtained from the Schiller and Naumann model as described in Eq. 4.17; d_p is the particle diameter and λ is

the Kolmogorov length scale calculated based on the local flow conditions using the relation:

$$\lambda = \left(\frac{\nu_{mix}^3}{\epsilon}\right)^{0.25} \tag{4.19}$$

where, ν_{mix} is mixture kinematic viscosity and ϵ is obtained from turbulence model.

4.4.3.5 Modified Brucato Drag Correlation

Khopkar et al. [78] suggested a modification to the Brucato correlation by substituting 10^{-05} instead of 10^{-04} in Eq. 4.18 to achieve a better fit for stirred tank flows. Kasat et al. [76] implemented this model and reported good agreement with experimental results in their work. The modified Brucato drag correlation is given by:

$$C_{D,modBru} = C_D\left[1 + 8.76 \times 10^{-05}\left(\frac{d_p}{\lambda}\right)^3\right] \tag{4.20}$$

4.4.3.6 Pinelli Drag Correlation

Another widely used drag correlation found in the literature is proposed by Pinelli et al. [84], which is again based on empirical observations. The empirical drag coefficient is expressed as:

$$C_{D,Pinneli} = C_D\left[0.6 + 0.4tanh\left(16\frac{\lambda}{d_p} - 1\right)\right]^{-2} \tag{4.21}$$

where, C_D is obtained from Schiller and Naumann model as described earlier.

4.5 Results and Discussion

The numerical model used in this work is first validated by comparing the predictions of solid concentration against experimental measurements of Micheletti et al. [15] in stirred tanks using Rushton turbine. To compare and contrast the performance of numerical model used in this study, solids concentration predictions of CFD model used in Tamburini et al. [63] are also shown. Due to the unavailability of experimental measurements of solids concentration inside generic flotation cells, numerical model is quantitatively validated against reported experimental measurements in stirred tanks. Both stirred tank and flotation cell share many similarities in terms of design and operating conditions. Therefore, the Eulerian-Eulerian TFM is assumed to perform accurately in the case of flotation cells as well.

4.5.1 Validation of Numerical Approach

Micheletti et al. [15] performed solid suspension experiments and measured concentration profiles using conductivity probe of 1 cm^3 volume in a lab-scale stirred tank with solids fraction equal to 9.2% by volume. Figure 4.3(a) shows axial solids concentration profiles at a radial distance of r equal to $0.35T$ obtained from our CFD model using Gidaspow drag model compared against measurements from Micheletti et al. [15]. As shown in Eq 4.15, the Gidaspow drag model includes solids concentration term in its formulation and has been shown to provide reasonably accurate predictions for moderately dense slurry flows in stirred tanks [80]. In addition, CFD results from Tamburini et al. [63], who used both the MRF and sliding grid (SG) approach along with the Brucato drag model in their CFD model, are also shown in Figure 4.3(a).

Comparison of solids concentration profiles between experimental measurements and predictions from our numerical model suggests that the trends agree remarkably well in the lower part of the tank. However, it is obvious that our numerical model under-predicts the solids concentration above the impeller disc level (disc is at $z = 0.33H$, 100 mm). In contrast, models used by Tamburini et al. [63] predict solids concentration accurately above the disc level but under-predict below disc level.

A comparison of numerical predictions of different drag models used in this work along with experimental measurements by Micheletti et al. [15] and CFD results of Tamburini using the MRF approach are shown in Figure 4.3(b). The axial concentration profiles are taken at a radial distance of $r = 0.35T$. All the drag models predict very identical trends and make accurate predictions below disc level with the exception of the mod-Brucato model. Compared to the Tamburini-MRF model, all the models used in this work make accurate predictions in the lower part of the tank, where the turbulence levels are significantly higher compared to the top region.

Overall, comparison of CFD predicted α with experimental measurements of Micheletti et al. [15] shows that Gidaspow and Brucato drag models are able to provide slightly better predictions compared to other models, especially close to the impeller region where flow is characterized by intense turbulence. Clearly, inclusion of turbulence effect in the Brucato model modifies the Schiller-Naumann model to correctly predict mean α in the intense turbulence region. Furthermore, the Gidaspow

model performs equally well compared to the Brucato model in stirred tanks as previously reported by Ochieng and Onyango [80], which has been reestablished here. However, it must be noted that the prediction of ϵ directly affects the drag coefficient and therefore, appropriate turbulence model must be selected based on the concentration of dispersed phase fraction in the flow. In summary, Brucato and Gidaspow drag models, which clearly perform better than other drag models based on their ability to accurately predict local solids concentration in stirred tank reactors, are considered for flotation cells.

4.5.2 Qualitative Validation

Experimental measurements of particle cloud height are performed using images extracted from videos (24 Hz) of slurry flows in lab-scale flotation cell. Minor differences in the geometries used in the CFD model and experimental setup such as difference in shaft diameter and stator ring thickness exist. These differences are assumed not to affect the overall behavior of a particle cloud and for practical purposes, the CFD and experimental can be assumed to be identical. The experimental setup consisting of a flotation cell filled with clear water is shown in Fig 4.4(d). For each tested operating condition, a minimum of 40 images are considered covering a few transient cycles during which the cloud undergoes periodic motion. Using an image analysis code in Matlab, horizontal location of cloud is tracked along the tank width for a set of images. By analyzing the data sets across different images for each condition, mean cloud height, mean cloud position at 40 preselected horizontal points, and cloud height fluctuation range expressed through both standard deviation and differential between maximum and minimum are calculated as shown in Fig 4.4. The experimental images selected and included in the background of Figs 4.4(a)-(c) show the representative behavior of the cloud at chosen conditions. Also included in Figs 4.4(a)-(c) are average cloud height profiles on the outer wall predicted by CFD using Gidaspow drag model at tested conditions. It must be noted that the particle sizes used in the experiments have a distribution with only mean sizes (160 and 520 microns) corresponding to discrete sizes used in CFD simulations. The particle size distribution based on cumulative percent passing for the two particle classes is shown

in Figure 4.5. It can be seen that a significant fraction of both undersize and oversize material exists over the assumed mean size, which explains some differences between CFD predictions and experimental cloud height measurements.

In general, the CFD predictions satisfactorily agree with the experimental measurements for both particle sizes for all tested cases. For 160 micron particles in Figure 4.4(a), a dilution layer is present above the cloud, which represents a region of low mixing and it mainly contains particles belonging to the size class under 160 microns [76]. For 520 micron particles, the interface separating the particle cloud from the fluid is clear at both speeds as shown in Figure 4.4(b) and (c). Even the presence of a particle bed along the wall at both speeds is predicted by CFD for 520 micron particles. The qualitative comparison of cloud heights further validates the CFD model used in this work.

4.5.3 Mean Flow - Flotation Cells

To illustrate the general flow characteristics of moderately dense slurry flows in flotation cells, a case with 160 micron particles at volume loading of 9.2% and C equal to 25 mm are considered. Velocity vectors of solid phase superimposed on solid volume fraction contours are shown in Figure 4.6(a). The solid phase motion is characterized by double loop flow, which is typical of radial flow impellers [47]. The contour plot suggests good mixing between the phases as evidenced by a fairly large region of intermediate α value in the lower part of the cell. The velocity vector plot further indicates that the solids are carried by the radial jet and upon encountering the tank wall, the jet splits into upper and lower recirculation zones. The particles in the lower recirculation zone follow the tank wall before acquiring radial velocity and eventually move towards the impeller.

In one of our previous numerical studies on single phase flows in lab-scale flotation cell, we observed radial flow behavior characterized by double loop flow [89]. Furthermore, due to adopted impeller/stator assembly design and and proximity to the tank floor, a solids exclusion region is created below the impeller as shown in Figure 4.6(a). The region below the impeller is shown to have significant vorticity for single phase flows as reported by [47]. The solid particles are known to preferentially concentrate in the regions of high vorticity [52], thus creating a solids exclusion region (a blue

region (online version) below the impeller in Figure 4.6(a)).

Due to the combined effect of drag and inertia, a large fraction of solid particles do not follow the fluid flow completely in the upper recirculation zone as suggested by vectors pointing in the upward direction. Instead, the velocity vectors indicate that the solid phase flows down and recirculates above the stator level. A relatively small fraction of the solid phase can be seen moving towards the top of the tank.

Figure 4.6(b) shows the solids α along 5 horizontal planes located at vertical distance of 1, 35, 75, 130, and 200 mm from the tank floor, which are named P1–5 based on their order from the tank floor. Preferential concentration of solid particles is common in the regions of turbulence characterized by high vorticity and shear rates [52]. A region of low solids α can be observed in the core of the trailing vortex while high α is visible outside the trailing vortex bounds. Here, a region of low concentration is formed directly underneath the impeller surrounded by small concentric fillets of silica particles that rise due to the impeller action. Insignificant number of particles reach the top of the vessel as they are carried by the flow.

A clear particle cloud can be observed for monosized particles using an isosurface plot as shown in Figure 4.6(c). The isosurface shows a surface of constant solids α value of 0.01 that is located at an approximate distance of 200 mm from the tank floor. The curved nature of isosurface makes it difficult to calculate single value of cloud height [8].

Slip velocities directly control the mass transfer characteristics in multiphase flows [79], as nondimensional mass transfer coefficient, Sherwood number (Sh) is related to Re_p as $Sh \propto Re_p^{1/2} Sc^{1/3}$. Contour plots of Slip velocities (V_s) and its components are shown in Figure 4.7. The slip velocities are mostly equal to zero in the bulk of the tank except in the impeller-stator region and near the top of the tank where tangential slip velocity (V_{st}) is found to be highest. It should be noted that though, near the top region, the solid phase concentration (α) is extremely low and, therefore, the product of V_s and α, which quantifies the mass transfer rate, will be low. This observation has been previously made for axial flow impellers by Ljungqvist and Rasmuson [79].

The above discussion shows that the selected impeller-stator configuration is successful in suspending majority of the solid particles at 1000 RPM (tip speed =

3.125 m/s, Re = 60,000), which is at the lower end of operational speed for flotation cells. The chosen design results in formation of a solids exclusion region below the impeller, which positively affects mixing and improves flotation efficiency when used with air, because very limited air holdup is reported below the impeller in general [47]. Furthermore, formation of localized high concentration leads to microinstabilities and improves collisions with air bubbles thus promoting higher flotation efficiency.

4.5.4 Effect of Particle Size and Agitation Rate

The solids volume fraction in all the cases considered is equal to 9.2% (v/v), which corresponds to 20% mass fraction (w/w) of solid phase. The impeller speeds tested in this work correspond to the impeller tip speeds frequently encountered in the industrial flotation cells (3.125 - 6.25 m/s). Two mononsized particles classes of 160 and 520 microns are considered. Based on the comparison of drag models for stirred tank reactors, Gidaspow and Brucato models are considered for flotation cells. For 160 micron particles, mod-Brucato model is also additionally considered to contrast the effect of empirical parameter on predictions. For 520 micron particles, which represents the coarse end of the floatable particle size range, only Gidaspow and Brucato models are compared for speeds between 1000-2000 RPM (3.125 - 6.25 m/s).

4.5.4.1 160 Micron Particles

CFD data are extracted in the axial direction at four radial locations of r = 35, 50, 85 and 125 mm from the center of the tank as shown in Figure 4.6(d). Figs. 4.8 and 4.9 show comparison of solid volume fraction and velocities in the axial direction by Gidaspow, Brucato, and Mod-Brucato models at four radial locations. Pinelli and Mod-Brucato drag model predictions are found to be mostly identical and therefore, not included in the plots to reduce clutter. Below the impeller close to the tank floor, $\alpha_{Bru} > \alpha_{Mod-Bru} > \alpha_{Gid}$, which follows the observation made for a stirred tank reactor. The discontinuities in the α profiles at r equal to 50 mm are due to the presence of the stator ring. The largest deviations in the predictions occur along the impeller height and close to the floor. The Brucato model takes the effect of free stream turbulence into consideration and as a result, higher drag force is experienced

by the dispersed phase. Furthermore, higher drag makes the particles difficult to suspend, which explains the higher α close to tank floor. The preceding discussion shows that different drag models can lead to very different α prediction, especially in the regions characterized by intense turbulence and vorticity.

Solid phase velocities ($v_{sil-160}$) at the same radial locations shown in Figure 4.9 suggest that solid phase velocities predicted by different models do not differ as notably as α. The large gradients in $v_{sil-160}$ lead to high rates of mass and momentum transfer as seen close to impeller. Clear peaks are observed at r equal to 35 and 50 mm. At $r = 50$ mm, peak $v_{sil-160}$ drops by 43 % to 1.576 m/s and the peak vanishes leading to somewhat uniform profile at r equal to 85 and 125 mm. Velocities in the rest of the tank, especially at the top half portion of the tank remain low at all axial locations. $v_{sil-160}$ values go to zero on the surface of stator following no slip condition for both phases. Moving further away from impeller at r equal to 85 and 125 mm, $v_{sil-160}$ are low throughout the length of the cell. It should be noted that even though $v_{sil-160}$ is predicted in the top half the tank the solids concentration is very low ($\leq$ 1%) as seen in Figure 4.8.

The effect of impeller speed on particle suspension and mixing is studied by increasing impeller rotation speed from 1000 to 2000 RPM and considering Gidaspow and Brucato models. Figure 4.10 shows the isosurface plot predicted by the Gidaspow model for three α values at three agitation rates. The evolution of particle cloud (α $\approx$ 0.01) can be visualized by observing the changing profile of blue colored surface with agitation rate. Comparison of α in the axial direction at different speeds and radial locations is shown in Figure 4.11. In addition contour plots in Figure 4.12 are offered to help visualize the solids distribution in radial and axial planes. Increase in speed over 1500 RPM improves mixing in both axial and radial directions as shown in both axial α profiles and contour plots. Based on the contour plots at P1, it is evident that solid particles concentrate into six bands along the tank floor at 1000 RPM. With increasing impeller speed, more solids are lifted and the thickness of particle bed can be seen decreasing gradually. Brucato model predicts higher α in the bottom portion of the tank at speeds upto 1500 RPM for all radial locations in comparison to Gidaspow model. Also evident is lower average cloud height marked

by low α values for all speeds. Interestingly, the solid exclusion region is not predicted by the Brucato model at 1000 RPM, but predicted by the Gidaspow model for all speeds which is more physical and matches the visual observations made from videos taken from a camera placed under the tank. The nonphysical prediction by Brucato model at 1000 RPM could be due to inability of the drag correction modification to correctly capture the suspension behavior at lower level of turbulence. However, a more in-depth analysis is needed to fully explain this behavior.

In summary, both Brucato and Gidaspow models predict qualitatively similar solids distribution in the tank except at 1000 RPM near the tank floor. Differences in the predicted α profiles are obvious in the impeller stream but the profiles converge in the bulk. Also, the difference in predicted values are higher at lower speeds and become more similar at higher speeds. In general, the Brucato model predicts higher concentration of solids below impeller level and lower cloud height. Speeds at 1500 RPM and over result in excellent mixing of solid phase both in axial and radial direction and small spatial heterogeneities are present only in the regions of high vorticity. Importantly, the difference in predictions between drag models observed at 1000 RPM especially close to the tank floor clearly highlights the need to validate and check the models for correctness before using them at conditions outside their range of applicability.

4.5.4.2 520 Micron Particles

Coarse particle flotation involving particle sizes over 200 microns is also performed for certain ores. When applicable, the ability to perform froth flotation at coarser sizes results in huge savings in terms of saved comminution costs, which is, by far, the most expensive mineral processing operation. To this end, simulations involving coarser size fractions are performed to further understand the particle suspension and mixing conditions in mechanical flotation cells. Since Gidaspow and Brucato models are found to perform better than other models for stirred tanks, for 520 micron particles only Gidaspow and Brucato models are considered. For the Gidaspow model, speeds of 1000, 1250, 1500, and 2000 RPM are considered, whereas for the Brucato model only low (1000 RPM) and high (2000 RPM) speeds are considered. The solids

concentration profiles predicted by both the models is found to be very similar and therefore, only results from Gidaspow model will be presented and discussed in the following.

Axial α profiles at different impeller speeds and radial locations r are shown in Figure 4.13. Contour plots along a vertical plane passing midway between two blades for one-half of the tank are shown in Figure 4.14. The plots in Figure 4.13 are characterized by high values of α in the lower part of the tank. At 1000 RPM, solid volume fractions at all radial locations are very similar. Under this condition, high settling that is characterized by the presence of a completely packed bed ($\alpha \approx 0.63$), can be observed near the tank floor. At 1250 RPM, the solid mixing is marginally improved and some solid phase is present over the top of stator. At 1500 RPM, more particles are suspended and the height of particle cloud also increases coupled with a thinning particle bed. Another important feature is the increase in the size of vortex core region in the impeller stream with increasing speed. Larger particles have a tendency to accumulate at the periphery of vortices and formation of trailing vortices due to impeller rotation also causes preferential concentration of particles [52].

In Figure 4.14, the effect of N on preferential concentration can be clearly observed. With increasing N, the vortex core region expands and pushes the region of high particle concentration around trailing vortex further outward, thereby increasing its size with speed. At 2000 RPM, a small almost circular region with very low α, resulting in solids exclusion region at the center of the vortex is predicted. Furthermore, at 2000 RPM the particle bed with $\alpha \approx 0.63$ is present only below the impeller. The particle cloud reaches roughly 50% of the tank height along the vertical wall, while the concentration of particles above the impeller close to the shaft remains low. The solids exclusion region below the impeller that was previously predicted for 160 micron particles is not observed for 520 micron particles at any speeds tested. The presented results and discussion show the effect of increased particle size on suspension and mixing properties at different impeller speeds.

4.6 Performance Analysis in Flotation Cells

The suspension condition in flotation cells can be assessed using different methods reported in the literature. Tamburini et al. [8] have reviewed and compared different methods to calculate N_{js} and compared the values against the widely accepted Zwietering correlation prediction for the Rushton turbine stirred tank. Furthermore, Tamburini et al. [8] suggested modifications to several methods, such as using sufficient suspension speed instead of widely used N_{js}. Among different methods compared by Tamburini et al. [8], variation coefficient and power number methods can be extended to results obtained in this work. Furthermore, suspension homogeneity defined by Hosseini et al. [90] for experimental work is extended to CFD results, and comparison across different impeller speeds is presented. Variation coefficient σ can be used to asses the suspension quality which is calculated as:

$$\sigma_v = \sqrt{\frac{1}{n}\sum_{i=1}^{n}\left(\frac{\alpha_i}{\alpha_{avg}} - 1\right)^2} \tag{4.22}$$

where, n is the total number of finite volumes (cells) in the CFD model, α_i is the solid volume fraction in a finite volume i (i = 1-n) and α_{avg} is the average solids loading, which in all the cases is 0.092 or 9.2%. Referring to the earlier works of Kasat et al. [76] and Tamburini et al. [8], it is clear that a value under 0.8 is desired to ensure creation of conditions close to just suspension. Similarly, homogeneity χ can be defined as:

$$\chi = 1 - \sqrt{\frac{\sum_{i=1}^{n}(\alpha_i - \alpha_{avg})^2}{n}} \tag{4.23}$$

A χ value of close to 1 implies a completely homogeneous mixture. The torque (τ) values generated on rotating parts of the flotation cell can be used to calculate power number ($N_{p\tau}$) as:

$$N_{p\tau} = \frac{P}{\rho_m N^3 D^5} \tag{4.24}$$

where, P is the power draw and N is speed in rev/sec. Mixture density (ρ_m) and power draw are given by:

$$\rho_m = \rho_s \alpha_{avg} + \rho_l(1 - \alpha_{avg}) \tag{4.25}$$

$$P = 2\pi N \tau \tag{4.26}$$

where, ρ_s and ρ_l are densities of solid and liquid phase, respectively. All the results are tabulated in Table. 4.1. It is clear that different models predict widely different σ_v values at same agitation rates. For 160 micron particles at 1000 RPM, the Gidaspow model predicts lowest σ_v value of 1.24 and Pinelli and Brucato models predict the highest σ_v value of 1.88. With an increase in agitation rate, mixing is improved, which leads to lower σ_v values. At 1500 RPM, S-N model predicts the highest σ_v value of 1.13 which is twice the value predicted by Syamlal model.

According to previous CFD studies of slurry flows in stirred tanks by Kasat et al.[76] and Tamburini et al. [8], a σ_v value between 0.2-0.8 suggests just suspension conditions in the tank. Extending their findings to the present work, it can be observed that just suspension conditions are achieved at 1500 RPM. At 2000 RPM, the σ_v value predicted by Gidaspow and Brucato models are very similar and suggest conditions well beyond just suspension.

For 520 micron particles, σ_v values are large since particles settle and form a packed bed. Even at 2000 RPM, the suspension is far from just suspension condition as evident from the presence of fillets below impeller in Figure 4.13(d). Looking at the χ values, it is clear that 1000 RPM is sufficient to achieve acceptable level ($\chi \geq 0.75$) of homogeneity in the tank for 160 micron particles. With increase in agitation rate, mixing is improved and a maximum value of 0.955 is predicted at 2000 RPM with the Gidaspow model. For 520 micron particles, χ values are low and increase marginally with increase in speed.

Power numbers calculated based on torque are also presented in Table. 4.1. The general trend for 160 micron particles indicates that $N_{p\tau}$ value does not change appreciably for speeds tested here. However, a few small variations in the $N_{p\tau}$ are evident and such behavior is reported for stirred tanks as well [76]. For instance, Kasat et al. [76] observed $N_{p\tau}$ to peak at an intermediate speed before reaching a steady value at higher speeds. The Gidaspow model predicted peak $N_{p\tau}$ value at 1250 RPM . In contrast, Brucato predicted $N_{p\tau}$ values increase steadily with impeller speed. Angst and Kraume[91] reported increased power numbers for the pitched blade impeller and attributed this to the presence of a particle bed which effectively created low clearance conditions. Similar observations have been made for disk turbine by

Barresi and Baldi[92].

For 520 micron particles, the $N_{p\tau}$ values are under-predicted compared to corresponding values for 160 micron particles. The single phase $N_{p\tau}$ value for fully turbulent flow in an identical tank is found to be about 5.15 by the authors in one of their earlier studies [89]. Compared to the single phase power numbers, the power numbers for slurry flows are clearly under-predicted, more so for a larger particle size class, which is consistent with the previous observations made for radial impellers [93, 94]. Both the authors reported a decrease in power number for coarser particles compared to finer particles at identical operating conditions. This behavior, also observed for flotation cells in our studies is due to reduced pumping and circulation of continuous phase by the impeller which results in lower power consumption. Moreover, the particles directly affect the turbulence magnitude by modulating it based on their size and concentration [52, 91]. When the turbulence is suppressed by dispersed phase, shear stress developed is reduced leading to lower power consumption [91].

4.7 Conclusions

Eulerian-Eulerian simulations of moderately dense slurry flows inside lab scale stirred tanks and flotation cells are performed. Multiphase two-fluid model CFD model is validated both quantitatively for stirred tanks and qualitatively for flotation cells by comparing CFD predictions against experimental concentration and cloud height measurements, respectively. Turbulence in the flow is modeled using mixture standard $k-\epsilon$ model. Based on the comparison of experimentally measured local concentration by Micheletti et al. [15] against predictions for stirred tanks, it is established that Gidaspow and Brucato drag models perform better than other drag models considered. The CFD model gave excellent predictions in the lower half for stirred tanks but slightly under-predicted in the upper half for stirred tanks.

Slurry flow in flotation cell with 9.2% volume loading (20% (w/w)) of 160 micron particles is considered. Radial flow with sharp velocity and concentration gradients are observed in the impeller swept volume and impeller stream. A solids exclusion region develops exactly below the impeller causing solids to concentrate around the vortex. A detailed account of performance of different drag models is presented and

their predictions are critically compared for 160 micron particles. Good mixing is reported in both axial and radial directions for speeds over 1500 RPM based on contour plots and analysis of solids concentration using variation coefficient and homogeneity calculations. The effect of particle size on mixing and suspension conditions in the tank is compared at different speeds by considering the 520 micron particle at similar mass loading. Based on variation coefficient and homogeneity calculations, the suspension for 520 micron particles is found to be far off from just suspension condition even at 2000 RPM. Also, the values of the variation coefficient predicted by different drag models are found to vary significantly at identical flow conditions. The power numbers calculated based on the torque values on rotating parts are under-predicted in comparison to single phase power numbers for 520 micron particles which is consistent with observations made by other researchers.

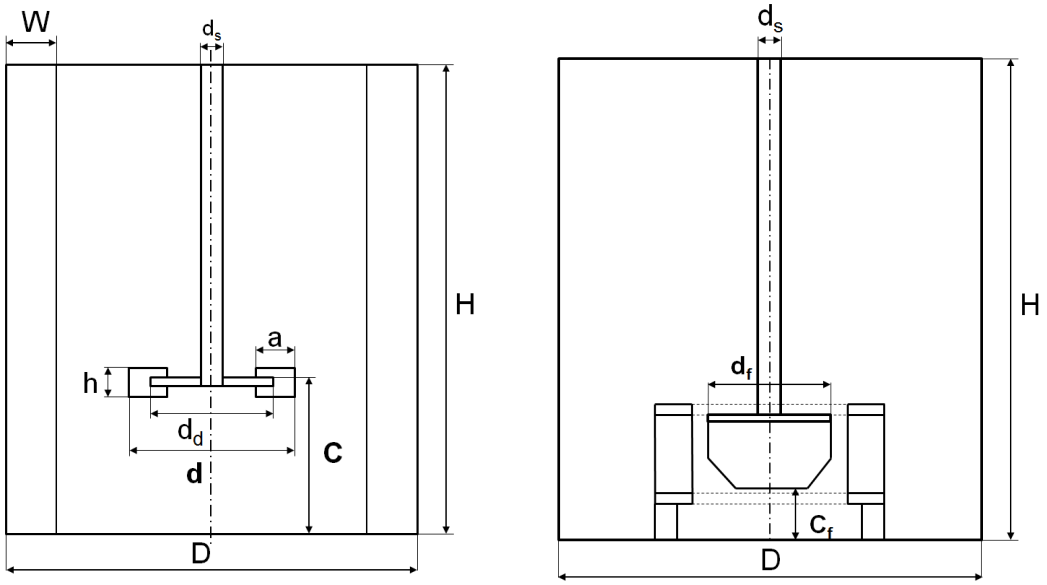

(a) Schematic of stirred tank fitted with Rushton turbine

(b) Schematic showing geometrical details of flotation cell

Figure 4.1. Schematic showing details of stirred tank and flotation cell used in CFD simulations.

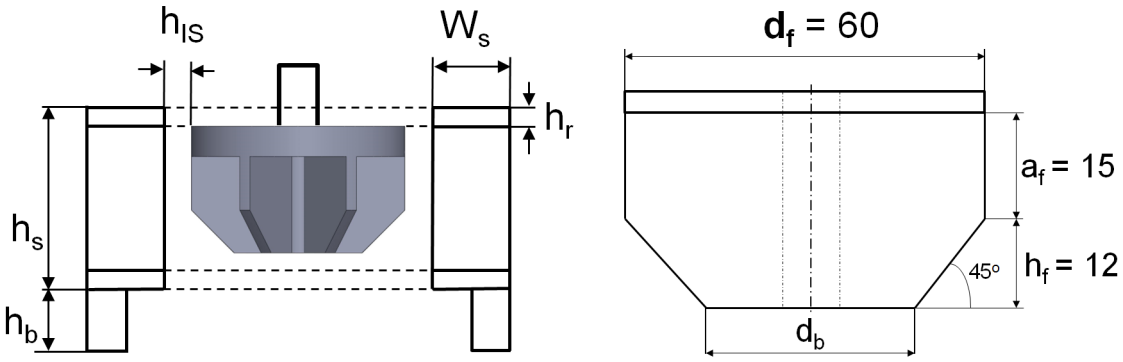

(a) Schematic of impeller-stator configuration used

(b) Schematic of impeller with dimensions

Figure 4.2. Impeller-stator and flotation impeller schematic with dimensions used in this work; all dimensions are in mm.

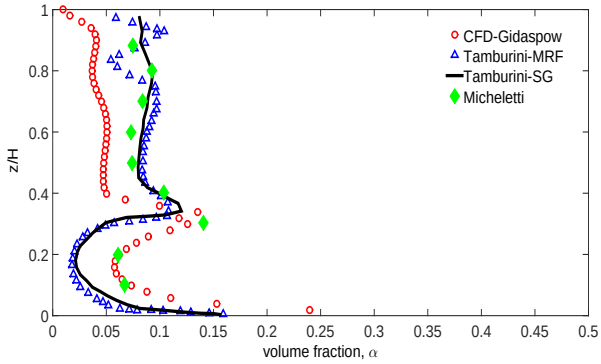

(a) Comparison of solids concentration profiles at 700 RPM

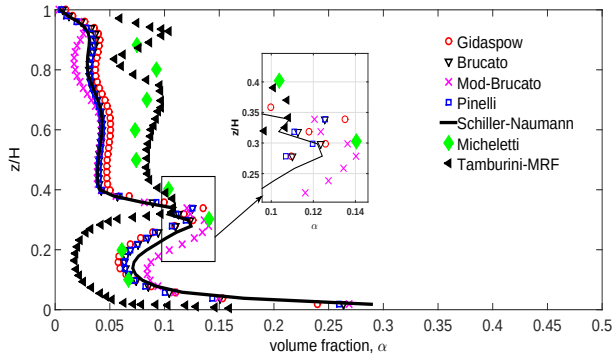

(b) Comparison of different drag model predictions at 700 RPM

Figure 4.3. Comparison of axial solids concentration profiles obtained from CFD and experimental measurements at a radial distance of $r = 0.35T$:(a) CFD predictions (red circle) versus experimental measurements of Micheletti et al. [15] (green diamond) and CFD predictions of Tamburini et al. [63] - MRF (black line) and SG (blue triangle) (b) CFD predictions using different drag laws compared against experimental measurements.

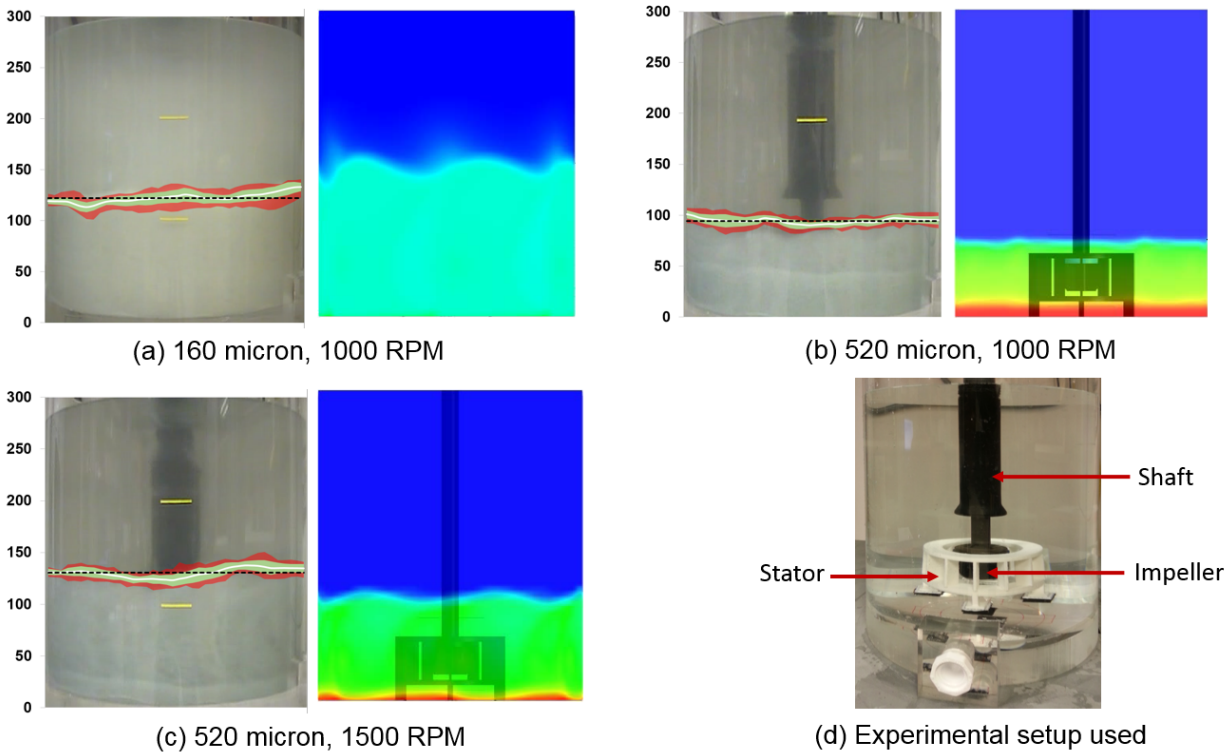

Figure 4.4. Figures showing the comparison of cloud heights obtained from image analysis of transient cloud height and CFD predictions for 160 and 520 micron particles (a)-(c). For experimental images, dashed black line represents the mean cloud obtained across multiple images, continuous white line represents mean cloud position at different positions, the green shaded region represents the one standard deviation above and below mean and red shaded region indicate the maximum and minimum at each location along the tank width (see online version for colors) (d) Image of the flotation cell with 3D printed parts used in the cloud height measurements.

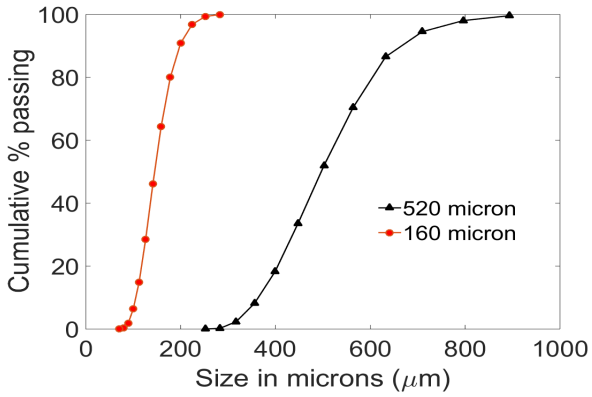

Figure 4.5. Plot showing the cumulative percent passing for two particle size classes used in the transient cloud height measurement experiments.

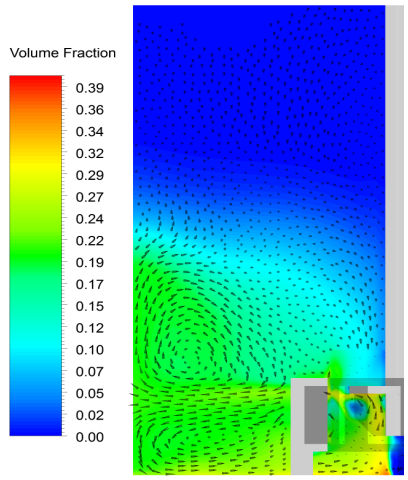

(a) Solids α contour plot and solids velocity vectors superimposed

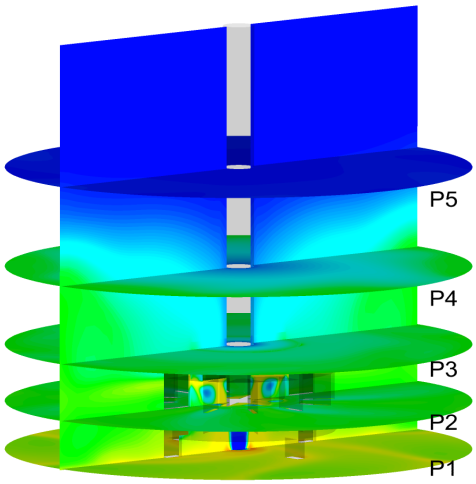

(b) Solids α along different z planes

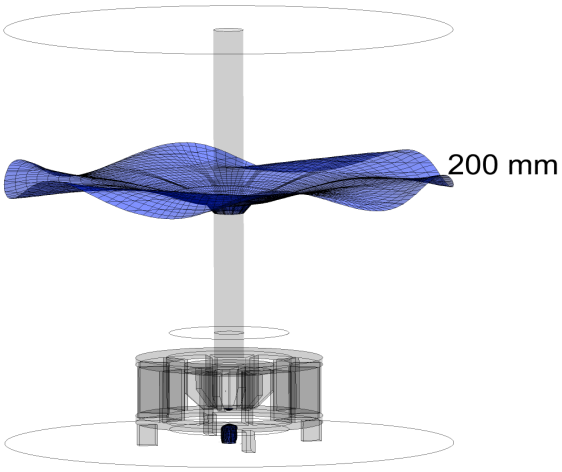

(c) Particle cloud, $\alpha = 0.01$

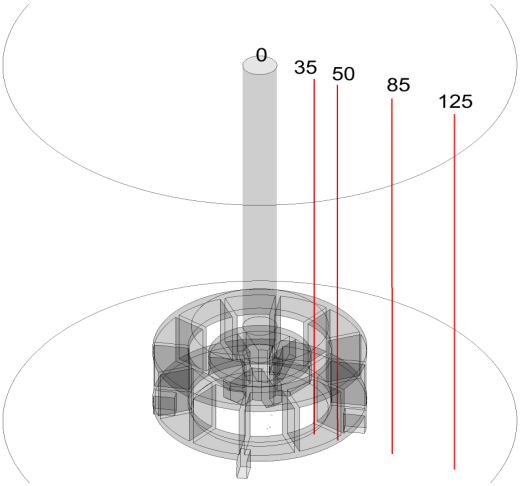

(d) Radial locations where CFD data are extracted

Figure 4.6. Solid phase volume fraction and velocity vectors in flotation cells showing the flow pattern for silica particles of size 160 microns at 1000 RPM (a) Velocity vectors on vertical plane, (b) Volume fraction α contours along five horizontal planes, (c) Isosurface of $\alpha = 0.01$ showing the shape and position of particle cloud, (d) Radial locations where CFD data are extracted for comparison.

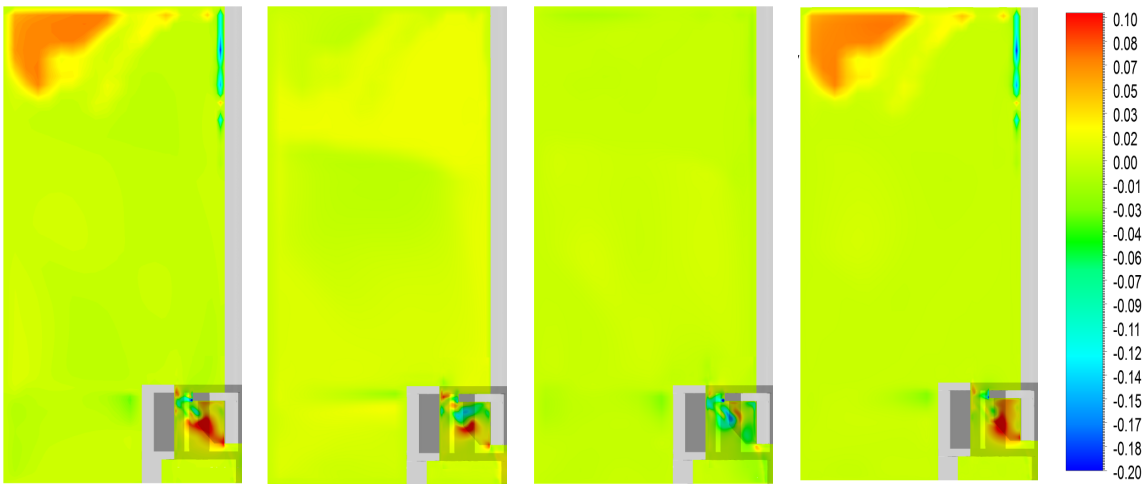

(a) Slip velocity magnitude V_s (b) axial component V_{sa} (c) radial component V_{sr} (d) tangential component V_{st}

Figure 4.7. Contours of slip velocity (V_s) and its components on a vertical plane for 160 micron particles in flotation cell at 1000 RPM (a) slip velocity magnitude, (b) Axial component, (c) Radial component, and (d) Tangential component.

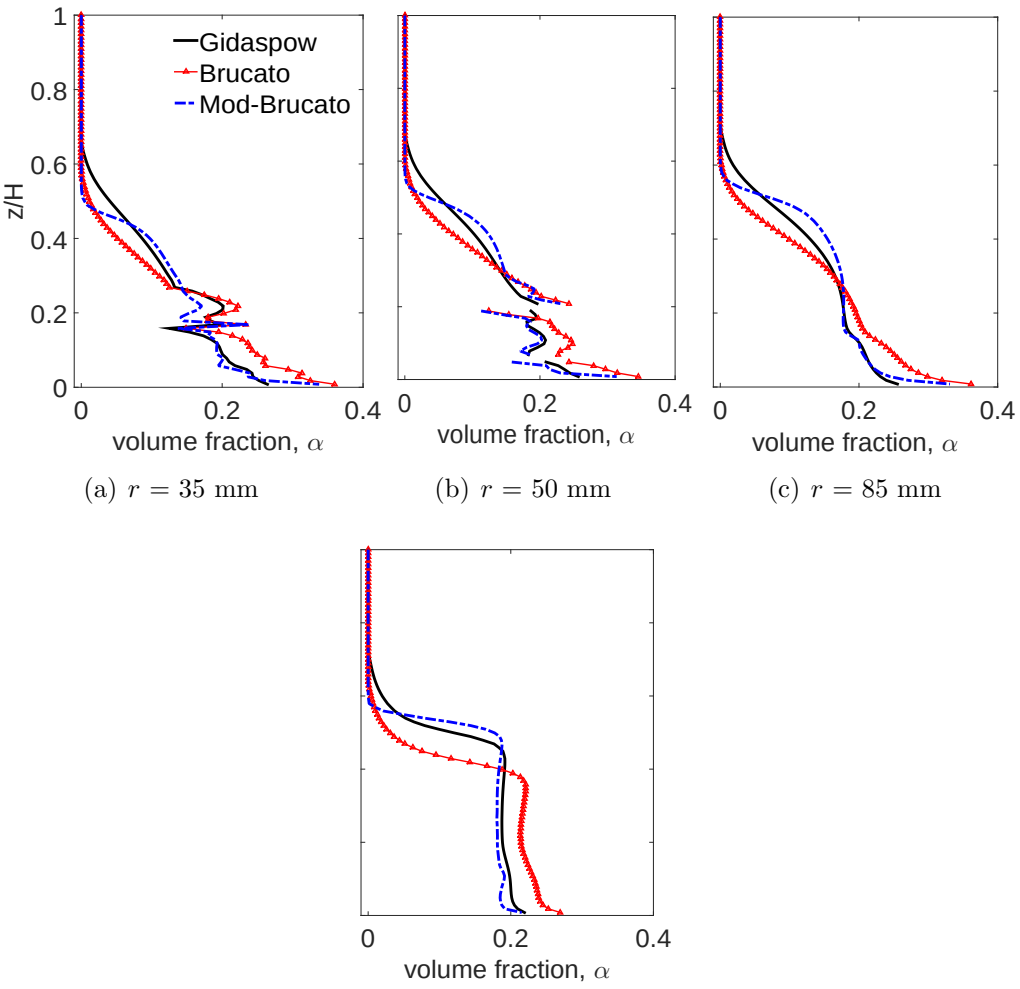

(a) $r = 35$ mm (b) $r = 50$ mm (c) $r = 85$ mm

(d) $r = 125$ mm

Figure 4.8. Axial profiles of solids volume fraction (α) at 1000 RPM at radial locations: (a) $r = 35$ mm, (b) $r = 50$ mm, (c) $r = 85$ mm, (d) $r = 125$ mm.

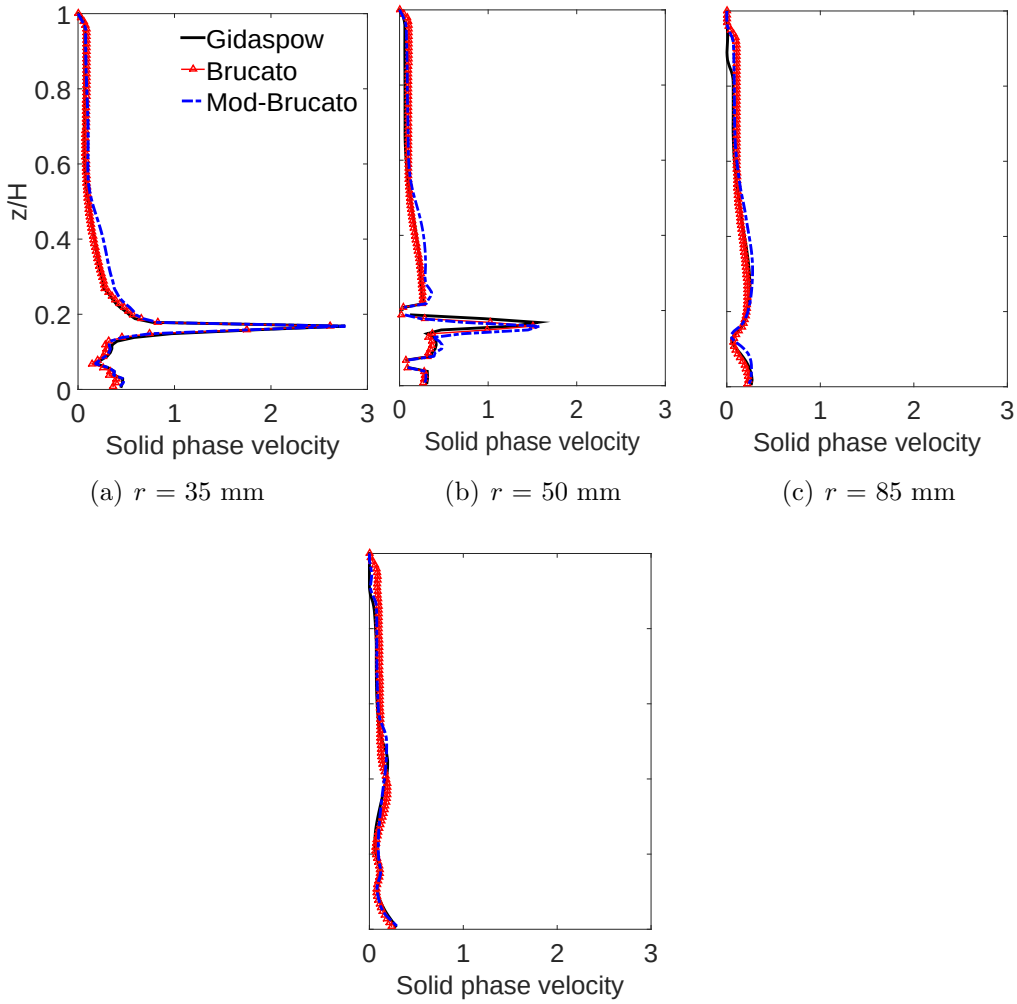

(a) $r = 35$ mm (b) $r = 50$ mm (c) $r = 85$ mm

(d) $r = 125$ mm

Figure 4.9. Axial profiles of solids velocity ($v_{sil-160}$)in m/s at 1000 RPM for 160 micron particles at radial locations (a) $r = 35$ mm, (b) $r = 50$ mm, (c) $r = 85$ mm, (d) $r = 125$ mm.

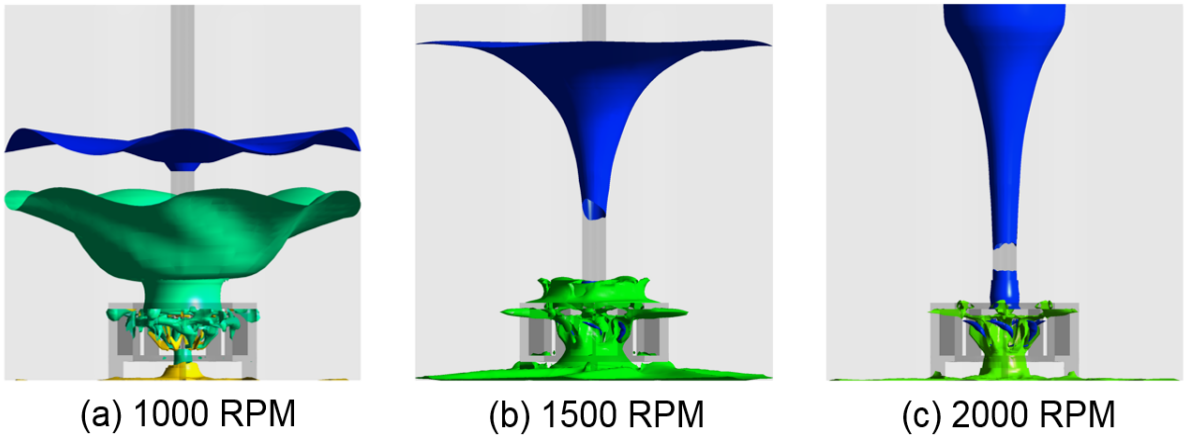

Figure 4.10. Plots showing CFD predicted (Gidaspow model) isosurfaces for three solids volume fraction (α) values - 0.3 (yellow), 0.15 (green), and 0.01(blue) for 160 micron particles at three agitation speeds (see online version for color images).

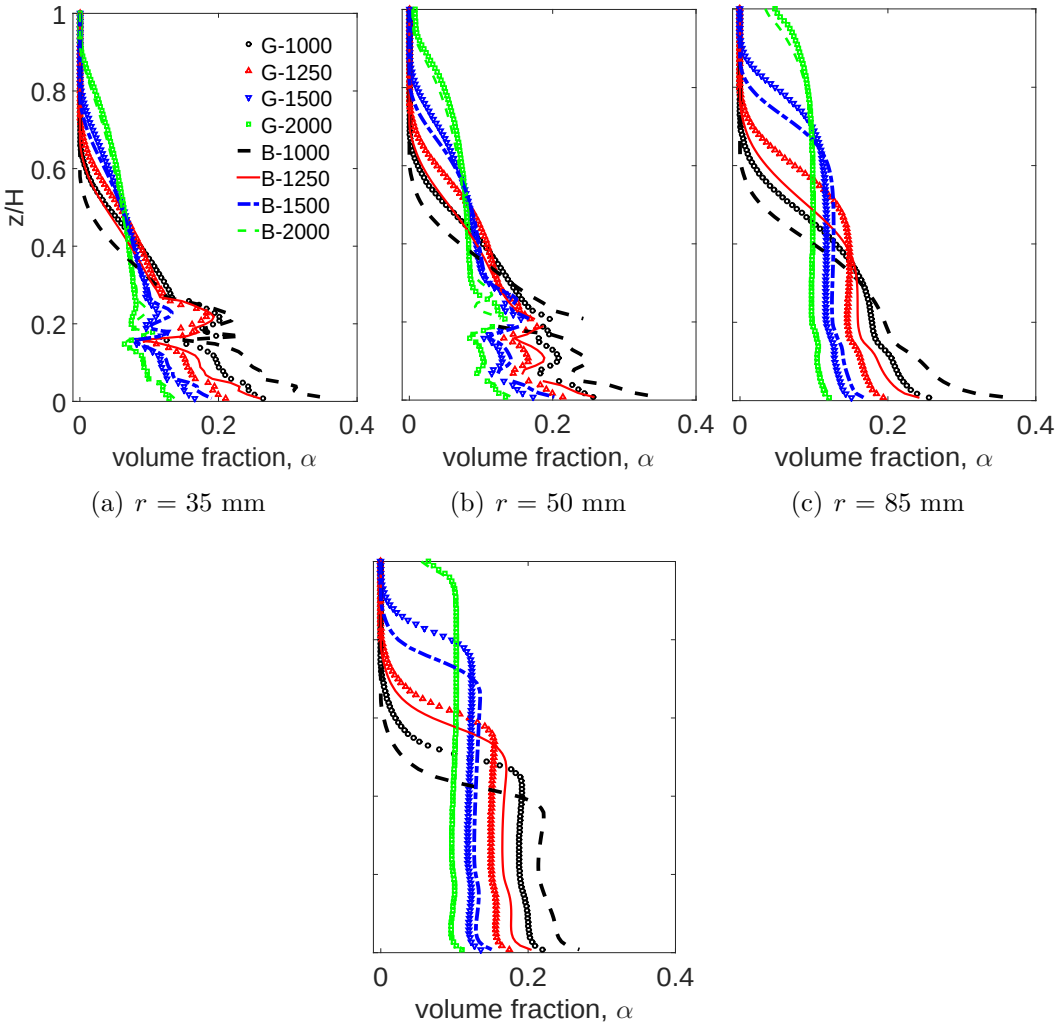

(a) $r = 35$ mm (b) $r = 50$ mm (c) $r = 85$ mm

(d) $r = 125$ mm

Figure 4.11. Axial profiles of solids volume fraction (α) at different speeds for 160 micron particles using Gidaspow (G) and Brucato (B) drag models at r values of (a) $r = 35$ mm, (b) $r = 50$ mm, (c) $r = 85$ mm, (d) $r = 125$ mm.

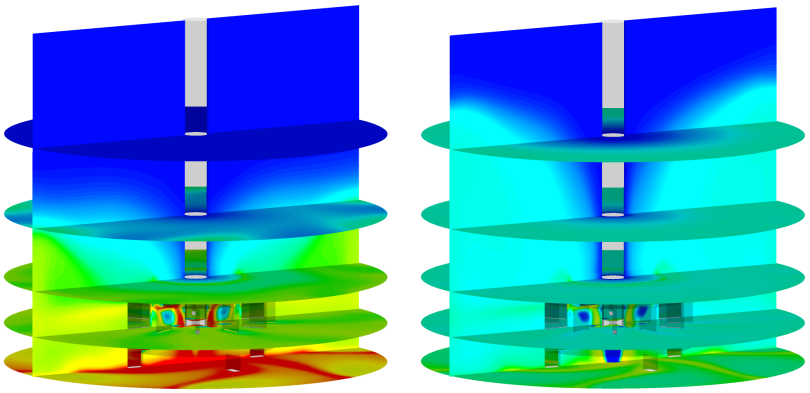

(a) Brucato, 1000 RPM

(b) Brucato, 1500 RPM

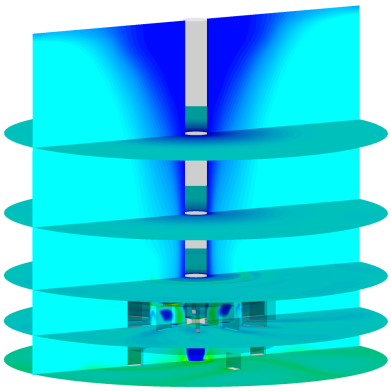

(c) Brucato, 2000 RPM

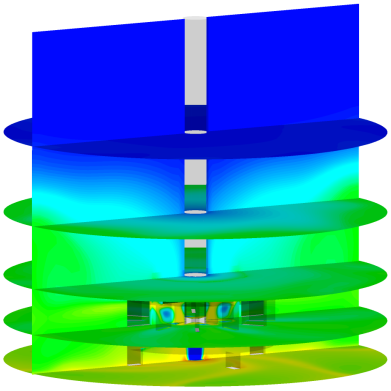

(d) Gidaspow, 1000 RPM

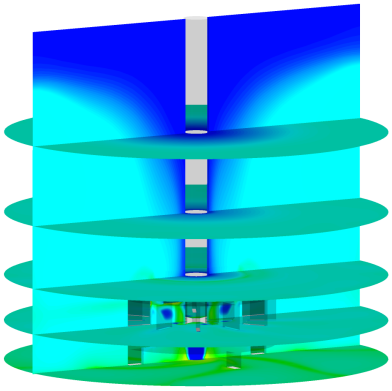

(e) Gidaspow, 1500 RPM

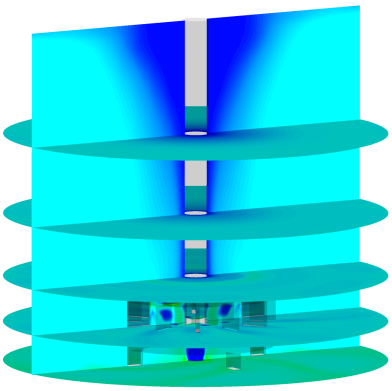

(f) Gidaspow, 2000 RPM

Figure 4.12. Contour plots of solids volume fraction (α) for 160 micron particles on five horizontal planes (P1 to P5) located at vertical height of 20, 85, 150, 220 and 290 mm at four impeller speeds (a) Brucato-1000 RPM, (b) Brucato-1250 RPM, (c) Brucato-1500 RPM, (d) Gidaspow-1000 RPM, (e) Gidaspow-1500 RPM, (f) Gidaspow-2000 RPM.

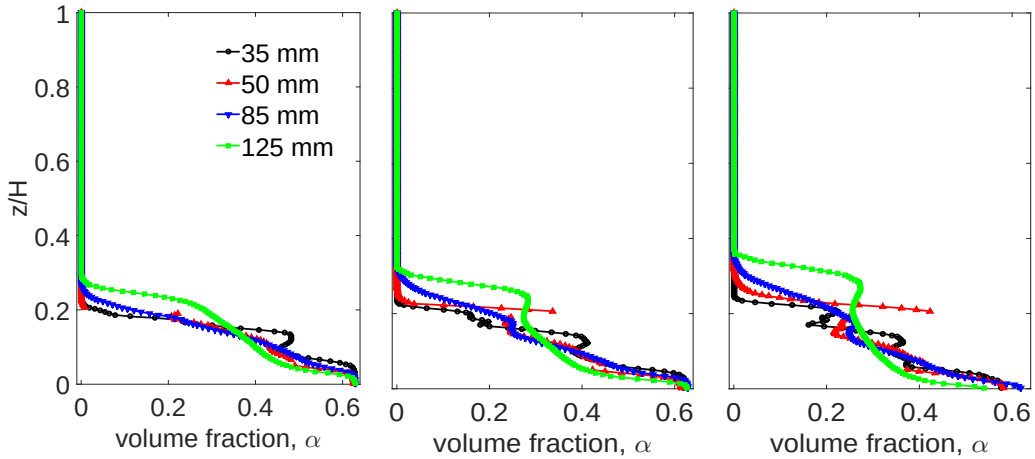

(a) $N = 1000$ RPM (b) $N = 1250$ RPM (c) $N = 1500$ RPM

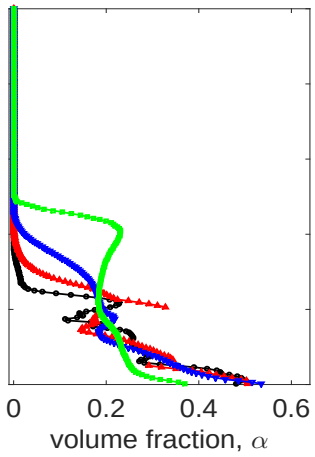

(d) $N = 2000$ RPM

Figure 4.13. Axial profiles of solids volume fraction (α) for 520 micron particles different speeds using Gidaspow model at different impeller speeds: (a) 1000 RPM, (b) 1250 RPM, (c) 1500 RPM, (d) 2000 RPM.

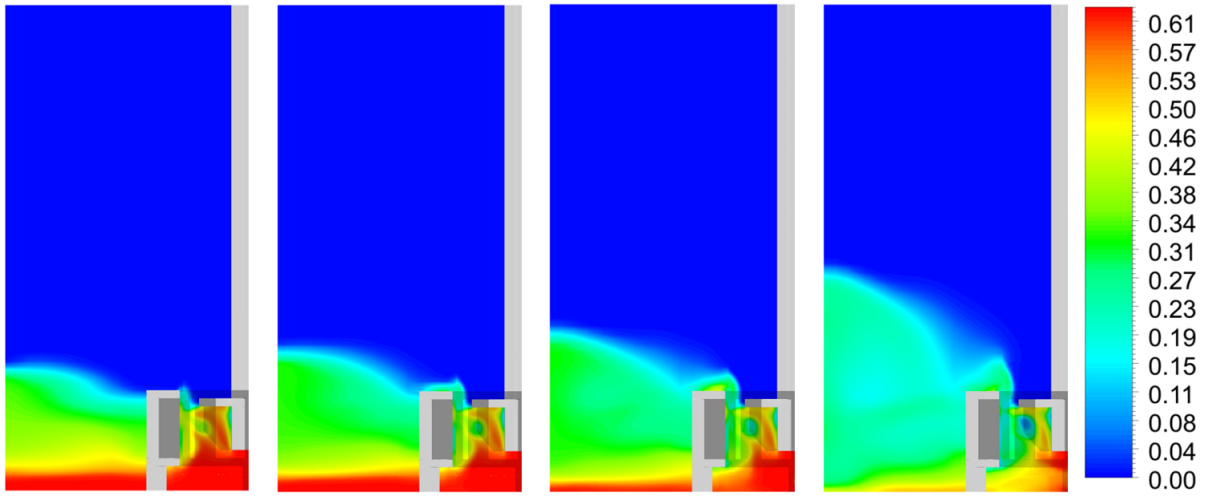

Figure 4.14. Contour plots of 520 micron (α) shown on vertical plane passing midway between the impeller blades at different impeller speeds: (a) $N = 1000$ RPM, (b) $N = 1250$ RPM, (c) $N = 1500$ RPM, (d) $N = 2000$ RPM.

Table 4.1. Variation coefficient σ_v, suspension quality χ, and power number $N_{p\tau}$ for flotation cell flows.

Particle size (μm)	N (RPM)	Drag Model	σ_v	χ	$N_{p\tau}$
160	1000	Gid	1.24	0.887	4.55
160	1000	Bru	1.88	0.829	4.22
160	1000	Mod-Bru	1.60	0.855	4.35
160	1000	Pin	1.88	0.828	4.25
160	1250	Gid	0.93	0.916	5.06
160	1250	Bru	1.20	0.891	4.48
160	1500	Gid	0.66	0.940	4.71
160	1500	Bru	0.81	0.926	4.67
160	1500	Mod-Bru	0.78	0.929	4.90
160	1500	Pin	0.80	0.927	4.71
160	1500	S-N	1.13	0.897	4.67
160	2000	Gid	0.49	0.955	4.72
160	2000	Bru	0.54	0.951	4.71
520	1000	Gid	3.44	0.686	3.11
520	1250	Gid	3.27	0.702	3.35
520	1500	Gid	3.08	0.719	3.50
520	2000	Gid	2.57	0.765	3.67
520	2000	Bru	3.04	0.723	3.41

CHAPTER 5

USING ELECTRICAL RESISTANCE TOMOGRAPHY MEASUREMENTS AND CFD SIMULATIONS TO STUDY SOLID PHASE SUSPENSION AND MIXING

5.1 Abstract

In this work, a thorough investigation into solid phase suspension and mixing are carried out by making nonintrusive measurements in a lab-scale flotation cell using electrical resistance tomography technique (ERT). Computational fluid dynamics (CFD) simulations using Eulerian-Eulerian (EE) two-fluid model (TFM) and coupled CFD discrete element method (CFD-DEM) Eulerian-Lagrangian (EL) approaches are used to study the dispersed phase behavior, mixing level in detail, and to identify regions of particle segregation, which is not possible by experiments due to limitations in resolution of the experimental technique. The Eulerian-Eulerian approach is validated by comparing the numerical predictions of mean axial solids holdup against the ERT measurements. A thorough grid independence study is performed which revealed that a grid with approximately 500,000 cells is sufficient to obtain a grid independent solution. Using both the CFD and ERT data, homogeneity levels inside the tank are calculated at different geometric and operating conditions such as impeller speed, impeller size, solids loading, and impeller off-bottom clearance. The Eulerian-Eulerian CFD simulations revealed the presence of solids accumulation regions near the impeller in the trailing vortices and also on the tank floor with six well defined bands (fillets) at lower impeller rotation speeds. When larger and denser particles are used in the dilute CFD-DEM simulations, similar observations are made. However, the formation of a band is also noticed near the top of the cell close to the tip of the particle cloud. The difference in the ERT measurements and CFD predictions

is attributed to the difference in the particle properties used in the respective studies.

5.2 Introduction

An extensive review of the literature dealing with the slurry flows in stirred vessels is already given in the last chapter. In the interest of keeping this section brief, a short overview of some of the recent works dealing with ERT and CFD-Discrete Element Method (CFD-DEM) approach is presented in this section.

Froth flotation is one of the most commonly used mineral separation technologies applied for concentration of various ore types. The flow in a flotation cell is multiphase, involving liquid, solids, and gas phases, and highly multiscale in nature; hydrodynamics of the flow is highly complex and spans multiple length and time scales. Furthermore, the flow is highly turbulent with particularly high values of turbulent kinetic energy, k, and dissipation rate, ϵ, in the impeller jet region. Solid particles and dispersed air bubbles are introduced into the tank in substantial amounts (>10% v/v for solids and >10% v/v for air), which alters the single phase hydrodynamics critically through complex interphase interactions. Both bubbles and particles are found to modulate the turbulence in dense multiphase flows with the preferential concentration of particles occurring based on their size and density [52]. Therefore, complex interactions of particles and bubbles in different regions of the tank in addition to complex surface chemistry make the flotation process very difficult to model and study.

Before an attempt to study the complex interactions of all three phases in the system, it is important to understand the dynamics of the individual discrete phases under different conditions. Suspension of solid particles from the particle bed and their mixing throughout the tank is still not completely understood in the context of flotation [70, 71]. To achieve high material recoveries, it is of great importance to suspend all the particles in the cell in order to increase the probability of particle-bubble collision events. Among the factors affecting the particle suspension processes in mechanical flotation cells, impeller speed, design, size, and off-bottom clearance, as well as fluid viscosity, particle density, and size, and particle loading are the most important.

Application of direct experimental monitoring and measurements of opaque multiphase systems using traditional flow visualization techniques, like particle image velocimetry (PIV) and laser Doppler velocimetry (LDV), is nearly impossible especially for dense systems. Conductivity probes are frequently used to measure solids concentration at discrete spatial locations within the tank [15]. However, such probes are intrusive by nature and tend to alter the flow when not aligned with the flow [15]. Electrical resistance tomography is a nonintrusive measurement technique that is widely used to study multiphase flows in stirred vessels [90, 95] By means of ERT and Maxwell's equation, conductivity measurement domain can be extended to the entire cell and a 3D map of the dispersed phase concentration can be obtained in real time. Recently, Hosseini et al. [90] used ERT to investigate solid-liquid flows in lab scale stirred tank using axial flow impellers. The ERT approach has been widely used to study phenomena such as mixing, gas dispersion, solids suspension, food processing, and fluidization among many others [95]. The application of ERT to study multiphase flows in flotation cells has been rather limited especially for slurry flows. This work is one of the first attempts to use ERT to study solid phase mixing in flotation cells.

With the increase in computational resources available for research in the last two decades, CFD has become an important tool for both fundamental and applied research. Recently, the coupled capability of CFD-DEM was realized and has been applied to fluidized beds [96], centrifuges [97], and stirred tanks [98] among other applications. The CFD-DEM approach is a detailed Eulerian-Lagrangian approach with a four-way coupling of fluid and solid phases. The fluid flow field is solved in the Eulerian frame of reference while detailed interactions of solid particles are modeled by treating particles as hard spheres and through tracking their collisions and displacements in time. The exchange of momentum between fluid elements is accounted for by including relevant momentum exchange forces like drag, lift, virtual mass, among others. Even though CFD-DEM is capable of providing detailed transport and mixing of the dispersed phase, there is still a limit on the scale of the problem that can be simulated in a practical time frame as the number of collisions becomes prohibitive for moderate to dense flows (over 100 million particles).

In order to gain a better understanding of transport and mixing phenomena of solid particles of different sizes, Eulerian-Eulerian CFD and CFD-DEM numerical simulations, and ERT measurements in lab-scale flotation cell are performed over a range of operating conditions.

5.3 Experimental

5.3.1 Electrical Resistance Tomography

The ERT system operates by injection of a known amount of current through one electrode pair and measurement of the voltage across all other electrode pairs, excluding the electrodes used for current injection. The process is repeated such that 104 measurements are taken along the plane of interest, with each plane containing 16 rectangular electrodes made of stainless steel. The ERT measurement procedure is shown in Figure 5.1 where the current is injected from electrode pair 1-2 in Figure 5.1(a) and 3–4 in Figure 5.1(b). By comparing the measured conductivity against a reference measurement and using Maxwell's equation, dispersed phase concentration is calculated. In the current work, ERT measurements are taken along six planes as shown in Figure 5.2. The bottom plane is at 60 mm from the tank floor and each plane above it is separated by a fixed distance of 40 mm. The p2+ ERT setup and the associated software used in this work are supplied by Industrial Tomography Systems (ITS) based in Manchester, UK.

Using the conductivity values at different planes, axial and radial solids concentration profiles along with the level of homogeneity, defined as the level of dispersed phase mixing in the axial direction, can be calculated. The solids concentration at each axial level is obtained by averaging the discrete values in the concentration tomograms, thus providing a single concentration value at each axial plane. It should be noted that ERT measures a 3D region (ellipsoid) of the flow between the two electrode planes and therefore, the concentration value should be thought of as an average concentration in the volume contained between the electrode planes.

The image reconstruction process involves using the boundary voltage measurements to create a conductivity map using a linear back projection (LBP) algorithm. The linear back projection algorithm is a noniterative solver and offers fast and reasonably accurate image reconstructions when the difference between the con-

ductivities between the phases is sufficiently high [90]. The reconstruction process involves solving two problems, namely, forward and inverse problems as shown in Figure 5.3. The forward problem consists of solving for electrical potential and potential difference by knowing the distribution of conductivity (σ_c) and injected current value (I). The forward problem involves solving a finite element method (FEM) problem on 316 element grid (each plane) to obtain the sensitivity matrix, which is also called a Jacobian matrix. The inverse problem involves calculating the conductivity values from the voltage measurements. Once the conductivity map is known, Maxwell's equation can be used to calculate the concentration of dispersed phase (non-conducting) in each element as shown in Figure 5.3. Maxwell's equation is given by:

$$X_V = \frac{\sigma_l - \sigma_{mc}}{\sigma_l + 0.5(\sigma_{mc})} \tag{5.1}$$

where, X_V is the solids concentration, σ_l is the conductivity of liquid phase, and σ_{mc} is the reconstructed measured conductivity.

5.3.2 Experimental Details

For the purpose of ERT measurements, a flotation cell of 300 mm (12 inches) inner diameter (D) described in the previous chapter and shown in Figure 5.4 is used. The impeller and stator parts are made of acrylonitrile butadiene styrene (ABS), which is a thermoplastic polymer. The parts are created in-house using a LeapFrog Creatr 3D printer. Due to the thermal warping issues, minor differences in the dimensions between CAD model and the printed component are expected. Also, the complex shape of the stator required printing some of the parts separately and gluing them together to ensure structural rigidity. To ensure mechanical stability of the overall structure, thickness of some of the parts needed to be increased marginally resulting in a slight deviation from dimensions used in numerical simulations. It is expected that such small deviations do not influence the mean behavior of the flow significantly. Snapshots of the impeller and stator used in the ERT measurements are shown in Figure 5.5.

Tap water at room temperature and pressure is used in all the experiments. The experimental procedure involves filling up the cell with tap water up to the required

level, which in this case is always 300 mm. The distance from the shaft to cell edge is measured using a ruler to ensure the cell is centered. Furthermore, the position of the impeller is visually verified to ensure it is equidistant from the surrounding stator. A small amount of salt (typically 2.5 g) is added to increase the contrast in conductivity between continuous phase (water) and dispersed phase (solid particles) as suggested in the previous studies [99]. Next, the impeller is run at low speed to force any trapped air out of the cell that could affect the reference conductivity measurement. Also, running the impeller is essential to ensure all the added salt is dissolved completely. Once all the trapped air bubbles are removed, the impeller is turned off and the solution is allowed to come to rest. Using a hand held probe, temperature and conductivity of the solution are measured and recorded.

The next step involves calibrating the current and voltage gain map for the system. The current calibration is performed first by carefully injecting a known value of current that is recommended for a vessel of given size. The injected current value is then compared against the value returned by the data acquisition system based on the media inside the cell. The objective of the current calibration step is to ensure convergence of injected and system returned current values. Through consultation with the technical support at ITS and with experience gained from initial experiments, a current value of 15 mA is found to be ideal for the cell used in this work. Next, the voltage gain map is calibrated, which helps the DAS correctly scale the voltages based on the relative distance from electrode pair injecting the current to all the other electrode pairs that measure voltage. Once the calibration step is completed, a reference measurement needs to be taken. For the reference measurement, the current value obtained from calibration is injected and measurements from up to ten frames are averaged to account for any spatial and temporal inhomogeneities in the cell.

Based on the requirements of the experiments, dried solid particles of known mass are carefully introduced from the top. The excess water is removed to make the overall level equal to 300 mm. The temperature and conductivity measurements are taken again after the solid particles are introduced. The impeller is turned on and required speeds are set using a variable frequency drive (VFD) that controls the rotational speed of motor that drives the shaft. At each speed data from 120 to 150 frames

are averaged to obtain the mean conductivity and concentration distribution at every plane. Care is taken to ensure the flow adjusts to new speed completely before the data are considered to calculate concentration.

Technical quality solid glass spheres, provided by Potters Industries, of size from 106–212 μm are used in all the experiments. As mentioned earlier, the water level, H, is maintained at 300 mm in all the experiments. A flotation impeller with a standard blade design (SI) and diameter (d) equal to $D/5$ is used. Three different solids loading corresponding to volume fraction (%) of 5, 7, and 9.2 are used in the ERT experiments. Also, the effect of changing off-bottom clearance from 25 to 50 mm is studied at a constant volume loading of 9.2%. Fig 5.4 shows the schematic of the flotation cell used in this study with relevant symbols. All the other details about the setup used are explained in the previous chapter.

5.4 Numerical Approach

For the Eulerian-Eulerian simulations, steady state approximation is used and steady state Navier-Stokes equations are solved for both phases. Only drag and turbulent dispersion forces are shown to be dominant in the flows of this kind [86]. Therefore, interphase momentum exchange due to only drag and turbulent dispersion forces is considered. The drag model proposed by Gidaspow is used since it is reported to provide accurate predictions for dense slurry flows [80]. The turbulent dispersion model proposed by Simonin is used [86, 100]. The impeller rotation is handled by using the MRF technique, which is a steady state approximation widely used for stirred tanks and flotation cells [63, 101]. The solid phase is considered to be composed of monosized particles of mean diameter equal to 160 microns. The turbulence in the flow is modeled using mixture realizable $k-\epsilon$ model, which has been shown to provide accurate predictions for dense slurries [63].

For the CFD-DEM simulations, the flotation cell described earlier is used. The off-bottom clearance is set at 25 mm ($D/12$) and Reynolds number (Re) of the flow is equal to 120,000 corresponding to a tip speed of 6.3 m/s. In the CFD-DEM approach, the motion of continuous phase is modeled using a Eulerian approach and the turbulence in the flow is modeled using RANS based realizable $k-\epsilon$ model. Two

size fractions of silica particles are considered, namely 0.5 mm (80,000 particles) and 1 mm (40,000 particles). The motion of dispersed phase is modeled using DEM approach, which treats the particles as hard spheres and treats the interparticle collisions as momentum conserving events [97].

Dilute solid-liquid two-phase flow, corresponding to solids fraction of approximately 0.25% w/w, is simulated using the CFD-DEM approach for a total flow time of about 3 seconds. The coupled CFD-DEM simulation is performed by coupling the ANSYS Fluent 14.5 and EDEM 2.5 commercial solvers. A total of 120,000 spherical silica particles are used, of which 80,000 particles are of 0.5 mm and 40,000 particles are of 1 mm diameter. The mesh used for CFD simulation contains approximately 500,000 cells, which is fine enough to capture vortex structures in the impeller stream as recently reported by Guha et al. [102]. The mesh used for DEM consists of 1.082 million cells. As a function of number and size of particles, the calculated time step required for the accurate realization of the DEM part is found to be extremely small ($\sim 10^{-06}$ s). The lower time step required for DEM and a large number of particle collision events makes the simulation very resource intensive and slow. The simulations are run on 16 core Intel Xeon CPU workstation, and the total time required to simulate 3.07 s is approximately four weeks. Only qualitative results from CFD-DEM simulation are presented here.

5.5 Results and Discussion

Measuring and predicting the average distribution of solid particles and the level of mixing both in the radial and axial directions are the most important goals of this study. Therefore, the mean concentration of solid phase along axial and radial directions are presented and discussed. Using these mean concentration data, homogeneity level in the tank is quantified by using homogeneity calculations. The CFD-DEM simulation predictions are used to understand the qualitative behavior of the coarse sized particles and their segregation tendencies.

5.5.1 Grid Independence Study

To establish the minimum number of cells required to achieve an accurate grid independent CFD solution, predictions from three grids are compared. Both local

velocity and solids volume fractions along with global power draw behavior are compared at an impeller speed of 1000 RPM for 160-micron silica particles. The details of the grids used in the simulations are tabulated in Table. 5.1. Also, the torque value generated on the impeller surface and the maximum height of the particle cloud predicted by different grids are shown in Table. 5.1. To calculate the maximum height of the particle cloud, solid phase isosurface corresponding to a holdup value of 0.01 is generated and the maximum height of this curved surface is selected.

The mean axial profiles of silica velocity, silica volume fraction, and water velocity are shown in Figure 5.6. The location chosen is outside the stator at a radial distance of 75 mm from the center axis. From the axial profiles, it is clear that increasing the number of grid cells from approximately 250,000 (coarse) to 500,000 (medium) results in a significant change in both the velocity and volume fraction (hold up) profiles. The coarse grid under-predicts the mean velocity of both solid and liquid phases near the bottom half of the tank compared to other grids, which are most prominent near the peak value. As a result of lower momentum predicted by the coarse grid, the solids volume fraction is over-predicted in comparison. On the other hand, the predictions between medium and fine grid match closely except near the impeller level, where the peak velocity value is slightly under-predicted by the coarse grid. Similarly, the predictions of the volume fraction by medium and fine grid match closely. Moreover, the peak particle cloud height predicted by medium and fine grid also match closely as evident from Table. 5.1. From the analysis of results and the preceding discussion, it can be concluded that the medium grid is able to make accurate predictions with little discrepancy when compared to the predictions from fine grid. Therefore, the predictions obtained by using medium grid can be safely considered to be grid independent for the mean flow quantities of interest.

5.5.2 Eulerian-Eulerian CFD Predictions vs. ERT Measurements

The Eulerian-Eulerian model was validated earlier for a stirred tank in Chapter 4. Only qualitative validation was presented for flotation cells in the previous chapter by comparing the cloud height measurements against the predicted cloud height along the cell wall. In this work, a detailed comparison of the mean solid holdup (normalized)

obtained from ERT measurements and CFD simulations is presented at two impeller rotation speeds of 1000 and 1250 RPM. Figure 5.7 shows the comparison of mean ERT measurements against the CFD predictions. Since the electric potential field lines develop in all three dimensions during the ERT measurement, it must be noted that the mean values reported at different axial locations, in fact, represent the mean concentration of a volume enclosed between the electrodes.

As evident from the plots in Figure 5.7, the CFD predicted concentration values are high compared to ERT measurements in the lower three planes at 1000 RPM. However, the trend is correctly predicted by CFD at both the impeller speeds. We believe that the predominant reason for this discrepancy is the difference in the particle sizes used in experiments and simulations. In experiments, particles belonging to a size range of 106–212 microns are considered and the cumulative size distribution is shown in the previous chapter, whereas, in the case of CFD simulations, monosized particles of mean diameter equal to 160 microns are used. Since the drag coefficient depends nonlinearly on the particle size among other variables, the presence of larger particles results in high drag forces causing the larger particles to settle faster. Since the lowest ERT measurement plane is located 60 mm from the cell bottom, a high solids concentration at this plane confirms this behavior at 1000 RPM. However, at 1250 RPM, the momentum supplied by the mean flow is sufficiently high to suspend heavier particles. Also, note the higher concentration measured by ERT compared to CFD predictions at the top most plane (260 mm), which is clear at 1250 RPM. This shows that the smaller particles are easily lifted and stay suspended at high impeller speeds. Due to the 3D nature of ERT measurements, solids concentration measured by ERT is higher compared to CFD predictions. Moreover, at 1250 RPM, a surface vortex starts developing near the shaft that could also influence the dispersed phase concentration for the top one or two planes. The top plane is only 40 mm from free surface and therefore the concentration values there are easily influenced by the formation of free vortex. A closer examination of the presented results shows that the Eulerian-Eulerian CFD model is able to satisfactorily predict the suspension trend in flotation cells and the differences in the results can be mostly attributed to the differences in particle sizes used. However, due to differences in the particles used in

the current study, direct comparison of the results is limited. The comparison of the solids concentration at different speeds is shown in Figure 5.8 (a), which shows that even at a speed of 1250 RPM the majority of the solids are present in the lower half of the cell.

5.5.3 Mixing Evaluation

Achieving good mixing of solid particles in the lower part of the flotation cell ensures higher collision rates between the particles and bubbles, leading to increased flotation recovery. A simple method of calculating mixing level in flotation cell using ERT data is through calculation of homogeneity index, which is given by:

$$homogeneity = 1 - \sqrt{\frac{\sum_1^n (X_V - \overline{X}_V)^2}{n}} \tag{5.2}$$

where, n is the number of ERT planes, which is 6 in this case, X_V is the averaged solids concentration along a plane, and $\overline{X}_V$ is the vessel averaged concentration. The value of X_V is obtained by averaging the 316 concentration values obtained from the LBP solution and the magnitude of of X_V represents a mean holdup value at a particular axial height. Using the ERT data at different impeller speeds, homogeneity is calculated and reported in Figure 5.8 (b). The homogeneity value is low at lower speeds as expected and increases almost linearly after 875 RPM up to 1250 RPM. Also shown are the homogeneity values found using CFD predicted concentrations. In general, higher homogeneity values will be obtained depending on the axial distribution of solids concentration. If the axial concentration profile is straighter, then a homogeneity value close to 1 is obtained. The slight drop in the homogeneity between 500 to 875 RPM can be better explained by observing the axial profiles of solids concentration shown in Figure 5.8 (a). By increasing the impeller speed from 500 to 750 RPM, a small fraction of solid particles is suspended from the particle bed which results in increased concentration at two lower planes. However, the momentum is still not sufficient to fully suspend the particles in the axial direction that results in a lower homogeneity value as a result of unchanged flow conditions near the middle and top region of the cell at 750 RPM. The nature of homogeneity vs. impeller speed plot suggests that there is a critical impeller speed (or a narrow range) at which the flow

momentum collectively overcomes the drag force of settling particles and increases mixing and suspension of particles.

ERT measurements are also performed at different volume loading of silica particles. Figure 5.9 (a) shows the homogeneity at three different particle loading conditions against impeller speed at a fixed off-bottom clearance value of 25 mm. It should be pointed out that the thickness of the stator parts and impeller disc is different for this set of results compared to the previously presented results. However, similar behavior is observed at a loading of 9.2%, though the dip in homogeneity value is more pronounced when using thicker parts compared to results discussed earlier. Following the Figure 5.9 (a) it can be seen that all three particle loadings exhibit similar behavior, wherein the homogeneity level drops narrowly before increasing to higher values. Also, it is clear from the plot that better mixing and suspension can be achieved when using lower particle loading compared to higher loading. The effect of changing the off-bottom clearance on homogeneity for particle volume loading of 9.2% is shown in Figure 5.9 (b). It is clear from the plot that a higher clearance of 50 mm is better suited for suspending and mixing solids at intermediate and higher impeller speeds. The reason for better mixing at higher speeds is due to the ability of the radial jet to use its momentum more efficiently in suspending the particles. At lower clearance, the jet directly interacts with the particle bed. Thus, a significant amount of momentum is lost as a result of interparticle collisions. At higher clearance, the radial jet strikes the cell wall before interacting with the particles close to the wall, which is more efficient at suspending particles from the bed.

5.5.4 CFD-DEM Predictions

Figure 5.10 shows the snapshot of particle positions at different times obtained through CFD-DEM. A total of 120,000 particles are released below the impeller at time step equal to zero ($t = 0\ s$) and coupled to fully developed single phase flow with Reynolds number (Re) equal to 120,000, which corresponds to a tip speed of 6.3 m/s. Based on the careful observation of particle trajectories it can be seen that the introduced particle cluster is separated into six identical streams or bands. As the particles strike the wall, some are carried upwards by the upper recirculation loop of

the flow, while most particles begin to settle on the tank floor carried by the lower recirculation loop, which is clearly evident at $t = 0.37$ s. The effect of particle size on mixing phenomena can be better understood by comparing the maximum and average particle velocities in addition to visual particle position observation. The maximum obtained velocities for 1 mm and 0.5 mm particles are 5.94 m/s and 9.1 m/s, respectively. In addition, the average velocities for 1 mm and 0.5 mm particles are found to be 0.405 m/s and 0.54 m/s, respectively. As expected, smaller particles have higher peak and average velocities, which results in segregation of the particles at certain regions in the tank. This becomes clearly noticeable at the top of the tank where the particle cloud heights are different for different particle sizes. The average particle cloud heights for 1 mm and 0.5 mm are found to be 0.26 m and 0.278 m, respectively.

The particle trajectories reveal detailed mixing behavior of dispersed phase. From Figure 5.10 it can be observed that the particles stay segregated during their motion towards the tank top by the upper flow loop ($t = 1.27$ s) and are eventually mixed in the circumferential direction at the top ($t < 2.4$ s). As the particles initiate downward motion toward the impeller, the mixing between two size fractions is enhanced. The particles can be seen joining the upper recirculation loop again at $t = 3.07$ s, at which point the system is reasonably mixed, though thin concentrated particle rings are still visible near the top. The results also indicate that the flow retains a strong circumferential velocity component in the top half region of the tank which can be visually verified from Figure 5.10 ($t = 0.67$ s). In this case, the particles experience circumferential motion as the mean flow is not radially directed by the presence of stator. At 3.07 s of simulation, the total number of particles on the tank floor is found to be 24,668, of which 4907 are 1 mm and remaining are 0.5 mm.

5.6 Conclusions

Electrical resistance tomography (ERT), a nonintrusive multiphase flow imaging technique, is used to measure the distribution of solids within the flotation cell for the first time. The measurements are compared against the CFD model predictions obtained using the Eulerian-Eulerian modeling approach. A grid independence study

is performed to ascertain the minimum number of cells required to achieve grid independent solution. Using a grid with approximately 500,000 cells, steady state simulation for monosized silica particles at a volume loading of 9.2% is performed. The CFD predictions are able to correctly predict the trends of solids holdup in axial direction correctly, but over-predict the holdup values in the lower planes. The difference is attributed to the differences in the particle sizes used in the experimental and CFD studies. Using the ERT measurements, homogeneity values are calculated and used to compare axial mixing levels at different operating conditions. In general, homogeneity values are low at speeds under 900 RPM and increase considerably beyond that speed. The off-bottom clearance is shown to affect the homogeneity significantly with higher clearance clearly suitable when better axial homogeneity is sought.

Dilute solid-liquid flow has been simulated using the CFD-DEM approach by introducing silica particles of two size fractions into a fully developed flow field. Particle trajectories are obtained and the degree of mixing of dispersed phase is visualized and characterised. Particles initially segregate, particularly close to the tank top, but eventually, mix as they travel down towards the impeller and are suspended back into the bulk. The average particle cloud height for both size fractions is evaluated.

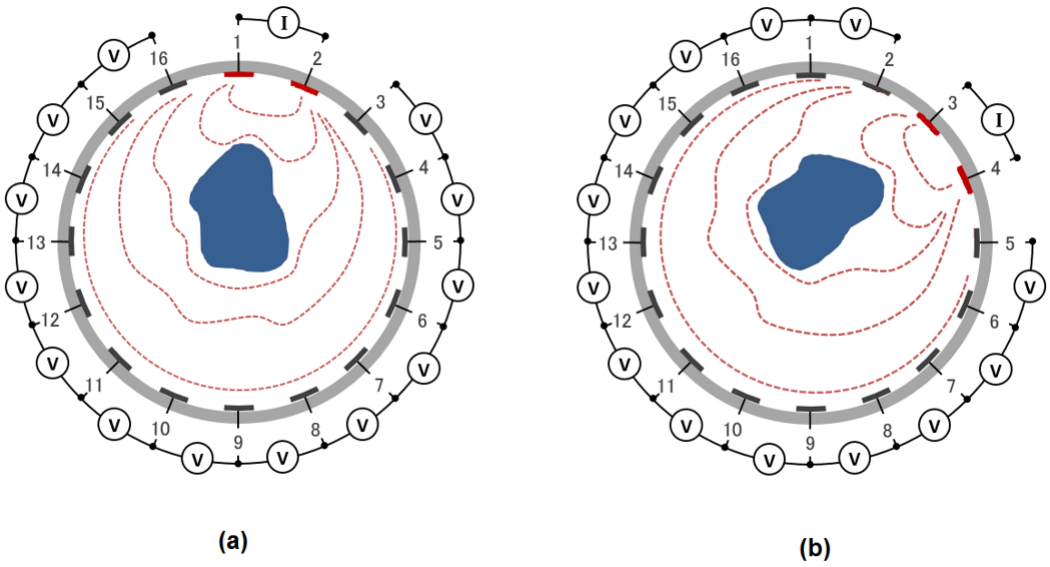

Figure 5.1. ERT measurement approach showing current injection and voltage measurement along a plane for successive current injection pairs (a) 1-2 (left) and (b) 3-4 (right).

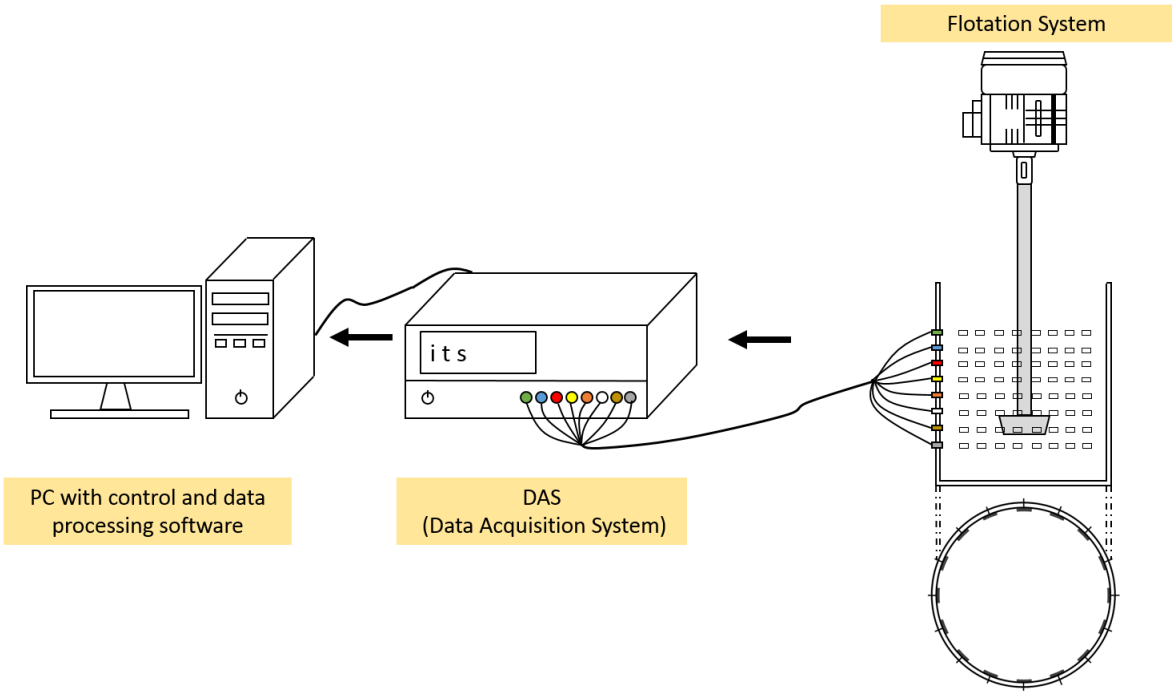

Figure 5.2. ERT setup showing all three basic components.

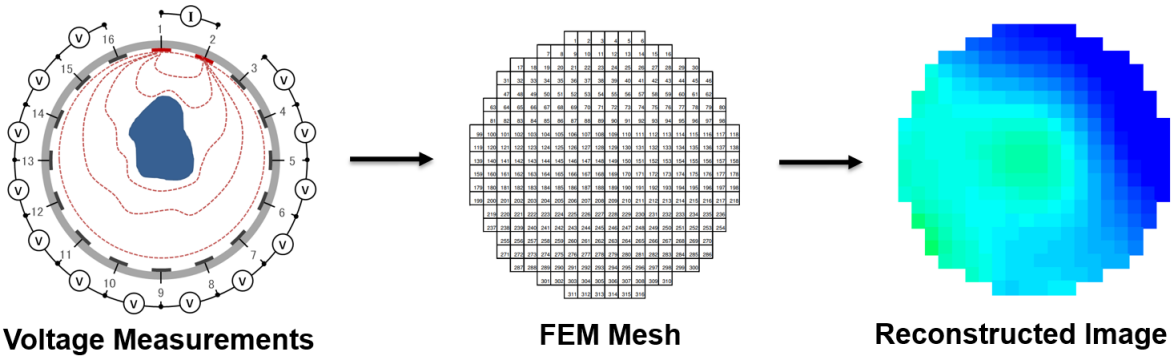

(a) ERT Reconstruction process showing FEM mesh and reconstructed conductivity map

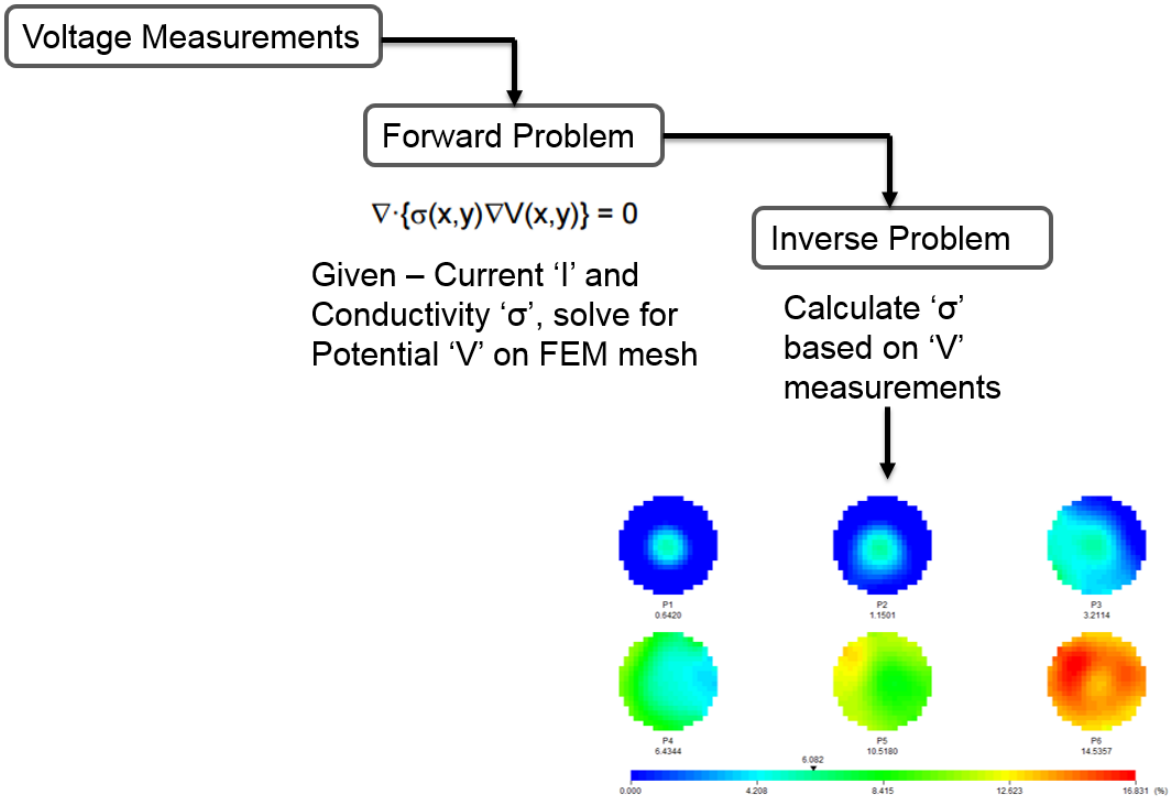

(b) Steps involved in ERT reconstruction of conductivity map

Figure 5.3. Figure showing the steps involved in using linear back projection (LBP) algorithm for reconstruction of conductivity and concentration maps.

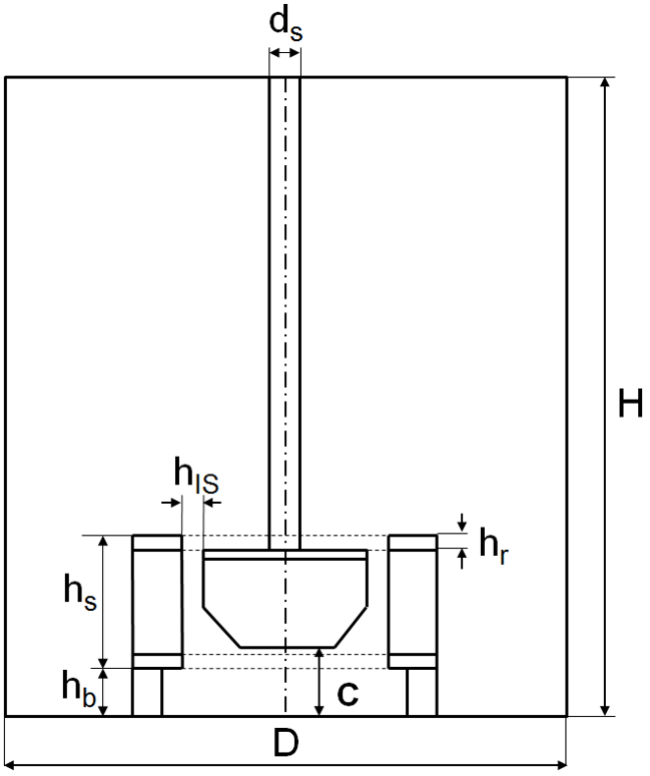

Figure 5.4. Schematic of the flotation cell used in the ERT measurements and numerical simulations.

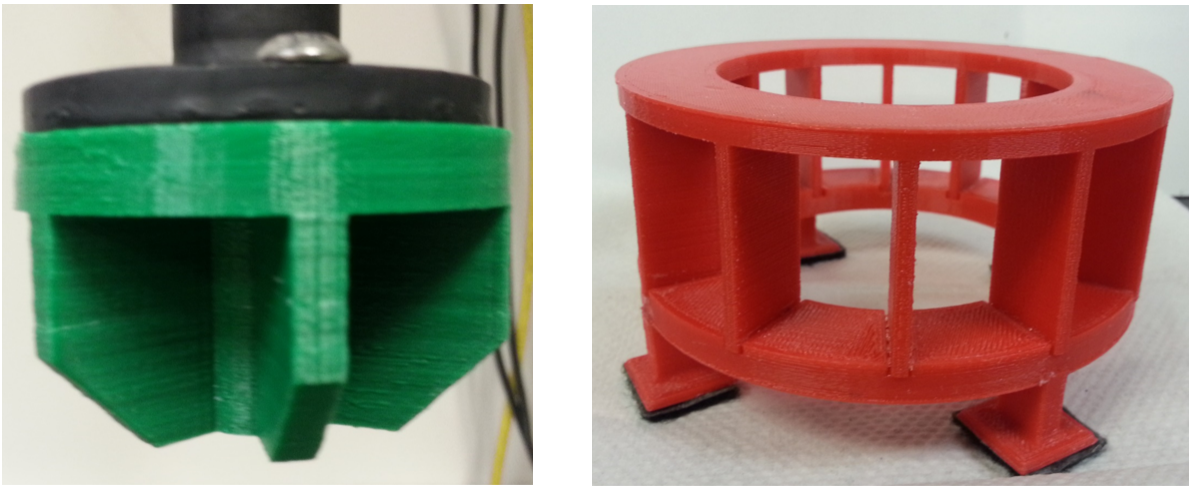

(a) 6 blade impeller

(b) 12 blade stator

Figure 5.5. Snapshot of the 3D printed impeller and stator used in the ERT measurements.

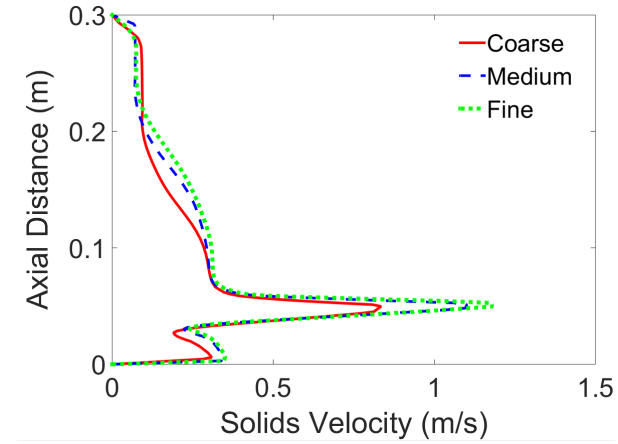

(a) Silica velocity (m/s)

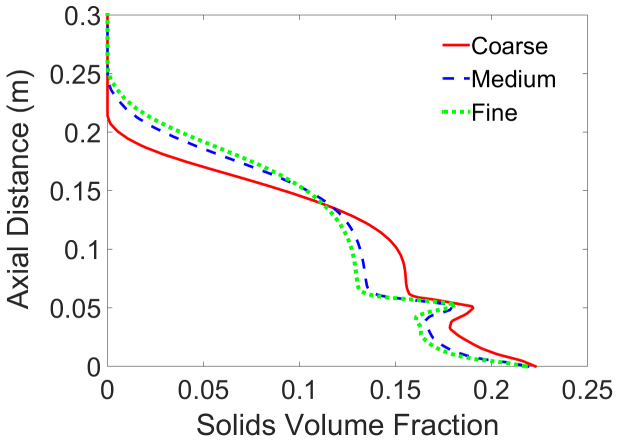

(b) Silica volume fraction

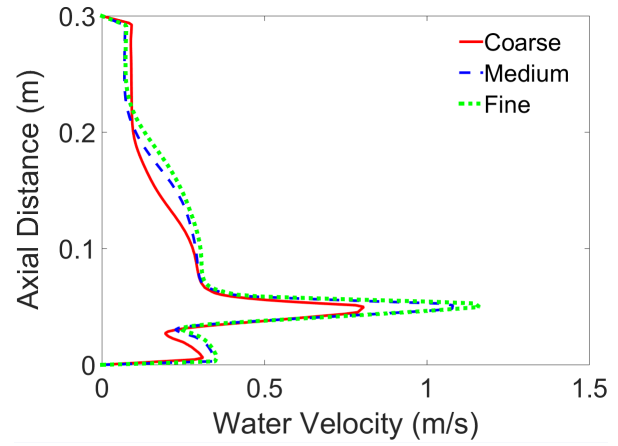

(c) Water velocity (m/s)

Figure 5.6. Plots showing the comparison of silica velocity and holdup, and water velocity for three different grids: coarse grid (solid line), medium grid (dashed line), and fine grid (dotted line). The radial location along which plots are generated is chosen at a distance of 75 mm from the center axis.

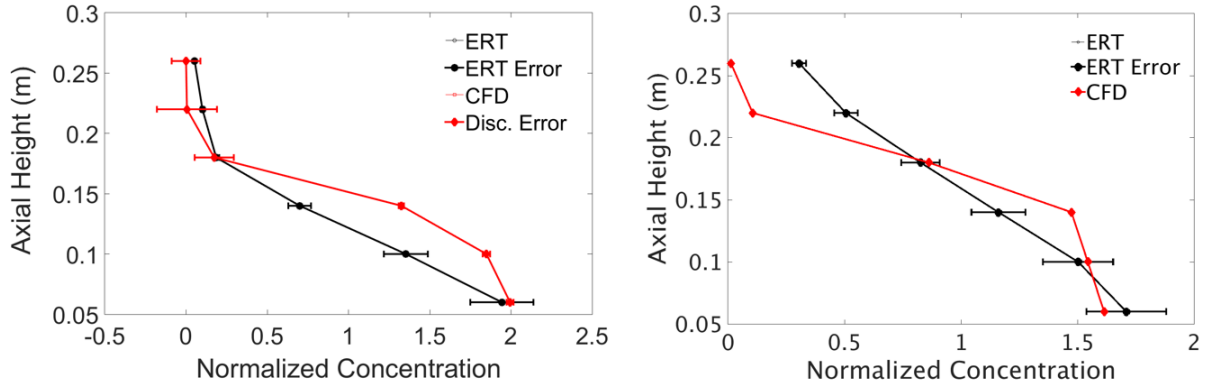

Figure 5.7. Comparison of plane and volume averaged CFD volume fractions against ERT measurements for 160 micron particles at volume loading of 9.2% at (a) 1000 RPM, (b) 1250 RPM.

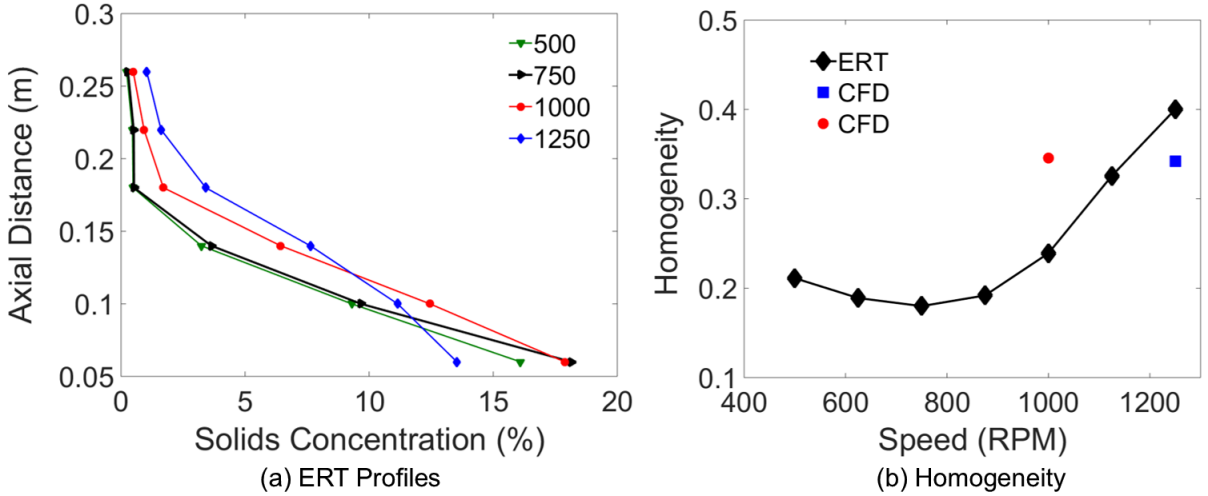

Figure 5.8. Plots showing (a) Axial profiles of solid phase holdup at different impeller rotation speeds as measurement using ERT, (b) Homogeneity values at different impeller speeds for 160 micron particles at volume loading of 9.2% obtained from ERT and CFD data.

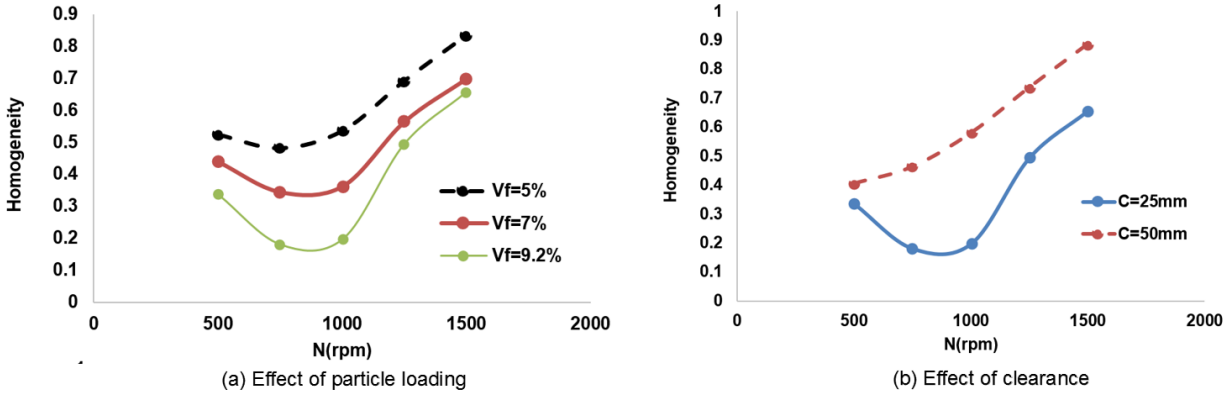

Figure 5.9. Homogeneity values at (a) different particle loading and (b) off-bottom clearance at constant particle loading of 9.2%.

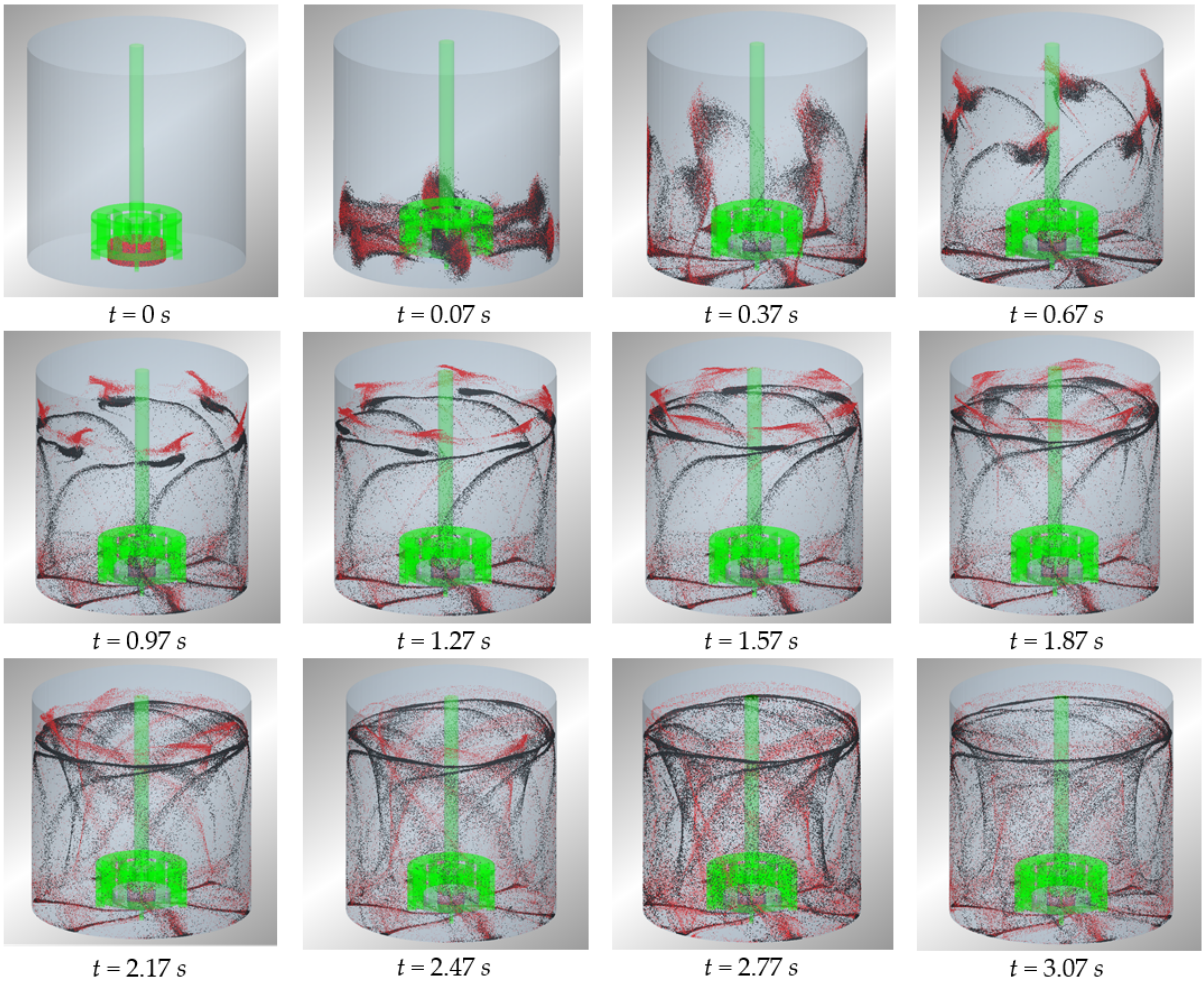

Figure 5.10. Images showing particle positions at different times obtained from CFD-DEM simulation. The size of particles shown in red are 0.5 mm (80,000 particles) and black are 1 mm (40,000 particles). The impeller tip speed is approximately 6.3 m/s and the flow Re is 120,000.

Table 5.1. Details of the grid independence study used for Eulerian-Eulerian slurry flow simulations

Mesh Type	Cells	Mass Fraction (%)	Speed (RPM)	Torque (Nm)	Cloud Height (mm)
Coarse	247,482	20	1000	0.233	198
Medium	501,246	20	1000	0.218	225
Fine	1,114,009	20	1000	0.202	231

CHAPTER 6

INVESTIGATION OF THE GAS DISPERSION CHARACTERISTICS IN STIRRED TANK AND FLOTATION CELL USING A CORRECTED CFD-PBM QUADRATURE BASED MOMENT METHOD APPROACH

6.1 Abstract

In this study, a population balance model (PBM) is coupled with computational fluid dynamics (CFD) to investigate steady-state bubble size distribution in two different process equipment, namely, standard Rushton turbine stirred tank reactor and generic lab-scale flotation cell. The coupling is realized using Fluent 15.07 software, and the numerical model is validated for stirred tank reactor. The population balance equation (PBE) is solved using the quadrature method of moments (QMOM) technique along with a correction procedure implemented to check and correct invalid moment sets. The breakage and coalescence of bubbles due to turbulence are considered. Breakage rate and daughter size distribution models proposed by Laakkonen et al. [1], as well as coalescence rate model of Coulaloglou Tavlarides [103], are implemented. The interaction between the phases is handled by considering the drag model proposed by Lane et al. [16] while ignoring other interphase forces. The correction algorithm has been successfully implemented, and improved predictions of gas volume fraction and Sauter mean diameter (SMD, d_{32}) have been observed with a good match between the predictions and experimental measurements. The local SMD predictions are compared against predictions from the past studies and superiority of current approach for moderate gassing rates is established. The CFD-PBM approach

is then used to study and characterize different flow regimes occurring in flotation cells at different aeration rates and impeller rotation speeds. Also, power numbers are calculated from torque data and are found to drop considerably with an increase in aeration rate and impeller rotation speed as the flow regime approaches recirculating flow. Predicted SMD for flotation cell indicates that smaller bubbles are concentrated near high turbulence impeller stream, lower recirculation region, and close to the tank walls. On the other hand, large bubbles are formed in the upper tank region and are concentrated around the shaft during flooding, loading, and transition flow regimes. In the future, the corrected QMOM approach will be further extended by implementing kinetic models capable of predicting flotation rate constant using local bubble size information obtained from CFD-PBM.

6.2 Introduction

Multiphase flows in flotation cells are highly turbulent and polydisperse in nature [12, 16, 41, 104]. The presence of all three phases, namely continuous phase (water) and dispersed phases (air bubbles and solid particles), and their complex interactions make studying flotation process a challenging task [3, 38, 104, 105]. Furthermore, the presence of many chemical reagents and their tendency to accumulate on the surface of dispersed phases (bubbles and particles) severely alters the behavior and dynamics of the dispersed phases in comparison to pure systems [4, 41, 104]. Information about the local bubble size distribution (BSD) is necessary to facilitate accurate prediction of flotation rate constant and valuables recovery [3, 4, 106]. Recent comprehensive experimental investigation of gas dispersion behavior and properties of various flotation cells has shown that BSD differs significantly in different regions of the cell [4]. Similar observations have been made by other researchers in both lab and pilot scale flotation cells [3, 5, 14]. Smaller bubbles are found in the region of high turbulence close to the impeller while larger bubbles, generated due to bubble coalescence and incomplete gas dispersion, are concentrated in the bulk region above the impeller.

The number of numerical studies focusing on fluid flow modeling and simulation in different process equipment has increased in recent years owing to availability of improved models and inexpensive computational resources [1, 12, 16, 39, 104, 107].

Computational fluid dynamics (CFD) simulations have been used in the past to study single-phase and multiphase flow behavior in stirred tanks and flotation cells [43, 47, 108]. In more recent papers, models describing specific flotation subprocesses have been implemented in the two-phase CFD model to facilitate prediction of flotation rate constant [11, 40, 41, 104, 105]. However, in the majority of the mentioned studies, single bubble size, or a single scalar equation solving the bubble number density, is considered to simplify the calculations and make the computational time tractable [41, 105, 109]. For instance, Evans et al. [12] investigated mixing and gas dispersion behaviors in flotation cells where the authors used a single bubble number density equation to predict BSD in the cell, which was not validated experimentally. These simplifications can lead to inaccurate predictions of flow phenomena [107, 110, 111] and implementation of the wrong fitting constants in flotation kinetic models [3]. More recently, the population balance model (PBM) has been successfully coupled with CFD to obtain reasonably accurate bubble sizes in process equipment such as stirred tanks [1, 110, 111]. The application of the CFD-PBM approach to simulate bubble size distribution in a flotation cell was demonstrated for the first time by Koh and Schwarz [3]. The experimental validation of numerical solutions was not offered in this work, but the authors conclude that the bubble size distribution has a significant effect on the predicted flotation rate constant; higher flotation rate constant values are observed when a full bubble size distribution range is considered compared to monosized bubbles.

Population balance equation (PBE) is an integro-partial differential equation describing the evolution of some selected property of the dispersed phase, such as size and composition [110, 112]. The solution of the continuous form of PBE is possible only for a few simple cases [1, 110, 112, 113]. A great number of numerical techniques have been proposed over the past two decades, of which many have found wide acceptance in multiphase flow applications [1, 110, 111, 114]. Of the many proposed PBE numerical solution techniques, the method of classes (MC) and the quadrature method of moments (QMOM) techniques have been reported to be the most suitable for multiphase gas-liquid flows [1, 3, 110, 114].

In the MC technique, the BSD is discretized into a sufficient number of finite size

classes or bins, and the transport equation of each size class is solved with appropriate sink and source terms depending on the physics of the problem [3, 112]. In the QMOM technique, PBE is transformed into a moment transport equation using the concept of a mathematical moment for density function, where each moment represents a different intrinsic property of a distribution [113, 115]. Marchisio et al. [116] reported that using the first six moments is sufficient to obtain meaningful results and good predictions for flows dominated by both breakage and coalescence when using the QMOM approach.

In chemical engineering, coupled CFD-PBM simulations have been carried out for various reactor types, such as bubble columns and stirred tank reactors, and a good match with experimental measurements has been reported in the literature [1, 110, 112, 117]. Laakkonen et al. [1, 118] performed experimental measurement of BSD in stirred tanks using three different experimental techniques. The local BSD measurements were compared with the numerical solutions obtained using coupled CFD-PBM approach. The CFD-PBM model using MC technique was developed and found to match the experimental measurements reasonably well based on fitted parameters for breakage and coalescence kernels [1].

Recently, Gimbun et al. [119] and Petitti et al. [110] studied gas-liquid flows in a stirred tank identical to the design used by Laakkonen et al.[1] by coupling CFD and QMOM technique. Both authors reported a good match between predictions and measurements of Sauter mean diameter (d_{32}) and overall holdup. Though the MC approach is reported to provide an accurate description of BSD and computationally robust, it is considered computationally intensive and usually requires a large number of size classes (80) for accurate predictions [120]. For instance, Selma et al. [120] compared MC and direct quadrature method of moments (DQMOM) and found MC technique to be over ten times more computationally expensive in comparison to DQMOM. In the DQMOM approach, the values of weights and abscissas are obtained directly by solving transport equations for weights and abscissas [121]. However, the DQMOM approach requires unsteady solution of governing equations and suffers from moment corruption issues when coupled with CFD [111]. Therefore, there is a great need for the development of an improved steady state numerical approach

based on QMOM, which, with the integration of a moment correction step, could be used to solve industrially relevant problems accurately and in a tractable time frame, i.e., within a few days as opposed to weeks. A comprehensive review of the literature dealing with flotation modeling and gas-liquid flow in stirred tank using radial impellers is given by Basavarajappa and Miskovic [122]. It is clear from the review of recent literature that benefits of QMOM and related family of methods (DQMOM and CQMOM), which have proven highly accurate for stirred tank flow at low gassing rates, could be further extended for multiphase flows in stirred tanks and flotation cells and moderately high gassing rates and holdup values ($> 3\%$).

One of the main advantages of QMOM over MC is the reduction in the number of equations that need to be solved to facilitate accurate prediction of dispersed phase properties such as SMD. However, QMOM is prone to error due to decoupling and independent advection of moments that can often give rise to a moment sequence not belonging to any physical distribution [123]. Such a moment sequence is called invalid or corrupted moment sequence/set. The issue and many causes of moment corruption have been explained in greater detail in the literature [123, 124], and useful checks and solutions are proposed to remedy the problems occurring as a result of moment advection. McGraw [124] introduced a fairly straightforward mathematical procedure to detect and correct invalid moment sets based on a minimization scheme by constructing difference tables [125]. Petitti et al. [110] implemented this correction in their investigation of gas-liquid flows in stirred tanks and reported encouraging results, especially at low aeration rates. Petitti et al. [110] successfully implemented QMOM in ANSYS Fluent by considering the first six moments with proper formulation of the source (birth) and sink (death) terms along with the moment correction step procedure. Similarly, Acher et al. [126] used the QMOM approach with correction procedure for bubble column and reported a good match between predictions and measurements.

The main objectives of this study are to develop and validate a coupled CFD-PBM approach by using QMOM technique coupled with the moment correction algorithm in ANSYS Fluent commercial software for moderate gas holdup values. The model is first validated by comparing the predictions against experimental measurements

of Laakkonen et al.[1] for stirred tank at moderate gassing rates (0.7 vvm). Grid convergence studies are performed to find the minimum number of cells required to achieve a reasonable balance between accuracy and simulation time. The validated numerical approach is further used to investigate gas dispersion characteristics and flow regimes developed in a generic flotation cell at different operating conditions different impeller rotation speeds and aeration rates. In the present work, the PBM module that comes standard with ANSYS Fluent 15.07 is used. The moment correction algorithm proposed by McGraw [124] is implemented over the QMOM solution obtained by Fluent using user defined functions (UDF). The developed model is intended to provide predictions of steady-state BSD for flotation cells in practical time frames, which in the future could be used be extended to include implementation of flotation kinetics models.

6.3 Numerical Model and Solution Strategy

The multifluid model (MFM) based Eulerian-Eulerian CFD approach is used in this work to perform numerical simulations, which consider interacting phases as an interpenetrating continuum [120]. Mass and momentum transport equations for both gas and liquid phases are discretized and solved using the finite volume (FV) technique in ANSYS Fluent 15.07 solver [100]. The general mass conservation equation for the continuous phase (represented by subscript c) and the dispersed phase (subscript d) are given as [100, 110]):

$$\frac{\partial(\alpha_c \rho_c)}{\partial t} + \nabla.(\alpha_c \rho_c \boldsymbol{U}_c) = 0 \tag{6.1}$$

$$\frac{\partial(\alpha_d \rho_d)}{\partial t} + \nabla.(\alpha_d \rho_d \boldsymbol{U}_d) = 0 \tag{6.2}$$

where, ρ_c and ρ_d are densities of continuous and disperse phases, respectively, α_c and α_d are the volume fractions of continuous and disperse phases, respectively, and $\boldsymbol{U}_c$ and $\boldsymbol{U}_d$ represent the mean velocities of continuous and disperse phases, respectively.

Similarly, the momentum conservation equations for continuous and disperse phases are written as [100, 110]:

$$\frac{\partial(\alpha_c \rho_c \boldsymbol{U}_c)}{\partial t} + \nabla.(\alpha_c \rho_c \boldsymbol{U}_c \boldsymbol{U}_c) = -\alpha_c + \alpha_c \rho_c g + \nabla.\boldsymbol{T}_c + \boldsymbol{F}_{cd} \tag{6.3}$$

$$\frac{\partial(\alpha_d \rho_d \boldsymbol{U}_d)}{\partial t} + \nabla.(\alpha_d \rho_d \boldsymbol{U}_d \boldsymbol{U}_d) = -\alpha_d + \alpha_d \rho_d g + \nabla.\boldsymbol{T}_d - \boldsymbol{F}_{cd} \tag{6.4}$$

where, p is the pressure shared by the phases, $\boldsymbol{g}$ is the acceleration due to gravity, $\boldsymbol{T}_c$ and $\boldsymbol{T}_d$ are strain rate tensors for continuous and disperse phases respectively, and $\boldsymbol{F}_{cd}$ is the interphase force term, which, in this case, is due to drag force.

The strain rate tensor for a generic phase 'p' is given as:

$$\boldsymbol{T}_p = \alpha_p(\mu_p + \mu_{t,p})(\nabla \boldsymbol{U}_p + (\nabla \boldsymbol{U}_p)^T) \tag{6.5}$$

where, μ_p and $\mu_{t,p}$ are molecular and turbulent viscosity, respectively.

The interaction between the phases is considered by taking into account only the drag force. The drag force equation is given by:

$$\boldsymbol{F}_{cd} = \frac{3}{4}\rho_c \alpha_d \frac{C_D}{d_b}|\boldsymbol{U}_d - \boldsymbol{U}c|(\boldsymbol{U}_d - \boldsymbol{U}c) \tag{6.6}$$

where, $\mathbf{F}_{cd}$ is the drag force, d_b is bubble diameter in the finite volume cell, which can be taken as d_{32}, and C_D is the drag coefficient, which is given by:

$$C_D = \frac{4d_b(\rho_c - \rho_d)g}{3\rho_c \boldsymbol{U}_\infty^2} \tag{6.7}$$

where, $\boldsymbol{U}_\infty$ is the terminal rise velocity of a bubble with diameter equal to d_b. The value of d_b is obtained by solving PBE in all the finite volume cells, details of which are provided in the later sections.

Initially, the drag model proposed by Montante et al. [127] was considered, since it was reported to provide the most accurate predictions of gas hold up and BSD in stirred tanks among other drag models available in the literature [110, 128]. However, the application of this drag model resulted in a divergence of the numerical model and generation of unphysical moments and gas holdup values. Moreover, this model requires specification of constant terminal rise velocity, which, though true for several specific cases, is limited in application since it cannot be universally applied to different flow regimes, and consequently adds numerical uncertainty to the model. Therefore, the universal drag law, which applies to gas-liquid bubbly flows across different flow regimes and bubble shapes was considered [100, 129]. The universal drag model requires no prior assumption of terminal rise velocity and uses different CD correlations for different bubble shape regimes [100, 129]. Recently, Evans et al. [12] and Karimi et al. [41] reported that the drag correlation proposed by Lane [130]

can capture reduction in terminal rise velocity due to turbulence correctly in stirred tanks. In this work, both Universal drag model [129] and Lane drag model [130] are considered. However, due to the superior performance of the Lane drag model, especially in the prediction of the overall gas holdup, only results obtained using Lane drag model are discussed.

The turbulence in the flow is modeled using standard $k-\epsilon$ dispersed turbulence model, which is applicable for multiphase flows where the secondary phase is dilute and dispersed [41]. The dispersed turbulence model only considers modified forms of turbulence kinetic energy (k) and turbulence kinetic energy dissipation rate (ϵ) transport equations for the continuous phase and the turbulence quantities for the dispersed phase are obtained from correlations defined by Tchen theory [100]. Readers are directed to ANSYS Fluent theory guide [100] for a complete form of turbulence transport equations and correlations used.

The importance of using an appropriate mesh for CFD simulations for stirred tanks, especially for multiphase flows, is recently highlighted by Klal et al.[128]. To correctly determine the choice of proper mesh, a detailed grid convergence study is performed and the grid offering the acceptable balance between accuracy and computation time is chosen to validate the numerical approach. For a stirred tank case, four grids with a total number of cells approximately equal to 89000, 205000, 317000, and 558000 are considered for 180-degree tank section. Only one-half section of the tank is simulated assuming symmetry, as has been done in the previous studies using similar geometry [1, 110]. Further details on the procedure used to ensure grid independent results along with validation of numerical approach are provided in the later section. A schematic of the stirred tank with surface mesh is shown in Figure 6.1 (a). For flotation cell, a mesh with approximately 500,000 cells is used for a 180-degree section of the tank. A schematic of flotation cell is shown in Figure 6.1 (b). A detailed description of both stirred tank and flotation cell geometries is provided in the following section.

The impeller rotation is modeled using multiple reference frames (MRF) approach, which has been shown to provide accurate results for both stirred tank and flotation cells in the past [1, 12, 110]. Steady-state simulations are initially performed using

low under relaxation factors to allow the solution to develop slowly and to avoid any divergence issues. Velocity inlet (air) boundary condition (BC) is applied at the sparger surface and velocity value is calculated based on the area of sparger and required gassing rate. Pressure outlet boundary condition is used for the top surface of the liquid where only air is allowed to escape and no backflow of air is allowed [110]. In all the simulations, inlet moments are specified for inlet gas velocity - the calculated moments are taken to follow a log-normal distribution with the mean equal to 3 mm and standard deviation of 0.5 mm. The first order discretization scheme is selected initially for all the flow variables, since higher order schemes are reported to produce solution divergence when QMOM is used [110]. Once the initial convergence is achieved, momentum and turbulence quantities are made second order, but first order schemes are retained for volume fraction and moments transport equation equations based on the recommendation from the literature using QMOM model [110, 131]. It should be noted that using first order schemes results in satisfactory convergence behavior and ensures boundedness of flow variables, but it occurs at the expense of solution accuracy. Finally, pressure-velocity coupling is achieved by using the phase-coupled SIMPLE scheme [100]. The solution convergence is established by monitoring solution residuals and the CFD solution is assumed to reach steady state when residuals for all the flow quantities fall below 10^{-04} [110, 120]. Also, the volume averaged gas holdup in the tank and local velocities and gas volume fractions are tracked at four discrete locations in the tank to ensure steady state is reached throughout the tank.

6.4 Population Balance Equation

Generalized PBE mathematically represents a change in some property (e.g., number density based on length or volume) for a population of particles with time. In the context of gas-liquid flows, the most critical property that controls the process performance is the number density function (NDF), which describes the distribution of probability of some property (usually diameter) in the flow. Number density function based on length (L), which represents bubble diameter in physical space around point $\boldsymbol{x}$ at time t, is written as:

$$n(L;x,t)dxdL \tag{6.8}$$

The PBE for breakage-coalescence dominated flows can be written as:

$$\frac{\partial[n(L)]}{\partial t} + \nabla.[\boldsymbol{U}_d n(L)] = B_{br}(L;x,t) - D_{br}(L;x,t) + B_{cl}(L;x,t) - D_{cl}(L;x,t) \tag{6.9}$$

where, $\boldsymbol{U}_d$ represents the average velocity of dispersed phase, B_{br}, D_{br}, B_{cl}, and D_{cl}, respectively, are birth due to breakage, death due to breakage, birth due to coalescence, and death due to coalescence. Mathematical moment of order 'k' of continuous function $n(L)$ can be written as:

$$m_k = \int_0^\infty n(L)L^k dL \tag{6.10}$$

By using the definition of moment Eq. 7.3, PBE in Eq. 6.9 can be transformed into a general moment transport equation that is written as:

$$\frac{\partial m_k}{\partial t} + \nabla.[\boldsymbol{U}_d^k m_k] = [\overline{B_k} - \overline{D_k}] \tag{6.11}$$

where, $\boldsymbol{U}_d^k$ represents the velocity of the k^{th} order moment. The source terms due to bubble breakage and coalescence can be written as [110]:

$$[\overline{B_k} - \overline{D_k}] = \frac{1}{2}\int_0^\infty n(L)\int_0^\infty h(L,\lambda)[(L^3+\lambda^3)^{k/3} - L^{k/3} - \lambda^{k/3}]n(\lambda)d\lambda dL + \int_0^\infty L^k \int_0^\infty g(\lambda)\beta(L,\lambda)n(\lambda)d\lambda dL - \int_0^\infty L^k g(L)n(L)dL \tag{6.12}$$

In this work, the first six moments are considered, which is reported to be sufficient to predict local BSD accurately when coupled with multifluid CFD model [110, 121]. In the QMOM technique, numerical quadrature approximation is used to represent distribution of moments using weights and abscissas [113]:

$$m_k = \int_0^\infty n(L)L^k dL = \sum_{i=1}^{n} r_i^k w_i \tag{6.13}$$

The calculation of weights w_i and abscissas r_i^k is achieved by using the product-difference (PD) algorithm [110, 113]. The reader is referred to seminal works of Gordon [132] and McGraw [113] for more details on the PD algorithm. Occasionally, calculated moment sequence becomes invalid, which results in incorrect or unphysical size distribution [110, 123, 124]. McGraw [124, 133] proposed a solution algorithm

to identify and correct such moment sequences through the use of difference tables and alpha matrices/sequences. A brief overview of the procedure to identify and correct invalid moment sets produced during QMOM simulation is presented in the following section. Sometimes, the correction procedure proposed by McGraw [124] fails to produce consistent moment sequence even after a large number of iterations [110, 123, 134]. In such cases, a new distribution is constructed using two log-normal distributions derived from the lower order moments of the original moment sequence [110, 123, 134]. The objective of this work is to implement this correction in the commercial CFD solver ANSYS Fluent 15.07 using user-defined functions (UDF) to investigate the complex gas-liquid flow behavior in stirred tanks and flotation cells across different operating conditions.

The coupling between CFD and PBM model is achieved through the calculation of Sauter mean diameter, d_{32}, which is obtained from the calculated moments as:

$$d_{32} = \frac{m_3}{m_2} \tag{6.14}$$

The d_{32} is then used in the calculation of the interphase exchange forces between the phases, thus completing the coupling.

6.4.1 Bubble Breakage and Coalescence Kernels

Evolution of the BSD in a process equipment is caused by breakage and coalescence mechanisms while nucleation and growth mechanisms can be ignored for gas-liquid flows in stirred tanks and flotation cells when heat and mass transfer mechanisms are neglected [1, 12, 110]. Breakage kernels have three parts, namely, breakage or breakup rate, the number of daughter particles or fragments, and the daughter size distribution. In this work, only binary breakage is considered, which is a standard practice in coupled CFD-PBM studies reported in the literature [110, 117, 120]. Therefore, the number of daughter particles formed following a successful breakage event is always two. A schematic of the bubble breakage event is shown in Figure 6.2. The majority of the breakage kernels proposed in the literature assume that successful breakage can only occur when the size of the eddy is equal to or smaller than the size of the interacting bubble. Otherwise, eddies only transport the bubble as shown in Figure 6.2. In this work, the breakage model adapted for gas-liquid flows

by Laakkonen et al. [1] that was originally developed by Alopaeus et al. [135] for liquid-liquid systems is used. The breakup rate ($g(L)$) is given by:

$$g(L) = C_1 \epsilon^{1/3} erfc\left(\sqrt{C_2 \frac{\sigma}{\rho_c \epsilon^{2/3} L^{5/3}} + C_3 \frac{\mu_c}{\sqrt{\rho_c \rho_d} \epsilon^{1/3} L^{4/3}}}\right) \tag{6.15}$$

The daughter size distribution (β) is given by:

$$\beta(L, \lambda) = 180 \left(\frac{L^2}{\lambda^2}\right) \left(\frac{L^3}{\lambda^3}\right)^2 \left(1 - \frac{L^3}{\lambda^3}\right)^2 \tag{6.16}$$

where, ϵ represents dissipation rate of turbulence kinetic energy and σ is the surface tension between the phases. The Laakkonen breakage model [1] is provided with PBM module in Fluent, and default values for constants (C_1, C_2, and C_3) are used as recommended by Petitti et al.[110].

Coalescence of bubbles is modeled as an event that occurs when two bubbles collide due to turbulence fluctuations in the flow [136]. Coalescence kernel has two parts, namely, collision rate and coalescence efficiency. The coalescence rate is modeled as the product of collision rate and coalescence efficiency. A schematic showing the outcome of a collision between two bubbles is shown in Figure 6.3. The coalescence rate model proposed by Coulaloglou and Tavlarides [103] is reported to provide good prediction by Petitti et al. [110] and is, therefore, implemented through the UDF in this work. The coalescence rate (h) is given by:

$$h(\lambda, L) = C_7 \epsilon^{1/3} (\lambda + L)^2 (\lambda^{2/3} + L^{2/3})^{1/2} exp\left(-C_8 \frac{\mu_c \rho_c \epsilon}{\sigma^2} \left(\frac{\lambda L}{\lambda + L}\right)^4\right) \tag{6.17}$$

where, C_7 and C_8 are parameters that must be obtained from experiments. For stirred tanks, C_7 and C_8 values equal of 0.88 and 6e+09, respectively, are recommended [1, 110]. For more information about the breakage and coalescence models available in the literature, readers are referred to recent reviews on the topic by Liao and Lucas [50, 136]. The possible range of bubble sizes is limited to 0.1-8 mm based on the resolution of the experimental techniques used by Laakkonen [137]. Previous CFD studies by Petitti et al.[110] and Laakkonen et al. [1] have also made similar assumptions.

6.4.2 Moment Sequence Corruption and Solution Procedure

When CFD solution is coupled with PBE through the solution of moment transport equations, the calculated moments have a tendency to form invalid sequences as

a result of numerical problems [110, 123, 124, 126]. The moments of a distribution uniquely determine a bounded distribution and are linked by proper relationships [110, 123]. When the moment transport equations are solved independently, the resulting moments obtained through inversion procedure might not preserve these relationships, leading to an invalid moment sequence [123, 124]. A valid moment sequence contains information about a physical distribution, whereas an invalid moment sequence does not represent a physical distribution [110, 123, 124]. One of the ways of checking the validity of any moment sequence is by ensuring Hankel-Hadamard determinants are positive ($\nabla_n \geq 0$) [124]. This condition constitutes a necessary and sufficient condition for moment validity. The issues of moment corruption when using QMOM approach were first reported for aerosol flows, which have been discussed in detail by Wright [123] and McGraw [124].

The solution procedures proposed by McGraw [124, 133] are easy to implement and work in a minimally disruptive manner by only changing the moments that are found to be corrupted and this way the majority of the moments obtained from solving the moment transport equations are left unchanged. The first step involves the construction of a difference table by taking the natural logarithm of the raw moments obtained from ANSYS Fluent. An example of a difference table constructed with a corrupt moment sequence is shown in Figure 6.4. Notice the appearance of negative second order differences (d_2), which is an indication of moment sequence corruption [124]. The third order differences (d_3) are used to identify the order of the moment that is corrupted and to provide an optimal correction by minimizing the sum of the squared differences of the second order differences, which ensure smoothness of $ln(m_k)$ sequence.

Let $\boldsymbol{a}_0$ represent initial third order difference vector (for e.g., [-3 9 -12]). For unit change in $ln(m_k)$ for k = 0-5, six response vectors ($\boldsymbol{b}_k$) are obtained, which represent the change in third order moments caused by the unit change in $ln(m_k)$. These response vectors are given by [133]:

$\boldsymbol{b}_0$ = [-1, 0, 0]; $\boldsymbol{b}_1$ = [3, -1, 0]; $\boldsymbol{b}_2$ = [-3, 3, -1]; $\boldsymbol{b}_3$ = [1, -3, 3]; $\boldsymbol{b}_4$ = [0, 1, -3]; $\boldsymbol{b}_5$ = [0, 0, 1];

The index k, which returns or causes the maximum value of $cos^2(\boldsymbol{a}_0, \boldsymbol{b}_k)$, represents

the moment that is corrupted and k^* represents the order of this moment. The $cos(\boldsymbol{a}_0, \boldsymbol{b}_k)$ can be calculated as:

$$cos(\boldsymbol{a}_0, \boldsymbol{b}_k) = (\boldsymbol{a}_0 \bullet \boldsymbol{b}_k)/(|\boldsymbol{a}_0||\boldsymbol{b}_k|) \tag{6.18}$$

Using this procedure ensures that maximum smoothness in $ln(m_k)$ sequence is achieved. Once the index of corrupt moment is known, it is adjusted using the following equation:

$$lnm_k(1) = lnm_k(0) - \frac{(\boldsymbol{a}_0.\boldsymbol{b}_k^*)}{|\boldsymbol{b}_k^*|^2} \tag{6.19}$$

where, LHS represents the corrected/adjusted moment to increase the smoothness, and the first term of RHS represents the initially corrupted moment of order k. This process is repeated iteratively until the convexity condition is satisfied. Once the moment sequence satisfies the convexity condition, which is a necessary condition for moment sequence validity, the moment sequence is then subjected to positive alpha sequence enforcement (PASE) test, which forms the sufficient condition. Working with the first six moments leads to an alpha sequence (α_n) with six elements (α_1 - α_6), which are calculated as:

$$\alpha = \alpha_1, \alpha_2, \alpha_3, ... \tag{6.20}$$

$$\alpha_1 = m_0 \tag{6.21}$$

$$\alpha_2 = \frac{m_1}{m_0} \tag{6.22}$$

$$\alpha_3 = \frac{m_2 m_0 - m_1^2}{m_1 m_0} \tag{6.23}$$

$$\alpha_4 = \frac{(m_1 m_2 - m_2^2) m_0}{m_1 (m_0 m_2 - m_1^2)} \tag{6.24}$$

$$\alpha_5 = \frac{(m_0 m_1 m_2 m_4 - m_0 m_1^3 m_4 - m_0^2 m_1 m_3^2 + 2 m_0 m_1^2 m_2 m_3)}{m_0 (m_1 m_3 - m_2^2)(m_0 m_2 - m_1^2)} \tag{6.25}$$

$$\alpha_6 = \frac{(m_1^2 - m_0 m_2)(m_1(m_3 m_5 - m_4^2) - m_2(m_2 m_5 - m_3 m_4) + m_3(m_2 m_4 - m_3^2))}{(m_1 m_3 - m_2^2)(m_0(m_2 m_4 - m_3^2) - m_1(m_1 m_4 - m_2 m_3) + m_2(m_1 m_3 - m_2^2))} \tag{6.26}$$

The moment sequence is valid if, and only if, the following condition is satisfied:

$$\alpha_n \geq 0; (n = 1 - 6) \tag{6.27}$$

In some cases, the moment sequence cannot be corrected in a reasonable number of iterations using the procedure proposed by McGraw [124], and therefore, a new

moment sequence needs to be created using two lognormal distributions as described by Binkowski [134] for aerosol flows and Petitti et al. [110] for gas-liquid flows in stirred tank. In this work, the McGraw correction is applied iteratively ten times. If the resulting moment sequence still fails convexity or PASE conditions, a new sequence is generated using two lognormal distributions as described in the next part. A flow chart clearly explaining the steps involved in the moment correction procedure described is shown in Figure 6.5.

The same algorithm is implemented in every cell (control volume) of the computational domain iteratively. Since the number of iterations directly affects the computation time, a reasonable number (10) is selected based on experience and the need to keep the computation time in check. As shown in the later sections, using mentioned settings resulted in physical and accurate prediction of d_{32}. However, further work investigating the effect of using higher number of iterations (>10) on the resulting moment sequence needs to be performed in the future.

6.4.3 Reconstruction Using Log-Normal Distribution

Sometimes, correction procedure enters an infinite loop or needs a large number of iterations to enforce correction, which is undesirable when simulating a coupled CFD-PBM problem with a large number of finite volume cells. In such cases, based on the recommendation of Binkowski [134], valid moment sequence is recovered using two log-normal distributions by retaining the zeroth (m_0) and third (m_3) moments from the original moment sequence. For a log-normal distribution, a generic moment can be written as [110]:

$$m_k = N_T exp\left(k\mu + \frac{k^2\sigma^2}{2}\right) \tag{6.28}$$

where, N_T is the number of bubbles in a unit volume, μ is the mean bubble size, and σ^2 is the variance of the bubble size distribution.

In the first distribution, the three distribution descriptors (N_T, μ, σ^2) are calculated by using m_0, m_1, and m_3 from the original moment sequence. Similarly, for the second log-normal distribution, the three distribution descriptors are calculated using m_0, m_2, and m_3.

6.5 Tank/Cell Design and Operating Conditions

Two geometries or designs are used in this work. Firstly, a stirred tank reactor fitted with Rushton impeller that was experimentally and numerically investigated by Laakkonen et al. [1] is used to validate the numerical approach. Secondly, a generic flotation cell is considered to study gas dispersion characteristics in the forced aerated flotation cell.

6.5.1 Stirred Tank Design

A schematic of the stirred tank with all the relevant internal parts is shown in Figure 6.6(a). The tank height (H) and diameter (T) are equal to 0.63 m. A standard Rushton impeller of diameter (d) equal to 0.21 m ($T/3$) fixed at constant off-bottom clearance (C) equal to 0.21 m ($T/3$) is used for gas dispersion and mixing [1]. A ring sparger, with the mean diameter equal to 0.8 times of the impeller diameter, located 55 mm from the tank floor, is used to inject gas at different flow rates (vvm). The simulations are performed at impeller speeds of 300 and 390 RPM and aeration rates between 0.1-1.0 vvm that correspond to experimental conditions used by Laakkonen et al. [1] for similar geometry using the air-water system.

6.5.2 Flotation Cell Design

A schematic of the flotation cell investigated in this study is shown in Figure 6.6(b). The cell height and diameter are both equal to 0.6 m. A six-blade, rectangular profile impeller along with a 16-vane stator is chosen for this study. The impeller diameter and impeller clearance (distance from impeller top to tank floor) are both 0.15 m, which is equal to 25% (one-fourth) of the tank diameter. The gap between the impeller and stator is 15 mm (0.015 m), which corresponds to 2.5% of the impeller diameter. A ring sparger, with a mean diameter equal to 0.12 m (120 mm) and a sparging width of 6 mm, is located 25 mm from the tank floor. The information about the operating conditions, namely, aeration and agitation rates, is given in the results section.

6.5.3 Flow Regimes - Flotation Cells

It is possible to characterize the aerated flow inside the flotation cell, over different aeration rates and impeller speeds, as shown in Figure 6.7. The flow number, Fl, defined as the ratio of aeration rate and impeller-induced flow rate, and Froude number, Fr, defined as the ratio of an impeller driven acceleration to gravitational acceleration, can be used to characterize the nature of flow regime inside the mixing vessels. Similarly, using the predicted torque value on rotating parts, power number, N_p, can be calculated. The flow number, Froude number, and power number can be calculated as:

$$Fl = \frac{Q_g}{Nd^3} \tag{6.29}$$

$$Fr = \frac{N^2 d}{g} \tag{6.30}$$

$$N_p = \frac{P}{N^3 D^5 \rho} \tag{6.31}$$

where, Q_g is the gas flow rate, N is the impeller speed in revolutions per second (rps), d is the impeller diameter in meters, g is acceleration due to gravity, P is power consumption (J/s, W) and ρ is the fluid density (kg/m^3).

At high Fl values, the aeration rate is high compared to the flow rate of fluid leading to flooding regime. On the other hand, low Fl values suggest that the flow rate induced by the impeller is high, leading to loading or transition regime, whereas high Fr values suggest impeller-induced acceleration dominates over gravitational acceleration, which produces a better dispersion of gas phase and leads to transition or recirculating regime at high operating speeds (Figure 6.7).

6.6 Results and Discussion

6.6.1 QMOM Correction

To investigate the effectiveness of QMOM correction, one test case is simulated using both the default QMOM model, which is available within the ANSYS Fluent software, and identical QMOM model with the moment correction algorithm applied. Figure 6.8 shows the comparison of the distribution of the 0^{th}, 2^{nd}, and 5^{th} moments of dispersed phase with and without the correction algorithm.

The default QMOM simulation results shown are generated after 50,000 iterations and corrected QMOM results after 93,000 iterations at which point the simulation had converged. Continuing the default QMOM simulation further did not lead to any improvement in the results. From Figure 6.8 (top row) it can be clearly seen that very high values (notice peak values on contour plot scales) of moments are generated by ANSYS Fluent QMOM model for all the three moments shown. The resulting prediction of d_{10} or d_{32} using incorrect moments is erroneous. On the other hand, the predictions made by corrected QMOM model are physical in nature and show that the correction algorithm can identify and stop the corruption of moment sequence. It must be noted, though, that default QMOM and corrected QMOM models make very similar predictions of volume fraction distributions. This is due to the fact that both volume fraction and QMOM equations are decoupled, and coupling between the Eulerian and the QMOM model is achieved through specification of local d_{32}, which is used to calculate interphase forces in the hydrodynamic model.

6.6.2 Grid Convergence Study - Stirred Tank

A comprehensive grid convergence study is performed to determine the number of cells needed to accurately represent the two-phase gas-liquid flow in stirred tank. Four grids of increasing mesh density are selected by carefully refining the mesh, especially close to impeller where the gradients of velocity and turbulence are high. Table 6.1 lists the details of the mesh and the corresponding predictions of vessel averaged gas hold up, SMD (d_{32}), and number averaged mean diameter (d_{10}). By comparing the predicted hold from CFD and experimentally measured hold up reported by Laakkonen et al. [1], it can be concluded that Fine grid with approximately 317,200 cells predicts the most reasonable values. Increasing the total number of cells over 317,200 resulted in a reduction in holdup prediction and further analysis is needed to fully understand the reason for this behavior, which is outside the scope of this work. One of the possible reasons is that the grid size close to the impeller becomes comparable to bubble size or even smaller, which contradicts the requirements of the Eulerian-Eulerian model [138]. Moreover, previous CFD investigations using the same stirred tank also reported grid independent results using grids with approximately

230,000 cells for a half tank section [110, 119]. As expected, both d_{32} and d_{10} decrease with increase in impeller speed at constant gassing rate of 0.7 vvm. This trend has been captured correctly by CFD across all the grids as shown in Table 6.1.

It is well known that the power consumption of Rushton impeller decreases significantly under gassing condition as a result of the formation of gas cavities in the trailing vortices. Several correlations are proposed in the literature to predict gassed power consumption and power number using the ungassed power consumption data, operational conditions inside the tank, such as gassing rate and impeller rotation speed, and tank design data, such as tank diameter, height and impeller size [1, 119]. Furthermore, Laakkonen et al. [1] reported good results when using correlation proposed by Midoux and Charpentier [139], which is given by:

$$P_g = 0.34\sqrt{N_{p,u}}\left(\frac{(P_u^2 N d^3)}{Q_g^{0.56}}\right)^{0.45} \tag{6.32}$$

where, P_g is power consumption under gassed conditions, P_u is power consumption under un-gassed conditions, and $N_{p,u}$ is the ungassed power number, which was measured to be 5.8 by Laakkonen et al. [1].

Alternately, Bujalski et al. [140] proposed a correlation to predict un-gassed power number for Rushton turbines using vessel size (D), impeller blade thickness (h) and impeller diameter (d) as:

$$N_{p,u} = 2.512\left(\frac{h}{d}\right)^{-0.915} T^{0.063} \tag{6.33}$$

Using the correlation proposed by Bujalski et al. [140], a $N_{p,u}$ value of 5.06 is found for our case, which agrees with the value of $N_{p,u}$ found in the literature for Rushton turbines [119, 141]. Gimbun et al.[119] found the correlation proposed by Smith [142] to correctly predict the power number ratios which is given by:

$$\frac{P_g}{P_u} = 0.18 Fr^{-0.2} Fl^{-0.25} \tag{6.34}$$

Table 6.2 shows the CFD and correlation predicted power numbers for gassed conditions ($N_{p,g}$) at two impeller speeds of 300 and 390 RPM. The CFD predicted power numbers are calculated using Eq. 6.31 and from the torque value on impeller and shaft. By comparing the CFD and correlation predicted torque values, it can

be clearly seen that correlation by Midoux and Charpentier citepMidoux1984 fits the data well at the lower speed of 300 RPM, whereas the correlation by Smith [142] fits the CFD predicted data better at a higher speed of 390 RPM. As noted earlier, the highest power number at both speeds is predicted by Fine grid in comparison with Fine-2 grid. It appears that the prediction accuracy, though related to a total number of cells, begins to suffer when finer grids are used. The gassed power numbers reported by Laakkonen et al. [118] at 300 and 390 RPM are approximately equal 3.0 and 2.5 and the corresponding gassed power number predicted by CFD-PBM model using Fine grid are 3.19 and 2.34. The following results and discussion show that Fine grid with approximately 318,000 cells can be used to predict the gas holdup and gassed power number with the acceptable accuracy based on the comparison with the experiments. Moreover, further improvement in mesh density results in underestimation of both gas holdup and power number with the combination of models. Thus, the Fine grid is assumed to provide grid independent results and considered for further analysis.

6.6.3 Predicted Bubble Sizes and Gas Holdup - Stirred Tank

One of the advantages of QMOM correction algorithm is its ability to predict the moments of the distribution correctly. When the moments obtained from the QMOM simulation are accurate, the resulting particle or bubble size distribution will also be accurate [110, 124]. To further validate the numerical model used in this work, the predictions from our numerical model are compared with the measurements from Laakkonen et al. [1]. Figures 6.9 (a) and (b) show the contour plots of of predicted d_{32} and air volume fraction along an axial plane at 390 RPM and aeration rate of 0.7 vvm, respectively. The local d_{32} values are calculated as the ratio of corrected third and second moments.

Some observations about the distribution of d_{32} can be easily made from Figure 6.9 (a). Smaller bubbles are concentrated near the impeller region, lower recirculation zone, and close to the wall. The impeller motion creates a highly turbulent region close to the impeller in the radial direction, which results in breakage of bubbles. The buoyancy forces on these newly formed smaller bubbles cannot overcome the inertial

forces due to recirculation and pumping of water caused by continuous impeller rotation. Therefore, the majority of small bubbles are trapped in the lower recirculation region. However, some bubbles manage to escape along the walls as seen from Figure 6.9 (a). The higher residence time of bubbles in this high turbulence zone results in repeated breakage and small d_{32} values in the bottom half of the tank. The larger bubbles have been shown to escape through the middle of the tank where values are lowest [1, 110]. In this low region, bubble coalescence dominates over breakage, which results in comparatively larger d_{32} values.

Local d_{32} values from the simulations are compared with experimental measurements of Laakkonen et al. [1] at five locations (A-E) as shown in Figure 6.9 (a). Experimentally measured values are shown in bold text (first line), and our predictions are underlined (second line). To further compare our model predictions with other CFD-PBM simulation results, predictions from Laakkonen et al. [1] and Petittie et al. [110] are also shown inside square brackets and curly brackets, respectively. By comparing our predictions against the measurements, it is clear that the numerical approach used in this work is capable of providing good predictions of local bubble sizes and predicted bubbles sizes are within 10-15% of the measured values. Furthermore, the approach used in this work provides improved predictions of local d_{32} than previous CFD-PBM studies as evidenced from the comparison shown in Figure 6.9 (a). Minor disagreements between measurements and predictions can be further improved by choosing other breakage and coalescence models or adjusting the parameters of models used in this work to provide a better match. Along with the local d_{32} values, Laakkonen et al.[1] also reported experimentally measured normalized volumetric bubble size distributions. Using the moments obtained from the converged QMOM solution, it is possible to reconstruct BSD at discrete locations in the process equipment [143]. The simplest way of reconstructing the BSD is by assuming a priori distribution function such as a normal or a gamma function [143]. Additionally, an alternative approach based on statistically most likely distribution proposed by Pope [144] for turbulent flows, and successfully extended for PBM can be used to reconstruct BSD [145, 146]. In this work, both the approaches are used to reconstruct BSD and compared against measurements of Laakkonen et al. [1]. The

normal distribution is found to fit the experimental data more closely compared to other common distributions and therefore considered here. The probability density function of a normal distribution is given by:

$$f(L) = \frac{1}{\sigma\sqrt{2\pi}} exp\left(-\frac{(L-\overline{L})^2}{2\sigma^2}\right) \tag{6.35}$$

where,

$$\overline{L} = \frac{m_1}{m_0} \tag{6.36}$$

and

$$\sigma_n = \overline{L}\sqrt{\frac{m_0 m_2}{m_1^2} - 1} \tag{6.37}$$

The second approach involves assuming the following functional form for number density:

$$n(L) = exp\left(\sum_{i=0}^{N_{mom}-1} A_i L^i\right) \tag{6.38}$$

where, N_{mom} is the number of moments used which in this case is 6, and A_i are coefficients that need to be found. Using the definition of moment we can write:

$$m_k = \int_0^\infty n(L)L^k dL = \int_0^\infty \left(\sum_{i=0}^{N_{mom}-1} A_i L^i\right) L^k dL \tag{6.39}$$

Since the moments from CFD-PBM are known, the reconstruction problem involves finding A_i such that the QMOM moments and moments calculated from Eq. 36 are under certain tolerance level. In this work, *lsqnonlin* solver in Matlab Optimization Toolbox was used to calculate the coefficients (A_i) in Eq. 6.38. The support for distributions reconstructed in mm is [0, 10].

Comparison of the reconstructed BSD, which are given as volumetric bubble size distributions, using the two methods along with the experimental data reported by Laakkonen et al. [1] are shown in Figure 6.10. The normal shape function can correctly capture the location of the distribution peak at most locations. However, when the experimental distribution has a negative skewness, the normal function tends to over-predict the tail of the distribution. On the other hand, the statistically most likely distribution is able to predict bimodal distributions, as evidenced from points A and C. The statistically most likely distribution technique predicts acceptable trends at locations A, D, and E. Both applied methods fail to capture the trend correctly

at point B, with both techniques predicting narrow distributions. The comparison study shows that predicting the correct distribution shape using the moments is a nontrivial task and advanced mathematical methods for more accurate prediction of the size distribution are still being developed [143, 147].

The presented results for the stirred tank show that the CFD-PBM approach used in this work is capable of providing physical flow features for gas-liquid flows with accurate predictions of BSD. The validated QMOM model is further applied to study flows in flotation cells, and the results are presented in the following section.

6.6.4 Mean Flow and Gas Dispersion Behavior in Flotation Cells

Numerical simulations of gas-liquid flows in flotation cell are performed using the validated QMOM model under several different operating conditions with the aim of (a) characterizing different flow regimes in the cell, (b) gaining a better understanding of the gas dispersion behavior, and (c) making accurate predictions of mean BSD in the cell. Contour and velocity vector plots are plotted along vertical and horizontal planes to describe both mean distribution and behavior of air and water phases. Two vertical planes perpendicular to each other spanning the full length of the flotation cell as well as six horizontal planes at vertical distance of 0, 100, 200, 300, 400, 500, and 595 mm from the tank floor are selected as shown in Figures 6.11 (a-d). A total of thirteen different operating conditions are chosen and simulated to cover a wide range of flow regimes expected in the flotation cell. Information about the impeller speed, superficial gas velocity, Fr, Fl, holdup, and flow regime description for all the simulated conditions is given in Table 6.3. Four representative cases, each belonging to a different flow regime, are chosen to delineate the mean flow behavior observed at different operating conditions using mean gas volume fraction and velocity distributions along with the gas and liquid velocity vectors plots. Flooding and loading regimes are found at low impeller speeds for the lower range of aeration rates while better dispersion can be observed at higher impeller speeds leading to transition and recirculating regimes as evident from Table 6.3.

Contour plots of air volume fraction at four different flow conditions are shown in Figures 6.11 (a)-(d). At 100 RPM and low superficial gas velocity of 0.26 cm/s, loading flow regime is predicted. The majority of the air can be seen escaping through

the narrow rotor-stator gap and moving to the top by taking a path close to the center of the cell. Some dispersion of air still occurs as seen from the low volume fraction region near the stator. The volume fraction distribution plot indicates that the impeller speed is not sufficient to fully disperse the air. By keeping the superficial velocity constant at 0.26 cm/s, impeller speed is increased to 250 RPM. Increase in impeller speed results in a transition of the flow regime from loading to recirculating, where the incoming air becomes fully dispersed. The recirculating regime is characterized by an improved dispersion of air in the radial direction, wherein the dispersed phase follows the fluid in the radial jet toward the tank wall and partially to the lower recirculation region.

A better understanding of the transition in the mean flow behavior can be achieved by observing corresponding air velocity and vector plots in Figures 6.12 (a) and (b). At 100 RPM, the mean air flow has significant axial velocity component near the impeller and the air can be seen moving in the upward direction with negligible recirculation in the upper region of the cell. At 250 RPM (Figure 6.12 (b)), velocity vectors in the high energy intensity region are aligned with the main jet coming from the impeller, parallel to the tank floor, indicating that the momentum generated by impeller rotation is able to overcome the buoyancy forces and result in increased breakage and better recirculation of the air bubbles.

Mean liquid velocity contour and velocity vectors at corresponding conditions are shown in Figure 6.13 (a) and (b). For both cases, the peak air velocity is observed in the impeller wake region where the gas accumulates due to the creation of a low-pressure region behind the impeller blades. Increasing the air flow rate to achieve a superficial gas velocity of 0.5 cm/s at 250 RPM results in the flow transition from recirculating to transition regime. Under the transition flow regime, as illustrated in Figure 6.11 (c), while most of the incoming air are dispersed radially, a considerable fraction of air still escapes through the rotor-stator gap moving to the top close to the shaft.

Further increase in impeller speed to 350 RPM and the superficial gas velocity to 0.62 cm/s results in another flow regime transition from the transition regime to fully recirculating regime as shown in Figure 6.11 (d). With an increase in the impeller

speed, higher momentum is generated in the mean flow, enabling maximum dispersion of the incoming air and its recirculation through both lower and upper recirculation loops. From the velocity vector plots shown in Figures 6.12 (d) and 6.13 (d), the formation of weaker secondary upper recirculation loop can be observed. In the flotation process, froth dynamics and particle recovery at the pulp-froth interface are greatly controlled by the presence, size, and intensity of the secondary upper recirculation loop. For instance, the inward direction of the upper recirculation loop (flow is moving toward the shaft) would increase froth residence time at the surface, which would in return create stagnant froth zones, froth collapse, and consequently particle detachment.

In froth flotation, the flow regime developed using 350 RPM agitation rate and superficial gas velocity of 0.62 cm/s is highly desirable since it successfully disperses the incoming air in the radial direction and improves local recirculation of the dispersed air. Increased recirculation of the dispersed air (bubbles) leads to a higher probability of breakage and formation of smaller air bubbles, which in turn improves flotation kinetics.

Three dimensionless numbers, namely Fl, Fr, and power number, N_{pg}, in addition to vessel averaged gas holdup data are also given in Table 6.3. Some general trends can be established from the data, which are comparable to the previous observations made for stirred tanks [1, 110, 141].

In general, at a constant aeration rate, an increase in impeller agitation rate results in higher gas holdup. The high gas holdup is created as a result of improved mixing and a greater level of turbulence in the cell leading to increased bubble breakage rate, generation of smaller bubbles, and longer gas residence time in the cell. For stirred tanks, power number, N_{pg}, was found to decrease with decreasing Fl values [1, 141]. Similar behavior can be observed in the case of a flotation cell as well, which is shown in Table 6.3 N_{pg} decreases significantly with an increase in aeration rate and impeller speed.

6.6.5 Predicted Bubble Size Distribution - Flotation Cell

Bubble size is one of the most important process parameters in a flotation operation. Accurate prediction of local BSD could enable development of superior flotation

cell design and lead to optimal process operation. Figure 6.14 shows the contours of d_{32} for four different operating conditions, along with reconstructed normalized volumetric bubble size distribution plots at four distinct points in the cell. The points marked with numbers from 1 to 4 in Figure 6.14 (a) are chosen such that all the critical regions of the flow are represented. Previously described BSD reconstruction methods, which have been applied to the stirred tank case shown in Figure 6.10 and described in Eq. 6.35– 6.38, are used to generate BSD plots from the available moment sets.

In general, large bubbles are expected to form in the regions of low turbulence in the flotation cell as a result of coalescence of smaller bubbles. Smaller bubbles are concentrated in the impeller region and the radial jet stream where the turbulence dissipation rates are high. It should be noted that turbulent fluctuations result in both bubble breakage, when eddies interact with bubbles, and coalescence, when bubbles collide as a result of mean or fluctuating velocity gradient. In our case, small bubbles are found to form in a lower part of the cell and close to the cell walls. Similar observation has been made in stirred tank reactors by other authors [1, 110, 114].

At low speeds, only a small fraction of sparged gas is broken and radially dispersed since the created level of turbulence is not sufficiently high, especially at 100 RPM. A gas cavity is formed behind the impeller blades and most of the bubbles escape through the impeller-stator gap, as seen in Figure 6.11 (a). The blue region in Figure 6.14 (a) indicates an absence of bubbles in a large part of the cell volume.

Under constant superficial gas velocity, the effect of impeller speed on BSD can be observed from Figures Figure 6.14 (a) (100 RPM) and (c) (250 RPM). At different speeds, the effect of increased turbulence level manifests as increased breakage rate of bubbles. Formation of bands of smaller bubble sizes is evident at 250 RPM near the impeller/stator assembly in the impeller jet region, which is visible both in the vertical and horizontal contour plots. Clearly, the increase in impeller speed from 100 to 250 RPM results in better recirculation of air in the lower part of the cell, which is coupled to the formation of smaller bubbles. Larger d_{32} values can be observed at 250 RPM, especially between the fourth and fifth horizontal planes. These bubbles are formed as a result of coalescence of bubbles recirculating in the upper part of the

tank. It should be pointed out that the corresponding volume fractions of air are very low in the regions with large d_{32} values, so we can conclude that the larger bubbles form in small numbers under these conditions.

At constant agitation rate of 250 RPM, the increase in superficial gas velocity from 0.26 cm/s to 0.50 cm/s results in a significant change in d_{32} distribution profile and the formation of larger bubbles in the upper zone of the cell, which is the region with high air volume fractions. At agitation rate of 350 RPM and superficial velocity of 0.62 cm/s, the d_{32} distribution is considerably different between the upper and lower parts of the cell, with smaller bubbles forming mainly in the impeller stream. A part of the smaller bubbles that are trapped in the lower recirculation region coalesces, resulting in increased values of d_{32}. A band of large bubbles is evident in the upper zone of the cell, which corresponds to an area with low air volume fraction (Figure 6.12 (d)). We could, therefore, conclude that while large bubbles are present in this area, their number is small.

The reconstructed BSDs predicted by both methods show that distributions tend to be narrow in the lower parts of the cell (points 1 and 2), where breakage dominates over coalescence. However, due to coalescence in the upper cell region, the distributions become wider as evident from reconstructed BSDs at points 3 and 4. Generally, the Pope method predicts unimodal distribution when the flow regime corresponds to a fully recirculating flow type and bimodal for a transition regime. It is important to mention here that the results obtained in this work are for frother and collector free, two-phase air-water system. In the presence of flotation reagents, coalescence is suppressed, leading to a narrow size distributions and lower d_{32} values in the cell [5, 14]. However, comprehensive breakage and coalescence kernels for air-water turbulent systems in the presence of frothers and collectors are not available in the literature. Currently, the authors are working towards developing a high-order population balance model to estimate parameters in breakage and coalescence kernels for gas-liquid flows in the presence of frothers, which could be adapted for the future CFD-PBM studies.

6.7 Conclusions

In this work, a correction algorithm capable of successfully identifying and correcting moment sequence obtained from ANSYS Fluent QMOM solution is presented. The correction algorithm has been successfully implemented for the case of gas-liquid flows in stirred tanks and flotation cells. The obtained predictions from the corrected QMOM model are compared against the experimental measurements of Laakkonen et al. [1] leading to a satisfactory agreement between the two. Some differences in the predictions and measurements can be attributed to the choice of breakage and coalescence models and the fitting constants used in the models, which is still a field of active research, especially for gas-liquid flows in flotation cells. The SMD (d_{32}) predictions for stirred tank reactor using corrected QMOM model are compared against other CFD-PBM predictions available in the literature, namely Laakkonen et al. [1] and Petitti et al. [110], and show that the current approach is considerably better than previously published results, particularly at moderate hold up values.

Using the corrected CFD-PBM approach, information about the mean flow behavior and Sauter mean diameters is obtained and presented for a generic lab-scale flotation cell. Thirteen different operating conditions, covering four different flow regimes in the flotation cell, namely flooding, loading, transition, and recirculating, are selected for this study. At low agitation and moderate aeration rates, which corresponds to high flow number (Fl) and low Froude number (Fr), the flow is found to operate in flooding and near-loading regimes. The increase in agitation rate results in better gas dispersion, leading to the development of a complete loading regime at moderate flow and Froude numbers. Further increase in impeller speed leads to the flow regime transition from loading to transition regime, which is characterized by improved gas mixing in both the axial and radial directions. The gas holdup is found to increase and power number decrease with an increase in agitation rate, which is in agreement with other observations made in the literature [12, 141]. The BSD results indicate the presence and concentration of smaller bubbles in the impeller stream and lower part of the cell when operating at transition and recirculating regimes. As a result of bubble coalescence and insufficient impeller agitation, large bubbles concentrate in low numbers in the upper, quiescent region of the cell. The power

numbers predicted under gassing conditions followed expected trends and dropped significantly, especially when operating at high agitation and high aeration rates. Using the proposed approach, accurate BSD and gas volume fraction data can now be generated and used to predict flotation rates by implementing flotation kinetic models proposed in the literature for gas-pulp flows.

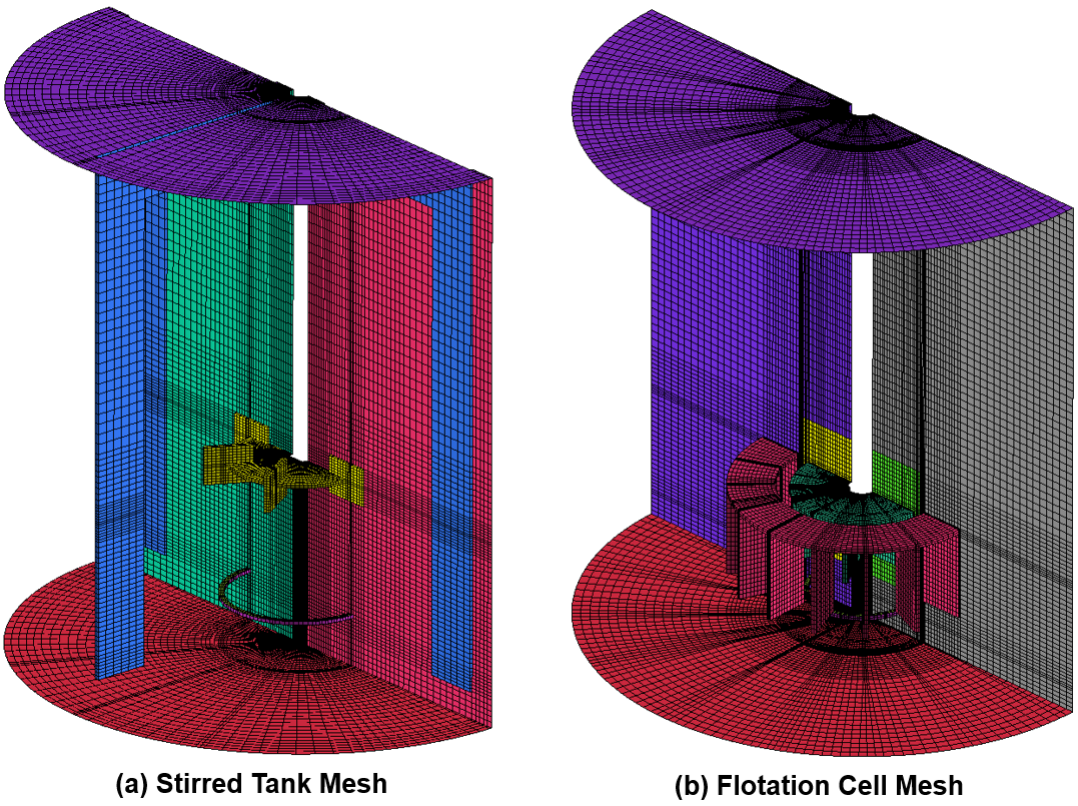

Figure 6.1. Image showing the details of surface meshes used for (a) Stirred tank reactor (b) Flotation cell.

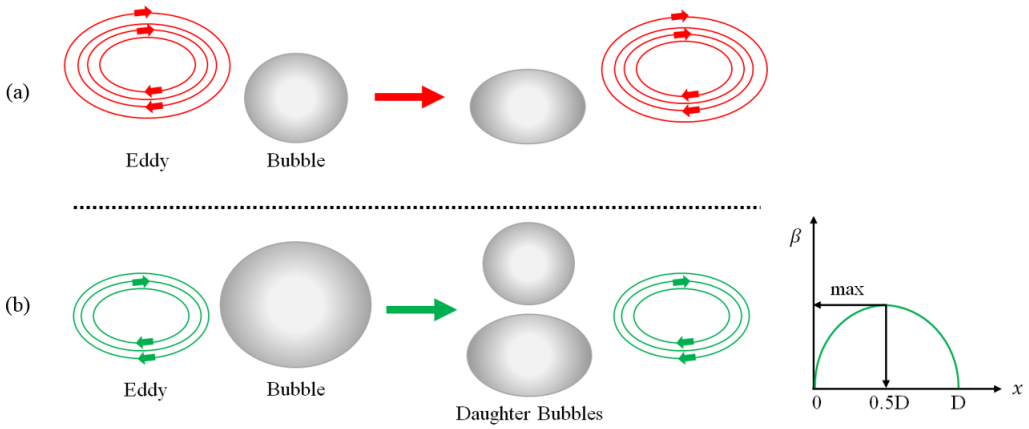

Figure 6.2. Bubble breakage event showing the interaction between a turbulent eddy and a bubble. (a) When the eddy is larger than a bubble, it merely transports or advects the bubble. (b) If the eddy is of similar or smaller size than the bubble, the collision can result in breakage if energy supplied by the eddy is greater than the increase in surface energy needed to create another bubble.

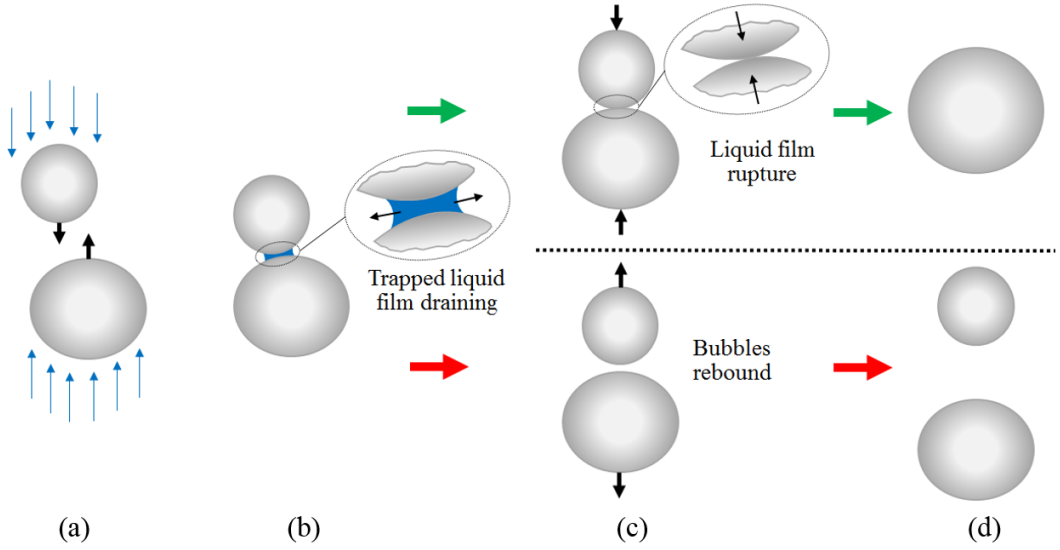

Figure 6.3. Bubble coalescence event showing the interaction between a pair of bubbles in three stages: (a) collision of bubbles results in contact and trapping of a small amount of liquid between them; (b) drainage of the trapped liquid; (c-top) when critical film thickness is reached, film ruptures and bubble coalesce occurs; (d-top) one larger bubble is formed. If the bubble interaction or drainage time is not long enough, the bubbles will separate (c-bottom) and will be transported by the mean flow (d-bottom).

k	Ln(m_k)	d_1	d_2	d_3	d_4	d_5
0	0	1	2	-3	12	-33
1	1	3	-1	9	-21	N
2	4	2	8	-12	N	N
3	**6**	10	-4	N	N	N
4	16	6	N	N	N	N
5	**22**	N	N	N	N	N

(a)

k	Ln(m_k)	d_1	d_2	d_3	d_4	d_5
0	0	1	2	**0**	**0**	**0**
1	1	3	**2**	**0**	**0**	N
2	4	**5**	**2**	**0**	N	N
3	**9**	**7**	**2**	N	N	N
4	16	**9**	N	N	N	N
5	**25**	N	N	N	N	N

(b)

Figure 6.4. Difference table showing first (d_1) to fifth (d_5) order differences obtained by taking natural logarithm of a moment sequence for corrupted (a) and uncorrupted (b) moment sequences.

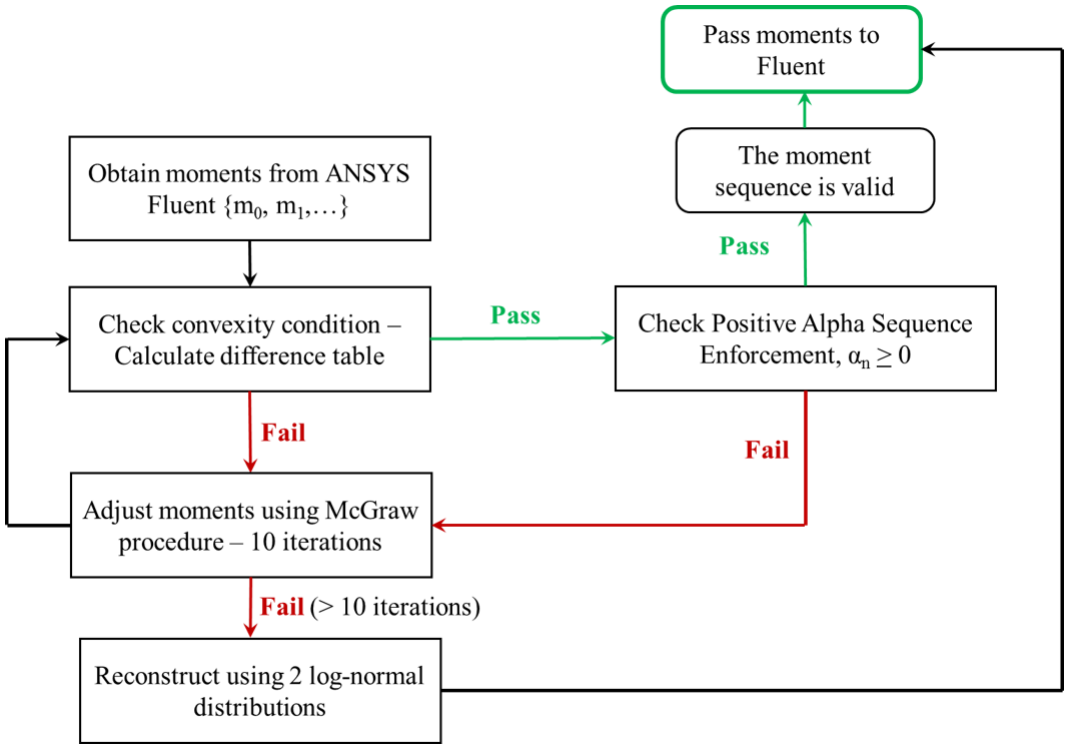

Figure 6.5. Flow chart showing the moment correction procedure used in this work to identify and correct invalid moment sequences.

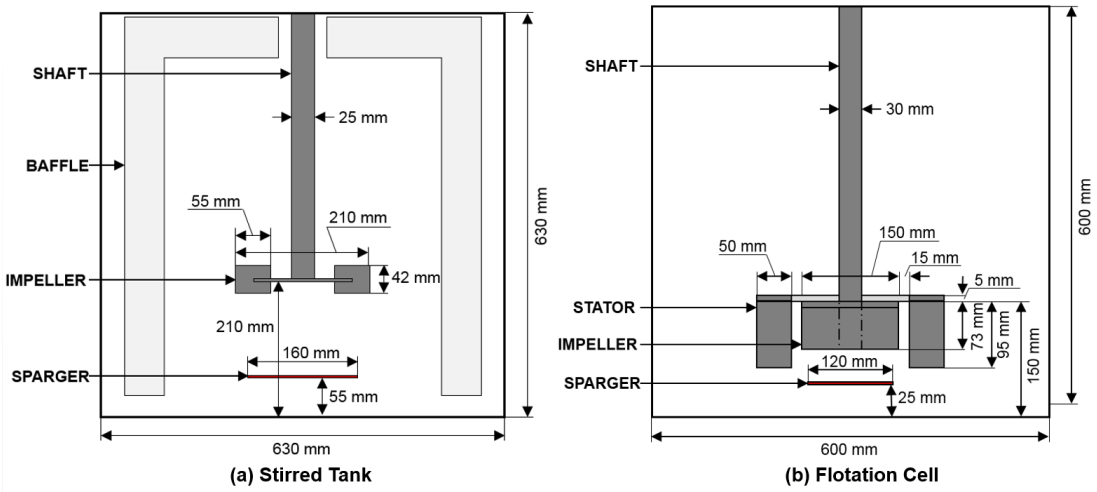

Figure 6.6. Schematics of process equipment used in this study (a) Schematic of the stirred tank used in experiments by Laakkonen et al. [1] with all relevant parts and key dimensions; (b) Schematic of the flotation cell used in this study with all dimensions.

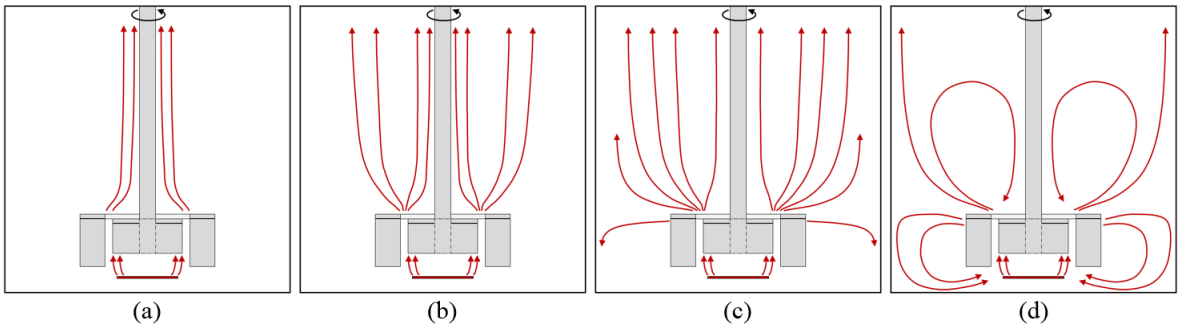

Figure 6.7. Schematics of four main types of flow regimes expected in a flotation cell at different operating conditions: (a) flooding; (b) loading; (c) transition; (d) recirculating.

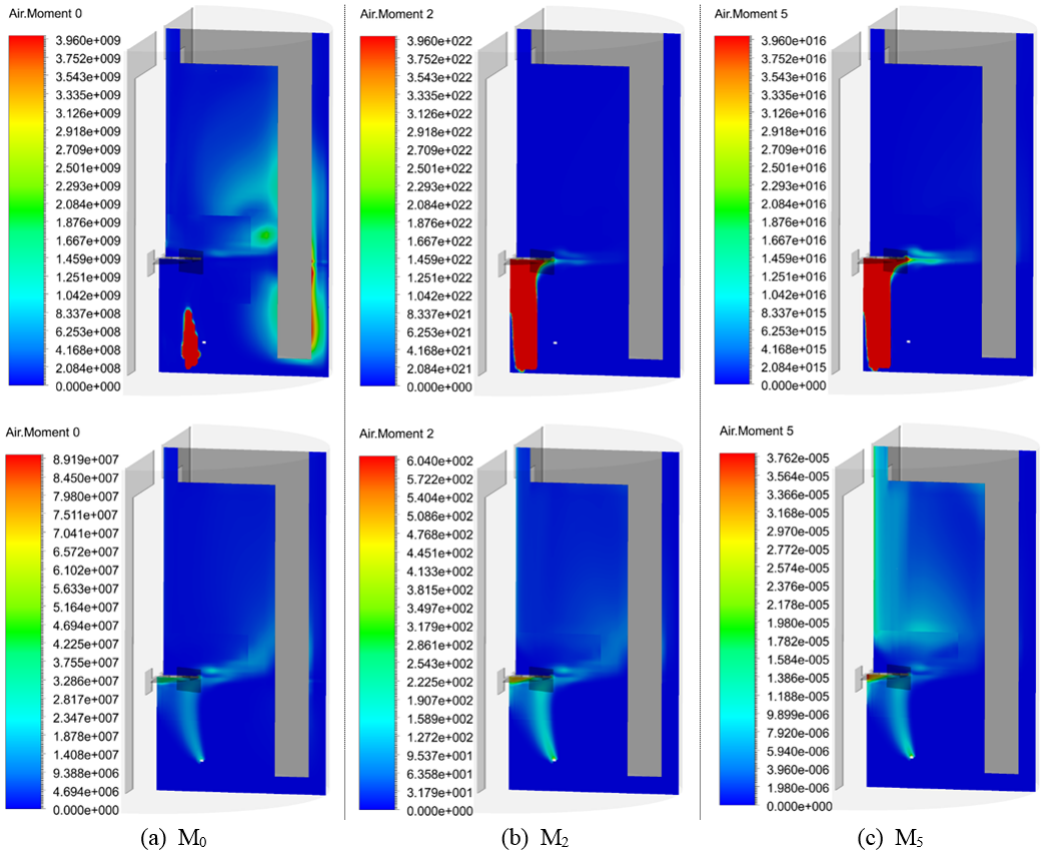

Figure 6.8. Contour plots of the 0^{th}, 2^{nd}, and 5^{th} moments showing the QMOM results without (top) and with (bottom) correction algorithm at 300 RPM and $Q =$ 0.7 vvm. Notice the high peak and range of moment values for uncorrected moments on scales of associated contour plots.

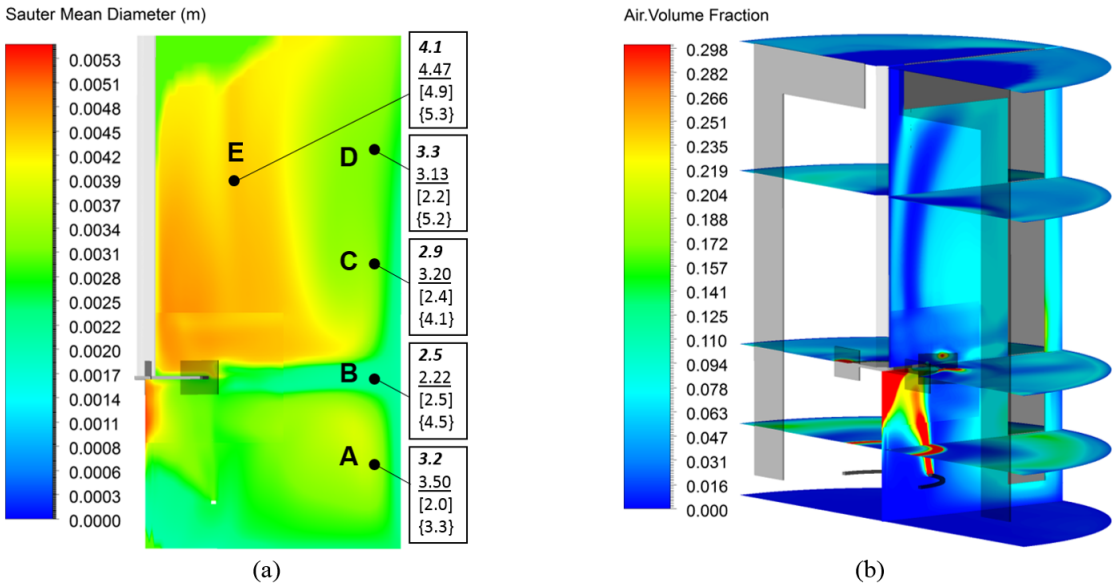

Figure 6.9. Stirred tank results (a) Predicted sauter mean diameter (SMD, d_{32}) contours at 390 RPM and $Q = 0.7$ vvm. The numbers given from top to bottom at each measurement point represent d_{32} in mm: Experimental measurement reported by Laakkonen et al. [1]; our QMOM predictions (underlined); CFD-PBM predictions (Laakkonen-CFD) by Laakkonen et al. [1] (square brackets); CFD-PBM predictions (Petitti-QMOM) by Petitti et al. [110] (curly brackets), (b) Predicted gas volume fraction along axial and horizontal planes at 390 RPM and $Q = 0.7$ vvm.

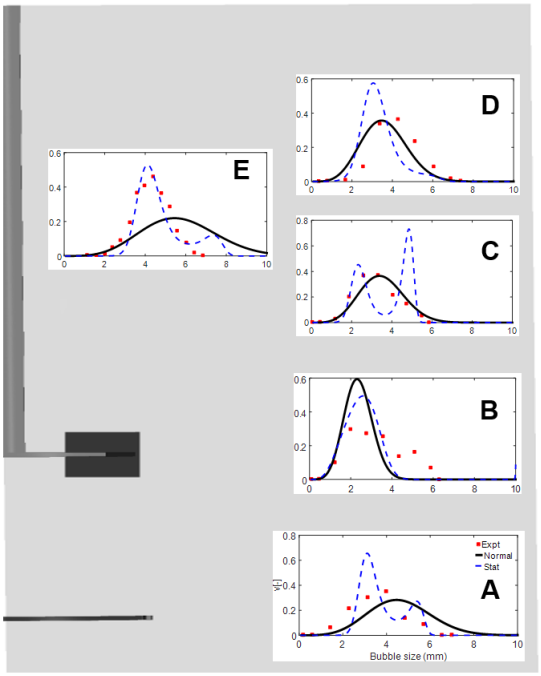

Figure 6.10. Comparison of experimental volumetric bubble size distribution results (squares) against reconstructed bubble size distribution curve using normal distribution shape function (full line) and statistically most likely distribution curve (discontinuous line) at five locations A-E shown in Figure 6.9.

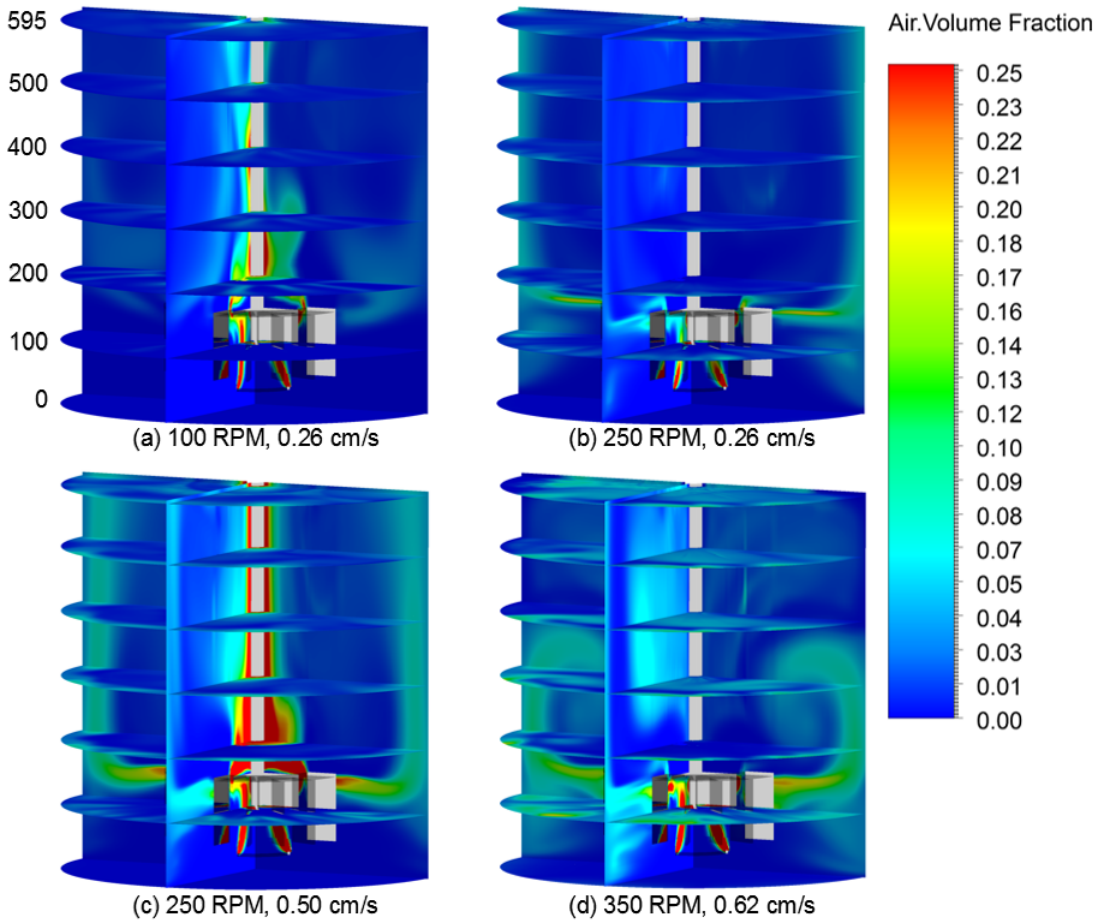

Figure 6.11. Contour plots showing mean volume fraction of gas at different conditions in the flotation cell: (a) $N = 100$ RPM and $J_g = 0.26$ cm/s, (b) $N = 250$ RPM and $J_g = 0.26$ cm/s, (c) $N = 250$ RPM and $J_g = 0.50$ cm/s, (d) $N = 350$ RPM and $J_g = 0.62$ cm/s.

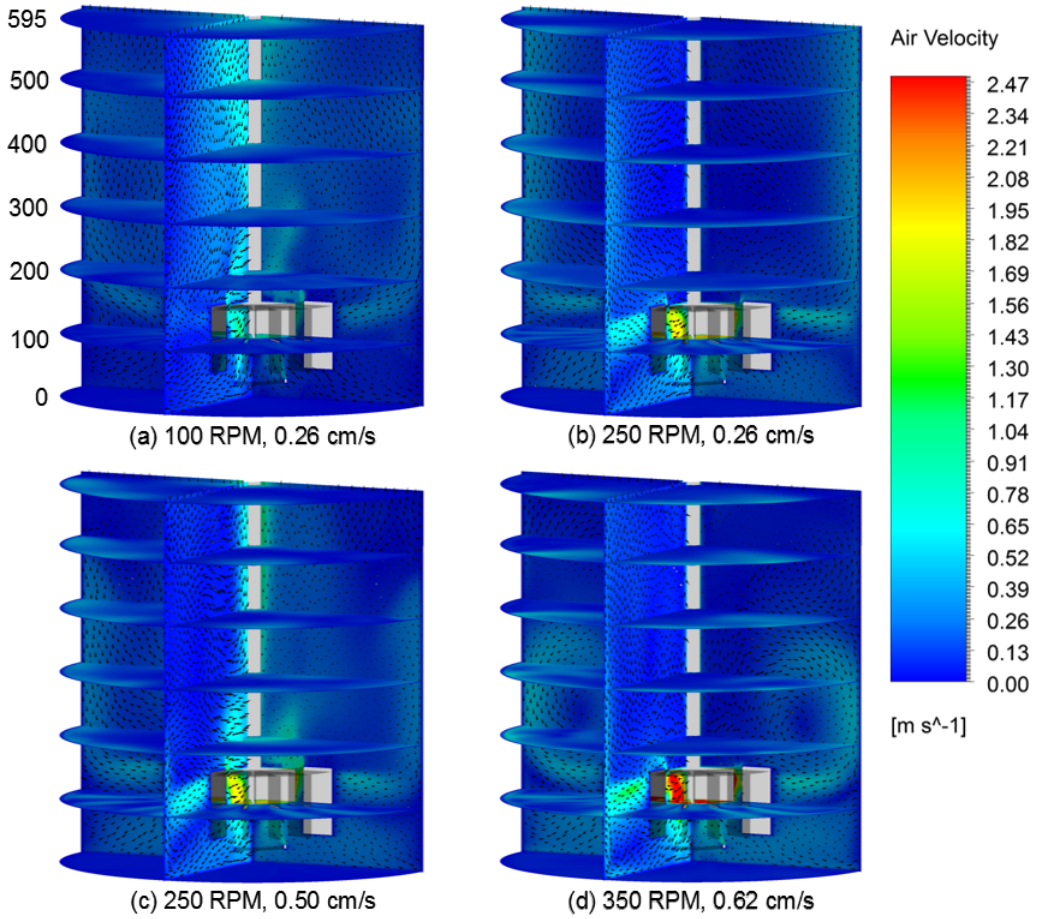

Figure 6.12. Contour plots of mean gas velocities and velocity vectors at four different operating conditions in the cell: (a) $N = 100$ RPM and $J_g = 0.26$ cm/s, (b) $N = 250$ RPM and $J_g = 0.26$ cm/s, (c) $N = 250$ RPM and $J_g = 0.50$ cm/s, (d) $N = 350$ RPM and $J_g = 0.62$ cm/s.

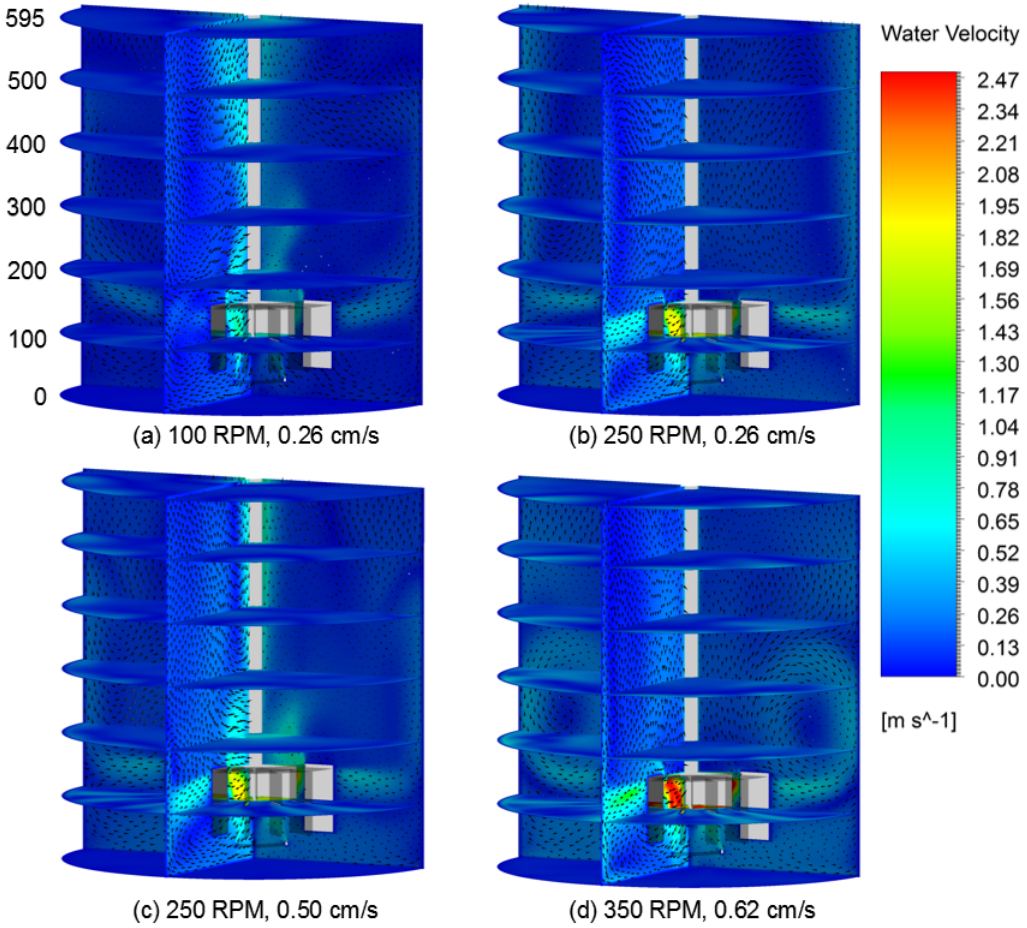

Figure 6.13. Contour plots of mean liquid velocities and velocity vectors at four different operating conditions: (a) $N = 100$ RPM and $J_g = 0.26$ cm/s, (b) $N = 250$ RPM and $J_g = 0.26$ cm/s, (c) $N = 250$ RPM and $J_g = 0.50$ cm/s, (d) $N = 350$ RPM and $J_g = 0.62$ cm/s.

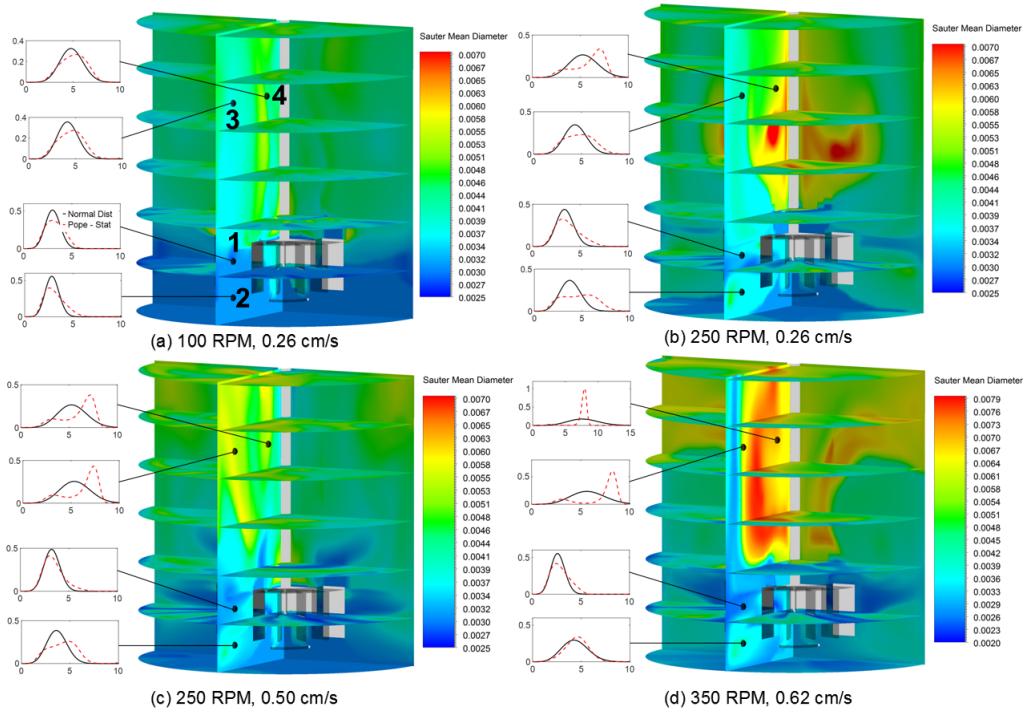

Figure 6.14. The contour plots of SMD (d_{32}) and reconstructed normalized volumetric BSD (continuous line normal distribution; discontinuous line Pope method [144]) at different superficial velocities and impeller rotation speeds: (a) $N = 100$ RPM and $J_g = 0.26$ cm/s, (b) $N = 250$ RPM and $J_g = 0.26$ cm/s, (c) $N = 250$ RPM and $J_g = 0.50$ cm/s, (d) $N = 350$ RPM and $J_g = 0.62$ cm/s. Note: The SMD scale is different for (d) case.

Table 6.1. Details of meshes used in grid convergence study and predicted holdup and diameters at impeller rotation speeds of 300 and 390 RPM and gassing rate of 0.7 vvm.

Mesh Type	Number of Cells	Gas Holdup %				$d_{32}(mm)$		$d_{10}(mm)$	
		Agitation Rate (RPM)							
		300	300	390	390	300	300	390	390
		exp	CFD	exp	CFD	exp	CFD	exp	CFD
Coarse	89,152	4.4	3.50	5.8	3.93	3.64	3.40	2.57	2.12
Medium	205,048	4.4	3.93	5.8	4.43	3.64	3.45	2.57	1.85
Fine	317,258	4.4	**3.97**	5.8	**4.98**	3.64	3.44	2.57	2.05
Fine-2	558,830	4.4	3.80	5.8	4.75	3.64	3.32	2.57	2.47

Table 6.2. CFD predicted power number for different meshes along with power number predictions from correlations. The ratio of gassed to ungassed power consumption obtained from CFD predictions and correlations are also given.

Mesh Type	Number of Cells	$d_{32}(mm)$											
		Agitation Rate (RPM)											
		300			390			300			390		
		CFD	5.32	5.33	CFD	5.32	5.33	CFD	5.32	5.33	CFD	5.32	5.33
Coarse	89,152	3.02	3.24	2.27	2.28	3.01	2.20	0.501	0.538	0.377	0.377	0.496	0.363
Medium	205,048	3.12	3.26	2.28	2.20	3.03	2.21	0.515	0.538	0.377	0.351	0.496	0.363
Fine	317,258	3.19	3.26	2.28	2.34	3.04	2.22	0.527	0.538	0.377	0.383	0.496	0.363
Fine-2	558,830	2.77	3.25	2.28	2.09	3.04	2.21	0.459	0.538	0.377	0.377	0.496	0.363

Table 6.3. Impeller agitation rate, superficial velocity, characteristic dimensionless numbers, overall gas holdup, and regime classification for different flow conditions considered in this work. The highlighted cases have been chosen for further analysis as shown in Figures 6.11 - 6.14.

N (RPM)	J_g (cm/s)	Q_g (m^3/s)	Fl (-)	Fr (-)	N_{pg} (-)	ϵ_g (%)	$Regime$ (-)
100	0.26	0.00073	0.130	0.0425	3.33	1.05	Loading
100	0.39	0.00109	0.195	0.0425	3.06	1.37	Flooding
100	0.52	0.00145	0.259	0.0425	3.18	1.84	Flooding
250	0.26	0.00073	0.052	0.2655	2.60	1.39	Recirculating
250	0.36	0.00102	0.073	0.2655	2.54	1.84	Recirculating
250	0.41	0.00116	0.083	0.2655	2.47	2.40	Recirculating
250	0.50	0.00141	0.101	0.2655	2.52	2.37	Transition
250	0.64	0.00182	0.129	0.2655	2.50	2.70	Transition
250	1.03	0.00292	0.207	0.2655	2.39	3.50	Transition
350	0.62	0.00175	0.089	0.5203	2.20	3.44	Recirculating
350	0.77	0.00219	0.111	0.5203	2.14	3.05	Transition
350	1.03	0.00292	0.148	0.5203	2.06	3.65	Transition
350	1.29	0.00364	0.185	0.5203	1.98	4.15	Loading

CHAPTER 7

A HIGH-ORDER MOMENT-CONSERVING METHOD OF CLASSES (HMMC) BASED POPULATION BALANCE MODEL FOR MECHANICAL FLOTATION CELLS

7.1 Abstract

In this paper, a high-order moment-conserving method of classes (HMMC) based population balance model (PBM) is developed to predict bubble size distribution, number mean and Sauter mean diameters (SMD) in mechanical flotation cells. The population balance model uses vessel averaged turbulence kinetic energy dissipation rate and dispersed phase hold-up as model inputs along with the initial bubble size distribution. Experimental measurements are made in a 0.8 m^3 pilot scale XCELL^{TM} mechanical flotation cell at different aeration rates and impeller tip speeds. All the experimental measurements using MIBC frother are performed at frother dosage value over critical coalescence condition (CCC). Therefore, coalescence process is not considered in the PBM. Nonlinear least squares function *lsqnonlin* and constrained nonlinear multivariable minimization function *fmincon* in optimization toolbox of MATLAB programming language are used to minimize the objective function and estimate corresponding parameters. Three breakage models, namely breakage models proposed by Coulaloglou and Tavlarides [103], Chen et al. [148], and Alopaeus et al.[135], each requiring estimation of adjustable parameters from the experimental data are selected. Moreover, parameter sensitivity studies of selected models are performed and the predictive capability of developed model is demonstrated at operating conditions close to conditions used in model development. Also, 95% confidence intervals for estimated breakage parameters are calculated using a bootstrap based resampling technique. The confidence interval levels are found to be narrow and

the distribution of parameters values is used make both qualitative and quantitative observations about sensitivity of parameters. The developed model is capable of providing acceptable predictions of bubble size distribution, number mean diameter, and SMD for a wide range of operating conditions and has the potential to be developed further for three phase air-water-solid systems and finally integrated into flotation circuits.

7.2 Introduction

Froth flotation is a widely used mineral concentration process which involves selective separation of valuable mineral bearing particles from finely ground ore feed. Flotation exploits chemical and physical behavior of surfaces and gas bubbles to achieve high separation efficiency in equipment that renders itself to continuous processing. Past studies have shown that the valuable particle removal efficiency in mechanical flotation cell is intimately related to bubble sizes generated [2, 149]. Frother, which is a type of surface active agent commonly known as surfactant, is used to aide in the formation of smaller bubbles in the pulp phase and latex stabilize the froth [4, 9]. Due to the addition of frother, bubble coalescence is suppressed leading to generation of smaller bubbles [4, 5, 17]. The reason behind increased breakage and decreased coalescence rates, and the resulting narrow size distribution in the presence of frother is not yet completely understood and only empirical theories have been proposed so far to explain this phenomenon [4, 9]. Finch et al. [9] offered some qualitative evidence on the effect of frother and its concentration on increased breakup rate of bubbles drawing evidence from droplet breakage studies.

Measurements in lab, pilot, and plant scale mechanical flotation cells have been made and reported in the literature over the past two decades [4, 5, 9, 14, 17, 150, 151]. Gorain et al. [150] used a capillary tube suction measurement technique to measure bubble sizes in industrial scale flotation cell using a combination of four impellers at different operating conditions. They reported that both mean bubble size and bubble size distribution vary within the cell. In general, they observed that mean bubble size increases with an increase in air flow rate and decreases with an increase in impeller speed, keeping other conditions constant. Based on their study of bubble size

measurements, Cho and Laskowski[152] were the first to propose the concept of critical coalescence concentration (CCC), which is an empirically determined concentration over which Sauter mean bubble size (D_{32}) does not change noticeably. Grau and Heiskanen [5, 14] developed a new visualization based bubble size measurement technique and used it to study bubble size distribution in lab and pilot scale Outokumpu mechanical flotation cells at different operating conditions and frother dosages. Grau and Laskowski [153] discussed the relative effects of coalescence and breakup processes on measured BSD and provided possible explanations about why a certain family of frothers is efficient in creating smaller bubbles at lower concentrations. The authors believe that an increase in the Marangoni dilational modulus in the presence of even small concentrations of surface active agents at the air-water interface results in the modification of surface elasticity of a bubble, leading to suppression of film rupture between colliding bubbles.

Finch and co-workers [9, 154, 155] have developed empirical theories to shed more light on bubble behavior and relative importance of breakage and coalescence in the presence of frother. Finch et al. [9] have shown that SMD does not change appreciably with impeller speed, thereby rejecting the energy theory in the presence of frother. In this study, authors reported SMD for pilot scale Metso flotation cell at varying concentrations of DF-250 frother between impeller tip speeds of 4.6 to 9 m/s. In a more recent paper, Amini et al. [156] measured vessel averaged turbulence kinetic energy and BSD for 5 and 60 L lab scale flotation cells at different superficial gas velocity (J_g) and impeller tip speeds (v_{tip}) and found that BSD at both scales showed variation with J_g and v_{tip} up to volume averaged turbulence kinetic energy (k) value of 0.18 m^2/s^2, above which no effect on BSD is noticeable, especially for the 60 L cell. However, a number of other experimental studies focusing on bubble size measurements inside mechanical flotation cells of different scales reported continuous decrease in SMD with increasing impeller speeds [4, 5, 150, 157].

There seems to be a divergence in common opinion about the effect of energy input on mean bubble size due to the differences in geometries, physical conditions, chemical conditions, and measurement techniques used by different authors. Since the power consumption in stirred mixing vessels scales directly as the third power of

impeller speed, it is of fundamental importance to achieve better understanding of bubble generation mechanism and the relationship between hydrodynamic conditions and SMD in the flotation cells.

More recently, Jvor et al. [158] studied the validity of CCC at static and dynamic conditions by performing experiments in a specially designed experimental setup. They concluded that the definition of CCC strictly applied to static conditions only when hydrodynamic conditions do not contribute to breakup or coalescence of bubbles. The authors further report that frothers play a key role in the early stages of bubble formation and that both nature and concentration of frother, along with the local hydrodynamic conditions, affect the outcome of bubble collisions, which are precursor events occurring before coalescence. Jvor et al. [159] compared the effect of highly and weakly surface active frothers on the dynamic surface properties of air-water interface to gain further insight into adsorption/desorption properties of frothers. Based on the experimental data, Jvor et al.[159] concluded that strong and weak frothers cause reduction in mean bubble sizes through different mechanisms that control initial bubble formation, breakup, and coalescence. Specifically, they reported that weakly surface active frothers are diffused across air-water interface rapidly and SMD decreases slowly with increasing concentrations of such frothers. On the other hand, highly surface active frothers show slow adsorption/desorption kinetics possibly due to reorientation of molecules, which results in considerable variation in dynamic surface properties leading to creation of a large number of small bubbles even at low concentrations of frother.

Bubble size distribution and SMD are some of the most important input parameters in the flotation kinetic models [151, 160, 161]. Nesset et al.[151] proposed a simple power law model to predict SMD (D_{32}), which consisted of prescribing two fitting parameters that depend on bubble production mechanism, chemistry, and slurry properties. Recently, Nesset et al. [161] proposed a more comprehensive model for predicting D_{32} that takes into account the frother type and concentration for two phase air-water system, which is found to perform well at different conditions based on experimental data taken from 199 tests. The authors also reported good results for three phase solid-gas-liquid systems using the new model. More recently, Kowalczuk

[162] proposed a model to predict CCC value from the information about the chemical structure of the frother. This model is extended to predict SMD for different flotation frothers with good accuracy by using available BSD data from the literature.

Even though these models are constructed from an extensive pool of experimental data generated in different testing campaigns, they still include parameters that need to be empirically determined. A more fundamental approach that takes the effects of physical conditions inside the cell along with pulp/liquid properties to model and analyze microprocesses such as bubble breakup and coalescence is required. Sawyerr et al.[160] were the first to extend the concept of population balances to develop a BSD model for flotation cells by considering both breakage and coalescence processes. Deglon et al. [149] used this model to simulate full BSD in flotation cell under noncoalescing conditions and reported good qualitative match between measurements and predictions. However, the study showed comparison for a single case and was not further developed. The application of population balance framework seems to be underutilized for froth flotation process, though several studies where CFD and coupled computational fluid dynamics - population balance model (CFD-PBM) have been used to study hydrodynamics, BSD, and flotation kinetics are reported in the past [3, 47, 122].

Although much progress has been made over last two decades in understanding the role of frother in flotation systems by performing both macroscale measurements, such as bubble size distribution, SMD, and holdup [4, 9], and micro/nano-scale measurements, such as dynamic surface tension, Marangoni dilational modulus, and adsorption/desorption kinetics [153, 159], using different types of frothers at different concentrations, a concerted effort is lacking that combines the knowledge and development in different areas to develop predictive macroscale models. The objective of this work is to develop a population balance model for gas-liquid flows in mechanical flotation cells that is capable of predicting full bubble size distribution and SMD accurately using hydrodynamic inputs obtained from measurements, such as overall gas holdup, vessel averaged dissipation rate, and viscosity and density of continuous and disperse phases, at frother concentrations over CCC (noncoalescing conditions). The main contributions of this paper are as follows. Development of a

high-order population balance model capable of accurately predicting the bubble size distribution and the moments of the distribution, using which number and Sauter mean diameters can be easily calculated. Experimental bubble size measurements are made in a pilot scale 0.8 m^3 XCELL^{TM} flotation cell and corresponding number frequency distributions are used in the estimation of adjustable parameters found in three breakage models, which are modified to make them applicable to gas-liquid flows. Moreover, an empirical bootstrap technique is used to calculate confidence intervals of the point estimates of parameters found through optimization procedure.

7.3 Population Balance Model

Population balance equation is an integro-partial differential equation that describes the evolution of desired property for a population of particles subjected to different processes that result in creation and disappearance of particles [112]. Analytical solutions of PBE are possible only for very simple cases, which are usually representations of oversimplified physical systems. For complex multiphase flow problems, no closed form solution to governing PBE can be derived and instead numerical solution methodologies are generally applied [112]. In the case of gas-liquid flows in flotation cells, leading mechanisms causing change in the bubble size are breakage and coalescence processes. Since frother concentrations over CCC are used in this study, only breakage process is considered. A PBE describing the rate of change of number density function based on internal coordinate selected as bubble size ($n(L)$), considering only breakage process in a homogeneous system/volume is given as:

$$\frac{d(n(L))}{dt} = \underbrace{\int_L^\infty \beta(L,\lambda)g(\lambda)n(\lambda)d\lambda}_{\text{Birth by breakup}} - \underbrace{g(L)n(L)}_{\text{Death by breakup}} \tag{7.1}$$

The term on the left represents the local rate of change of $n(L)$ in a homogeneous system. The first term on the right represents the birth of new particles as a result of breakup of larger particles, while the second term represents death of particles due to breakage. In Eq.7.1, β describes the daughter size distribution as a result of successful bubble breakup, g describes the breakage rate of bubbles [163].

Since finding an analytical solution of PBE is not possible for complex problems using phenomenological kernels [112, 163], PBE is discretized to ensure that the numerical solution techniques can be applied. The discretization of PBE results in converting the continuous form of $n(L)$ into its discrete counterparts. Similarly, the integrals appearing on right hand side of Eq. 7.1 are replaced by summations with proper limits. The resulting discretized form of PBE transforms into a coupled set of ordinary differential equations. For a size class 'i', the discretized PBE is given by:

$$\frac{dY_i}{dt} = \sum_{j=1}^{NC} \beta(L_i, L_j)\Delta L_i g(L_j) Y_j - g(L_i)Y_i \tag{7.2}$$

where, Y represents the particle number concentration ($1/\mathrm{m}^3$), NC represents the total number of size categories or classes, $\beta(L_i, L_j)$ represents the probability that a bubble of size L_i when a bubble of size L_j breaks ($1/\mathrm{m}$), $g(L_i)$ and $g(L_j)$ represent the breakup rate of bubbles belonging to size category i and j, respectively, and L_i represents the size of category i. The discretized PBE is written and solved in such a way that any event can lead to birth of new particles in any category [163]. This assumption is shown to improve solution stability and accuracy, especially when considering coarse grids in the previous studies [163]. In this work, a high-order method of classes (MC) approach is used to solve the discretized form of PBE due to its robust nature and straightforward implementation. Moreover, MC based solution approach directly solves for the full particle size distribution, which is a desirable feature for many particulate processes including froth flotation, unlike other popular techniques that are based on method of moments (MOM) [163, 164].

When solving PBE using method of classes approach, a grid with a suitable number of categories is created and initial number density is prescribed either from measurements or experience. When new particles are formed either due to breakage or coalescence, the resulting size of a new particle may or may not belong to one of the size categories in the original grid. When such a situation arises, the solution accuracy can be maintained by conserving some important properties of the newly created particle [112, 165]. Kumar and Ramkrishna [165] proposed an efficient framework called fixed pivot (FP) technique to achieve this objective. The FP method is based on redistributing any two moments of the newly formed particle to two nearby size

classes and thus ensuring accuracy of numerical solution. For example, the moments that are chosen to be conserved could be zeroth and third order moments (m_0 and m_3), in which case the resulting particle number and volume will be accurately preserved, when internal coordinate is number density based on particle size (length or diameter). Vanni [166] performed a direct comparison of different MC techniques and found the FP method to be most accurate and robust for a wide range of challenging problems. Alopaeus et al. [163], further generalized the fixed pivot approach such that more than two moments of the newly formed particle can be conserved. This approach has been shown to provide very accurate solutions on relatively coarse grids [163].

7.3.1 High-order Moment Conserving Method of Classes

The main advantage of a high order technique such as HMMC over low order technique such as FP is its ability to predict final particle size distribution with a very high accuracy for all of the conserved moments on a relatively coarse grid. Alopaeus et al. [163] have compared the solutions from HMMC and FP techniques for many problems and demonstrated the advantages of conserving between 4 to 6 moments for breakage and aggregation problems. The k^{th} order moment of a continuous function ($n(L)$) is given by:

$$\mu_k = \int_0^\infty n(L) L^k dL \tag{7.3}$$

The moment definition for discrete function defined only at discrete sizes can be extended as:

$$\mu_k = \sum_{i=1}^{NC} Y_i z_i^k \tag{7.4}$$

By storing the particle sizes at different categories in a vector v, we can rewrite Eq. 7.4 as:

$$\mu_k = \sum_{i=v(1)}^{v(N)} Y_i z_i^k \tag{7.5}$$

where, z_i represents the pivot element (particle size) in this case and N represents number of conserved moments. The pivot elements are dirac delta functions where their magnitude is directly related to the number density at that particle size or pivot. Therefore, the number density for size class or category is described by a single scalar

value. The number density at each size class can be obtained from a continuous number distribution function using the following equation:

$$Y_i = \int_{L_{i-}}^{L_{i+}} n(L)dL \tag{7.6}$$

where, L_{i-} and L_{i+} represent the lower and upper bounds of size class i, respectively.

In a pure breakage process, $\beta(L_i; L_j)$ describes the daughter size distribution of a function and returns the probability that a particle of size L_i is formed when a mother particle of size L_j breaks. In such a breakage process, conservation of moments is established if the moments of continuous and discrete daughter size distributions are equal. The moments of a continuous distribution are given by:

$$\mu_{\beta k} = \int_0^L \beta(L, \lambda)L^k dL \tag{7.7}$$

which can be transformed into a discrete distribution encompassing all categories and written as:

$$\mu_{\beta,k} = \sum_{i=1}^{NC} \beta(L_i, L_j)\Delta L_i z_i^k \tag{7.8}$$

When a particle of size L_j breaks forming a particle of size L_i, the moments of a continuous number density function can be written as:

$$\mu_{\beta ki} = \int_{L_-}^{L_+} \beta(L, \lambda)L^k dL \tag{7.9}$$

The limits in the above equation L_- and L_+ are $L_i - \Delta L_i/2$ and $L_i + \Delta L_i/2$, respectively, when a particle of size i is formed. On a nonuniform grid upper and lower sizes used in the above integral function will be suitably chosen and the HMMC model is designed to work with non-uniform grid as well. Moments are conserved in a breakage process by constructing a β table in such a way that moments of the daughter particles formed due to breakage, belonging to each category or size class, are conserved by distributing the moment contributions evenly to a chosen number of categories and fully preserved. Using the above description, a linear transformation between β and μ can be written as:

$$\mu_{\beta i} = [A](\beta_i(v_i, L_j)\Delta L_v) \tag{7.10}$$

where, $[A]$ is a linear operator that transforms the contribution of breakage from the number distribution space to the moment space [163]; $(v_i, L_j)\Delta L_v$ describes the

contribution of breakage when a particle in j^{th} category breaks leading to creation of a particle in i^{th} category. The array v_i consists of the categories to which moments will be distributed. The $[A]$ matrix can be written as:

$$[A] = (z_{v(n)})^{\omega(i)} \tag{7.11}$$

where, $\omega(i)$ is an array consisting of the moments that are meant to be conserved (e.g. ω =[0, 1, 2, 3] if the first four moments are to be conserved). The elements of β matrix can then be easily calculated using the following matrix inversion procedure:

$$\beta_i(v_i, L_j)\Delta L_v = [A]^{-1}(\mu_{\beta i}) \tag{7.12}$$

A similar approach can be adopted for an agglomerate formed as a result of coalescence process wherein the moments of the agglomerate are conserved by creating a relevant table. For a detailed theory on HMMC approach applicable to breakage and coalescence problems the reader is referred to the original paper by Alopaeus et al. [163].

7.3.2 Breakage Modeling

Breakage of fluid particles can occur due to many mechanisms, such as turbulent fluctuations and collision, viscous shear stress, shearing off, surface instability, and also due to coalescence assisted breakage that leads to the formation of very small bubbles [50, 167]. Recently, Liao and Lucas [50] reviewed many of the widely used breakage rate and daughter size distribution models for different mechanisms listed above. Previous studies have shown that dominant breakage mechanism in stirred tanks and mechanical flotation cells is due to turbulent pressure fluctuations on the surface of fluid particles [1, 50, 109, 149, 160]. The validity of this assumption in the case of mechanical flotation cells is further strengthened by the physical and chemical conditions prevalent in flotation systems. Impeller rotation results in the formation of a region of high turbulence and shearing zone close to impeller. In addition, formation of large bubbles is suppressed due to frother and collector addition [9]. Since the addition of chemical reagents causes surface properties of the air-liquid interface to change significantly, the adjustable parameters appearing in the breakage models need to be re-estimated using bubble size measurements for mechanical flotation cells. In

other words, many breakage models that have been successfully applied for gas-liquid flows in equipment such as bubble columns and stirred tanks, among others, which do not contain fitting parameters, cannot be used here.

The breakage model consists of three parts, namely breakage rate or frequency, number of daughter particles, and daughter size distribution. Breakage rate ($g(L_i)$) gives the number of fluid particles of size L_i breaking per unit time. Daughter size distribution provides the information about the sizes of daughter particles resulting from a successful breakup event. The number of daughter particles in this study is assumed to be two, which has been shown to be a fair approximation from valid from bubble breakage studies in the past [168, 169]. In this work, three breakage rate models are considered, namely Coulaloglou and Tavlarides (CT) model [103], Chen model [148], and Alopaeus model [135], all of which contain fitting parameters.

The breakage rate equation by Coulaloglou and Tavlarides [103], which was further modified for gas-liquid flow based on the recommendation from literature [50, 170], has two adjustable parameters and is given by:

$$g(L) = k_1 L^{-2/3} \frac{\epsilon^{1/3}}{(1+\phi)} exp\left(-\frac{k_2 \sigma (1+\phi)^2}{\rho_c \epsilon^{2/3} L^{5/3}}\right) \tag{7.13}$$

where, k_1 and k_2 are fitting parameters, ϵ is the averaged dissipation rate of turbulence kinetic energy, ϕ is the dispersed phase holdup, σ is the equilibrium surface tension between continuous and discrete phases, and ρ_c is the continuous phase density.

Chen et al. [148] used the breakage rate model by Coulaloglou and Tavlarides[103] as a starting point and modified it in such a way that the resulting breakage rate monotonically increases with fluid particle size and has three fitting parameters. They assumed that the breakage time for droplet is constant, which has been shown to be true for high Weber number cases [169]. Chen breakage rate model with three adjustable parameters (k_1, k_2, and k_3) is given by:

$$g(L) = k_1 exp\left(-\frac{k_2 \sigma (1+\phi)^2}{\rho_c L^{5/3} \epsilon^{2/3}} - \frac{k_3 \mu_d (1+\phi)}{\rho_d L^{4/3} \epsilon^{1/3}}\right) \tag{7.14}$$

where, μ_d is dispersed phase viscosity and ρ_d is the dispersed phase density. It should be pointed out that Chen et al. [148] originally used dispersed phase density (ρ_d) in the denominator of the first term inside exponential. In this study, ρ_c is used instead

of ρ_d resulting in breakage rate having peak value instead of monotonically increasing behavior. More details on the nature of the breakage rate models are given in the later section.

Alopaeus et al. [135] used the breakage rate model proposed by Narsimhan et al. [171], which models the arrival frequency of eddies on fluid particle surface as a Poisson process and modified it to include the effects of dispersed phase viscosity. Laakkonen et al. [1, 118] successfully used this model for gas-liquid flows in stirred vessels and estimated parameters based on a multicompartment population balance model. The breakage rate model has three fitting parameters (k_1, k_2, and k_3) and is given by:

$$g(L) = k_1 \epsilon^{1/3} erfc \left(\sqrt{\frac{k_2 \sigma}{\rho_c \epsilon^{2/3} L^{5/3}} + \frac{k_3 \mu_c}{\sqrt{\rho_c \rho_d} \epsilon^{1/3} L^{4/3}}} \right) \tag{7.15}$$

where, *erfc* represents the complementary error function. Laakkonen et al. [1] suggest that the parameter k_3 should be fixed in the case when experimental data of particle breakage in different continuous phase viscosity values are not available. It should be noted that Alopaeus model does not contain dispersed phase volume fraction (ϕ) in the breakage rate equation unlike CT and Chen models.

For the daughter size distribution (β), a mathematical function with one adjustable parameter (b_1) that was previously used for gas-liquid flows in stirred tanks by Laakkonen et al. [1, 118] is considered. Binary breakage is observed when the value of b_1 is equal to 2.0 [1]. The advantage of using this model is that it allows multibreakage events based on the fitted value of b_1 and it does not involve evaluation of double and triple integrals, which are present in more complex models [1, 50]. The daughter size distribution function giving the probability of formation of a bubble of size L due to breakage of a bubble of size λ is given by:

$$\beta(L, \lambda) = \frac{1}{2}(1 + b_1)(2 + b_1)(3 + b_1)(4 + b_1) \left(\frac{L^2}{\lambda^3} \right) \left(\frac{L^3}{\lambda^3} \right)^2 \left(1 - \frac{L^3}{\lambda^3} \right)^{b_1} \tag{7.16}$$

Based on preliminary simulations, it was found that the parameter b_1 did not change appreciably for the test cases used in this work. Also, due to insufficient evidence of multibreakage events in flotation cells [154, 155], a binary breakage is

assumed in all of the simulations, which results in daughter size distribution of the form:

$$\beta(L,\lambda) = \frac{180L^2}{\lambda^3}\left(\frac{L^3}{\lambda^3}\right)^2\left(1-\frac{L^3}{\lambda^3}\right)^2 \tag{7.17}$$

For the DSD function above, moments can be analytically computed for breakage from size category L_j to L_i using the following equation [163]:

$$\mu_{\beta k}(L_i) = \frac{180}{L_j^9}\left(\frac{L_+^{k+9}-L_-^{k+9}}{k+9} - 2\frac{L_+^{k+12}-L_-^{k+12}}{L_j^3(k+9)} + \frac{L_+^{k+15}-L_-^{k+15}}{L_j^6(k+15)}\right) \tag{7.18}$$

Finch et al. [9] put forward an empirical theory which describes the bubble generation mechanism in flotation cells. Their theory regards bubble generation as a complementary process in which (a) breakage of bubbles is enhanced due to increased air-water interfacial stresses and corresponding surface instabilities due to the adsorbed frother molecules and (b) coalescence is prevented when bubbles with adsorbed frother molecules collide [172]. As recently reported by Jvor et al. [159], weakly surface-active frothers, such as, MIBC are able to quickly adsorb across the air-water interface and assist in the formation of small bubbles by mainly suppressing coalescence between bubbles and possibly by marginally enhancing breakage as discussed below [9].

A schematic (phenomenological) of a turbulent eddy interaction mechanism with a bubble that has non-uniform distribution of frother molecules across the interface is shown in Figure 7.1(a) and (b). Due to non-uniform distribution of the frother molecules at the air-liquid interface, surface instabilities are generated leading to higher local surface stresses [9]. As a result, small bubbles are pinched off when the excess energy needed for breakup is supplied by the turbulent eddy, whose size is smaller than the mother bubble size, leading to formation of new bubbles. These smaller bubbles loaded with the frother molecules do not coalesce since the contact time upon their collision is typically not sufficient to drain the trapped fluid [136, 172, 173]. Strong experimental evidence has been presented recently that supports the notion that frothers play a key role in initial formation of bubbles [159, 174].

7.4 Experimental Methods

In this work, a series of gas dispersion measurements are performed in a 0.8 m^3 pilot-scale XCELL^{TM} flotation cell, which is shown in Figure 7.2(b). The cell is

operated as a batch, two-phase (water/air) reactor in the presence of MIBC frother. To enable measurements of all key gas dispersion parameters, the cell is equipped with a number of sensors, including bubble sampling probe, superficial gas velocity probe, gas holdup probe, power draw meter, and air flow meter. The bubble sampling, superficial gas velocity, and gas holdup probes are all submerged into the quiescent zone of the cell, 10 inches from the pulp-foam interface. A state-of-the-art process control and data acquisition system are developed and deployed to allow continuous collection and analysis of the process data (Figure 7.2(a)). A detailed schematic of the experimental test rig, including information about all sensors and process control equipment used and a snapshot of the flotation cell is shown in Figure 7.2.

The inner diameter (D) of the flotation cell is 1.016 m, inner cell height (H), which corresponds to tank bottom to lip of the launder, is 1.168 m, impeller diameter (d) is 0.254 m ($D/4$), and the impeller height is 0.165 m. During the operation of the cell, the total volume of the gas-liquid mixture remained constant at 0.8 m^3. The Reynolds number (Re) of the flow based on mixture properties varied between 400,000–563,500 for the range of operating conditions used in this work. Two parameters, namely, gas holdup (ϕ) and cell averaged turbulence kinetic energy dissipation rate (ϵ), are used in the HMMC model. The ϵ (W/kg) value for gas-liquid mixture is calculated from the power measurements obtained through variable frequency drive (VFD) including 10–15% transmission losses in the drive, which was confirmed through direct torque measurements on the shaft. For the purpose of this study, standard experimental procedures used for measurement of superficial gas velocity and gas holdup in flotation cells are adopted. The reader is referred to an article by Gomez and Finch [175] for background material and additional details.

In order to collect representative samples of local bubble populations from the quiescent region of the flotation cell, a photographic technique is used. In our work, modified McGill ex-situ bubble sampling method [175], which consists of a sampling tube connected to a closed inclined viewing chamber that is illuminated from the back, is used to sample and record bubble images. This method represents a well-designed solution for bubble sampling from the upper quiescent region of mechanical flotation cells. When the sampling tube is submerged into the flotation cell, the air

is drawn from the chamber by a vacuum pump until the chamber is filled with the pulp. Bubbles are drawn into the viewing chamber from the bulk of the tank due to buoyancy, where they are recorded using a GEViCAM GP-21400 Gigabit Ethernet high-speed CCD camera. For the selected CCD camera, the hardware is set at 23 fps using 1392×1040 pixels with a minimum pixel size of 4.65 μm. To ensure uniform light gradient and improved border definition in recorded images, a bright LED backlight sheet with a light diffuser is installed. The first bubbles entering the chamber are the largest in a population due to their higher rise velocity. For that reason, image acquisition is initiated after the appearance of small bubbles in the chamber. Due to an inclined glass window, bubbles create a monolayer as they rise along the viewing chamber and thus reduce the number of overlapped bubbles in the images. For more information about the bubble sampling and image analysis procedure used in this work, the reader is referred to Miskovic and Luttrell [157].

To investigate and quantify the impact of different operating conditions on the gas dispersion properties of the flotation cell, a wide range of impeller tip speeds, namely 5, 6, and 7 m/s, and air flow rates, 24, 30, and 36 m^3/h, are selected for analysis. The concentration of MIBC frother is kept constant, and a frother dosage of 20 ppm, which is above CCC for this frother, is used to ensure that the system is operating under noncoalescing condition [153]. For each operating condition, all variables are recorded for at least 15 minutes and then averaged. During the experiments, measured gas flow rate is observed to be very stable.

7.5 Results and Discussion

A total of nine conditions were used in the BSD measurements. Three impeller tip speeds, namely 5, 6, and 7 m/s are selected, of which 5 and 7 m/s are used in the parameter estimation procedure. The estimated parameters are then used to study the capability of PBM to predict BSD, D_{10}, and D_{32} at 6 m/s.

The breakage rate profiles predicted by CT, Chen, and Alopaeus models at dispersed phase volume fraction (ϕ) value of 0.075 and vessel average turbulence kinetic energy dissipation rate (ϵ) value of 1 m^2/s^3 against bubble diameter are shown in Figure 7.4. CT and Chen models, shown in Figures 7.4(a) and 7.4(b),

respectively, demonstrate similar trends with both breakage rate profiles rising sharply and predicting a peak at low diameter values. Alopaeus model predicts monotone increasing behavior at low diameter values before flattening out at higher diameters. As indicated earlier, the dispersed phase density in Chen model was replaced with continuous phase density as shown in Eq. 7.14. For the purpose of comparison, the breakage rate predicted by using dispersed phase density is shown as an inset in Figure 7.4(b).

Using density of air (dispersed phase) results in very low breakage rates for bubble diameters upto 20 mm, which is not physical in nature. Therefore, the proposed modification of the Chen model in the context of gas-liquid flows is justified. Also, as will be shown in the next sections, the modified Chen model with three adjustable parameters gives the most accurate predictions. The behavior of DSD function (Eq. 7.16) for different b_1 values is shown in Figure 7.4(d). In this work, the DSD profile corresponding to b_1 value of 2 is used. The experimental data showing the representative image of bubbles and summarizing the important operating flow variables and measurements at different operating conditions are tabulated in Figure 7.3.

7.5.1 HMMC Model Development

Since experimental measurements of bubble size distribution are available for a wide range of impeller tip speeds and aeration rates, different strategies are adopted in the development of population balance model and corresponding parameter estimation procedure. The HMMC model and the optimization procedure are implemented in Matlab programming language. Based on preliminary tests, it is found that the unconstrained nonlinear least squares solver ($lsqnonlin$) converges faster compared to constrained minimization solver ($fmincon$) when estimating breakup kernel parameters for individual cases. Many tests are performed using different breakup models and operating conditions to ensure both solvers converged to very similar global minimum values. The $fmincon$ solver is found to be more accurate than $lsqnonlin$ when using multiple data sets and is therefore used for all the coupled and combined runs, which are explained in the following.

The main objective of this work is to identify the empirical parameters found in the breakage rate models for air-water flow systems in mechanical flotation cells

using weakly active frother (e.g., MIBC) at concentrations well over CCC. Different approaches are adopted to identify these parameters and test their usefulness by comparing overall BSD fit and predicted D_{10} and D_{32} against experimental measurements. Different approaches used in this work are:

- *Individual*: Parameters are estimated by considering each operating condition individually. For example, at impeller tip speed of 5 m/s and flow rate of 24 m^3/h, parameters are estimated for all three breakage rate models. This procedure is repeated for a total of four operating conditions, namely 1, 2, 5, and 6 as shown in Figure 7.3.

- *Common–Speed (CS)*: In this approach, parameters are fitted considering two cases at constant impeller tip speed and different aeration (or air flow) rate. For example, at impeller tip speed of 5 m/s, common parameters are identified considering BSD at flow rates of 24 and 36 m^3/h.

- *Combined*: In this approach, common parameter values are identified considering four different operating conditions, namely at two flow rates of 24 and 36 m^3/h and at two impeller tip speed values of 5 and 7 m/s.

Before the optimization problem is solved, the experimental number frequencies shown in Figure 7.3 are interpolated on a finer numerical grid that is used in HMMC solution, using *interp* function in Matlab. The initial BSD is assumed to be constant for all the cases with mean value of 3 mm and standard deviation of 0.5 mm. Based on preliminary investigations, the HMMC predicted BSD is found to be insensitive to initial BSD. For estimating the adjustable model parameters, operating conditions at two impeller tip speeds of 5 and 7 m/s are used. The model predictive capabilities are tested by using the obtained parameters at 5 and 7 m/s agitation rate, and comparing predictions at 6 m/s against experimental measurements. The HMMC model parameters used for the parameter estimation procedure and other simulations are listed in Table 7.1. Based on initial tests, approximate parameter values are identified and used as initial guesses to reduce the simulation time needed to find

the final optimized parameters. The optimization problem is set up such that the following objective function value is minimized:

$$\Psi = \frac{\sum_{i=1}^{i=NC} [\hat{n}_i(L) - n_i(L)]^2}{\sum_{i=1}^{i=NC} [n_i(L)]^2} \tag{7.19}$$

where, $\hat{n}_i(L)$ and $n_i(L)$ are the HMMC predicted and experimental number frequency values at i^{th} size category, respectively.

The results obtained using *Individual* approach and *lsqnonlin* solver are tabulated in Table. 7.2. Breakage rate parameters are estimated at four operating conditions corresponding to V_{tip} values of 5 and 7 m/s and air flow rates of 24 and 36 m^3/h. New parameters at V_{tip} equal to 6 m/s are evaluated by performing a simple arithmetic average of parameters obtained at V_{tip} equal to 5 and 7 m/s at both flow rates. The corresponding predictions of bubble size distributions along with the experimental measurements, plotted on the same numerical grid used in the HMMC model, are shown in Figure 7.5. An example of BSDs of initial, experimental, and HMMC predictions obtained using different models is shown in Figure 7.5(a). Table. 7.2 shows the experimental and HMMC predicted bubble diameters, objective function (Ψ), which represents the measure of fit between experimental and HMMC bubble size distributions, and the estimated parameters (k_1, k_2, and k_3). For each operating condition, the lowest Ψ value is highlighted in bold in the table to identify the best performing breakage model. By comparing the experimental and HMMC predicted BSD in Figures 7.5(a)-7.5(d) and the diameters in Table. 7.2, it can be reported that the modified Chen model is able to both correctly capture the BSD and predict D_{10} and D_{32} within reasonable accuracy compared to CT and Alopaeus models. However, when the averaged parameters are used to predict BSD and diameters at 6 m/s, Alopaeus model is observed to make the most accurate predictions based on comparison of D_{10} and D_{32} and relative magnitude of Ψ. The modified Chen model predicts low diameter values at 6 m/s and 24 m^3/h but gives better predictions at higher flow rate of 36 m^3/h. It should be noted that, in some cases, a good match between experimental and HMMC prediction of mean diameters is observed, even though the bubble size distributions do not match well. This scenario

can be highlighted by considering the example of the CT model predictions at 6 m/s and 24 m^3/h, where D_{32} match closely while the bubble size distributions do not agree well as shown in Figure 7.5(f) and corresponding Ψ value of 2.91e-01.

As described earlier, parameters are also estimated by considering more than one operating condition and associated BSD. From the preliminary simulations, the $fmincon$ solver is found to be more accurate and faster compared to $lsqnonlin$ solver when the initial parameter guess and the bounds on the parameter space are properly prescribed. The initial parameter guess values are selected based on the final converged values found using the $Individual$ approach. Table 7.3 shows the D_{10}, D_{32}, Ψ, and parameter values (k_1, k_2, and k_3) calculated using *Common-Speed* (CS) approach. Corresponding normalized bubble size distribution profiles are presented in Figure 7.6. Again, the parameter values are estimated at V_{tip} equal to 5 and 7 m/s and used to test their applicability at two different operating conditions at V_{tip} of 6 m/s. Even though a good match between experimental and HMMC predicted BSD is observed for all the cases, the D_{32} values are under-predicted by all three models at higher gas flow rate of 36 m^3/h. At 5 m/s, the CT model is found to make the most accurate prediction. However, there is considerable variability associated with the experimental D_{10} and D_{32} values at air higher flow rate of 36 m^3/h. As pointed out in the earlier section, Alopaeus model does not contain dispersed phase volume fraction (ϕ) in the formula and therefore, the predicted BSD profiles and associated mean diameters do not change appreciably with an increase in air flow rate. At 7 m/s, the Chen model is observed to make the most accurate predictions, which can be supported by the low Ψ in the table. At 6 m/s, where the averaged model parameter values are used in the HMMC model, all the models significantly under-predict D_{32}. At both air flow rates at 6 m/s, all three models fail to correctly capture the shoulder region between 1–2 mm leading to low D_{32} values. The presence of a bimodal type distribution indicates the possibility of either broken bubbles coalescing or some fraction of bubbles not undergoing breakage, both of which could be possible at high aeration rates. If, in fact, a noticeable number of bubbles coalesce after the breakup, then the inclusion of a coalescence model would potentially improve the BSD and associated mean and overall diameter predictions.

Finally, an attempt is made to estimate the parameters by considering four different operating conditions. The results obtained using *Combined* approach is tabulated in Table 7.4 and the resulting BSD profiles are shown in Figure 7.7. At 5 m/s, both CT and Alopaeus models fail to capture the BSD profile correctly leading to over-prediction of both D_{10} and D_{32} values. On the other hand, Chen model is able to capture the trend correctly resulting in acceptable BSD and mean diameters. At 7 m/s, the BSD peak location is under-predicted by all the models, but the overall trend is captured correctly unlike at 5 m/s. The Chen model emerges as the most accurate model when Psi values are compared. However, it under-predicts D_{32} because the HMMC predicted number frequency values are consistently less than experimentally measured values near the shoulder region. Extending the parameter values from *Combined* approach at 6 m/s results in HMMC BSD profiles matching the experimental data noticeably better. Of the three investigated breakage models, the Chen model predicts the BSD most accurately, while the CT model prediction of D_{32} is closest to the experimental data.

7.5.2 HMMC Model Extensibility

To test the usefulness of the HMMC population balance model and the estimated parameters at operating conditions outside the development space, exploratory simulations are carried out and the predictions are compared against measurements. For all three optimization approaches described previously, data at V_{tip} equal to 5 and 7 m/s are used to estimate breakage parameters, which are used to test model predictive capability at 6 m/s. The plots showing the comparison of HMMC predicted and experimental BSD at 6 m/s are shown in Figs. 7.5(e) and 7.5(f), Figs. 7.6(e) and 7.6(f) and Figs. 7.7(e) and 7.7(f) for *Individual*, *Coupled-Speed*, and *Combined* approaches.

In general, all the tested models qualitatively recover the major features of the BSD at 6 m/s. One notable exception is the Chen model at V_{tip} equal to 6 m/s and $Q = 24$ m^3/h, where the predicted BSD differs from the experimental noticeably. Overall, the Alopaeus model performs better than the other two at predicting the peak frequency location correctly. Another important observation is significantly

improved performance of both CT and Alopaeus models at 6 m/s compared to their prediction at 5 m/s when using *Combined* approach. A potential reason behind this observation is that the breakage models are usually more sensitive to dissipation rate (ϵ) so, with increased power input, they are able to correctly capture the physical behavior of breakup of higher fraction of bubbles leading to improved predictions at 6 m/s.

For the three applied parameter estimation approaches, the Coupled-Speed approach is found to be the most suitable procedure to test the applicability of breakup models outside their region of development. This approach takes into account both the effect of dispersed phase volume fraction (ϕ) and energy input (ϵ), at extreme operating conditions (5 and 7 m/s) to predict BSD at intermediate condition (6 m/s).

7.5.3 Breakage Model Comparison

One of the important objectives of this work is to compare the performance of different breakage models applicable to froth flotation. However, it should be noted that a model with the greater number of adjustable parameters (3 for Chen model) will result in better fitting than a model with fewer parameters (2 for CT model) but the parameters are typically more correlated. For the purpose of comparison, parity plots of D_{10} and D_{32}, along with distribution of Ψ at different operating conditions are shown in Figure 7.8. The number averaged bubble diameter (D_{10}) is calculated as the ratio of first and zeroth moments from the predicted BSD. Similarly, Sauter mean diameter (D_{32}) is calculated as the ratio of third and second moments. In the preceding discussion and results, it is shown that the general shape of the experimental BSD is generally well predicted by all three breakup models, with the exception of the Chen model prediction at 6 m/s and 24 m^3/h using *Individual* approach and CT and the Alopaeus model prediction using *Combined* approach at V_{tip} equal to 5 m/s. Since the general shape and peak location of the experimental BSD are well predicted by all three models, the resulting D_{10} are typically accurately predicted as seen from Figs. 7.8(a), 7.8(d), and 7.8(g). As pointed out earlier, Chen model consistently has the lowest Ψ, which is reflected in most of the predicted D_{10} values falling within

the 15% bounds. In contrast, CT model predictions are more dispersed about the diagonal line while the Alopaeus model seems to under-predict D_{10} and D_{32} as the majority of the majority of values are found to lie above the diagonal.

Since the second and third moments are proportional to the area and volume of the bubbles, larger bubbles have a greater influence on their values. As has been highlighted in the preceding section, the experimental BSD is characterized by two smaller peaks near the shoulder of the distribution, which are prominent at 5 and 6 m/s. None of the breakage models can capture these peaks accurately and they all have a tendency to under-predict frequencies at larger diameters due to the optimization algorithm adopted and the inherent structure of the models. By comparing the parity plots of D_{32} in Figure 7.8, it can be seen that CT model predictions are more distributed with most of the predictions lying outside the 15% bounds. The Chen model has some tendency to under-predict both D_{10} and D_{32} for the reasons previously discussed. Finally, Alopaeus model has a strong tendency to under-predict D_{10} and D_{32}, but this trend flattens out at increased aeration and agitation rates leading to lower D_{32} values prediction compared to other two models, which is also followed by a better BSD match especially at large bubble diameters. By comparing the distribution of Ψ for the three breakage models, it could be concluded that the Chen model followed by the Alopaeus model is the most accurate and provides the best fit at most operating conditions compared to the CT model.

7.5.4 Uncertainty in Predicted Parameters

Empirical bootstrap is a statistical technique widely used to estimate the variation of point estimates, which in this case are the parameters of breakage models calculated in the preceding section. The bootstrap technique offers a simple yet robust methodology to estimate confidence intervals on estimated model parameters by repeatedly resampling from the sample population. The empirical bootstrap procedure given in [176, 177] is used to estimate 95% confidence intervals (CIs) for point estimates for breakage model parameters. The basic steps in the empirical bootstrap procedure adopted in our study are as follows:

1. Calculate the HMMC predicted BSD using the parameter values found through

Common–Speed optimization approach.

2. Calculate residuals, $e_i = (Y_i)_{Exp}$ - $(Y_i)_{HMMC}$, at each size category, i, on the numerical grid used. The size of e_i is equal to NC (the number of size categories used in the PBM model).

3. Generate a new set of residuals (e_i^*) of length NC from the original residuals array (e_i) by applying resample with replacement approach.

4. Create a new independent bootstrap (replicate experiment) data set by adding the residuals calculated in the previous step to HMMC predicted BSD from the first step, $(Y_i)^*_{boot} = (Y_i)_{HMMC} + e_i^*$.

5. Using the *Common–Speed* optimization approach, calculate and store new breakage model parameters for bootstrap data set.

6. Repeat steps 3–5 500 times and store all the bootstrap generated breakage model parameters.

7. Calculate 95% CIs by computing the 97.5^{th} and 2.5^{th} percentile values a set of 500 bootstrap parameters.

The CIs are estimated only for parameters obtained using *Common–Speed* optimization approach since *Common–Speed* is found to be the most appropriate approach for developing flotation cell population balance model. However, the same procedure can be applied to calculate CIs for breakage parameters estimated using *Individual* and *Combined* approaches as well. The scatter plots showing the distribution of 500 parameters calculated using bootstrap technique for all three breakage models at V_{tip} equal to 5 m/s are shown in Figure 7.9. The location of the breakage parameters obtained using *fmincon* solver, and previously reported in Table 7.3, is also shown in the scatter plots (Calculated Parameter). The scatter plots are useful in qualitatively understanding the relative importance and sensitivity of breakage model parameters [178]. The 95% CIs for all three breakage models at V_{tip} equal to 5 and 7 m/s are shown in Table 7.5. It is found that the majority of calculated bootstrap parameters lie within approximately 1.5% about the reported point parameter estimates in Table 7.3.

For the CT model, the calculated 95% CIs are within 0.2% for both the parameters across two V_{tip} values, similarly, for the Alopaeus model, the 95% CIs are within 0.3% of the point estimates. For the Chen model, the 95% CIs are within 1.5% of the point estimates reported in Table. 7.4. Narrow CIs for all three models indicate a high confidence in the estimated parameter values and also suggest that 500 bootstrap samples represent a sufficiently large number of samples.

7.5.5 Discussion and Future Work

While it has been widely accepted that frothers cause reduction in bubble diameters in froth flotation systems, there are no fundamental theories explaining the formation of smaller bubbles in their presence. Finch et al. [9] proposed an empirical theory wherein both breakage and coalescence processes act as paired events to ensure the generation of smaller bubbles in the system. In their most recent work, Jvor et al. [158, 159] have shown that adsorption and desorption rates of different frothers vary significantly, and that each frother acts through a different mechanism to produce a narrow BSD. The presence of smaller peaks near the shoulder region of the BSD at V_{tip} equal to 5 and 6 m/s points to two possibilities. First, the turbulence level at these impeller speeds and corresponding gas holdup rates might be insufficient to cause breakage of all the bubbles in the impeller zone. Since the frother used in the current study is MIBC, which is a weakly surface active frother, the frother molecules are expected to adsorb across the air-water interface quickly when frother is uniformly mixed and its concentration is sufficiently high [159]. Secondly, it is possible that frother molecules could detach/desorb from the air-water interface locally due to various hydrodynamic effects such as interaction with turbulent eddy, viscous and turbulent shear, etc. If such conditions are to persist or occur in the mechanical flotation cell, then coalescence between bubbles is possible even when bulk frother concentrations are over CCC.

Maindarkar et al. [179] have recently shown that incorporating a coalescence model improves the prediction for liquid-liquid systems in the presence of surfactants for high pressure homogenization process. It is expected that including a suitable phenomenological coalescence model, which has adjustable parameters that could be

estimated from available experimental data, could improve the predictions of D_{32} and BSD. Since the impeller motion in flotation creates a region of high shear, it is possible that including turbulent shear induced breakage kernel along with the kernel developed for turbulence pressure fluctuation mechanism could lead to further improved predictions. Raikar et al. [180] developed an improved breakage model by considering turbulent shear induced breakage for relatively larger sized droplets and used it for liquid-liquid dispersion droplet size distribution prediction and reported a good match. However, care must be taken against over fitting, and relationship between breakage and coalescence parameters must be studied before developing a comprehensive population balance model for flotation cell. Finally, experiments must be carefully designed to gain further insights into breakage events in the flotation cell at different concentration of frothers.

7.6 Conclusions

The present work develops a mathematical model capable of predicting BSD and bubble diameters from moments of the predicted BSD for mechanical flotation cells. The model uses hydrodynamic operating conditions, namely cell averaged turbulence kinetic energy dissipation rate, dispersed phase holdup, and initial bubble size distribution, as inputs. The experimental bubble size measurements used to estimate the adjustable parameters in the model are performed in a 0.8 m^3 pilot scale XCELL^{TM} flotation cell. The concentration of frother (MIBC) is fixed at 20 ppm in all the experiments. A modified McGill ex-situ bubble sampling method is used to sample the bubbles from quiescent region of the cell. The BSD data at operating conditions corresponding to impeller speeds of 5, 6, and 7 m/s and air flow rates of 24 and 36 m^3/h are considered for population balance model development.

Since the frother dosage is over CCC, coalescence process is ignored and the population balance equation is solved directly by discretizing the number density function. A high-order moment-conserving method of classes (HMMC) approach was proposed by Alopaeus et al. [163] is used to solve the discretized PBE. Three breakage rate models, which require nonlinear estimation of adjustable parameters, are used in this study. Some breakage rate model modifications were necessary so are

suitably made to CT and Chen breakage rate models as suggested in the literature and from our preliminary results. Nonlinear optimization solvers, namely $lsqnonlin$ and $fmincon$, available in Matlab programming language, are used for estimating the parameters by formulating a suitable minimization or cost function. Three different approaches are used to calculate the paramaters, namely $Individual$, *Coupled–Speed*, and *Combined*. When $Individual$ approach is used, an appreciably good match between experimental and HMMC predicted BSD and diameters is observed for all three breakage models. All the models predict the shape of BSD accurately, though frequencies of the larger bubble sizes are almost always slightly under-predicted. Similar observations are made when using *Coupled–Speed* approach, especially at impeller speed of 5 m/s and air flow rate of 36 m^3/h; the turbulence level in the cell at those conditions could be insufficient to cause breakage of larger bubbles leading to formation of a smaller peak near the shoulder of the distribution. Accurate prediction of the BSD peak and its general shape by HMMC results in D_{10} values matching for all three models at majority of the operating conditions. The under-prediction of frequencies by CT and Alopaeus models when using $Individual$ and *Coupled–Speed* approaches, results in under-prediction of D_{32}, even though the BSDs match fairly well. In general, large deviations are observed between experimental data and HMMC predictions when using *Combined* approach, which is not recommended for flotation cells.

Based on the calculation of Ψ values, the Chen model with three adjustable parameters provides the best match between experimental and HMMC predicted BSDs across all three optimization approaches for all experimental conditions used in the model development. When averaged parameters are used to test the model extensibility at impeller speed of 6 m/s, it is found that the Chen model has a tendency to under-predict BSD peak location and frequencies of larger bubble diameters slightly, leading to under-prediction of D_{32}. The Alopaeus model, on the other hand, gave generally good predictions of diameters at 6 m/s across all three approaches. It is expected that a better initial estimate of the fixed parameter (k_3) could additionally improve the overall the overall prediction accuracy. To estimate the variability of point estimates of breakage model parameters, 95% confidence intervals are calculated

using bootstrap technique for *Coupled–Speed* approach. Based on the calculated CIs it is shown that estimated parameters are calculated with very high confidence. The model shown here can be improved by including a suitable coalescence model, which could improve the prediction of the BSD behavior at larger bubble sizes. The proposed predictive model can be easily extended to three phase gas-solid-liquid flows and eventually used as a nonlinear model predictive control platform for flotation units and circuits in the future.

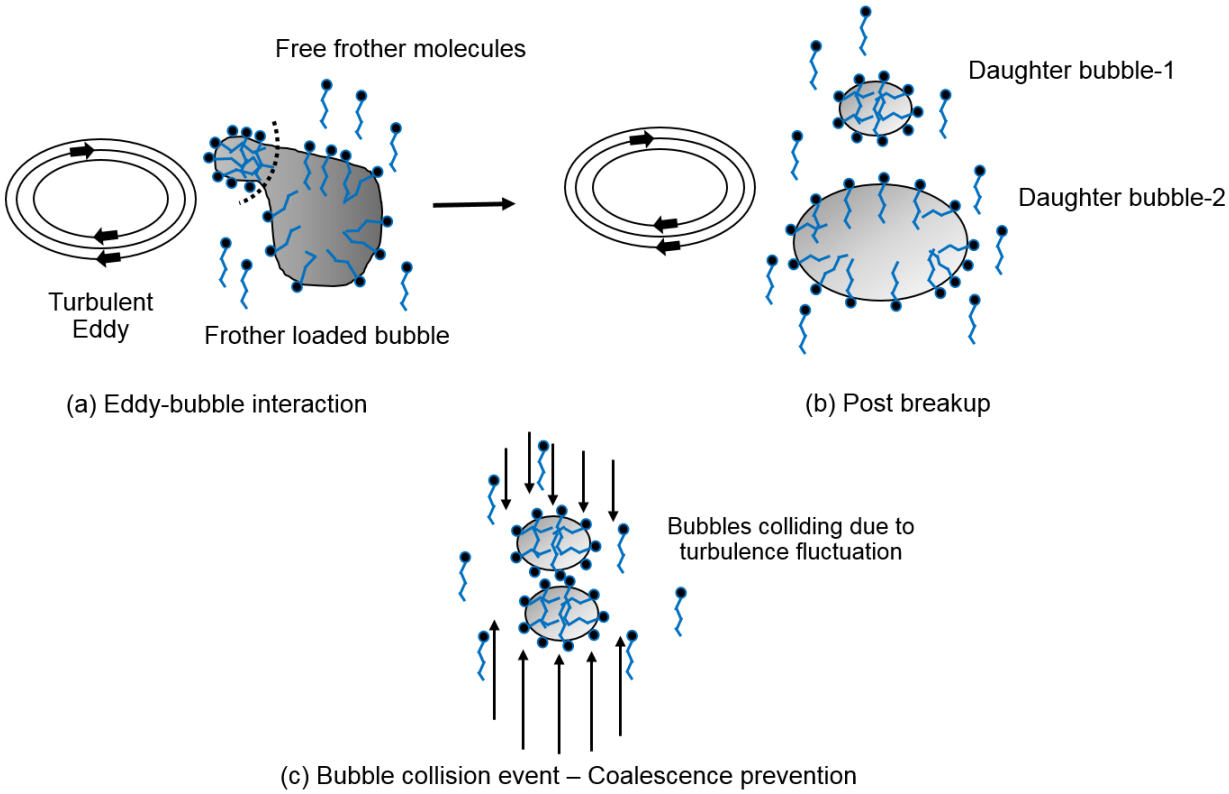

Figure 7.1. Schematic showing (a) A successful breakup event when a turbulent eddy interacts with an air bubble that has slightly non-uniform distribution of frother molecules on its surface. The turbulent eddy supplies kinetic energy that is used in the creation of excess surface during the breakup process, (b) Successful breakup of mother bubble into two bubbles of unequal sizes, and (c) two bubbles interacting in turbulent flow but not coalescing due to increase in drainage time when frother molecules are adsorbed along the air-water interface.

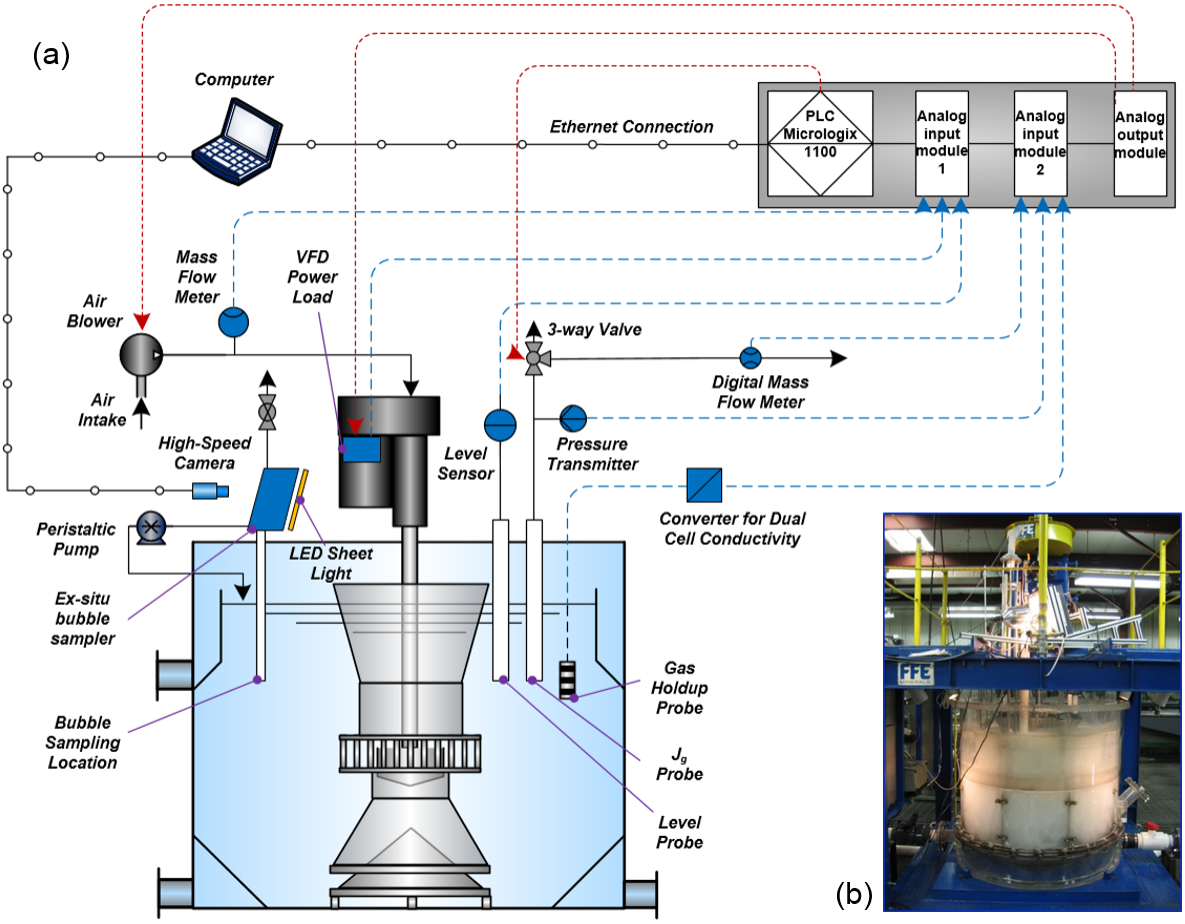

Figure 7.2. Schematic and snapshot of the pilot scale flotation cell (a) Schematic of the experimental rig used for gas dispersion measurements in 0.8 m^3 XCELL^{TM} flotation cell along with data acquistion system (b) Snapshot of 0.8 m^3 pilot scale flotation cell in use.

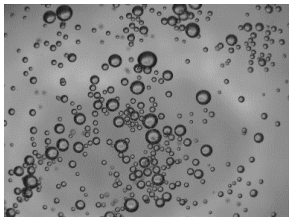 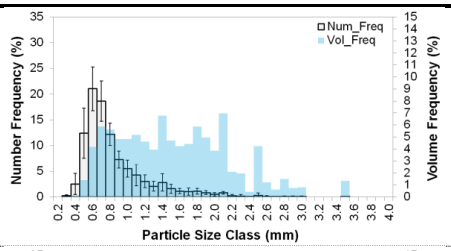	**1**	V_{tip} (m/s)	5
		Q (m^3/h)	24
		J_g (cm/s)	0.935
		ϕ (%)	5.345
		ϵ (W/kg)	0.721
		D_{10} (mm)	0.819
		D_{32} (mm)	1.281
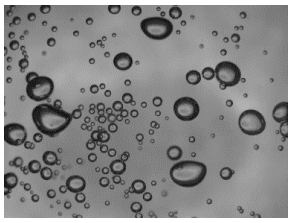 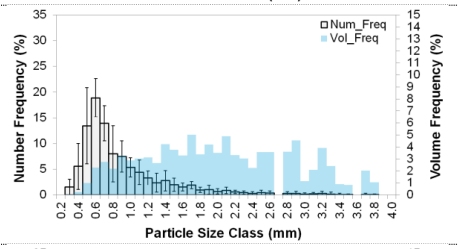	**2**	V_{tip} (m/s)	5
		Q (m^3/h)	36
		J_g (cm/s)	1.209
		ϕ (%)	6.679
		ϵ (W/kg)	0.701
		D_{10} (mm)	0.877
		D_{32} (mm)	1.681
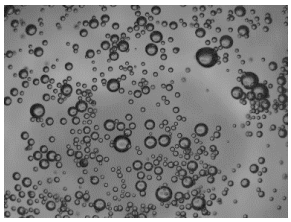 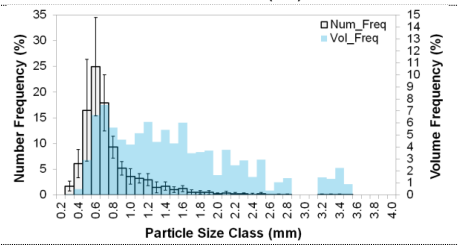	**3**	V_{tip} (m/s)	**6**
		Q (m^3/h)	**24**
		J_g (cm/s)	**1.211**
		ϕ (%)	**8.305**
		ϵ (W/kg)	**1.629**
		D_{10} (mm)	**0.733**
		D_{32} (mm)	**1.210**
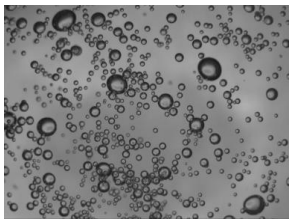 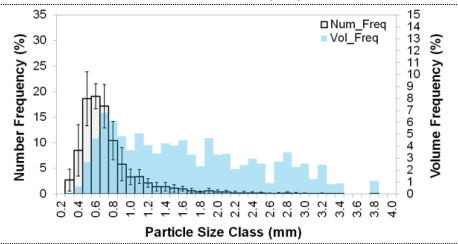	**4**	V_{tip} (m/s)	**6**
		Q (m^3/h)	**36**
		J_g (cm/s)	**1.632**
		ϕ (%)	**10.376**
		ϵ (W/kg)	**1.593**
		D_{10} (mm)	**0.731**
		D_{32} (mm)	**1.251**
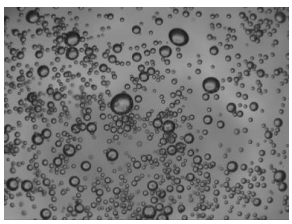 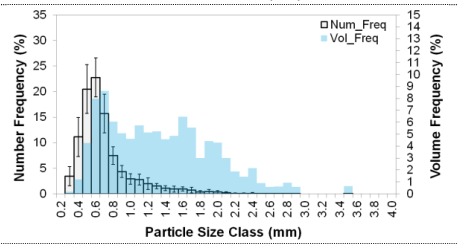	**5**	V_{tip} (m/s)	7
		Q (m^3/h)	24
		J_g (cm/s)	1.194
		ϕ (%)	9.067
		ϵ (W/kg)	2.684
		D_{10} (mm)	0.671
		D_{32} (mm)	1.055
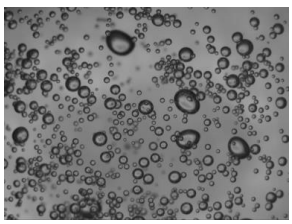 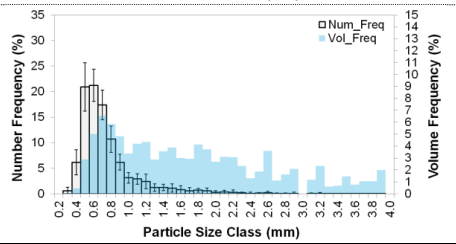	**6**	V_{tip} (m/s)	7
		Q (m^3/h)	36
		J_g (cm/s)	1.694
		ϕ (%)	11.185
		ϵ (W/kg)	2.623
		D_{10} (mm)	0.733
		D_{32} (mm)	1.318

Figure 7.3. Figure showing the representative image of bubbles, number and volume density histograms with standard deviation for number density, and operating conditions along with mean.

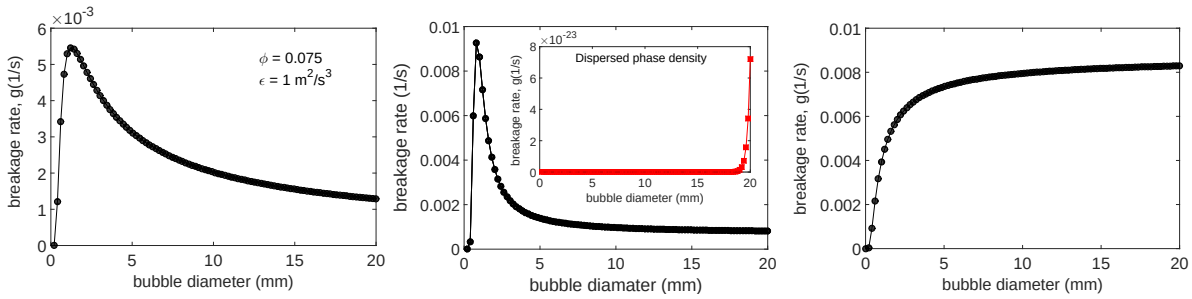

(a) CT model

(b) Chen model

(c) Alopaeus model

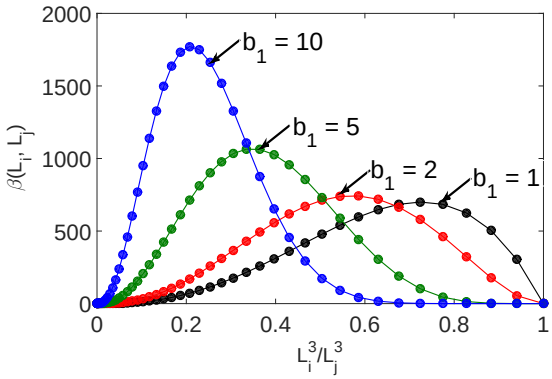

(d) Daughter size distribution profiles

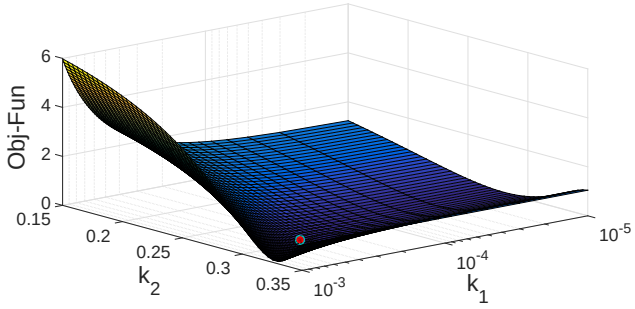

(e) Objective function for different parameter values

Figure 7.4. Details of breakage models and optimization procedure (a)–(c) Plots of breakage rates predicted by different models used in this work at dispersed phase volume fraction (ϕ) value of 0.075 and turbulence kinetic energy dissipation rate (ϵ) value of 1 m^2/s^3, (d) daughter size distribution profile for different values of adjustable parameter, and (e) objective function contour plot at different values of CT breakup model parameters showing the global minimum.

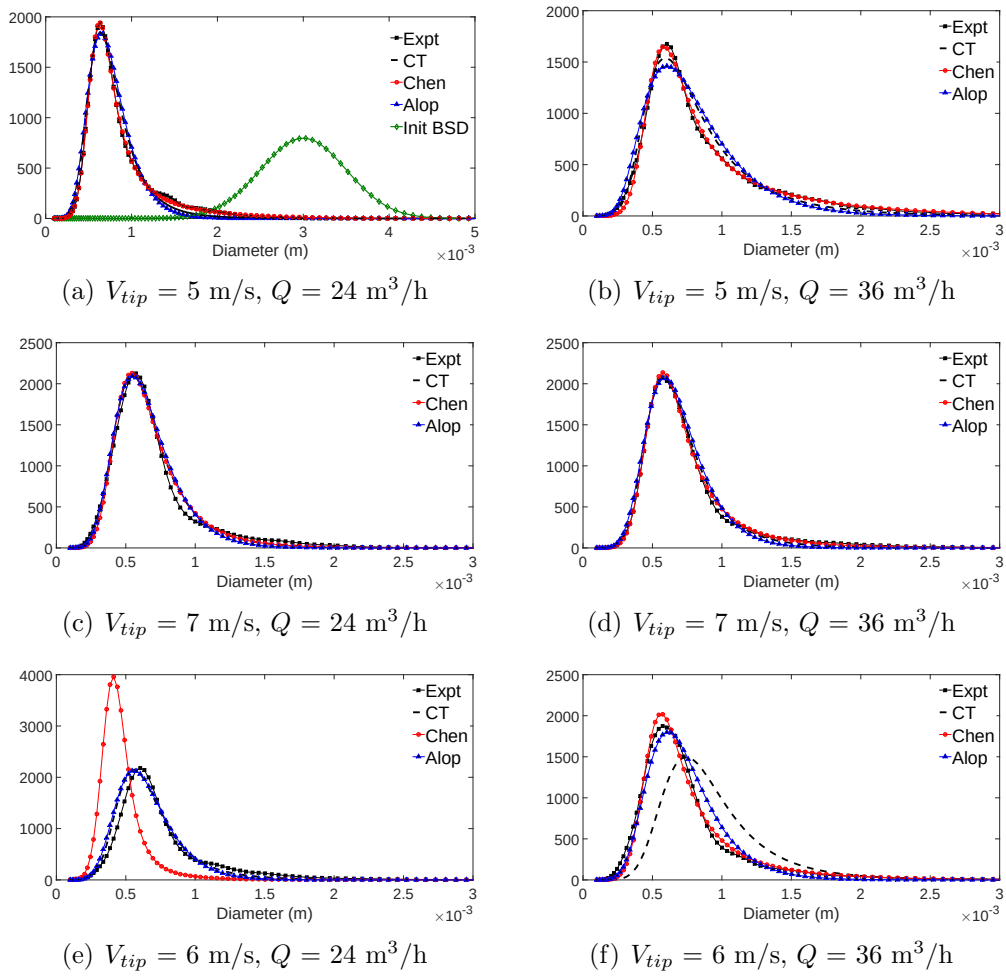

(a) $V_{tip} = 5$ m/s, $Q = 24$ m^3/h

(b) $V_{tip} = 5$ m/s, $Q = 36$ m^3/h

(c) $V_{tip} = 7$ m/s, $Q = 24$ m^3/h

(d) $V_{tip} = 7$ m/s, $Q = 36$ m^3/h

(e) $V_{tip} = 6$ m/s, $Q = 24$ m^3/h

(f) $V_{tip} = 6$ m/s, $Q = 36$ m^3/h

Figure 7.5. Comparison of normalized number frequencies (Y-axis) of experimental measurements (squares) against HMMC predictions using different models, namely *CT* (discontinuous line), Chen (circles), and Alopaeus (triangles), at different operating conditions. The BSD plots at $V_{tip} = 6$ m/s are generated using averaged breakage kernel parameters obtained at $V_{tip} = 5$ m/s and 7 m/s. All the plots are generated using *Individual* optimization approach. Initial BSD is shown in 7.5(a) alone (diamonds).

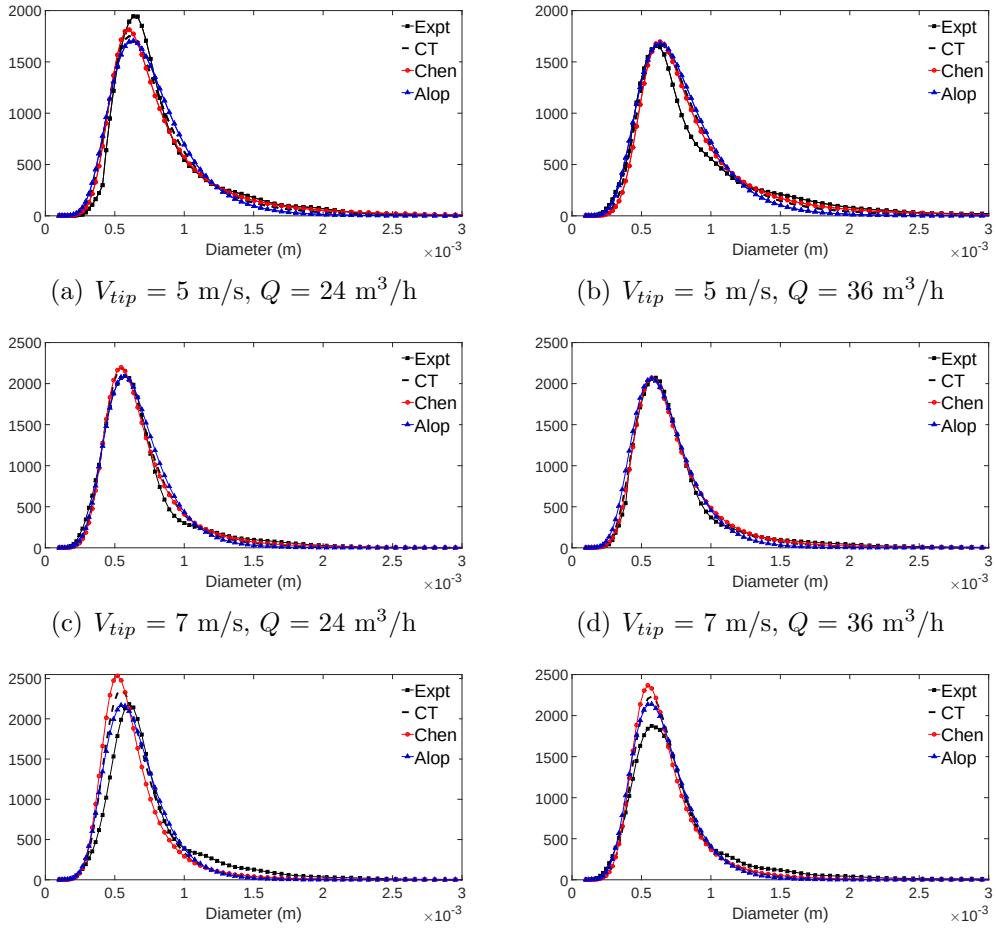

(a) $V_{tip} = 5$ m/s, $Q = 24$ m^3/h

(b) $V_{tip} = 5$ m/s, $Q = 36$ m^3/h

(c) $V_{tip} = 7$ m/s, $Q = 24$ m^3/h

(d) $V_{tip} = 7$ m/s, $Q = 36$ m^3/h

(e) $V_{tip} = 6$ m/s, $Q = 24$ m^3/h

(f) $V_{tip} = 6$ m/s, $Q = 36$ m^3/h

Figure 7.6. Comparison of normalized number frequencies (Y-axis) of experimental measurements (squares) against HMMC predictions at different operating conditions using *Common–Speed* optimization approach. The BSD plots at $V_{tip} = 6$ m/s are generated using averaged breakage kernel parameters obtained at $V_{tip} = 5$ m/s and 7 m/s.

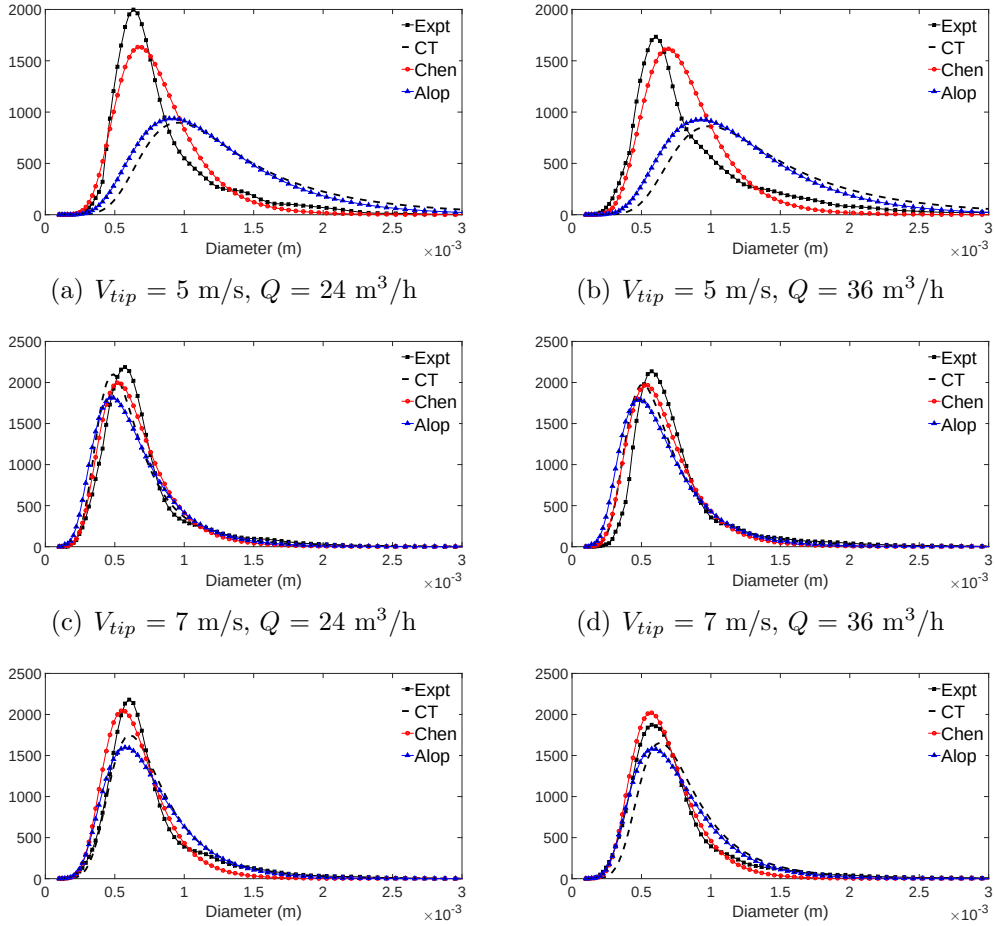

(a) $V_{tip} = 5$ m/s, $Q = 24$ m^3/h

(b) $V_{tip} = 5$ m/s, $Q = 36$ m^3/h

(c) $V_{tip} = 7$ m/s, $Q = 24$ m^3/h

(d) $V_{tip} = 7$ m/s, $Q = 36$ m^3/h

(e) $V_{tip} = 6$ m/s, $Q = 24$ m^3/h

(f) $V_{tip} = 6$ m/s, $Q = 36$ m^3/h

Figure 7.7. Comparison of normalized number frequencies (Y-axis) of experimental measurements (squares) against HMMC predictions obtained using *Combined* optimization approach, where the data at $V_{tip} = 5$ m/s and 7 m/s are used. The BSD plots at $V_{tip} = 6$ m/s are generated using breakage kernel parameters obtained using *Combined* optimization approach.

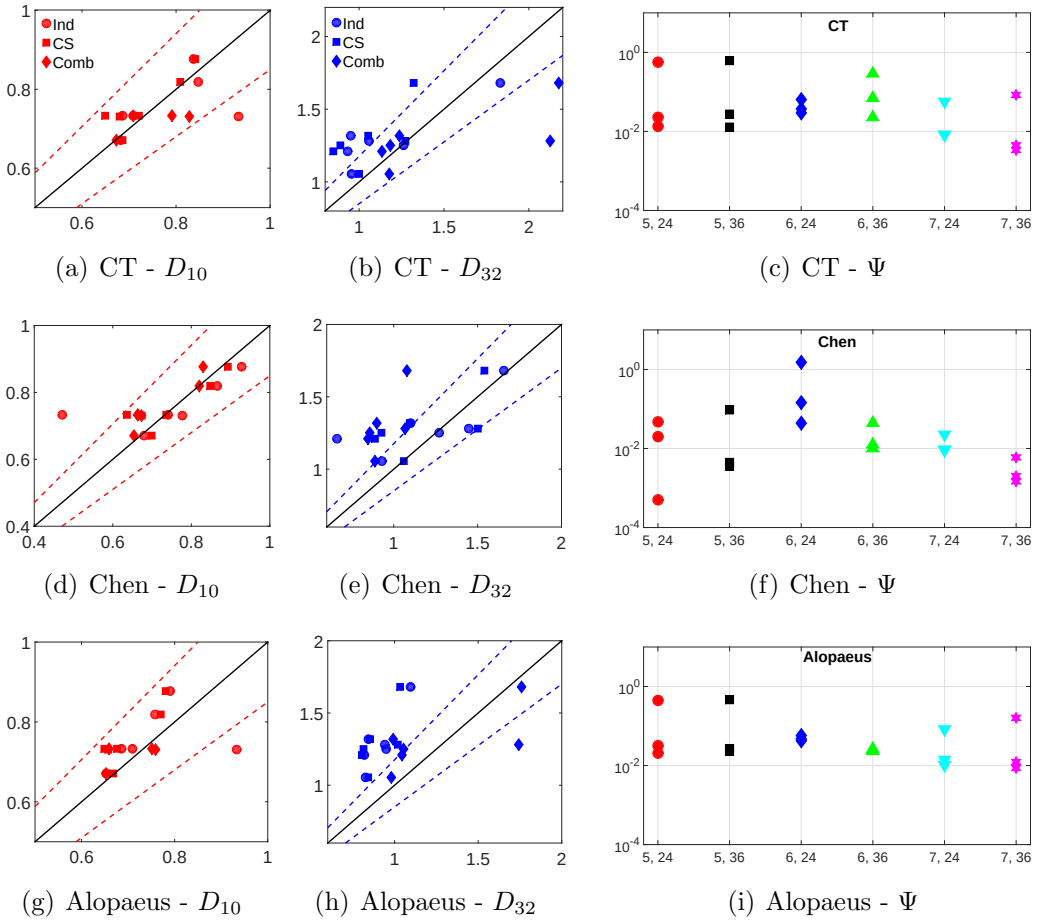

(a) CT - D_{10} (b) CT - D_{32} (c) CT - Ψ

(d) Chen - D_{10} (e) Chen - D_{32} (f) Chen - Ψ

(g) Alopaeus - D_{10} (h) Alopaeus - D_{32} (i) Alopaeus - Ψ

Figure 7.8. Parity plots for number averaged bubble diameter (D_{10}) and Sauter mean bubble diameter (D_{32}) predicted by different breakup models. The units of X and Y axis for parity plots are in mm. Discontinuous line represents the upper and lower 15% value about the mean. Objective function values (Ψ) at different operating conditions for all three breakup models are shown in Figure 7.8(c), 7.8(f), and 7.8(i) where the X axis represents different operating conditions (e.g. 5, 24 represents V_{tip} = 5 m/s and Q = 24 m^3/h) and Y axis represents the Ψ value.

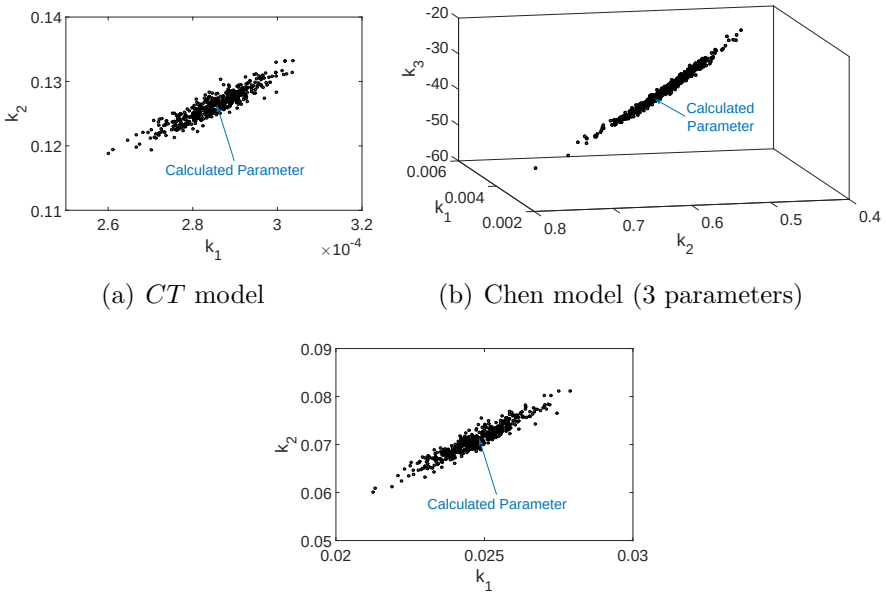

(a) *CT* model

(b) Chen model (3 parameters)

(c) Alopaeus model

Figure 7.9. Scatter plot of parameter values obtained from bootstrap simulation for different breakage models.

Table 7.1. HMMC model parameters used for optimization and model prediction.

Parameter	Value
Number of categories (NC)	100
Integration time (t)	600 seconds
Number of moments conserved (nmom)	4
Discretization parameter (idisc)	1.02

Table 7.2. PBM prediction versus experimental measurements of number mean and Sauter mean diameters using *Individual* optimization approach. All the parameters are estimated using *lsqnonlin* solver. The parameter values for two operating conditions at $V_{tip} = 6$ m/s are obtained by averaging optimized parameter values at V_{tip} values of 5 and 7 m/s. For Alopaeus model, k_3 is not fitted but fixed (*) based on recommendations from Laakkonen et al. [1].

Model	V_{tip} (m/s)	Q (m^3/h)	Experimental (mm)		HMMC (mm)		Ψ	Parameter value		
			D_{10}	D_{32}	D_{10}	D_{32}		k_1	k_2	k_3
CT					0.847	1.058	1.34e-02	2.756e-04	1.415e-01	–
Chen	5	24	0.819±0.044	1.281±0.096	0.866	1.447	**5.03e-04**	1.410e-03	1.042e+00	-6.806e+01
Alopaeus					0.758	0.942	2.04e-02	2.659e-02	8.746e-02	0.01*
CT					0.837	1.832	1.29e-02	1.780e-04	9.269e-02	–
Chen	5	36	0.877±0.082	1.681±0.265	0.928	1.656	**3.52e-03**	1.460e-03	7.338e-01	-5.071e+01
Alopaeus					0.790	1.096	2.70e-02	1.560e-02	4.551e-02	0.01*
CT					0.682	0.955	**8.20e-03**	1.795e-04	2.441e-01	–
Chen	**7**	24	0.671±0.048	1.055±0.060	0.680	0.930	9.06e-03	9.242e-03	5.406e-01	-1.861e+01
Alopaeus					0.653	0.827	1.03e-02	1.729e-02	1.541e-01	0.01*
CT					0.709	0.951	3.40e-03	2.038e-04	2.711e-01	–
Chen	**7**	36	0.733±0.054	1.318±0.157	0.741	1.100	**1.47e-03**	4.050e-03	1.239e+00	-5.339e+01
Alopaeus					0.685	0.844	8.72e-03	1.949e-02	1.900e-01	0.01*
CT					0.686	0.932	**2.94e-02**	2.276e-04	1.928e-01	–
Chen	**6**	24	0.733±0.048	1.210±0.197	0.471	0.662	1.51e+00	5.326e-03	7.913e-01	-4.334e+01
Alopaeus					0.655	0.818	4.23e-02	2.194e-02	1.208e-01	0.01
CT					0.933	1.262	2.91e-01	1.909e-04	2.576e-01	–
Chen	**6**	36	0.731±0.051	1.251±0.144	0.777	1.270	**1.01e-02**	2.755e-03	9.864e-01	-5.205e+01
Alopaeus					0.739	0.949	2.40e-02	1.755e-02	1.178e-01	0.01

Table 7.3. PBM prediction versus experimental measurements of number mean and Sauter mean diameters using *Common-Speed* optimization approach. All the parameters are estimated using $fmincon$ solver. The parameter values at $V_{tip} = 6$ m/s are obtained by averaging optimized parameter values obtained at V_{tip} values of 5 and 7 m/s.

Model	V_{tip} (m/s)	Q (m^3/h)	Experimental (mm)		HMMC (mm)		Ψ	Parameter value		
			D_{10}	D_{32}	D_{10}	D_{32}		k_1	k_2	k_3
CT	5	24	0.819±0.044	1.281±0.096	0.809	1.273	2.30e-02	2.849e-04	1.263e-01	–
		36	0.877±0.082	1.681±0.265	0.841	1.322	2.74e-02			
Chen		24	0.819±0.044	1.281±0.096	0.848	1.501	**1.99e-02**	4.291e-03	5.783e-01	-3.595e+01
		36	0.877±0.082	1.681±0.265	0.893	1.540	**2.84e-02**			
Alopaeus		24	0.819±0.044	1.281±0.096	0.770	1.019	3.18e-02	2.472e-02	7.114e-02	0.01*
		36	0.877±0.082	1.681±0.265	0.781	1.033	3.82e-02			
CT	7	24	0.671±0.048	1.055±0.060	0.686	1.000	8.46e-03	2.409e-04	2.742e-01	–
		36	0.733±0.054	1.318±0.157	0.721	1.054	4.47e-03			
Chen		24	0.671±0.048	1.055±0.060	0.699	1.059	**9.42e-03**	8.316e-03	8.469e-01	-3.297e+01
		36	0.733±0.054	1.318±0.157	0.736	1.096	**1.98e-03**			
Alopaeus		24	0.671±0.048	1.055±0.060	0.668	0.842	1.40e-02	2.091e-02	1.767e-01	0.01*
		36	0.733±0.054	1.318±0.157	0.676	0.853	1.22e-02			
CT	**6**	24	0.733±0.048	1.210±0.197	0.649	0.848	6.44e-02	2.633e- 04	2.003e-01	–
		36	0.731±0.051	1.251±0.144	0.680	0.890	2.29e-02			
Chen		24	0.733±0.048	1.210±0.197	0.636	0.887	1.44e-01	6.337e-03	7.061e- 01	-3.420e+01
		36	0.731±0.051	1.251±0.144	0.674	0.927	4.42e-02			
Alopaeus		24	0.733±0.048	1.210±0.197	0.649	0.805	**4.69e-02**	2.287e-02	1.239e-01	0.01
		36	0.731±0.051	1.251±0.144	0.657	0.814	**2.31e-02**			

Table 7.4. PBM prediction versus experimental measurements of number mean and Sauter mean diameters using *Combined* optimization approach. All the parameters are estimated using *fmincon* solver. The parameter values at V_{tip} = 6 m/s are obtained by averaging optimized parameter values obtained at V_{tip} values of 5 and 7 m/s.

Model	V_{tip} (m/s)	Q (m^3/h)	Experimental (mm)		HMMC (mm)		Ψ	Parameter value		
			D_{10}	D_{32}	D_{10}	D_{32}		k_1	k_2	k_3
CT	5	24	0.819±0.044	1.281±0.096	1.380	2.126	5.70e-01	1.776e-04	1.933e-01	–
		36	0.877±0.082	1.681±0.265	1.426	2.177	6.23e-01			
	7	24	0.671±0.048	1.055±0.060	0.673	1.178	5.70e-02			
		36	0.733±0.054	1.318±0.157	0.709	1.237	8.37e-02			
	6	24	0.733±0.048	1.210±0.197	0.791	1.135	3.71e-02			
		36	0.731±0.051	1.251±0.144	0.828	1.183	6.99e-02			
Chen	5	24	0.819±0.044	1.281±0.096	0.820	1.067	**4.70e-02**	1.936e- 02	1.000e-20^X	7.713e+00
		36	0.877±0.082	1.681±0.265	0.830	1.078	**9.54e-02**			
	7	24	0.671±0.048	1.055±0.060	0.654	0.887	**2.26e-02**			
		36	0.733±0.054	1.318±0.157	0.664	0.898	**5.91e-03**			
	6	24	0.733±0.048	1.210±0.197	0.663	0.845	**4.36e-02**			
		36	0.731±0.051	1.251±0.144	0.673	0.856	**1.26e-02**			
Alopaeus	5	24	0.819±0.044	1.281±0.096	1.222	1.742	4.47e-01	1.233e-02	7.504e-02	0.01*
		36	0.877±0.082	1.681±0.265	1.236	1.759	4.63e-01			
	7	24	0.671±0.048	1.055±0.060	0.652	0.980	8.27e-02			
		36	0.733±0.054	1.318±0.157	0.659	0.992	1.61e-01			
	6	24	0.733±0.048	1.210±0.197	0.751	1.044	5.71e-02			
		36	0.731±0.051	1.251±0.144	0.759	1.054	2.66e-02			

Note the under-prediction of D_{32} by all the models. This is because of the under-prediction of HMMC predicted number frequency near the shoulder region as shown in Figure 7.7. The presence of shoulder region indicates presence of unbroken large bubbles and the possibility of limited coalescence.
X: lower limit of k_2 for Chen model.

Table 7.5. 95% CIs for breakage model parameters estimated using *Coupled–Speed* optimization approach and $fmincon$ solver. Bootstrap resampling technique with 500 repetitions is used to calculate the CIs. The original point parameter estimates are reported in Table 7.3.

V_{tip} (m/s)	Breakage Model	95% CIs		
		k_1	k_2	k_3
5	CT	[2.844e-04, 2.856e-04]	[1.261e-01, 1.265e-01]	–
	Chen	[4.263e-03, 4.348e-03]	[5.749e-01, 5.832e-01]	[-3.631e+01, -3.571e+01]
	Alopaeus	[2.464e-02, 2.481e-02]	[7.071e-02, 7.129e-02]	[0.01, 0.01]
7	CT	[2.404e-04, 2.411e-04]	[2.739e-01, 2.745 e-01]	–
	Chen	[8.262e-03, 8.385e-03]	[8.397e-01, 8.511e-01]	[-3.333e+01, -3.275e+01]
	Alopaeus	[2.083e-02, 2.093e-02]	[1.763e-01, 1.771e-01]	[0.01, 0.01]

CHAPTER 8

SUMMARY AND RECOMMENDATIONS

8.1 Summary

In this research work, the hydrodynamics in lab scale flotation cells are investigated using the latest experimental and numerical techniques available. The presence of a stator around the impeller in the case of flotation cells makes it very difficult, if not impossible, to make credible measurements of flow velocities in the impeller stream. Moreover, there is a severe lack of published experimental data dealing with the single and multiphase hydrodynamics for generic flotation cell designs. To circumvent this problem, the mean flow behavior of a flotation impeller is studied in a stirred tank using a noninvasive PIV technique. Without the stator, the flow is observed to transition from a radial to axial-type flow below a critical value of off-bottom clearance. A steady state CFD study of the flow is carried out and the model predictions are compared against experimental measurements. The CFD model is able to correctly predict the mean flow pattern and local radial and axial velocities within reasonable accuracy. The flow transition to axial type flow results in a significant drop in power number, which has been reported in the past for the Rushton impeller. Using the developed CFD approach, the effect of impeller blade shape on mean flow behavior is studied, which suggested that the blade design with the largest surface area is the most efficient based on pumping efficiency calculations.

Single phase flows offer information about the bulk flow inside the flotation cell in general and are suitable for initial design exploration stage when using a complex multiphase model is not needed. However, the flows inside a flotation cell are both multiphase and polydisperse in nature. The volume fractions of both solid and gas phases are usually high enough to influence the behavior of continuous phase in flotation cells. Therefore, the multiphase flows are studied separately as solid-liquid and gas-liquid flows, since there are no mature models available in the current literature

that can deal with gas-solid-liquid flows in complex geometries. The Eulerian-Eulerian multifluid model is used to study the behavior of moderately dense slurries in lab scale flotation cell and stirred tank. The drag model is found to critically affect the mean solids holdup in the cell. Based on the comparisons against stirred tank flows, Gidaspow and Brucato models are found to perform satisfactorily. Electrical resistance tomography and cloud height measurements are made to further validate the numerical approach for flotation cell. The discrepancy between model predictions and measurements is attributed to the difference in particle sizes used. Also, the spatial resolution of ERT is limited which adds some error to the measurements. Overall, the developed CFD model offers a useful approach to study the behavior of dense slurries common to flotation.

Of all the hydrodynamic parameters affecting the efficiency of the flotation process, bubble size is perhaps the most important one. A coupled CFD-PBM model that uses the quadrature method of moments (QMOM) approach to solve moment transport equations is considered to study gas dispersion behavior, power draw behavior, and local bubble size distribution in stirred tanks and flotation cells. The predictions from CFD-PBM model are compared against measurements from Laakkonen et al. Laakkonen et al. [1] and from other CFD-PBM models proposed by Petitti et al.[110] and Laakkonen et al. [1]. Our model is observed to give accurate predictions of overall gas holdup and local bubble size distribution. For flotation cells, the effect of operating condition on flow regime revealed the formation of flooding and loading regimes at high aeration rates and low agitation rates, and transition and recirculating regimes are observed at moderate aeration rates and high agitation rates. The developed model can be extended to model flotation kinetics for small particle sizes assuming gas-pulp (liquid+solid) flow.

In plant operations, flotation cell is often modeled as a single unit and the important process parameter is the bubble size distribution and associated diameters. A simplified population balance model based on the assumption of spatial homogeneity inside the flotation cell is proposed. The high-order moment-conserving method of classes (HMMC) scheme is used to solve the nonlinear coupled population balance equations. Since the frother dosage over CCC is considered, coalescence in the

flotation cell is ignored and only bubble breakage is modeled. Using Matlab optimization solver, adjustable parameters in breakage rate models are identified using three optimization strategies. The 95% confidence intervals calculated using empirical bootstrap technique indicates high confidence in calculated point estimates. The HMMC model is found to accurately predict bubble size distribution for the majority of the cases, though the Sauter mean diameter is under-predicted for some cases because of formation of larger bubbles due to coalescence, which is not considered in the model.

8.1.1 Comments on Flotation Cell Design

Based on the experimental and numerical studies undertaken in this work, some general design guidelines for an efficient mechanical flotation cell can be prescribed. Though the number of studies comparing geometric variations is limited, some general remarks can be made, which are listed as follows:

- Based on the pumping performance comparison of four impeller blade profiles, the rectangular blade shape is found to be the most efficient design. Rectangular blade shape creates high turbulence dissipation rate values close to impeller, which is beneficial in the bubble breakup process. Moreover, the rectangular blade shape creates a strong lower recirculation zone compared to designs with smaller lip lengths. A strong recirculation zone is beneficial in many ways. For instance, it helps to suspend solid particles and enhances mixing and helps in better recirculation of smaller bubbles in the lower part of the cell.

- Impeller off-bottom clearance also plays a crucial role when dispersed phases are present. From the ERT experiments and Eulerian-Eulerian CFD simulations it is found that a higher clearance is more efficient at suspending and mixing solid particles at impeller speeds over 800 RPM for 60 mm impeller in a 300 mm diameter flotation cell. However, a high off-bottom clearance may be detrimental to formation of a stable froth in the quiescent zone of the cell when all three phases are considered. Therefore, an intermediate value between $D/12$ and $D/6$ must be considered. For the gas-liquid flows, an off-bottom clearance

of $D/8$ is used and found to be appropriate at moderate agitation and aeration rates.

- Impeller size also plays an important role in a flotation cell, though care must be taken since the power consumption scales as the fifth power of impeller diameter. In this work, two impeller sizes are used for multiphase flow studies: a small impeller corresponding to 20% of the tank diameter (D) and a large impeller corresponding to 25% of the tank diameter. For slurry flows, it is observed that a larger impeller is able to efficiently suspend and mix solid particles at lower rotation speeds at low off-bottom clearance of $D/12$. For gas-liquid flows, a rectangular blade impeller corresponding to 25% of tank diameter is used and found to disperse gas efficiently at both low and high aeration rates when agitation rate is sufficiently high. Therefore, using an impeller of larger size corresponding to 25% of the tank diameter can allow good mixing of solid phase and dispersion of air even at low impeller speeds and off-bottom clearance values.

8.2 Recommendations

The following recommendations are suggested as follow-up studies to improve the models used in this work and guide the development of new models specific to flotation cells.

- Extensive bubble size distribution measurements need to be made in generic flotation cell designs, which could be used to guide the development of new and advanced CFD models. Detailed bubble size distribution data, especially in the impeller stream and close to walls, can reveal the relative importance of breakage and coalescence events at different operating conditions.

- Recent work by Miskovic [4] has shown that considerable difference in local bubble size distribution exists inside the flotation cell even with the bulk concentration of frother over the so-called critical coalescence concentration. There is a need to develop newer nonintrusive bubble size measurement technique that can be used in the pulp region with confidence to obtain accurate bubble size

distribution measurements. Accurately estimating the bubble size distribution will help in the development of physical models for flotation rate constant estimation and minimize the number of fitting parameters.

- A network of zones or multiblock model based on the interconnected well mixed zones or blocks that is capable of predicting bubble size distributions in different regions of the cell could be developed. Laakkonen et al. [1] have developed a multiblock model for stirred tanks and used the bubble size distribution measurements to identify the adjustable parameters in breakage and coalescence models. The flow rates of continuous and dispersed phases between the zones can be obtained experimentally using techniques such as PIV or through CFD predictions of Laakkonen et al. [1]. Availability of the experimental data in generic cell designs with detailed description of cell design will make undertaking such studies possible.

- One of the bottlenecks faced during the course of our research was the limitation on the number of computational cores that could be used due to the license related limitation for ANSYS Fluent solver. Using matured open source alternatives like OpenFOAM will resolve the issues with license costs and allow solutions to more complicated cases. Also, open source codes allow users a greater freedom to add their own submodels or even change terms of the governing equation to suit their problem at hand. Moreover, models developed using open source codes are easier to share and make it easier to collaborate.

- The conditional quadrature method of moments (CQMOM) has been recently applied to gas-liquid flows in stirred tank [107]. The CQMOM approach offers a bivariate extension of QMOM approach with only a minor increase in computational time. A coupled CFD-PBM based on CQMOM approach can be used to track any two dispersed phase variables such as bubble size and frother coverage through mass transfer model. Using this information the local breakage and coalescence model parameters can be calculated based on the fractional coverage of bubble surface.

- In flotation cells, the two dispersed phases, namely solid and gas phase, are present in significant concentration. Also, due to the addition of flotation reagents their interaction becomes far more complex than what is usually observed in pure systems (pure water without contaminants or surfactants). Therefore, there is a need to develop both fundamental (microscale/nanoscale) and mesoscale (particle/bubble scale) models through experiments that could be used to develop multiscale CFD models considering the physicochemical effects.

- Finch et al. [9] have suggested that frother acts to (a) increase breakage rate of bubbles by increasing the surface stresses as the bubble is continuously deformed resulting in adsorption and desorption of frother molecules from the bulk, and (b) inhibit coalescence of bubbles by increasing the drainage time required to cause film rupture. To improve the understanding of breakage process, breakage cell must be devised and breakage events at different frother concentrations should be studied. Similarly, studies must be designed to measure the film drainage times at different frother concentrations to study the relative effect of bulk concentration on drainage rates. These studies will be useful towards creating fundamental breakage and coalescence models for flotation, which could be used in the population balance model to predict steady state bubble size distribution in the cells.

CHAPTER 9

WORKS CITED

[1] Laakkonen, M.; Moilanen, P.; Alopaeus, V.; Aittamaa, J. *Chemical Engineering Science* **2007**, *62*, 721–740.

[2] Ahmed, N.; Jameson, G. *International Journal of Mineral Processing* **1985**, *14*, 195 – 215.

[3] Koh, P.; Schwarz, M. *Minerals Engineering* **2008**, *21*, 989 – 993.

[4] Miskovic, S. An investigation of the gas dispersion properties of mechanical flotation cells: An in-situ approach. Ph.D. thesis, Virginia Polytechnic Institute and State University, 2011.

[5] Grau, R.; Heiskanen, K. *Minerals Engineering* **2005**, *18*, 1164 – 1172.

[6] Joshi, J.; Nandakumar, K. *Annual Review of Chemical and Biomolecular Engineering* **2015**, *6*, 347–378.

[7] Jones, R. M.; III, A. D. H.; Acharya, S. *Journal of Fluids Engineering* **2001**, *123(3)*, 640–648.

[8] Tamburini, A.; Cipollina, A.; Micale, G.; Brucato, A.; Ciofalo, M. *Chemical Engineering Journal* **2012**, *193-194*, 234 – 255.

[9] Finch, J. A.; Nesset, J. E.; Acua, C. *Minerals Engineering* **2008**, *21*, 949 – 957.

[10] Yianatos, J. B.; Bergh, L. G.; Daz, F.; Rodrguez, J. *Chemical Engineering Science* **2005**, *60*, 2273 – 2282.

[11] Koh, P.; Schwarz, M. *Minerals Engineering* **2003**, *16*, 1055–1059.

[12] Evans, G. M.; Doroodchi, E.; Lane, G. L.; Koh, P. T. L.; Schwarz, M. P. *Chemical Engineering Research and Design* **2008**, *86*, 1350–1362.

[13] Quinn, J.; Kracht, W.; Gomez, C.; Gagnon, C.; Finch, J. *Minerals Engineering* **2007**, *20*, 1296 – 1302.

[14] Grau, R.; Heiskanen, K. *Minerals Engineering* **2003**, *16*, 1081 – 1089, Froth Flotation.

[15] Micheletti, M.; Nikiforaki, L.; Lee, K. C.; Yianneskis, M. *Industrial & Engineering Chemistry Research* **2003**, *42*, 6236–6249.

[16] Lane, G. L.; Schwarz, M. P.; Evans, G. M. *Chemical Engineering Science* **2005**, *60*, 2203–2214.

[17] Cho, Y.; Laskowski, J. *International Journal of Mineral Processing* **2002**, *64*, 69 – 80.

[18] Comley, B.; Harris, P.; Bradshaw, D.; Harris, M. *International Journal of Mineral Processing* **2002**, *64*, 81 – 100.

[19] Joshi, J. B.; Nere, N. K.; Rane, C. V.; Murthy, B. N.; Mathpati, C. S.; Patwardhan, A. W.; Ranade, V. V. *The Canadian Journal of Chemical Engineering* **2011**, *89*, 23–82.

[20] Joshi, J. B.; Nere, N. K.; Rane, C. V.; Murthy, B. N.; Mathpati, C. S.; Patwardhan, A. W.; Ranade, V. V. *The Canadian Journal of Chemical Engineering* **2011**, *89*, 754–816.

[21] Montante, G.; Brucato, A.; Lee, K. C.; Yianneskis, M. *The Canadian Journal of Chemical Engineering* **1999**, *77*, 649–659.

[22] Montante, G.; Lee, K.; Brucato, A.; Yianneskis, A. M. *Chemical Engineering Science* **2001**, *56*, 3751–3770.

[23] Zhipeng, L.; Yuyun, B.; Zhengming, G. *Chemical Engineering Science* **2011**, *66*, 1219–1231.

[24] Galletti, C.; Brunazzi, E.; Pintus, S.; Paglianti, A.; Yianneskis, M. *Chemical Engineering Research and Design* **2004**, *82*, 1214 – 1228.

[25] Murthy, B.; Deshmukh, N.; Patwardhan, A.; Joshi, J. *Chemical Engineering Science* **2007**, *62*, 3839–3848.

[26] Singh, H.; Fletcher, D. F.; Nijdam, J. J. *Chemical Engineering Science* **2011**, *66*, 5976 – 5988.

[27] Gimbun, J.; Rielly, C. D.; Nagy, Z. K.; Derksen, J. J. *AIChE Journal* **2012**, *58*, 3224–3241.

[28] Basavarajappa, M.; Miskovic, S. Numerical Study of Single Phase Liquid Mixing in Stirred Tanks Fitted With Rushton Turbine and Flotation Impeller. 2013.

[29] Ansys, ANSYS FLUENT Theory Guide Release 14.5. 2013.

[30] Ng, K.; Yianneskis, M. *Chemical Engineering Research and Design* **2000**, *78*, 334 – 341.

[31] Wilcox, D. C. *Turbulence Modeling for CFD*; DCW Industries, 2010.

[32] Wu, H.; Patterson, G. K. *Chemical Engineering Science* **1989**, *44*, 2207–2221.

[33] Rutherford, K.; Mahmoudi, S.; L, E. K.; Yianneskis, M. *Trans IChemE* **1996**, *74*, 369–378.

[34] Li, Z.; Mengting, H.; Yuyun, B.; Zhengming, G. *Industrial & Engineering Chemistry Research* **2011**, *51*, 2438–2450.

[35] Murthy, B.; Joshi, J. *Chemical Engineering Science* **2008**, *63*, 5468 – 5495.

[36] Montante, G.; Lee, K.; Brucato, A.; Yianneskis, M. *Computers & Chemical Engineering* **2001**, *25*, 729 – 735.

[37] Delafosse, A.; Line, A.; Morchain, J.; Guiraud, P. *Chemical Engineering Research and Design* **2008**, *86*, 1322 – 1330, International Symposium on Mixing in Industrial Processes (ISMIP-VI).

[38] Koh, P.; Schwarz, M. CFD models of Micocel and Jameson Flotation Cells. 2009.

[39] Basavarajappa, M.; Miskovic, S. Gas dispersion characteristics in lab-scale flotation cell using Coupled CFD-PBM Quadrature Based Moment Method. 2015.

[40] Koh, P. T. L.; Smith, L. K. *Minerals Engineering* **2011**, *24*, 442–448.

[41] Karimi, M.; Akgodan, G.; Bradshaw, S. *Minerals Engineering* **2014**, *69*, 214 – 222.

[42] Koh, P.; Manickam, M.; Schwarz, M. *Minerals Engineering* **2000**, *13*, 1455–1463.

[43] Koh, P.; Schwarz, M.; Zhu, Y.; Bourke, P.; Peaker, R.; Franzidis, J. Development of CFD Models of Mineral Flotation Cells. 2003.

[44] Liu, T. Y.; Schwarz, M. P. *Chemical Engineering Science* **2009**, *64*, 52875301.

[45] Newell, R. Hydrodynamics and Scale-up in Rushton Turbine Flotation Cells. Ph.D. thesis, University of South Australia, 2006.

[46] Xia, J.; Rinne, A.; Grnstrand, S. *Minerals Engineering* **2009**, *22*, 880 – 885.

[47] Basavarajappa, M.; Draper, T.; Toth, P.; Ring, T.; Miskovic, S. *Minerals Engineering* **2015**, *83*, 156–167.

[48] Shi, S.; Zhang, M.; Fan, X.; Chen, D. *International Journal of Mineral Processing* **2015**, *Article in press*, 1 – 8.

[49] Kumaresan, T.; Joshi, J. B. *Chemical Engineering Journal* **2006**, *115*, 173 – 193.

[50] Liao, Y.; Lucas, D. *Chemical Engineering Science* **2009**, *64*, 3389 – 3406.

[51] Basavarajappa, M.; Alopaeus, V.; Miskovic, S. Application of High Order Moment conserving Method of Classes to Polydisperse Flows in Flotation Cells. 2015.

[52] Balachandar, S.; Eaton, J. K. *Annual Review of Fluid Mechanics* **2010**, *42*, 111–133.

[53] Ducci, A.; Yianneskis, M. *Chemical Engineering Science* **2006**, *61*, 2780 – 2790.

[54] Kresta, S. *The Canadian Journal of Chemical Engineering* **1998**, *76*, 563–576.

[55] Escudi, R.; Lin, A. *Chemical Engineering Science* **2006**, *61*, 2771 – 2779.

[56] Deglon, D. A.; Meyer, C. J. *Minerals Engineering* **2006**, *19*, 1059–1068.

[57] Huchet, F.; Line, A.; Morchain, J. *Chemical Engineering Research and Design* **2009**, *87*, 369–376.

[58] Basavarajappa, M.; Miskovic, S. *submitted* **2015**,

[59] Adrian, R. J.; Christensen, K. T.; Liu, Z.-C. *Experiments in Fluids* **2000**, *29*, 275–290.

[60] Nienow, A. W. *Chemical Engineering Science* **1996**, *52*, 2557–2565.

[61] Li, M.; White, G.; Wilkinsin, D.; Roberts, K. J. *Chemical Engineering Journal* **2005**, *108*, 81–90.

[62] Zwietering, T. N. *Chemical Engineering Science* **1958**, *8*, 244–253.

[63] Tamburini, A.; Cipollina, A.; Micale, G.; Brucato, A.; Ciofalo, M. *Chemical Engineering Journal* **2013**, *223*, 875 – 890.

[64] Wadnerkar, D. Modelling and simulation of carbon-in-leach circuits. Ph.D. thesis, Curtin University, 2013.

[65] Ayranci, I.; Machado, M. B.; Madej, A. M.; Derksen, J. J.; Nobes, D. S.; Kresta, S. M. *Chemical Engineering Science* **2012**, *79*, 163 – 176.

[66] Ayranci, I.; Kresta, S. M.; Derksen, J. J. *Chemical Engineering & Technology* **2013**, *36*, 1957–1967.

[67] Ayranci, I.; Kresta, S. M. *Chemical Engineering Research and Design* **2014**, *92*, 413 – 422.

[68] Micale, G.; Grisafi, F.; Brucato, A. *Chemical Engineering Research and Design* **2002**, *80*, 893 – 902, Fluid Mixing {VII}.

[69] Shah, R. S. S. R. E.; Sajjadi, B.; Raman, A. A. A.; Ibrahim, S. *Reviews in Chemical Engineering* **2015**, *31*, 119147.

[70] Van der Westhuizen, A. P.; Deglon, D. *Minerals Engineering* **2007**, *20*, 233 – 240.

[71] Van der Westhuizen, A.; Deglon, D. *Minerals Engineering* **2008**, *21*, 621 – 629.

[72] Lima, O.; Deglon, D.; Filho, L. L. *Minerals Engineering* **2009**, *22*, 1147 – 1153.

[73] Bakker, C.; Meyer, C.; Deglon, D. *Minerals Engineering* **2009**, *22*, 944 – 950, Special issue: Computational Modelling Special issue: Computational Modelling.

[74] Bakker, C.; Meyer, C.; Deglon, D. *Minerals Engineering* **2010**, *23*, 968 – 972, Froth Flotation.

[75] Shabalala, N.; Harris, M.; Filho, L. L.; Deglon, D. *Minerals Engineering* **2011**, *24*, 1448 – 1453.

[76] Kasat, G.; Khopkar, A.; Ranade, V.; Pandit, A. *Chemical Engineering Science* **2008**, *63*, 3877 – 3885.

[77] Derksen, J. J. *AIChE Journal* **2003**, *49*, 2700–2714.

[78] Khopkar, A. R.; Kasat, G. R.; Pandit, A. B.; Ranade, V. V. *Industrial & Engineering Chemistry Research* **2006**, *45*, 4416–4428.

[79] Ljungqvist, M.; Rasmuson, A. *Chemical Engineering Research and Design* **2001**, *79*, 533 – 546, Fluid Flow.

[80] Ochieng, A.; Onyango, M. S. *Powder Technology* **2008**, *181*, 1 – 8.

[81] Du, W.; Bao, X.; Xu, J.; Wei, W. *Chemical Engineering Science* **2006**, *61*, 1401 – 1420.

[82] Wadnerkar, D.; Utikar, R. P.; Tade, M. O.; Pareek, V. K. *Advanced Powder Technology* **2012**, *23*, 445 – 453, Special Issue Featuring Articles from Chemeca 2011.

[83] Brucato, A.; Brucato, V. *The Canadian Journal of Chemical Engineering* **1998**, *76*, 420–427.

[84] Pinneli, D.; Nocentini, M.; Magelli, F. *Chemical Engineering Communications* **2001**, *188*, 91–107.

[85] Su, M.; Han, W.; Zhang, Z.; Li, R.; Li, Q.; Ma, W. *Procedia Engineering* **2012**, *31*, 850 – 856, International Conference on Advances in Computational Modeling and Simulation.

[86] Gohel, S.; Joshi, S.; Azhar, M.; Horner, M.; Padron, G. *International Journal of Chemical Engineering* **2012**, *2012*, 9 pages.

[87] Lun, C. K. K.; Savage, S. B.; Jeffrey, D. J.; Chepurniy, N. *Journal of Fluid Mechanics* **1984**, *140*, 223–256.

[88] Ding, J.; Gidaspow, D. *AIChE Journal* **1990**, *36*, 523–538.

[89] Basavarajappa, M.; Miskovic, S. *Engineering Applications of Computational Fluid Mechanics (Submitted)* **2015**,

[90] Hosseini, S.; Patel, D.; Ein-Mozaffari, F.; Mehrvar, M. *Chemical Engineering Science* **2010**, *65*, 1374 – 1384.

[91] Angst, R.; Kraume, M. *Chemical Engineering Science* **2006**, *61*, 2864 – 2870, Fluid Mixing {VIII} International ConferenceFluid Mixing {VIII} International Conference.

[92] Barresi, A. A.; Baldi, G. Power consumption in slurry systems. 2000.

[93] Sardeshpande, M. V.; Sagi, A. R.; Juvekar, V. A.; Ranade, V. V. *Industrial & Engineering Chemistry Research* **2009**, *48*, 9713–9722.

[94] Jafari, R.; Tanguy, P. A.; Chaouki, J. *Chemical Engineering Research and Design* **2012**, *90*, 201 – 212.

[95] Sharifi, M.; Young, B. *Chemical Engineering Research and Design* **2013**, *91*, 1625 – 1645.

[96] Zhang, M.; Chu, K.; Wei, F.; Yu, A. *Powder Technology* **2008**, *184*, 151 – 165.

[97] Fernãndez, X. R.; Nirschl, H. *Chemical Engineering Science* **2013**, *94*, 7 – 19.

[98] SHAO, T.; HU, Y.; WANG, W.; JIN, Y.; CHENG, Y. *Chinese Journal of Chemical Engineering* **2013**, *21*, 1069 – 1081.

[99] Carletti, C.; Montante, G.; Westerlund, T.; Paglianti, A. *Chemical Engineering Science* **2014**, *119*, 53 – 64.

[100] ANSYS, *ANSYS FLUENT Theory Guide V16.1*; 2015.

[101] Salem-Said, A.-H.; Fayed, H.; Ragab, S. *Minerals* **2013**, *3*, 284 – 303.

[102] Guha, D.; Ramachandran, P. A.; Dudukovic, M. P.; Derksen, J. J. *AIChE Journal* **2008**, *54*, 766–778.

[103] Coulaloglou, C.; Tavlarides, L. *Chemical Engineering Science* **1977**, *32*, 1289 – 1297.

[104] Schwarz, M. P.; Koh, P. T. L.; Verrelli, D. I.; Feng, Y. *Minerals Engineering* **2015**,

[105] Koh, P.; Schwarz, M. *Minerals Engineering* **2006**, *19*, 619–626.

[106] Koh, P.; Schwarz, M. *International Journal of Mineral Processing* **2007**, *85*, 16–24.

[107] Petitti, M.; Vanni, M.; Marchisio, D. L.; Buffo, A.; Podenzani, F. *Chemical Engineering Journal* **2013**, *228*, 1182–1194.

[108] Karimi, M.; Akdogan, G.; Bradshaw, S. *Minerals Engineering* **2014**, *69*, 214–222.

[109] Alopaeus, V.; Koskinen, J.; Keskinen, K. I. *Chemical Engineering Science* **1999**, *54*, 5887 – 5899.

[110] Petitti, M.; Nasuti, A.; Marchisio, D. L.; Vanni, M.; Baldi, G.; Mancini, N.; Podenzani, F. *AIChE Journal* **2010**, *56*, 36–53.

[111] Buffo, A.; Vanni, M.; Marchisio, D. L. *Chemical Engineering Science* **2012**, *70*, 31–44.

[112] Ramkrishna, D. *Population balances: Theory and applications to particulate systems in engineering*; Academic press, 2000.

[113] McGraw, R. *Aerosol Science and Technology* **1997**, *27*, 255–265.

[114] Kerdouss, F.; Bannari, A.; Proulx, P. *Chemical Engineering Science* **2006**, *61*, 3313–3322.

[115] Marchisio, D. L.; Vigil, R.; Fox, R. O. *Journal of Colloid and Interface Science* **2003**, *258*, 322–334.

[116] Marchisio, D. L.; Vigil, R. D.; Fox, R. O. *Chemical Engineering Science* **2003**, *58*, 3337–3351.

[117] Wang, T.; Wang, J. *Chemical Engineering Science* **2007**, *62*, 7107–7118.

[118] Laakkonen, M.; Alopaeus, V.; Aittamaa, J. *Chemical Engineering Science* **2006**, *61*, 218 – 228.

[119] Gimbun, J.; Rielly, C.; Nagy, Z. *Chemical Engineering Research and Design* **2009**, *87*, 437–451.

[120] Selma, B.; Bannari, R.; Proulx, P. *Chemical Engineering Science* **2010**, *65*, 1925–1941.

[121] Marchisio, D. L.; Fox, R. O. *Journal of Aerosol Science* **2005**, *36*, 43–73.

[122] Basavarajappa, M.; Miskovic, S. *Minerals Engineering* **2016**, *95*, 161–184.

[123] Wright, D. L. *Journal of Aerosol Science* **2007**, *38*, 352–369.

[124] McGraw, R. *Climate Models*; 2012; pp 1–20.

[125] Lanczos, C. *Applied Analysis (Dover Books on Mathematics)*; 2010.

[126] Acher, T.; Dems, P.; Lenz, S.; Gobert, C.; Polifke, W. *Journal of Computational Multiphase Flows* **2013**, *6*, 457–474.

[127] Montante, G.; Horn, D.; Paglianti, A. *Chemical Engineering Science* **2008**, *63*, 2107–2118.

[128] Kálal, Z.; Jahoda, M.; Fořt, I. *Chemical and Process Engineering* **2014**, *35*, 55–73.

[129] Kolev, N. I. *Multiphase Flow Dynamics 2 - Mechanical Interactions*; Springer, 2012.

[130] Lane, G. L. Computational Modelling of Gas-Liquid Flow in Stirred Tanks. Ph.D. thesis, The University of Newcastle, 2006.

[131] Drumm, C.; Attarakih, M. M.; Bart, H.-J. *Chemical Engineering Science* **2009**, *64*, 721–732.

[132] Gordon, R. G. *Journal of Mathematical Physics* **1968**, *9*, 655.

[133] McGraw, R. *Correcting moment sequence for errors associated with advective transport*; 2006.

[134] Binkowski, F. S. *Journal of Geophysical Research* **2003**, *108*, 4183.

[135] Alopaeus, V.; Koskinen, J.; Keskinen, K. I.; Majander, J. *Chemical Engineering Science* **2002**, *57*, 1815 – 1825.

[136] Liao, Y.; Lucas, D. *Chemical Engineering Science* **2010**, *65*, 2851–2864.

[137] Laakkonen, M. Development and Validation of Mass Transfer Models for the Design of Agitated Gas-Liquid Reactors. PhD Thesis, Helsinki University of Technology, 2006.

[138] Yeoh, G. H.; Tu, J. *Computational Techniques for Multiphase Flows*, 1st ed.; Butterworth-Heinemann, 2009; p 664.

[139] Midoux, N.; Charpentier, J. C. *International Chemical Engineering* **1984**, *24*, 249–287.

[140] Bujalski, W.; Nienow, A.; Chatwin, S.; Cooke, M. *Chemical Engineering Science* **1987**, *42*, 317–326.

[141] Khopkar, A. R.; Rammohan, A. R.; Ranade, V. V.; Dudukovic, M. P. *Chemical Engineering Science* **2005**, *60*, 2215–2229.

[142] Smith, J. *Chemical Engineering Research and Design* **2006**, *84*, 265–271.

[143] John, V.; Angelov, I.; Öncül, A.; Thévenin, D. *Chemical Engineering Science* **2007**, *62*, 2890–2904.

[144] Pope, S. B. *Journal of Non-Equilibrium Thermodynamics* **1979**, *4*, 309–320.

[145] Baldyga, J.; Orciuch, W. *Chemical Engineering Science* **2001**, *56*, 2435–2444.

[146] Sanyal, J.; Sanyal, J.; Marchisio, D. L.; Marchisio, D. L.; Fox, R. O.; Fox, R. O.; Dhanasekharan, K.; Dhanasekharan, K. *Industrial & Engineering Chemistry Research* **2005**, *44*, 5063–5072.

[147] Lebaz, N.; Cockx, A.; Spérandio, M.; Morchain, J. *Computers & Chemical Engineering* **2015**, *84*, 326–337.

[148] Chen, Z.; Pruss, J.; Warnecke, H.-J. *Chemical Engineering Science* **1998**, *53*, 1059 – 1066.

[149] Deglon, D.; Sawyerr, F.; O'Connor, C. *Minerals Engineering* **1999**, *12*, 599 – 608.

[150] Gorain, B.; Franzidis, J.-P.; Manlapig, E. *Minerals Engineering* **1995**, *8*, 615 – 635.

[151] Nesset, J. E.; Hernandez-Aguilar, J. R.; Acuna, C.; Gomez, C. O.; Finch, J. A. *Minerals Engineering* **2006**, *19*, 807 – 815, Selected papers from the Centenary of Flotation Symposium, 59 June 2005, Brisbane, Australia.

[152] Cho, Y. S.; Laskowski, J. S. *The Canadian Journal of Chemical Engineering* **2002**, *80*, 299–305.

[153] Grau, R. A.; Laskowski, J. S. *The Canadian Journal of Chemical Engineering* **2006**, *84*, 170–182.

[154] Kracht, W.; Finch, J. *International Journal of Mineral Processing* **2009**, *92*, 153 – 161.

[155] Kracht, W.; Finch, J. *International Journal of Mineral Processing* **2010**, *94*, 115 – 120.

[156] Amini, E.; Bradshaw, D.; Finch, J.; Brennan, M. *Minerals Engineering* **2013**, *45*, 146 – 150.

[157] Miskovic, S.; Luttrell, G. *Separation Technologies for Minerals, Coal, and Earth Resources*; 2012.

[158] Jávor, Z.; Schreithofer, N.; Heiskanen, K. *International Journal of Mineral Processing* **2014**, *127*, 16 – 22.

[159] Jávor, Z.; Schreithofer, N.; Heiskanen, K. *Minerals Engineering* **2015**, *70*, 109 – 118.

[160] Sawyerr, F.; Deglon, D.; O'Connor, C. *Journal of the South African Institute of Mining and Metallurgy* **1998**, *98*, 179–185.

[161] Nesset, J. E.; Zhang, W.; Finch, J. A. A benchmarking tool for assessing flotation cell performance. 2012.

[162] Kowalczuk, P. B. *Industrial & Engineering Chemistry Research* **2013**, *52*, 11752–11757.

[163] Alopaeus, V.; Laakkonen, M.; Aittamaa, J. *Chemical Engineering Science* **2006**, *61*, 6732 – 6752.

[164] Ramkrishna, D.; Singh, M. R. *Annual Review of Chemical and Biomolecular Engineering* **2014**, *5*, 123–146.

[165] Kumar, S.; Ramkrishna, D. *Chemical Engineering Science* **1996**, *51*, 1311 – 1332.

[166] Vanni, M. *Journal of Colloid and Interface Science* **2000**, *221*, 143 – 160.

[167] Tse, K.; Martin, T.; McFarlane, C.; Nienow, A. *Chemical Engineering Science* **2003**, *58*, 275 – 286.

[168] Andersson, R.; Andersson, B. *AIChE Journal* **2006**, *52*, 2020–2030.

[169] Rodriguez-Rodriguez, J.; Gordillo, J. M.; Martinez-Bazn, C. *Journal of Fluid Mechanics* **2006**, *548*, 69– 86.

[170] Lasheras, J.; Eastwood, C.; Martinez-Bazn, C.; Montas, J. *International Journal of Multiphase Flow* **2002**, *28*, 247 – 278.

[171] Narsimhan, G.; Gupta, J.; Ramkrishna, D. *Chemical Engineering Science* **1979**, *34*, 257 – 265.

[172] Ata, S.; Ahmed, N.; Jameson, G. J. *International Journal of Mineral Processing* **2003**, *72*, 255 – 266.

[173] Ata, S. *Langmuir* **2008**, *24*, 6085–6091, PMID: 18484761.

[174] Zhang, W.; Nesset, J. E.; Rao, R.; Finch, J. A. *Minerals* **2012**, *2*, 208–227.

[175] Gomez, C.; Finch, J. *International Journal of Mineral Processing* **2007**, *84*, 51 – 58.

[176] Efron, B.; Tibshirani, R. J. *An introduction to the bootstrap*; CRC press, 1994.

[177] Orloff, J.; Bloom, J. Introduction to Probability and Statistics. (Massachusetts Institute of Technology: MIT OpenCourseWare), 2014.

[178] Solsvik, J.; Becker, P. J.; Sheibat-Othman, N.; Jakobsen, H. A. *The Canadian Journal of Chemical Engineering* **2014**, *92*, 1082–1099.

[179] Maindarkar, S. N.; Raikar, N. B.; Bongers, P.; Henson, M. A. *Colloids and Surfaces A: Physicochemical and Engineering Aspects* **2012**, *396*, 63 – 73.

[180] Raikar, N. B.; Bhatia, S. R.; Malone, M. F.; Henson, M. A. *Chemical Engineering Science* **2009**, *64*, 2433 – 2447.